

# **Bacterial chemotaxis: sensory adaptation, noise filtering, and information transmission**

Dissertation to obtain the degree  
Philosophiæ Doctor (PhD) of Imperial College London  
and  
Diploma of Imperial College London (DIC)

presented by

Diana Claußnitzer  
born September 1, 1982 in Bautzen (Germany)  
College Identifier Number 00543225

Division of Molecular Biosciences  
Imperial College London

2011

Supervisors:

Dr Robert Endres	Prof Michael Stumpf
Imperial College London	Imperial College London

Examiners:

Dr Mauricio Barahona	Dr Thomas Duke
Imperial College London	University College London



---

I certify that this thesis, and the research to which it refers, are the product of my own work, and that any ideas or quotations from the work of other people, published or otherwise, are fully acknowledged in accordance with the standard referencing practises of the discipline. London, November 30, 2010.

---

Diana Claußnitzer

The copyright of this thesis rests with the author and no quotation from it or information derived from it may be published without the prior written consent of the author.

---

# Abstract

Chemotaxis is a fundamental cellular process by which cells sense and navigate in their environment. The molecular signalling pathway in the bacterium *Escherichia coli* is experimentally well-characterised and, hence, ideal for quantitative analysis and modelling. Chemoreceptors sense gradients of a multitude of substances and regulate an intracellular signalling pathway, which modulates the swimming behaviour. We studied the chemotaxis pathway in *E. coli* (*i*) to quantitatively understand molecular interactions in the signalling network, (*ii*) to gain a systems view of the workings of the pathway, including the effects of noise generated by biomolecular reactions during signalling, and (*iii*) to understand general design principles relevant for many sensory systems. Specifically, we investigated the adaptation dynamics due to covalent chemoreceptor modification, which includes numerous layers of feedback regulation. In collaboration with an experimental group, we undertook quantitative experiments using wild-type cells and mutants for proteins involved in adaptation using *in vivo* fluorescence resonance transfer (FRET). We developed a dynamical model for chemotactic signalling based on cooperative chemoreceptors and adaptation of the sensory response. This model quantitatively explains an interesting asymmetry of the response to favourable and unfavourable stimuli observed in the experiments. In a whole-pathway description, we further studied the response to controlled concentration stimuli, as well as how fluctuations from the environment and due to intracellular signalling affect the detection of input signals. Finally, the chemotaxis pathway is characterised by high sensitivity, a wide dynamic range and the need for information transmission, properties shared with many other sensory systems. Based on FRET data, we investigated the emergence, limits and biological significance of Weber's law which predicts that the system detects stimuli relative to the background stimulus. Furthermore, we studied the information transmission from input concentrations into intracellular signals. We connect Weber's law, as well as information transmission, to swimming bacteria and predict typically encountered chemical inputs.

---

# Acknowledgements

First and foremost, I would like to thank my supervisor, Robert Endres. Thanks for your continuous advice and always having time for discussions! I thank Victor Sourjik and his research group, in particular Olga Oleksiuk and Linda Løvdok, for providing experimental data. It was invaluable to work with you! I also thank Sylvain Tollis, Gerardo Aquino, Luke Tweedy and Anna Dart, who taught me a lot and made “life” in our research group interesting. I thank Michael Stumpf and Krishnan for their general advice and support. I thank Jeroen van Zon, Ozan Kahramanoğulları and Ruian Ke, who by now have moved on to new scientific challenges but made my start at Imperial College easy. Thanks also go to Heather Harrington, Mariano Beguerisse Diaz, Andy McDonagh and Piers Ingram who were fun and often had invaluable advice on questions ranging from science to philosophy. I thank Naomi Anderson-Eyles, Coralie Simmons, Suhail Islam and Louise English for administrative support throughout my PhD. Thanks also go to the many visitors to Imperial College who always brought new perspectives with them. In particular, I thank Ned Wingreen, Tom Shimizu and William Ryu for helpful discussions. Finally, I thank Allen Lister for offering his continuous support and perspective - I could not have done this without you.

# Contents

<b>Abstract</b>	<b>5</b>
<b>Acknowledgements</b>	<b>7</b>
<b>1. Introduction</b>	<b>17</b>
1.1. The biology of chemotaxis . . . . .	17
1.1.1. Chemosensory clusters . . . . .	20
1.1.2. The rotary motor . . . . .	24
1.1.3. Robustness of chemotaxis . . . . .	29
1.1.4. <i>In vivo</i> fluorescence resonance energy transfer (FRET) . . . . .	29
1.2. Previous modelling work on chemotaxis signalling . . . . .	30
1.2.1. Two-state model for independent chemoreceptors . . . . .	30
1.2.2. Signal amplification by cooperative chemoreceptors . . . . .	33
1.2.3. Robust and precise adaptation . . . . .	36
1.2.4. Models for the rotary motor . . . . .	37
1.3. Aims of this work . . . . .	38
<b>2. Sensory adaptation of receptors</b>	<b>40</b>
2.1. Synopsis . . . . .	40
2.2. Motivation & open questions . . . . .	41
2.3. Details of experimental measurements . . . . .	42
2.4. Dynamic Monod-Wyman-Changeux (MWC) model for chemotactic signalling	45
2.5. Comparison of experiment and theory . . . . .	50
2.6. Model predictions, verification and adjustments . . . . .	52
2.6.1. Data collapse of time courses for adaptation dynamics . . . . .	52
2.6.2. Quantification of adaptation imprecision . . . . .	56
2.6.3. Comparison of different adaptation models . . . . .	57



2.6.4. Demethylation dynamics . . . . .	58
2.7. Discussion . . . . .	61
<b>3. Weber’s law</b>	<b>64</b>
3.1. Synopsis . . . . .	64
3.2. Motivation & open questions . . . . .	64
3.3. Weber’s law in chemotactic signalling . . . . .	67
3.4. Threshold stimulus . . . . .	69
3.5. Perception . . . . .	70
3.6. Predicting typical gradients . . . . .	71
3.7. Discussion . . . . .	72
<b>4. Signal transmission and noise filtering</b>	<b>76</b>
4.1. Synopsis . . . . .	76
4.2. Motivation & open questions . . . . .	76
4.3. Simplified model for the pathway . . . . .	78
4.4. Signal transmission . . . . .	81
4.4.1. Definitions . . . . .	81
4.4.2. Experimental determination of the response function . . . . .	82
4.4.3. Analytical results for linear response function . . . . .	83
4.4.4. Model calibration . . . . .	84
4.4.5. Model analysis . . . . .	85
4.5. Noise creation, amplification and filtering . . . . .	86
4.5.1. Definitions . . . . .	86
4.5.2. Intensities and spectra of noise sources . . . . .	87
4.5.3. Analytical results for signalling noise spectra . . . . .	90
4.5.4. Model analysis . . . . .	91
4.6. Cell-to-cell variation of motor behaviour . . . . .	92
4.7. Signal-to-noise ratio . . . . .	93
4.7.1. Definition . . . . .	93
4.7.2. Receptor complex size and ambient concentration . . . . .	94
4.7.3. Adaptation rate constants . . . . .	96
4.8. Discussion . . . . .	97

<b>5. Information transmission</b>	<b>101</b>
5.1. Synopsis . . . . .	101
5.2. Motivation & open questions . . . . .	101
5.3. Results . . . . .	103
5.3.1. Mutual information for a Gaussian channel with small noise . . . . .	103
5.3.2. Optimal distributions of inputs and outputs . . . . .	104
5.3.3. FRET dose-response curves for Tar only cells . . . . .	106
5.3.4. Principal component analysis (PCA) . . . . .	107
5.3.5. Optimal input and output distributions for Tar only cells . . . . .	108
5.3.6. Scaling behaviour of predicted input distributions . . . . .	110
5.4. Discussion . . . . .	110
<b>6. Conclusions</b>	<b>114</b>
<b>Appendices</b>	<b>117</b>
<b>A. Whole-pathway model for chemotactic signalling</b>	<b>118</b>
A.1. Rescaling of parameters . . . . .	119
A.2. Steady-state concentrations . . . . .	120
A.3. Time courses and steady-state assumption . . . . .	121
<b>B. Additional data and best fit of dynamic MWC model</b>	<b>124</b>
<b>C. Unsuitable receptor signalling models</b>	<b>126</b>
C.1. Saturation model . . . . .	126
C.2. Imprecise adaptation model . . . . .	126
C.3. Phase-separation model . . . . .	127
C.4. Receptor lattice model . . . . .	127
<b>D. Parameters for static and dynamic MWC model</b>	<b>131</b>
<b>E. Comparison of different adaptation models</b>	<b>132</b>
<b>F. Analysis of adaptation noise</b>	<b>135</b>
<b>G. Weber's law for Tar and Tsr receptors</b>	<b>140</b>
<b>H. Derivation of the threshold activity from signalling noise</b>	<b>142</b>

<b>I. Probing the adaptation dynamics using exponential ramps</b>	<b>146</b>
<b>J. Response function and noise spectra for the full pathway model</b>	<b>150</b>
J.1. Stochastic differential equations . . . . .	150
J.2. Model for motor switching . . . . .	151
J.3. Linearisation of the model . . . . .	152
J.4. Response functions . . . . .	153
J.5. Noise spectra . . . . .	154
J.6. Parameters . . . . .	155
<b>K. Integrated signal response, variance and SNR of the total receptor activity</b>	<b>158</b>
K.1. Receptor complex size . . . . .	158
K.2. Methylation and demethylation rate constants . . . . .	159
<b>L. Master equation approach for receptor signalling</b>	<b>161</b>
<b>M. Langevin description for motor dynamics</b>	<b>163</b>
<b>N. Justification for linear noise approximation for intracellular signalling noise</b>	<b>165</b>
<b>O. High-frequency filters</b>	<b>167</b>
<b>P. Parameters for predicted input and output distributions</b>	<b>169</b>
<b>Bibliography</b>	<b>171</b>

# List of Figures

1.1. Chemotaxis strategy and signalling pathway in <i>Escherichia coli</i> . . . . .	19
1.2. Imaging chemoreceptors clusters. . . . .	21
1.3. Signalling by chemoreceptors. . . . .	22
1.4. Schematics of the <i>E. coli</i> rotary motor. . . . .	24
1.5. Experimental data for rotary motor stepping. . . . .	25
1.6. Experimental data for motor speed. . . . .	26
1.7. Experimental data for motor switching. . . . .	27
1.8. Response function and power spectrum of the motor. . . . .	28
1.9. <i>In vivo</i> FRET to measure chemotaxis signalling activity . . . . .	30
1.10. Two-state model for receptor. . . . .	32
1.11. Lattice model for chemoreceptors and analogy to ferromagnetism. . . . .	35
2.1. Time courses and dose-response curves from FRET. . . . .	44
2.2. Model ingredients for dynamic MWC model. . . . .	47
2.3. Adapted receptor methylation level as a function of ambient concentration. . . . .	48
2.4. Response of wild-type cells to step changes of MeAsp concentration. . . . .	50
2.5. Changes in the free-energy difference of a mixed-receptor complex upon concentration step changes. . . . .	51
2.6. Residual errors for dose-response curves for the static and dynamic MWC model. . . . .	51
2.7. Time courses of wild-type cells to concentration step changes. . . . .	52
2.8. Effect of ligand concentration-dependent receptor complex size on the pre- dicted data collapse. . . . .	53
2.9. Adaptation dynamics as function of receptor activity for wild-type cells for concentration step changes. . . . .	54
2.10. Imprecision of adaptation. . . . .	57

2.11. Comparison of different adaptation models. . . . .	58
2.12. Effects of steady-state activity and CheB regulation by phosphorylation on adaptation dynamics. . . . .	59
3.1. Extraction of the threshold stimulus from dose-response curves. . . . .	67
3.2. Weber's law in <i>E. coli</i> chemotaxis. . . . .	68
3.3. Perception in <i>E. coli</i> chemotaxis. . . . .	71
3.4. Perception of different spatial concentration profiles. . . . .	72
4.1. Switching rates of the motor as a function of the concentration of signalling mutant $Y^{**}$ . . . . .	81
4.2. Measured response function for the chemotaxis pathway. . . . .	84
4.3. Calculated chemotaxis pathway response upon impulse stimulation. . . . .	86
4.4. Calculated noise spectra for the chemotaxis pathway. . . . .	91
4.5. Effect of cell-to-cell variation on power spectrum of the motor. . . . .	93
4.6. Effect of varying ambient concentration and receptor complex size. . . . .	94
4.7. Effect of varying receptor methylation and demethylation rate constants. . . . .	96
4.8. Comparison of the chemotaxis pathway and other two-component systems. . . . .	100
5.1. Maximising the mutual information. . . . .	105
5.2. FRET dose-response curves for Tar only cells. . . . .	106
5.3. Illustration of principle component analysis. . . . .	107
5.4. Predicted optimal input and output distributions. . . . .	108
5.5. Log-normal scaling of the optimal input distributions. . . . .	111
5.6. Input distributions of simulated swimming bacteria. . . . .	112
A.1. Schematics of the chemotaxis pathway and biochemical reactions. . . . .	119
A.2. Steady-state concentrations of individual proteins and CheY-P/CheZ pairs for the whole-pathway model as a function of the receptor complex activity. . . . .	122
A.3. Time courses for the concentrations of phosphorylated proteins and CheY- P/CheZ pairs according to the whole-pathway model. . . . .	123
B.1. Dynamic MWC model, additional dose-response curves and best fit. . . . .	125
C.1. Alternative models for receptor signalling. . . . .	128

## List of Figures

---

G.1. Threshold stimulus for mixed Tar/Tsr receptor complexes and homogeneous Tar and Tsr receptor complexes. . . . .	141
I.1. Receptor complex activity for exponential concentration ramps. . . . .	147
M.1. Variance of the motor bias as a function of CheY-P noise intensity for Langevin and two-state dynamics. . . . .	164
N.1. Contributions from CheA autophosphorylation, CheY and CheB phosphorylation and dephosphorylation to the power spectrum of CheY-P. . . . .	166

# List of Tables

A.1. Parameters of the whole-pathway model for chemotaxis signalling. . . . .	121
D.1. Fitting parameters for the static and dynamic MWC model. . . . .	131
E.1. Parameters of the adaptation models when fitted to the rate of activity change from FRET. . . . .	133
J.1. Parameters of the full pathway model. . . . .	156
J.2. Intensities of noise terms in full pathway model. . . . .	156
J.3. Parameters of the linearised equations for the full pathway. . . . .	157
J.4. Fitting parameters for response function of the full pathway model. . . . .	157
J.5. Parameters for Fig. 4.5 in chapter 4. . . . .	157
P.1. Parameters of the fit of the MWC model to Tar only dose-response curves.	169
P.2. Number of principle components used for fitting the MWC model to Tar only dose-response curves. . . . .	169
P.3. Parameters for the fit of the variance in the FRET activity of Tar only cells.	170
P.4. Parameters of the fit of log-normal distributions to the predicted optimal input distributions. . . . .	170





# 1. Introduction

## 1.1 The biology of chemotaxis

---

Chemotaxis is a basic cellular process by which cells sense particular molecules in their environment and direct their motility along chemical gradients of those molecules. For unicellular organisms, chemotaxis is a means to navigate their physical environment, in order to find and colonise more favourable habitats. Besides nutrients and toxic substances a multitude of stimuli can be sensed, such as pH, temperature, oxygen, and light (Lux et al., 2000), reflecting the various sources of information cells need to integrate to generate an appropriate response to their environment. Often, chemotaxis is implicated in pathogenic, as well as symbiotic associations with host organisms (Pittman et al., 2001; O'Toole et al., 1999; Kim and Farrand, 1998; Pandya et al., 1999). Chemotaxis has also been implicated in social behaviours of unicellular organisms. For instance, the amoeba *Dictyostelium* secretes the molecule cAMP under starvation, which serves as a chemoattractant to other cells, triggering cellular aggregation (Gerisch, 1982). In multicellular organisms, chemotaxis occurs during development, and in the adult organisms it is normally only retained in specialised cells with crucial physiological functions, e.g. the cells of the immune system and sperm cells. However, it can become relevant in cancer metastasis when normally non-motile cells become motile, invasive tumour cells (Condeelis et al., 2001). The study of bacterial chemotaxis, specifically that of *Escherichia coli*, has progressed immensely, and is a paradigm for chemosensing in general (Lux et al., 2000).

Bacteria live in a variety of habitats, such as soil or the human intestines, and are typically faced with a dynamic chemical environment of temporal and spacial gradients. Furthermore, the colonisation of habitats often depends on the successful competition for nutrients with other microorganisms (Kennedy, 1987). The bacterium *Escherichia coli* is a member of the highly stable commensal microbiota inhabiting the gastrointestinal tract of humans and animals, where it grows in the mucus layer secreted by the intestinal epithelium (Poulsen et al., 1994; Gauger et al., 2007). The commensal microbiota, which

consists of hundreds of different bacterial species present at high cell densities (Poulsen et al., 1994), has important functions for the host, breaking down undigested food and thereby providing additional energy sources, as well as providing resistance against colonisation by pathogens (Nataro, 2005). On the other hand, there are a variety of pathogenic *E. coli* strains which can cause serious infections of the gastrointestinal and urinary tract (including enteropathogenic, enterohaemorrhagic, and uropathogenic *E. coli*, or short EPEC, EHEC and UPEC, respectively), as well as neonatal meningitis. These pathogenic strains have up to  $10^6$  bases larger genomes than commensal strains after acquiring so-called pathogenicity islands, i.e. large genetic clusters of virulence genes which are not found in non-pathogenic strains (Croxen, 2010). The intestinal mucus layer is highly dynamic, being constantly secreted by epithelial cells, degraded by the microbiota and washed into the lumen of the intestine. Colonisation, i.e. stable persistence, of microorganisms in this environment requires them to compete with the indigenous flora for nutrients, as well as replenishing their numbers at a rate equal to the rate of turnover of the mucus layer (Gauger et al., 2007).

The role of motility, and indeed chemotaxis, in the colonisation of the intestines is complex (Gauger et al., 2007; Girón, 2005). Microbial chemotaxis in the intestines can generally have several roles, including taxis to food or components of the mucus layer, penetration and persistence in the mucus layer, which is constantly washed into the lumen of the intestines, and finally to adhere to or invade epithelial cells. Chemotaxis has been implicated in the successful colonisation of the gastrointestinal tract of host animals by a number of pathogenic bacteria species, e.g. *Helicobacter pylori* and *Campylobacter jejuni*, which do not attach to the epithelium and instead use chemotaxis to stay within the mucus layer (Lee et al., 1986; Blaser, 1997; Butler and Camilli, 2005). Interestingly, for the cholera bacterium *Vibrio cholerae* it has been suggested there exists a chemical gradient guiding cells to a specific part of the intestinal tract (Butler and Camilli, 2005). Furthermore, *V. cholerae* uses chemotaxis to penetrate the mucus layer and move specifically to the intestinal crypts, sites of epithelial cells generation and enzyme production (Butler and Camilli, 2005).

The exact role of chemotaxis for *E. coli* in the intestines is unknown. However, similar mechanisms as those just described could be important and enable cells to remain in specific niches within the mucus layer (Kennedy, 1987; Hao and Lee, 2004; Rawls et al., 2007; Gauger et al., 2007). Alternatively, it may also have advantages for the survival outside

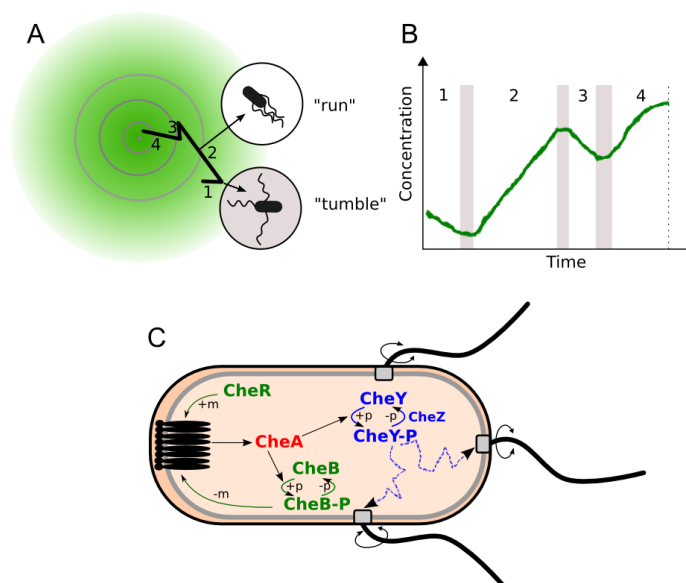


**Figure 1.1.:** Chemotaxis strategy and signalling pathway in *Escherichia coli*. (A) Swimming path consists of consecutive “runs” interrupted by “tumbles”. Runs are biased to be longer when swimming up attractant gradient, and shorter when swimming down attractant gradient. (B) The chemical concentration sampled by the bacterium along the swimming path in the gradient in panel A. (C) Chemotaxis signalling pathway from receptors to rotary motors and flagella, including phosphotransfer from CheA to CheY and CheB, CheY-P diffusion to rotary motors, and dephosphorylation of CheY-P by phosphatase CheZ. Adaptation involves receptor methylation by CheR and demethylation by CheB-P.

the host. Recent advances in experimental methods, such as *in vivo* endomicroscopy (Kim et al., 2010), may be used to elucidate the physiological role of chemotaxis in bacterial species in the intestines in the future.

Like most bacteria, *E. coli* senses gradients temporally, detecting the concentration of chemicals along its swimming path, rather than spatially by comparing concentration differences along its circumference. Temporal sensing is thought to be exhibited by small organisms as thermal fluctuations render concentration differences along the cell length unreliable (Berg and Purcell, 1977). The swimming strategy is a biased random walk towards a nutrient source or away from a toxin source (Berg, 2000; Falke and Hazelbauer, 2001; Sourjik, 2004; Wadhams and Armitage, 2004). The swimming path consists of runs, i.e. straight swimming of the cell, and tumbles characterised by lack of net movement and random reorientation of the cell (Fig. 1.1 A and B).

The molecular components of the chemotaxis signalling pathway and relationships between them are well-characterised (Kentner and Sourjik, 2009), and are shown schematically in Fig. 1.1 C. Transmembrane chemoreceptors sense various different ligands. Ligand binding to receptors induces their signalling across the membrane to the histidine kinase

CheA (chemotaxis protein A). When active, CheA autophosphorylates and rapidly passes on a phosphoryl group to its response regulators CheY and CheB. Phosphorylated CheY (CheY-P) diffuses to rotary motors, each of which drives a flagellum, i.e. a helical appendage protruding from the cell membrane. Upon binding to the motors, CheY-P induces a switch in their rotary direction, resulting in tumbling. CheZ is a phosphatase of CheY-P. Attractant binding reduces the activity of CheA, lowering the concentration of CheY-P in the cell, and therefore suppressing tumbling. In contrast, repellents cause an increase of activity, enhancing tumbling. There is also a mechanism for sensory adaptation, i.e. the reversal of the initial signalling response in the presence of a persistent stimulus. Adaptation is catalysed by the enzymes CheR and CheB. CheR methylates receptors to enhance their signalling activity. Phosphorylated CheB (CheB-P) demethylates receptors, which reduces their activity. During persistent stimulation by a chemical, the combined effect of receptor methylation by CheR and demethylation by CheB-P leads to adaptation of the kinase activity to a steady-state, allowing the sensing of new changes in attractant or repellent concentrations.

Chemotaxis belongs to a typical class of bacterial sensory systems, so-called two-component systems (Laub and Goulian, 2007). Two-component systems consist of a kinase activating a response regulator. Kinase and response regulators share structural similarities across different two-component systems and are responsible for wide ranging functions, such as sensing of nutrients, osmolarity, antibiotics, as well as quorum sensing.

### 1.1.1. Chemosensory clusters

Chemoreceptors span across the inner membrane with a ligand-binding domain facing the periplasm between inner and outer membrane, a transmembrane domain and a cytoplasmic domain. There are five different types of chemoreceptors in *Escherichia coli*, which sense a multitude of nutrients, such as amino acids, sugars and dipeptides, which act as attractants in chemotaxis. On the other hand, also toxins, like benzonate or indole, can be sensed and act as repellents. The two most abundant receptor types, Tar and Tsr, bind respectively the amino acids aspartate (and its non-metabolisable analogue MeAsp) and serine. Tsr also binds aspartate and MeAsp with much lower affinity. Besides specific chemicals, numerous other stimuli can be sensed, such as pH, temperature and oxygen (Lux et al., 2000).

Receptors form homodimers, and furthermore, mixed-type trimers of dimers (Ames

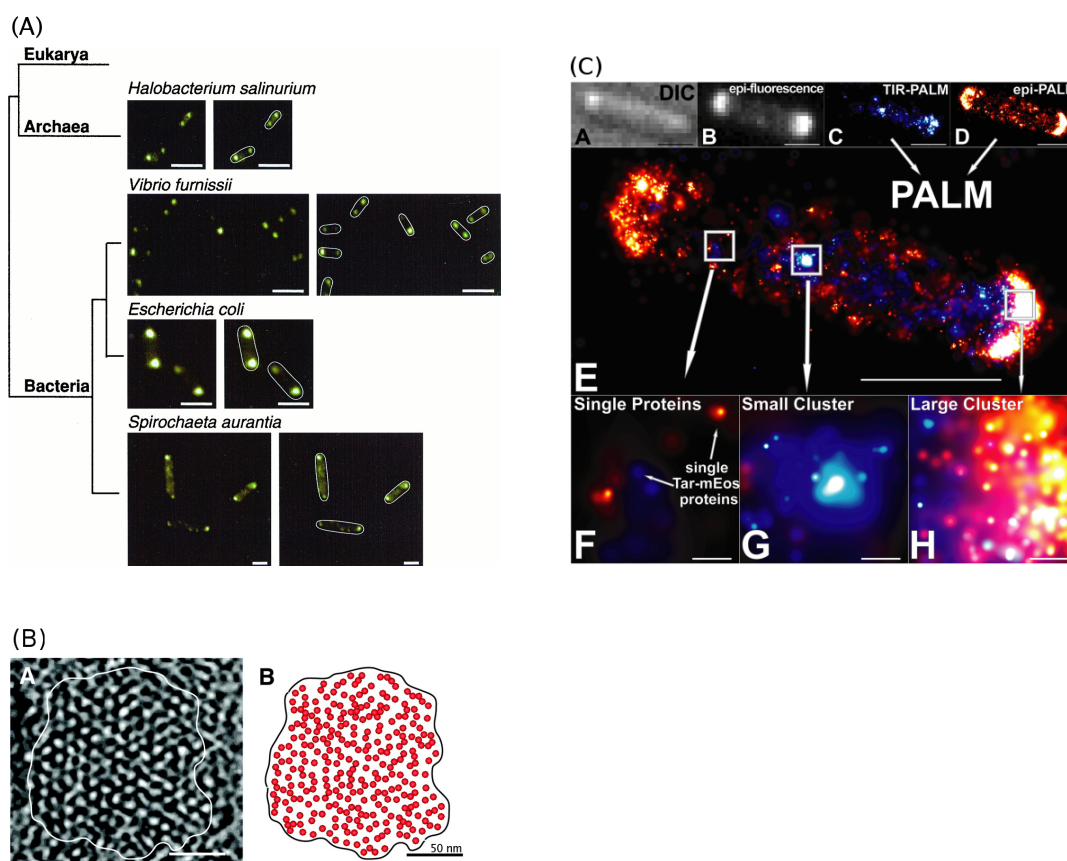


**Figure 1.2.:** Imaging chemoreceptors clusters. (A) Large chemoreceptor clusters located at the cell poles are conserved across various bacteria and archaea species. Cells were treated with antibodies against Trg receptor and subsequently visualised by a fluorescently labelled secondary antibody. Branches indicate evolutionary relationships. Duplicate images on the right outline the cell bodies. Scale bars indicate  $2 \mu\text{m}$ . Image taken from Gestwicki et al. (2000). (B) Polar chemoreceptor clusters form partially hexagonally ordered arrays in *Caulobacter crescentus* cells as measured by cryo-electron tomography. The left image shows a tomographic slice of a subregion of the polar cluster. The right image schematically shows the position of chemoreceptor trimers of dimers derived from the left image. The scale bars indicate 50 nm. Image taken from Khursigara et al. (2008a). (C) Single-molecule imaging revealed various sized receptor clusters. The top row shows images of a single cell using differential interference contrast microscopy (DIC; “A”), epi-fluorescence microscopy (epi; “B”), and a super-resolution microscopy image from so-called photoactivated localisation microscopy (PALM) using two different variants (total internal reflection, TIR; “C”, and epi-fluorescence; “D”). The middle image (“E”) shows a combined image of the two PALM images. The bottom row of images are zooms into three small regions indicated by the boxes in (“E”): single proteins (“F”), small cluster (“G”), and large polar cluster (“H”). Scale bars in (“A”-“E”) indicate  $1 \mu\text{m}$ . Scale bars in (“F”-“H”) indicate 50 nm. Image taken from Greenfield et al. (2009).

et al., 2002; Studdert and Parkinson, 2005; Boldog et al., 2006; Studdert and Parkinson, 2007). Chemoreceptors localise predominantly at the cell poles, where they form large clusters of thousands of molecules (Sourjik, 2004). This feature is conserved in many bacteria and archaea species (Gestwicki et al., 2000; Fig. 1.2 A). Receptors in these clusters are closely packed, and form partially ordered hexagonal lattices of densities consistent

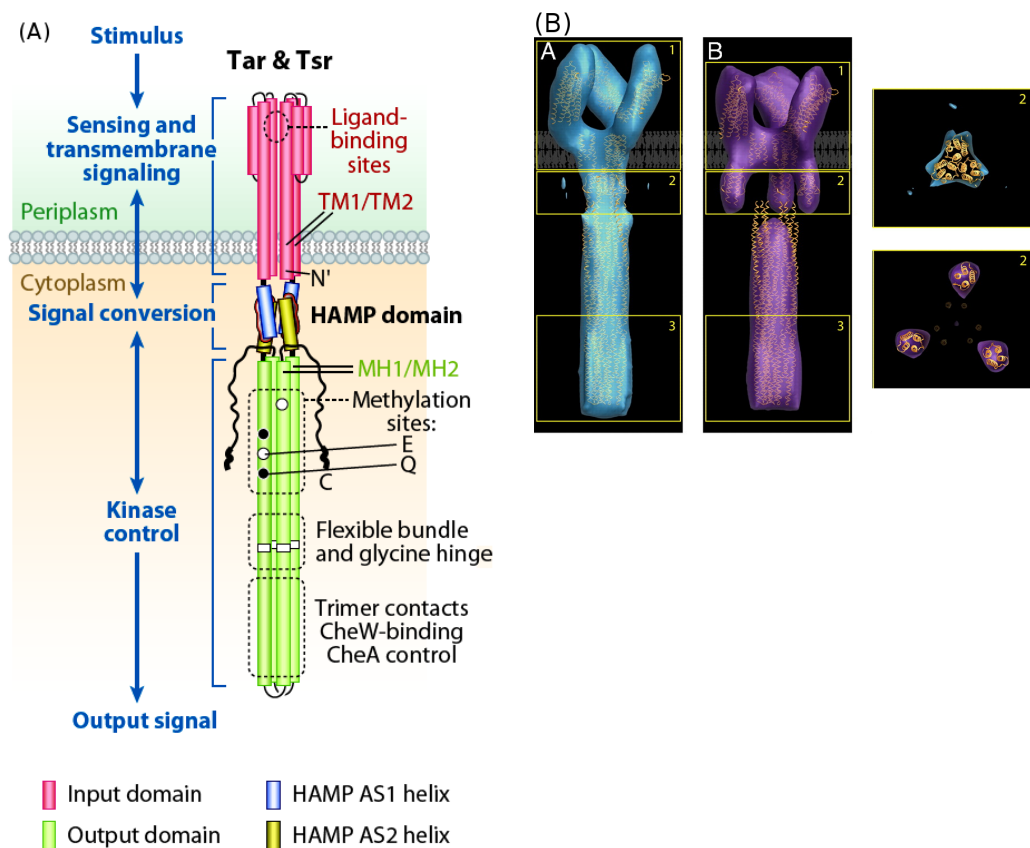


**Figure 1.3.:** Signalling by chemoreceptors. (A) Schematic representation of signalling by chemoreceptors, which is thought to involve the interaction of three distinct receptor modules: A stimulus is sensed by the “sensing and transmembrane signalling module”, and passes it on to the “signal conversion” module. The latter signals to the “kinase control module” (see text). Image taken from Parkinson (2010). (B) Trimers of receptor dimers assume one of two possible conformations. 3D-averaged cryo-electron tomography image of Tsr receptor trimer of dimers. The large images on the left show the trimer in a side view in the two distinct conformations (“A” and “B”, respectively), which differ in the expansion of their HAMP domains (denoted by “2”). Smaller images on the right show the arrangement of the HAMP domains within the trimer in a top-down view. Image taken from Khursigara et al. (2008b).

with trimers (Khursigara et al., 2008a; Briegel et al., 2008; Fig. 1.2 B). Recently, single-molecule experiments revealed that besides these large clusters, receptors also associate in smaller complexes which are distributed across the cell membrane (Greenfield et al., 2009; Fig. 1.2 C).

Transmembrane signalling of receptors is thought to consist of the interaction of three distinct receptor modules (Khursigara et al., 2008b; Hazelbauer and Lai, 2010): a sensing module, which consists of the periplasmic and transmembrane portion of the receptor and contains the ligand binding site, a signal conversion module and kinase control module in the cytoplasmic region. Ligand binding results in a small conformational change in the sensing module, impinging on the signal conversion module (Fig. 1.3 A). The signal

conversion module contains a highly conserved HAMP (histidine kinase, adenylyl cyclases, methyl-binding proteins, and phosphatases) domain, which is thought to convert signals between the sensing and kinase control module. This module was found to assume two different arrangements within trimers of chemoreceptor dimers in cryo-electron microscopy experiments by Khursigara et al. (2008b) (Fig. 1.3 B). The relative abundance of these states changes after addition of the attractant serine. The authors of that study suggest that the two conformations correspond to two specific signalling states, “kinase-on” and “kinase-off”, respectively. The kinase control module contains specific methyl-accepting residues, as well as interaction sites for the kinase CheA. Chemoreceptor methylation and demethylation reverses the conformational changes induced by ligand binding (Lai et al., 2006b). Tar and Tsr receptor monomers have four major residues which can be reversibly methylated. In addition, Tsr has two minor modification sites which are methylated less strongly (Chalah and Weis, 2005).

Most chemotaxis proteins associate with the receptor cluster. CheA, as well as the protein CheW (not shown in Fig. 1.1 C), have been suggested to be involved in receptor-receptor coupling and signal integration (Li and Weis, 2000; Gestwicki and Kiessling, 2002; Kentner and Sourjik, 2009). The histidine kinase CheA exists in a long (CheA<sub>L</sub>) form, as well as a short (CheA<sub>S</sub>) form, which lacks part of the protein domain which is phosphorylated and responsible for subsequent phosphotransfer to response regulators CheY and CheB (O’Connor and Matsumura, 2004). CheA forms homodimers and mixed dimers of the different forms of CheA. Autophosphorylation of CheA is based on binding an ATP molecule by one monomer of the dimer and phosphorylation of the histidine residue of the other monomer. CheY and CheB bind competitively to CheA (Li et al., 1995). CheZ binds specifically to CheA<sub>S</sub>, while still retaining its ability to interact with phosphorylated CheY (Sourjik, 2004). The main function of CheA<sub>S</sub> appears to be the localisation of CheZ to the sensory complex (Sourjik, 2004).

To modify receptors, CheR and CheB molecules bind to a specific tether sequence at the carboxyl-terminus of Tar and Tsr receptors, and act on several nearby receptors, so-called assistance neighbourhoods (Li and Hazelbauer, 2005). The various components of the chemoreceptor cluster have different molecule exchange dynamics consistent with their identified functions (Schulmeister et al., 2008). Receptors, CheA, CheW and CheZ were found to incorporate new components into the chemosensory cluster very slowly on the time scale of minutes (hours for receptors), and hence are stable during chemotactic

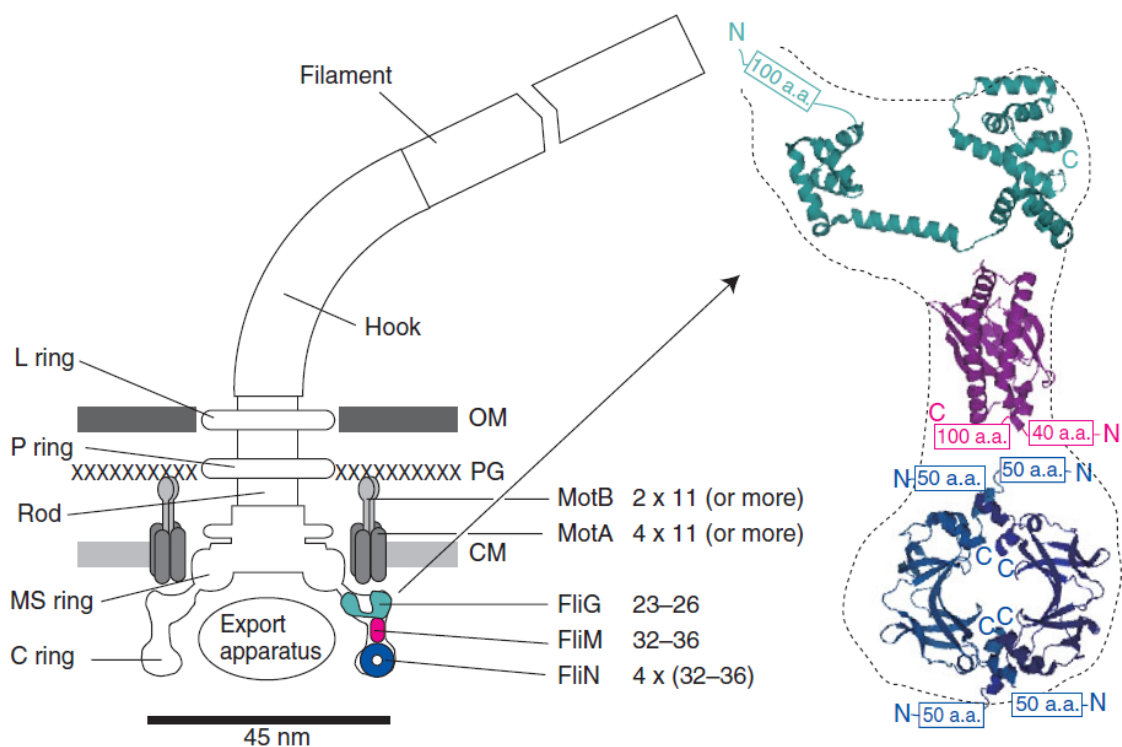


**Figure 1.4.:** Schematics of the *E. coli* rotary motor. (*Left*) Side view of the motor, including membrane structures (OM - outer membrane, PG - peptidoglycan layer, CM - cytoplasmic [inner] membrane), as well as proposed location and stoichiometry of motor components. Rotor components include C-ring (FliG, FliM, FliN), and rod, which are connected to the hook and flagellar filament. Stator components include MotA and MotB, which are bound to the PG layer. Further ring structures include MS-, P- and L-ring. (*Right*) Molecular structure of truncated FliG, FliM and FliN proteins, and proposed fit into the C-ring structure. The number of amino acids missing at the N- and C-termini are indicated. Figure taken from Sowa and Berry (2008).

responses and adaptation. CheR and CheB exchange on a time scale of several seconds, i.e. on the time scale of adaptation to saturating stimuli, which is suggested to ensure a uniform distribution of the enzymes in the cluster while providing sufficiently stable association to receptors during the slow adaptation process. CheY was found to exchange very fast, consistent with its role as diffusible response regulator.

### 1.1.2. The rotary motor

CheY-P is the rotational switching signal for the rotary motors which drive cell motility. The rotary motor (Fig. 1.4) is a protein complex consisting of about 13 different proteins, and a further 25 proteins are involved in its assembly (Macnab, 1996). It is embedded in the bacterial cell wall with some components remaining stationary (stator), and other components rotating (rotor) with respect to the cell body. Several ring structures have been observed in electron microscopy, which span from the cell interior (cytoplasmic (C-)



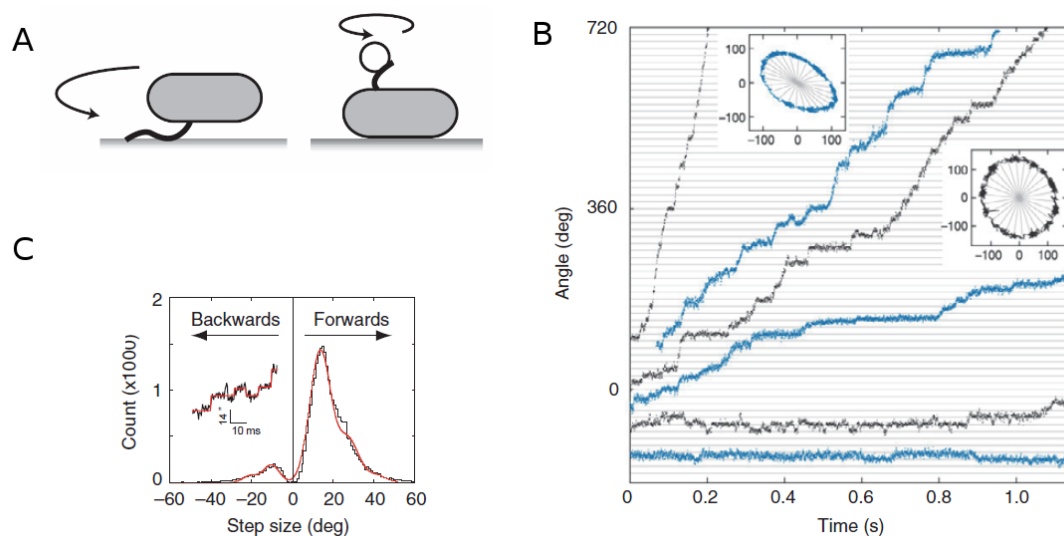


**Figure 1.5.:** Experimental data for rotary motor stepping. (A) Two experimental assays for motor rotation. (A, *Left*) Cell is attached to a microscope slide by a flagellum and the rotation of the cell body is observed. (A, *Right*) Cell body is stuck to a microscope slide and the rotation of a bead attached to the flagellum is observed. (B) Steps of the rotary motor observed for slow rotation and low IMF. Trajectories of the stepping angle (blue and black lines) measured by observing the rotation of a bead attached to the flagellum for different speeds, indicated by the slope of the trajectories, are shown. Insets show the positions of the beads in a plane for two example trajectories (scale in nm). Radial lines indicate angle increments of  $13.8^\circ$ . (C) Histogram of step sizes (black) obtained from a step-finding algorithm applied to the trajectory (cf. inset). A multiple Gaussian fit (red) is shown as well. Figures taken from Sowa and Berry (2008).

ring) across the various layers of the cell wall, including the membrane and supramembraneous (MS-) ring found at the inner membrane, peptidoglycan (P-) ring in the periplasmic space, and lipopolysaccharide (L-) ring in the outer membrane. At least the C- and MS-ring form part of the rotor; it is not known whether P- and L-ring rotate. The rotor is attached to the flagellar filament by a flexible hook.

The stator in *E. coli* consists of 10-12 complexes of MotA and MotB proteins, which form ion channels across the inner membrane around the periphery of the rotor. The stator complexes are anchored to the peptidoglycan layer through MotB. The torque, that drives the flagellar rotation is generated by the interaction of MotA with FliG, which is part of the C-ring. The motor rotation is driven by a so-called ion motive force (IMF), i.e. ions passing through an electrochemical gradient. Two different IMFs have been observed for different species: proton gradients (e.g. in *E. coli*) and sodium-ion gradients. The ion motive force is generated by an electrical potential due to a charge difference between the two sides of the membrane, as well as a chemical concentration gradient of ions. There are two main assays which have been used to study the motor rotation, shown in Fig. 1.5 A.

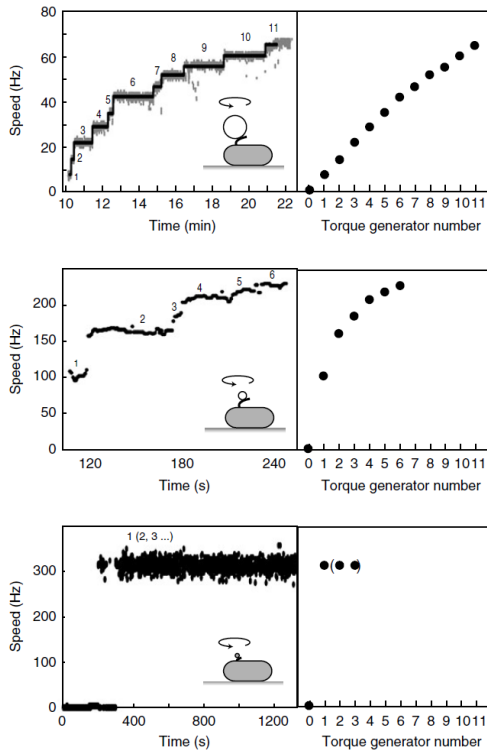


**Figure 1.6.:** Rotation speed as a function of the number of torque-generating units. In “resurrection experiments” expression of functional stator units (Mot proteins) was induced in cells with defective stator units. High load ( $1 \mu\text{m}$  beads; top), low load ( $0.3 \mu\text{m}$  beads; middle) and near-zero load ( $60 \text{ nm}$  gold beads attached to the hook; bottom) was applied to the cells. The resulting rotation speed is plotted as a function of time in the left panels, and as function of the number of torque-generating units (as deduced from the number of steps observed in panel A) in the right panels. Figure taken from Sowa and Berry (2008).

Firstly, cells can be tethered by a filament, and the rotation of the cell body is observed. Secondly, the cell is attached to the surface of a microscope slide, and the rotation of a filament or a bead attached to one filament is observed. The latter assay allows to vary the load on the motor by changing the bead size.

Using a chimeric motor driven by sodium ions in *E. coli* at slow motor rotation by a single stator unit, individual steps of the motor could be resolved (Sowa et al., 2005). The step size was measured to be  $13.7^\circ$  on average, and a histogram of dwelling angles showed that the rotor visits consistent discrete angles during successive rotation cycles (Fig. 1.5 B and C).

In so-called resurrection experiments, in which the expression of stator components is induced in mutants lacking the Mot genes, the speed of rotation increases in discrete increments, thought to be related to the number of independent stator units expressed (Fig. 1.6). At high load, the speed increase was found to be linear with the number of stator units, whereas at low load the relationship is nonlinear. At near-zero load, the speed of rotation is independent of the number of stator units (Yuan and Berg, 2008). This result has been interpreted as each torque-generating element having a rate-limiting step in the mechanochemical cycle, which cannot be sped up by the torque exerted by other elements (Sowa and Berry, 2008).

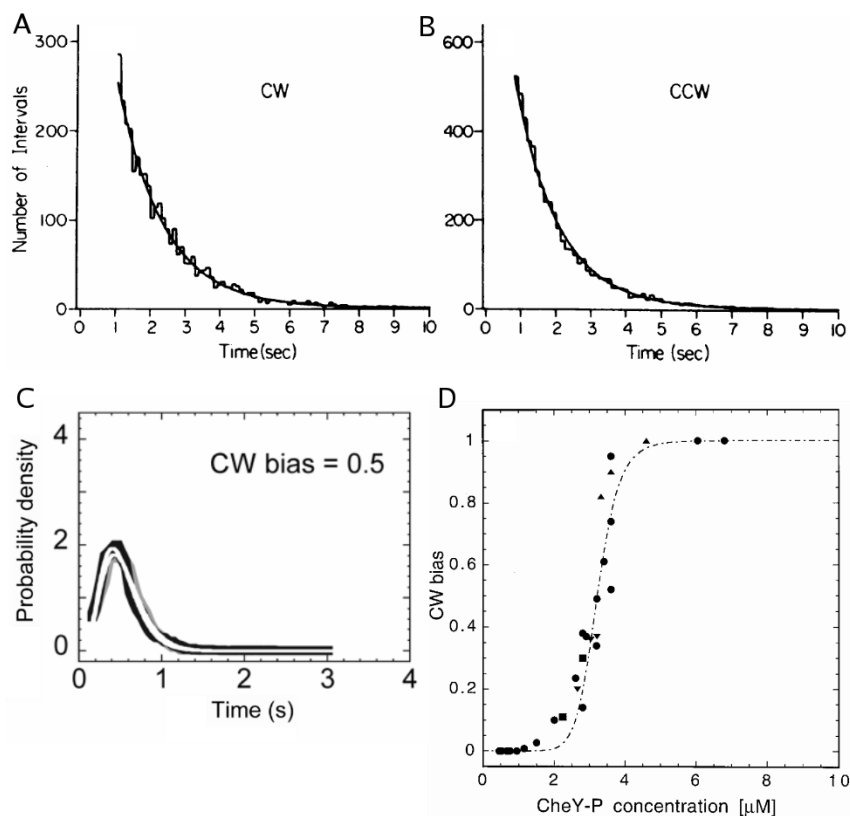


**Figure 1.7.:** Experimental data for motor switching. (A and B) Histograms of time intervals of clockwise (CW) and counter-clockwise motor rotation of adapted cells. Figures taken from Block et al. (1983). (C) Non-exponential distribution of time intervals of CW (black) and CCW (grey) at CW motor bias of 0.5. Figure taken from Korobkova et al. (2006). (D) Experimental measurement of CW bias as a function of CheY-P concentration (symbols) and fit to Hill function (line). Figure taken from Cluzel et al. (2000).

The motor switches rotational direction due to chemotactic signalling, when CheY-P binds to FliM on the C-ring. The dynamics of switching in the presence of CheY-P has been studied extensively. Observing rotating bacteria cells tethered by a flagellum, the distribution of time intervals spent in the CW or CCW state were found to be exponential with mean interval times of 1.33 s (CW) and 1.22 s (CCW), respectively (Fig. 1.7 A and B; Block et al., 1983; Bai et al., 2010). In other experiments, marked deviations from exponential distributions were measured observing beads attached to full-length flagella (Fig. 1.7 C; Korobkova et al., 2006). These cells showed distinct maxima in their interval distributions, which were well-fit by Gamma distributions. These peaks are not due to correlations between intervals, as re-shuffling of intervals yields the same distributions. It is not clear where the differences between these data sets originate. Besides using wild-type and mutant CheY respectively, the studies also differ in the experimental set-up. Block et al. (1983) used an assay where the rotation of the tethered cell body was observed and Bai

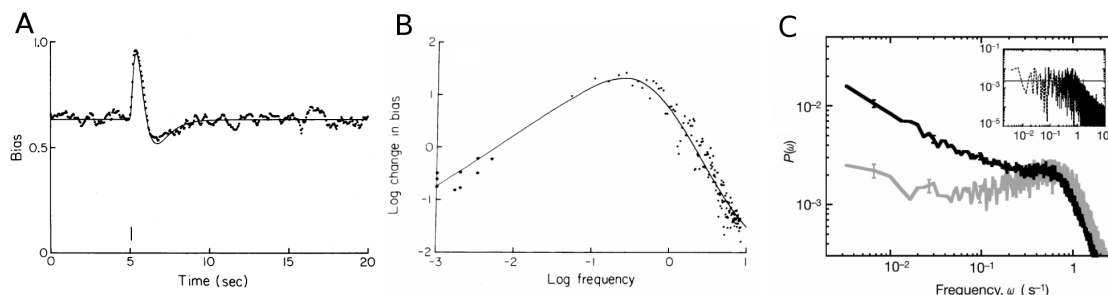


**Figure 1.8.:** Response function and power spectrum of the motor. (A) Time course of the motor bias in response to a short pulse of attractant (dots: measured data; line: fit). (B) Fourier transform of the time course in A (right data points) and response to periodic stimulation (left data points). The line is the Fourier transform of the smooth line in panel A. Figures taken from Segall et al. (1986). (C) Noise power spectrum of wild type cells (black line) and mutant lacking the signalling pathway (grey line). Figure taken from Korobkova et al. (2004).

et al. (2010) observed the rotation of truncated flagella, whereas Korobkova et al. (2006) visualised the rotation of full-length flagella.

Using a constitutively active mutant CheY, the rates of switching between CW and CCW were measured as a function of CheY concentration (Turner et al., 1999). The motor bias, i.e. the probability to spin in one direction, was measured as a function of CheY-P concentration (Fig. 1.7 D; Cluzel et al., 2000). It was found that the CW bias increases steeply around the steady-state concentration of  $3.2 \mu\text{M}$  CheY-P of unstimulated cells. This nonlinearity of the bias, however, is not due to cooperative binding of CheY-P to FliM (Sourjik and Berg, 2002a). The signalling response of the motor to chemotactic stimuli has been measured. Using impulse or periodic stimuli, the Fourier transformed linear response function of the motor bias was obtained (Fig. 1.8 A and B; Block et al., 1982; Segall et al., 1986). The chemotaxis pathway acts as a bandpass filter, transmitting best signals that change on a time scale of 1-10 s (corresponding to frequencies 0.1-1 Hz) and filtering out slowly changing, as well as rapidly changing stimuli. This can be seen from the Fourier transformed response function which decreases both, at low and high frequencies (Fig. 1.8 B). Furthermore, to characterise fluctuations in motor switching due to chemotactic signalling as well as intrinsic switching of the motor, the power spectrum has been measured by Korobkova et al. (2004). The power spectrum captures the correlations of motor rotation at two different time points. The signalling pathway filters out high-frequency fluctuations as the power spectrum decreases at high frequencies (Fig. 1.8 C). Interestingly, the power spectrum of wild-type cells has a larger low-frequency component than mutants lacking the signalling pathway, i.e. the pathway introduces long correlations in motor switching.

The structural basis for the two rotational directions was hypothesized to be FliN, which is part of the C-ring and forms tetramers in the structure of puckered rings. Tetramers could stack in two different ways corresponding to CW and CCW rotation (Sowa and Berry, 2008).

### 1.1.3. Robustness of chemotaxis

Chemotaxis protein levels can vary considerably, e.g. due to gene expression noise (Elowitz et al., 2002) and gene regulation under various conditions. Li and Hazelbauer (2004) found that the cellular content varies over an order of magnitude between growth in minimal and rich medium respectively. However, cellular stoichiometry of proteins and chemotaxis efficiency remains roughly constant. Alon et al. (1999) found that swimming behaviour shows precise adaptation, i.e. cells return precisely to their pre-stimulus swimming behaviour after a attractant concentration, when varying the CheR protein expression level over an order of magnitude. In a study by Kollmann et al. (2005), the chemotaxis efficiency was found to be affected little when chemotaxis protein levels co-varied by varying the level of an effector of their transcription. In addition, co-variation of either CheB and CheR, or CheY and CheZ, had little effect on the chemotaxis efficiency (Løvdkok et al., 2007). Hence, mechanisms to keep CheY-P robustly in the working range of the rotary motor must be at work (Løvdkok et al., 2007). It has been suggested that the organisation of protein expression in operons, as well as the pathway architecture of opposing enzymes, i.e. methylation and demethylation of receptors, as well as phosphorylation and dephosphorylation of CheY-P, keeps the proportion of the functional states constant over a large range of protein levels when these vary in concert (Kollmann et al., 2005; Løvdkok et al., 2007).

### 1.1.4. *In vivo* fluorescence resonance energy transfer (FRET)

The interactions between different proteins in the chemotaxis pathway during signalling have been well characterised. Specifically, fluorescence resonance energy transfer (FRET) measurements of the response regulator CheY-P and its phosphatase CheZ have elucidated the signalling in the chemotaxis pathway (Sourjik and Berg, 2002b, 2004; Kentner and Sourjik, 2009). The method is illustrated in Fig. 1.9: FRET is based on the energy transfer from a fluorophore, which is excited by a laser, to a fluorophore of lower-frequency excitation spectrum. This process is strongly dependent on the distance between the two

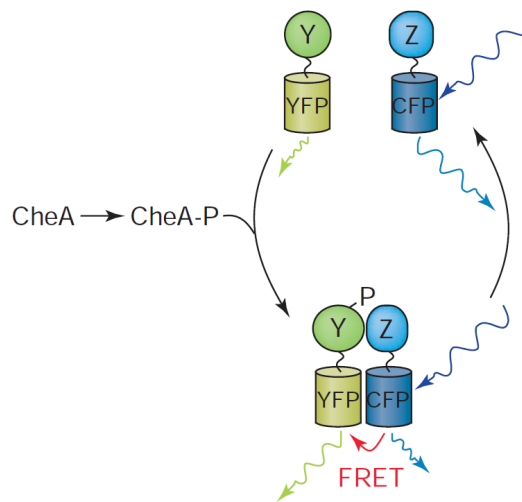


**Figure 1.9.:** *In vivo* fluorescence resonance energy transfer applied to measure the intracellular signalling activity in chemotaxis. CheY and CheZ are tagged with fluorescent protein tags. Cyan fluorescent protein (CFP) is excited. When CheY-P is dephosphorylated, CFP and yellow fluorescent protein (YFP) come close, and energy from excited CFP is transferred to YFP. A change in yellow (as well as blue) fluorescence is detected. Image taken from Sourjik (2004).

fluorophores (Wouters and Bastiaens, 2001). Here, chemotaxis proteins were fused with cyan and yellow fluorescent protein tags (CFP and YFP, respectively) and changes in FRET monitored during stimulation with chemoeffectors. In the case of CheY and CheZ, FRET is highly specific to the interaction of the two proteins during dephosphorylation, and hence is a read-out of the kinase activity when assuming a quasi steady-state with phosphorylation of CheY (Sourjik and Berg, 2002b).

## 1.2 Previous modelling work on chemotaxis signalling

---

The chemotaxis pathway has attracted immense interest not only from biologists, but also from modellers. In the following, we briefly review several mathematical models, including signal amplification by cooperative chemoreceptors, precise sensory adaptation, and the operation of the rotary motor, which are relevant as background for this thesis.

### 1.2.1. Two-state model for independent chemoreceptors

In the simplest model for chemoreceptor signalling, receptors signal independently and each receptor has two possible states (conformations), *on* (active) and *off* (inactive) (Asakura and Honda, 1984). As a microscopic object, the receptor constantly switches between *on* and *off* conformation due to thermal fluctuations (Fig. 1.10). Each of the states is assigned an energy  $f_i$ , with the receptor being more likely in the state with lower energy.

## 1.2. PREVIOUS MODELLING WORK ON CHEMOTAXIS SIGNALLING

---

The equilibrium properties of this model are determined by the free-energy difference between the *on* and *off* states. The probability to be in either of the states is determined by the Boltzmann distribution, with the probability for the *on* state given by  $e^{-f_{\text{on}}}/Z$ , and for the *off* state by  $e^{-f_{\text{off}}}/Z$ . The normalising factor  $Z = e^{-f_{\text{on}}} + e^{-f_{\text{off}}}$  is the partition function which sums over the Boltzmann factors  $e^{-f_i}$  of all states  $i$ , where  $f_i$  denotes their respective energies (all energies are given in units of  $k_B T$  with  $k_B$  the Boltzmann constant and  $T$  temperature). The probability of the *on* state is interpreted as the activity  $A$  of the receptor,

$$A(c, m) = \frac{1}{1 + e^{\Delta f(c, m)}} \quad (1.1)$$

$$\Delta f(c, m) = f_{\text{on}} - f_{\text{off}} = \Delta\epsilon(m) + \ln \left( \frac{1 + c/K_D^{\text{off}}}{1 + c/K_D^{\text{on}}} \right). \quad (1.2)$$

The free-energy difference  $\Delta f(c, m)$  is determined by the receptor methylation level  $m$  and the concentration of ligand  $c$ . This result is derived below in more detail. Briefly, the term  $\Delta\epsilon(m)$  is the free-energy difference between the *on* and *off* state in the absence of ligand. The concentration-dependent term describes the energetics of ligand binding and is due to a gain of binding energy upon ligand-receptor binding and loss of volume entropy due to removing ligand from the solvent. Receptors with different methylation levels are thought to bind ligand with the same dissociation constant (Skoge et al., 2006). Therefore, the dissociation constants  $K_D^{\text{on/off}}$  are assumed to not depend on receptor methylation level. For attractants, the *off* state is assumed to bind ligand at lower concentration compared to the *on* state, which is expressed by the dissociation constants  $K_D^{\text{off}} < K_D^{\text{on}}$ . Hence, increasing the ligand concentration favours the *off* state. Methylation of receptors reverses the effect of attractant binding (adaptation), i.e. increasing the methylation level favours the *on* state.

**Derivation of receptor activity I: Chemical equilibrium of ligand-receptor binding.** To understand the different contributions to the free-energy difference in Eq. 1.2, we first look at the simpler case of ligand-receptor binding. Binding and unbinding of ligand molecules  $L$  to a receptor  $R$  can be described in terms of the chemical equation



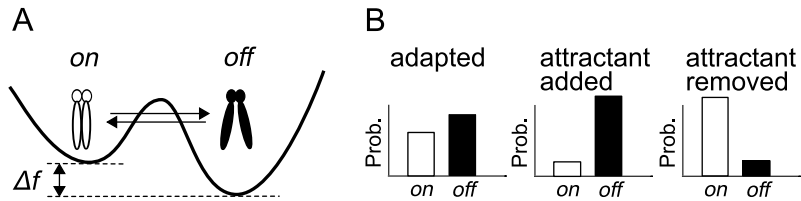


**Figure 1.10.:** Two-state model for receptor. (A) Receptor can assume two different conformations, which yield it active (*on*) or inactive (*off*), and switches constantly between them due to thermal fluctuations. The probability to be *on* is determined by the free-energy difference  $\Delta f$ . (B) In the adapted state the *on* state is slightly less probable than the *off* state (left panel). When attractant is added, the probability of the *on* state decreases (centre panel), whereas it increases when attractant is removed (right panel). Adaptation reverses the effect of ligand binding and restores the probabilities to match the left graph.

which can be translated into an ordinary differential equations for the concentrations of ligand  $c = [L]$ , unbound receptors  $[R]$ , and bound receptors  $[R - L]$ . The differential equation for  $[R - L]$  is

$$\frac{d[R - L]}{dt} = k_1 c [R] - k_2 [R - L]. \quad (1.4)$$

We are interested in the fraction of bound receptors at equilibrium  $P_b$ , hence we set the time derivative to zero, and obtain for  $P_b$

$$P_b = \frac{[R - L]}{[R - L] + [R]} = \frac{c/K_D}{1 + c/K_D}, \quad (1.5)$$

where  $K_D = k_2/k_1 = c[R]/[R - L]$  is the dissociation constant of ligand-receptor binding. From the above equation, the meaning of the dissociation constant is clear: at a concentration  $c = K_D$  the fraction of occupied receptors is  $1/2$ . Hence,  $K_D$  is a typical concentration for ligand-receptor interaction. Comparing Eq. 1.5 to Eq. 1.1, the free-energy difference associated with ligand-receptor binding is

$$\Delta f_b = -\ln\left(\frac{c}{K_D}\right). \quad (1.6)$$

Comparing this result to a statistical mechanical derivation (Phillips et al., 2009), the dissociation constant can be understood as the concentration at which gain of binding energy  $\Delta\epsilon_b$  and the loss of volume entropy balance each other,  $K_D = \frac{1}{\nu} e^{\Delta\epsilon_b}$  with  $\nu$  being the typical volume taken up by a ligand.

**Derivation of receptor activity II: Combining bound and unbound *on* states.** Assuming that the receptor has two conformational states, *on* and *off*, and in each of them can bind ligand molecules, results in four possible states of the receptor: (*on*, bound), (*on*,



unbound), (*off*, bound), and (*off*, unbound) with associated energies

$$f_{\text{on},0} \tag{1.7}$$

$$f_{\text{on},b} = f_{\text{on},0} - \ln\left(\frac{c}{K_D^{\text{on}}}\right) \tag{1.8}$$

$$f_{\text{off},0} \tag{1.9}$$

$$f_{\text{off},b} = f_{\text{off},0} - \ln\left(\frac{c}{K_D^{\text{off}}}\right), \tag{1.10}$$

where “0” denotes the receptor state without ligand bound, and “b” the receptor state with ligand bound. We assume that ligand binding equilibrates faster than switching between the states, so we can write the free energy of the bound state as the sum of the energy of the unbound state and the free-energy difference due to ligand-receptor binding in terms of the dissociation constants  $K_D^{\text{on/off}}$  as derived in Eq. 1.6. We are interested in the probability of the *on* state. Therefore, we sum over the probabilities of the *on* state with and without ligand bound, respectively,

$$\begin{aligned} P_{\text{on}} &= \frac{e^{-f_{\text{on},0}} + e^{-f_{\text{on},b}}}{e^{-f_{\text{on},0}} + e^{-f_{\text{on},b}} + e^{-f_{\text{off},0}} + e^{-f_{\text{off},b}}} \tag{1.11} \\ &= \frac{1 + c/K_D^{\text{on}}}{1 + c/K_D^{\text{on}} + e^{(f_{\text{on},0} - f_{\text{off},0})}(1 + c/K_D^{\text{off}})} \\ &= \frac{1}{1 + e^{\Delta f}}, \end{aligned}$$

where we obtain Eq. 1.2 and identify  $\Delta\epsilon = f_{\text{on},0} - f_{\text{off},0}$ .

### 1.2.2. Signal amplification by cooperative chemoreceptors

Two main classes of models for cooperative chemoreceptor signalling can be distinguished: lattice models of weakly interacting receptors and complexes of strongly interacting receptors, which will be described in the following paragraphs. These models of receptor-receptor interactions have been developed to explain the extreme sensitivity of chemosensing to small concentration changes. Broadly, in both classes of models, receptors influence the signalling state of their neighbours. By this mechanism, a conformational change caused by ligand binding to one receptor can spread to its neighbouring receptors to change their signalling state although being unoccupied. This cooperativity of receptors leads to signal amplification as ligand binding to one receptor affects signalling of more than one receptor.

**Receptor lattice model for chemoreceptors.** Lattice-type models for chemoreceptors were first introduced by Bray et al. (1998), and put in terms of an Ising model (known from physics as a model for ferromagnets) by Shi and Duke (1998) and Duke and Bray (1999). Later, Mello and Tu (2003a) used a mixed receptor lattice model with interactions between different receptor types to explain FRET signalling data. Individual receptors can assume two states as described above. Furthermore, neighbouring receptors interact such that if they are in the same state the total energy of the system decreases. This is equivalent to favouring aligned neighbouring receptors. The energy of a specific configuration  $k$  of receptors on a lattice of  $M$  receptors is

$$F_k = \sum_{i=1}^M \sigma_i^k \Delta f + \frac{1}{2} \sum_{\langle i,j \rangle} \left( \sigma_i^k - \frac{1}{2} \right) \left( \sigma_j^k - \frac{1}{2} \right) J, \quad (1.12)$$

with  $\sigma_i^k$  denoting the state of receptor  $i$  in the lattice configuration  $k$ ,  $\sigma = 1$  (*on*) or  $\sigma = 0$  (*off*), and  $\langle i,j \rangle$  denoting neighbouring receptors. The interaction energy  $J < 0$  lowers the energy of the lattice configuration when neighbouring receptors are in the same signalling state, and increases it when receptors are in different signalling states. Adding attractant concentration corresponds to adding a magnetic field in the equivalent model for ferromagnets, and tends to bias receptors towards the *off* state (Skoge et al., 2006; Fig. 1.11). The activity of the system is given by averaging over the state of each receptor in each lattice configuration, and over all receptors of the lattice,

$$A = \frac{1}{MZ} \sum_{i=1}^M \sum_{k=1}^{2^M} \sigma_i^k e^{F_k}, \quad (1.13)$$

where  $Z$  is the partition function for the receptor lattice, i.e. the sum over the Boltzmann factors of all lattice configurations. There is a phase transition in two-dimensional square lattices at a critical interaction energy ( $J_{\text{crit}} \approx -0.44$  in units of  $k_B T$ ), below which one of the activity states is favoured even if the free-energy difference  $\Delta f = 0$ .

While extended lattices of weakly interacting receptors are consistent with a number of experimental observations, they cannot reproduce signalling data for low-activity mutants (Skoge et al., 2006). These mutants lack the methylation enzyme CheR, i.e. receptors tend to be fully demethylated, resulting in a very low adapted activity. However, they show sensitivity (very low  $K_D$ ) similar to that of adapted wild-type cells. It was shown by Skoge et al. (2006) that extended lattices of weakly interacting receptors have a high

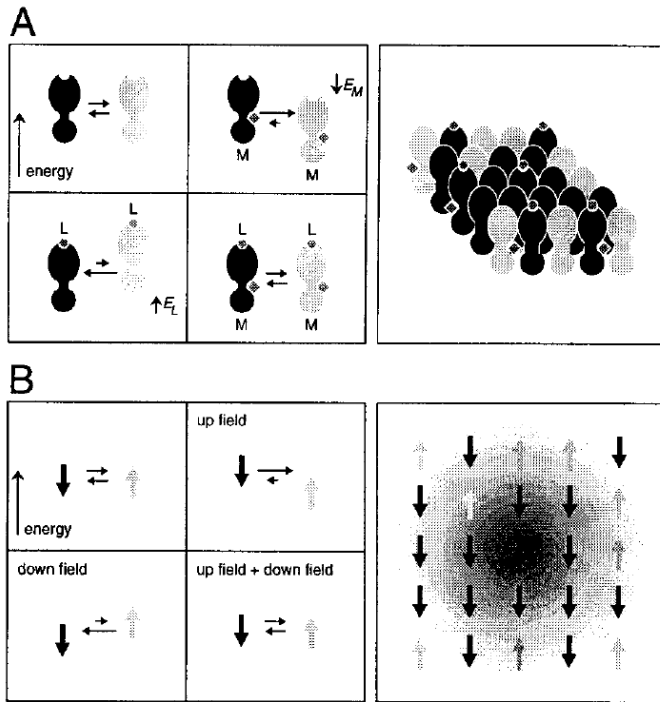


**Figure 1.11.:** Lattice model for chemoreceptors (A) and analogy to ferromagnetism (B). (A, *Left*) Switching of chemoreceptors between conformational states and associated energies. Receptors switch between *on* (grey) and *off* (black) states. Their relative energies are represented by the height along the energy axis. Ligand binding (L) lowers the energy of the *off* state, and methylation (M) reduces the energy of the *on* state, favouring the lower energy state. (A, *Right*) Lattice of receptors. Receptor-receptor interactions reduce the energy of the lattice state if neighbouring receptors are in the same conformational state. Hence, neighbouring receptors tend to be in the same conformational state. (B, *Left*) Switching of magnetic spins between *spin-up* and *spin-down* state and associated energies.

A magnetic field lowers the energy of spins aligned along the field, favouring these spin states. (B, *Right*) Lattice of coupled spins as model for ferromagnet. Cooperative interaction between adjacent spins lowers the energy of the spin configuration when spins have the same direction. Hence, neighbouring spins tend to be aligned. Image taken from Duke and Bray (1999).

sensitivity to ligand only when the free-energy difference between *on* and *off* state in the absence of ligand is close to zero, i.e. when the adapted activity is about 1/2, as only in this case the effective receptor clustering size (cooperativity) is significant.

**Monod-Wyman-Changeux model for chemoreceptors.** The Monod-Wyman-Changeux (MWC) model was developed to describe the allosteric activation of protein complexes consisting of several homogeneous subunits (Monod et al., 1965). In the context of chemoreceptors, receptors are thought to form small signalling complexes of strongly interacting receptors. Instead of the individual receptors in Sec. 1.2.1, complexes of  $N$  receptors switch cooperatively between two signalling states, *on* and *off*. The free-energy difference of the complex is  $\Delta F(c, m) = N \cdot \Delta f(c, m)$ ,  $N$  times the free-energy difference of an individual receptor given by Eq. 1.2. The activity is

$$A(c, m) = \frac{1}{1 + e^{\Delta F(c, m)}}. \quad (1.14)$$

The MWC model was first proposed as a model for chemoreceptor signalling by Sourjik and Berg (2004), and later studied by various groups, successfully explaining detailed experimental data of various signalling mutants measured by FRET (see Sec. 1.1.4; Sourjik and Berg, 2002b, 2004; Mello and Tu, 2005; Keymer et al., 2006; Endres and Wingreen, 2006; Endres et al., 2008). Keymer et al. (2006) identified two regimes of behaviour for homogeneous receptor complexes, *(i)* at large positive free-energy differences between *on* and *off* states (low activity in the absence of ligand), receptor coupling leads to high sensitivity to ligand, and *(ii)* at large negative free-energy differences between *on* and *off* states (activity  $\approx 1$  in the absence of ligand), receptor coupling yields large Hill coefficients. The first property explains the high sensitivity to ligand of low-activity signalling mutants, as there is a fixed complex size irrespective of the free-energy difference of individual receptors (Skoge et al., 2006), as opposed to lattice models with weakly interacting receptors (see above).

The MWC model emerges from a lattice model of interacting receptors in the limit of large interaction energies between receptors. Hence, while lattices of weakly interacting receptors seem to be inadequate to describe all experimental data, lattices of receptors with a domain structure, where receptors interact strongly within domains but not across domain borders, could be a realistic model for how chemoreceptors act in small signalling complexes (Skoge et al., 2006).

### 1.2.3. Robust and precise adaptation

Barkai and Leibler (1997) introduced the concept of robustness of biochemical networks, i.e. the invariance of certain system properties such as steady-state concentrations with respect to changes in parameter values. Guided by the example of the precise adaptation of bacterial chemotaxis, they studied a two-state receptor whose switching rates between active and inactive states are affected by ligand concentration and receptor methylation level. They assumed that CheB only demethylates active receptors, while CheR affects active and inactive receptors. The robustness of this system against wide variations of rate constants is due to the dynamics of modification depending only on the activity state of the receptor, but not on system variables such as methylation level or ligand concentration. The idea of robust precise adaptation in *E. coli* chemotaxis was further studied by others. Yi et al. (2000) placed the model by Barkai and Leibler in a more general framework of engineering principles and showed that integral feedback is the basic mechanism for

## 1.2. PREVIOUS MODELLING WORK ON CHEMOTAXIS SIGNALLING

---

precise adaptation in this model. In a more detailed model for chemotactic signalling, taking into account explicitly phosphorylation and methylation reactions, Mello and Tu (2003a) identified conditions required for precise and near-precise adaptation.

Kollmann et al. (2005) studied the robustness of different network architectures to variations in protein levels, and showed that the accepted pathway of chemotaxis has the smallest structure which yields robust buffering against varying expression protein levels. According to their analysis, robustness against concerted variations of all protein levels is due to the principle of opposing enzymes, i.e. kinase and phosphatase, which activate and deactivate the response regulator CheY, and receptor methylation and demethylation enzymes, which activate and deactivate the receptors.

Endres and Wingreen (2006) and Hansen et al. (2008) discussed that “assistance neighbourhoods”, i.e. groups of receptors that are accessible for modification by methylation and demethylation, are necessary to achieve precise adaptation. This is due to more modification sites being available within a neighbourhood than on an individual receptor; fully methylated or demethylated assistance neighbourhoods rarely occur, and hence the rates of modification of receptors in an assistance neighbourhood remain independent of their methylation level.

### 1.2.4. Models for the rotary motor

Early models for the motor focused on describing the two-state switching dynamics. Based on the exponential interval distributions of CW and CCW states, Block et al. (1982) discussed the switching dynamics as a Poisson process, i.e. switching between the two states occurring with constant mean rates. Scharf et al. (1998) and Turner et al. (1999) discussed two-state models based on an energy barrier between CW and CCW state. Turner et al. (1999) used an MWC model where the motor comprises of 26 units able to bind CheY-P shifting the free-energy difference between the two states, and all system units switch cooperatively between CW and CCW rotational state. Duke et al. (2001) devised an Ising-type model to study the conformational spread in rings of proteins, and applied it to the motor switch. They also discussed the limiting case of the MWC model. The non-exponential distributions of the switching times measured by Korobkova et al. (2006) could be fit by Gamma distributions. The authors discuss that this is due to a number of underlying hidden steps before a rotational switch occurs.

Recently, a number of mechanistic models have been developed. In particular, the

stepping mechanism has been the focus of study, i.e. how the coupling of an electrochemical ion gradient, contact forces between the near-periodic structures of rotor and stators, and external load give rise to the (noisy) generation of torque which drives the rotation of the motor in one direction (Xing et al., 2006; Meacci and Tu, 2009; Mora et al., 2009a,b). van Albada et al. (2009) considered a model which integrates the dynamics of stepping and switching between CW and CCW states, as well as polymorphic transitions of flagellar filaments between right- and left-handed helices after switching. The dynamics of stepping is modelled along the lines of the above references. Switching occurs according to an MWC model, i.e. all rotor units switch conformation in concert. The mechanical feedback of the flagellar filament and load on the motor dynamics is integral to the model: The flagellum transitions between different morphological states, which are associated with a position in an energy landscape feeding back into the dynamics of the load, and transitions between morphological states occur with rates determined by their differences in energy. Excluding the mechanical feedback from flagella, this model shows exponential distributions for the CW and CCW interval times. Including the mechanical feedback, it yields peaked interval distributions similar to experimental measurements by Korobkova et al. (2006).

### 1.3 Aims of this work

---

In this thesis, we investigate sensing by cell surface chemoreceptors, cell signalling and cell behaviour during chemotaxis in *E. coli*. The chemotaxis pathway is an ideal model system for cell sensing and signalling processes. Based on the wealth of published data and collaboration with experimentalists, we aim to address several fundamental topics:

**Sensory adaptation of receptors.** Sensory pathways often have a large working range as biochemical mechanisms allow for adaptation to a background stimulus. We aim to develop a detailed model for signalling and adaptation of chemoreceptors, which quantitatively describes time-course data from fluorescence resonance energy transfer.

**Weber's law.** In many sensory systems, e.g. human vision, it is found that the smallest noticeable change in stimulus increases with the background stimulus intensity. Weber's law states that this relation is roughly linear. For chemotaxis this relates to a small change in activity upon concentration changes. Using experimental data and our model for receptor signalling and adaptation, we study Weber's law in chemotaxis, and aim to

establish its molecular origin, limits, and biological significance in this system.

**Signal transmission and noise filtering.** We aim to model the complete signalling pathway from receptors to rotary motors, which drive the bacterium's flagella. Having a reasonable description of signalling by chemoreceptors, we will establish the various steps of the signalling cascade. We are going to study the effects of noise from input stimuli, as well as signal transduction. The question is what types of time-varying signals are transduced to the motors, and to what degree signalling noise is filtered out. Ultimately, we aim to study how the signalling pathway is optimised for efficient chemotaxis.

**Information transmission.** The chemotaxis sensory system has to transmit information about the bacterium's external environment to the intracellular signalling pathway, which results in a behavioural response. We argue that chemotaxis may be optimised for information transmission and aim to predict typical concentration inputs to characterise the bacterial microenvironment.

## 2. Sensory adaptation of receptors

### 2.1 Synopsis

---

Adaptation of the chemotaxis sensory pathway of the bacterium *Escherichia coli* is essential for detecting chemicals over a wide range of background concentrations, as it ultimately allows cells to swim towards sources of attractant and away from repellents. Its biochemical mechanism based on methylation and demethylation of chemoreceptors has long been known. Despite the importance of adaptation for cell memory and behaviour, the dynamics of adaptation is difficult to reconcile with current models of precise adaptation. In this chapter, we follow time courses of signalling in response to concentration step changes of attractant using *in vivo* fluorescence resonance energy transfer (FRET) measurements. To quantitatively explain the data, we develop a dynamic model for signalling and adaptation based on the attractant flow in the experiment, signalling by cooperative receptor complexes, and multiple layers of feedback regulation for adaptation. We use a condensed representation of adaptation time courses to quantify imprecision in adaptation, to efficiently evaluate different adaptation models and to extract the kinetics of the receptor methylation level. We experimentally confirm the predicted effects of changing the enzyme-expression level and bypassing the negative feedback for demethylation. Our data analysis suggests significant imprecision in adaptation for large concentration increases. Furthermore, our model predicts highly regulated, ultrafast adaptation in response to removal of attractant, which may be useful for fast reorientation of the cell and noise reduction in adaptation. This work was done in collaboration with Victor Sourjik's lab at the university of Heidelberg and has been published (Clausznitzer et al., 2010). Experiments were performed by Olga Oleksiuk and Linda Løvdok.



## 2.2 Motivation & open questions

---

Cells are able to sense and respond to various external stimuli. To extend the working range of their sensory pathways, biochemical mechanisms allow for adaptation to persistent stimulation, i.e. the reversal of an initial signalling response to a stimulus, resulting in only a transient response. The dynamics of adaptation is important as it often represents the cells' memory of previous environmental conditions, directly affecting cellular behaviour (Jaasma et al., 2007; Marwan et al., 1995; Hilliard et al., 2005; Zigmond and Sullivan, 1979; Shi and Zusman, 1994; Spehr et al., 2009; Muzzey et al., 2009). Fast adaptation means that cells stop responding and that their biochemical pathways quickly "forget" the stimulus. In contrast, slow adaptation leads to long-lasting effects in the cells. The dynamics of adaptation is often difficult to understand in detail, since it emerges from multiple, simultaneously occurring processes. In higher organisms, adaptation is best documented in the insect and vertebrate visual system, where multiple mechanisms adjust the receptor sensitivity to ambient light levels. For instance, phototransduction in the vertebrate eye involves up to nine different mechanisms for adaptation (Pugh Jr et al., 1999; cf. chapter 4). However, even in the well-characterised chemotaxis sensory system in *Escherichia coli* (Berg, 2000; Falke and Hazelbauer, 2001; Sourjik, 2004; Wadhams and Armitage, 2004; Baker et al., 2006), adaptation, in particular its molecular mechanism and dynamics, is not well understood. This constitutes a huge deficit as there has recently been immense interest in the chemotactic behaviour of bacteria (Clark and Grant, 2005; Vladimirov et al., 2008; Emonet and Cluzel, 2008; Zonia and Bray, 2009; Vladimirov and Sourjik, 2009) and noise filtering (Emonet and Cluzel, 2008; Andrews et al., 2006; Tu et al., 2008). Here, we use adaptation time-course data from *in vivo* fluorescence resonance energy transfer (FRET; see Sec. 1.1.4) measurements of chemotactic *E. coli* cells and quantitative modelling to address this problem.

Adaptation in *E. coli* is based on reversible methylation and demethylation of receptors at specific modification sites, catalysed by enzymes CheR and phosphorylated CheB (CheB-P), respectively. Receptor modification regulates the receptor activity and provides a recording of experienced concentration changes (Koshland, 1981; Li and Stock, 2009; Vladimirov and Sourjik, 2009). As a consequence, the rate of tumbling was found to adapt precisely for different ligand concentrations (Berg and Brown, 1972; Alon et al., 1999). To achieve the return of the receptor activity to its pre-stimulus value, receptor

activity-dependent phosphorylation of CheB provides a negative feedback on the receptor activity. In addition, the rates of methylation and demethylation depend on the receptor activity (Toews et al., 1979; Li and Hazelbauer, 2006; Lai et al., 2006a), representing further layers of feedback regulation. Although a lot is known about the components of the chemotaxis pathway, several open questions remain to be answered in adaptation: (i) Despite its importance for cell behaviour, memory and noise filtering, the dynamics of adaptation and the methylation level are largely unknown. This is because the methylation level is difficult to measure precisely, relying on quantification of receptor protein and radioactively labelled methylation substrate (methionine) incorporated into receptors (Kort et al., 1975; Chelsky et al., 1984; Lai and Hazelbauer, 2005; Chalah and Weis, 2005). So far, only the initial rate of adaptation was inferred from the rate of change in motor bias in response to saturating amounts of added attractant (Berg and Brown, 1972). (ii) The molecular mechanism of adaptation, in particular demethylation, remains unclear. While CheR binds strongly to the tether, suggested to increase its concentration in the vicinity of methyl-accepting sites (Wu et al., 1996), the binding affinity of CheB was found to be very low (Barnakov et al., 2002). Instead, binding of CheB-P to the tether induces an allosteric activation of the receptor, increasing the demethylation rate (Barnakov et al., 2002). Furthermore, while the receptor activity-dependence of the methylation and demethylation rates is believed to be a requirement for robust precise adaptation, it is not known if adaptation is precise at the receptor level. Time-course data from *in vivo* FRET experiments, monitoring receptor activity upon stimulation, is ideally suited to study the adaptation dynamics and address these questions.

### 2.3 Details of experimental measurements

---

**Bacteria strains.** To probe the dynamics and molecular mechanism of adaptation experimentally, we used different strains of *E. coli*. Two different wild-type strains and a mutant in adaptation were used. Wild-type strain 1 (WT1) expresses the FRET pair consisting of CheY-YFP and its phosphatase CheZ-CFP from a plasmid. Wild-type strain 2 (WT2) additionally expresses wild-type CheB from a plasmid. The CheB-mutant strain expresses non-regulatable CheB<sup>D56E</sup> instead. The D56E mutation prevents CheB phosphorylation, but allows the protein to retain a basal level of activity. Expression of CheB in WT and CheB mutant strains was induced such that they produced comparable kinase activity, as assessed by the change in FRET signalling activity upon saturating stimulation. The

### 2.3. DETAILS OF EXPERIMENTAL MEASUREMENTS

---

CheB protein level was estimated using Western blots with CheB antibodies, and was at approximately 0.5-fold (WT2) and approximately 5-fold (CheB<sup>D56E</sup> mutant) the native level of CheB<sup>1</sup>.

**Fluorescence resonance energy transfer (FRET) measurements.** Cells were tethered to a microscope cover slip, placed in a flow chamber and then subject to a constant fluid flow of buffer or the non-metabolisable attractant  $\alpha$ -methylaspartate (MeAsp) at indicated concentrations (flow speeds 1000  $\mu$ l/min for WT1, and 500  $\mu$ l/min for WT2 and CheB mutant, respectively). The concentration was changed abruptly by switching between buffer and MeAsp or between different MeAsp concentrations, resulting in concentration step changes (cf. Fig. 2.1 A and 2.2 C). FRET between excited donor, CheZ-CFP, and acceptor, phosphorylated CheY-YFP, in a population of 300-500 cells was monitored using an epifluorescence microscopy setup. Emission light from CFP and YFP was collected. The procedure is detailed in Sourjik and Berg (2002b).

The ratio  $R$  of YFP and CFP fluorescence intensity was used to calculate the time-dependent number of interacting FRET pairs of CheZ-CFP and phosphorylated CheY-YFP in the cell population, which reflects the intracellular kinase activity (Sourjik and Berg, 2002b): The number of FRET pairs  $n$  normalised by its adapted pre-stimulus value  $n_{\text{pre}}$  (after adaptation to the ambient concentration, but before concentration step changes)

$$\frac{n}{n_{\text{pre}}} = \frac{R - R_0}{(\Delta Y/\Delta C) - R} \frac{(\Delta Y/\Delta C) - R_{\text{pre}}}{R_{\text{pre}} - R_0}. \quad (2.1)$$

The parameters  $R_0$  and  $R_{\text{pre}}$  are the ratio for a saturating dose of attractant and the pre-stimulus value, respectively, both of which are measured in each experiment. The fluorescence efficiency ratio  $\Delta Y/\Delta C$  is determined by the experimental setup (Sourjik et al., 2007), and was 0.43 for WT1 (WT2 and CheB mutant) experiments. FRET measurements were taken with a time resolution of 0.2 s (1 s) for WT1 (WT2 and CheB mutant).

---

<sup>1</sup>Details of mutations and induction: Wild-type strain 1 is VS104  $\Delta(\text{cheY cheZ})$ ; expression of cheY and cheZ from a pTrc-based plasmid pVS88, which carries pBR replication origin and ampicillin resistance and is inducible by isopropyl  $\beta$ -D-thiogalactoside (IPTG) (Sourjik and Berg, 2002b). Wild-type strain 2 is VS124  $\Delta(\text{cheB cheY cheZ})$  transformed with pVS88 and pVS91, which carries pACYC replication origin and chloramphenicol resistance and encodes wild-type CheB under control of pBAD promoter inducible by L-arabinose. The CheB-mutant strain is VS124  $\Delta(\text{cheB cheY cheZ})$  transformed with pVS88 and pVS97, which is identical to pVS91 except it encodes the non-regulatable CheB<sup>D56E</sup>. The D56E mutation was introduced into CheB by PCR. Cells were grown at 275 rpm in a rotary shaker to mid-exponential phase ( $\text{OD}_{600} \approx 0.48$ ) in tryptone broth (TB) medium supplemented with 100  $\mu$ g/ml ampicillin, 34  $\mu$ g/ml chloramphenicol, and 50  $\mu$ M IPTG. WT and CheB mutant strains were induced by 0 and 0.0003% arabinose, respectively.

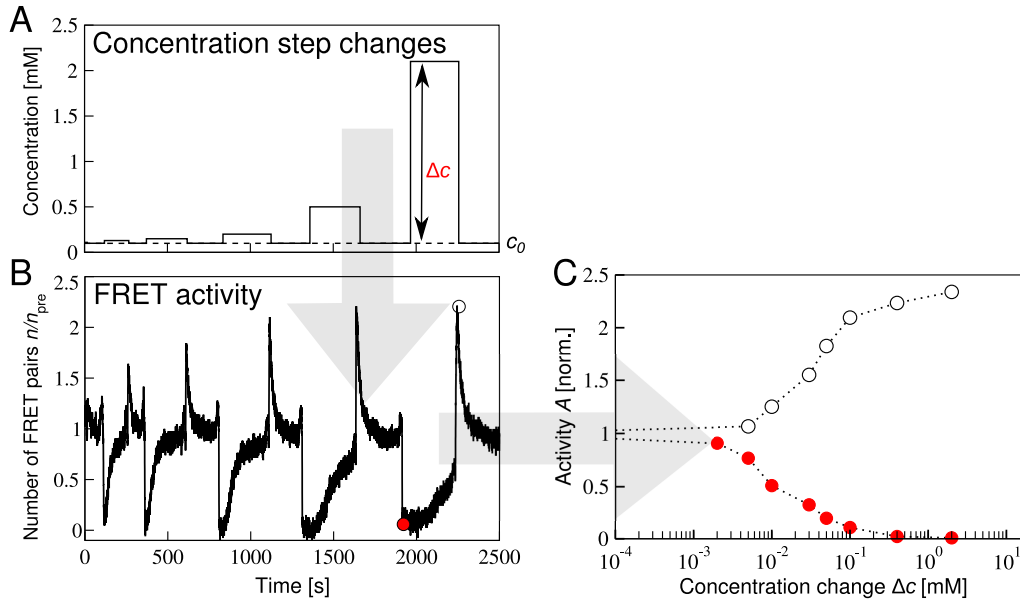


**Figure 2.1.:** Time courses and dose-response curves from FRET. (A) Time course of the applied concentration of attractant MeAsp. The ambient concentration is  $c_0 = 100 \mu\text{M}$ . A series of concentration step changes  $\Delta c$  of increasing size is added and subsequently removed. (B) Time course of the corresponding FRET activity (calculated as the number of FRET pairs). Cells are adapted to the ambient concentration, and respond and adapt to the concentration step changes applied. The red and white circles indicate the initial response to one added and removed example concentration step change, respectively. (C) A dose-response curve plots the initial signalling responses to a series of concentration step changes as a function of concentration step size  $\Delta c$  (indicated by the pair of circles in panel B for one example step change). The lower curve (red circles) is the addition dose-response curve, and the upper curve (white circles) is the removal dose-response curve.

**Time courses and dose-response curves from FRET.** Figure 2.1 shows a typical set of experimental data. Wild-type cells are adapted to an ambient concentration  $c_0$  of attractant MeAsp, and then a series of concentration step changes  $\Delta c$  of increasing size is added and, once cells are adapted, removed (Fig. 2.1 A). Cells respond by chemotactic signalling with an initial drop in signalling activity (characterised by the number of FRET pairs) when the concentration is increased, and then adapt roughly to their pre-stimulus activity. When the concentration step is removed again cells respond by a jump in chemotactic signalling activity, before adapting to their pre-stimulus activity (Fig. 2.1 B).

Dose-response curves summarise the initial response to attractant (Fig. 2.1 C). They are obtained by extracting the minimum (added steps) and maximum response (removed steps) from the response time course in Fig. 2.1 B, and plotting them as a function of the size of concentration steps (Sourjik and Berg, 2002b).

## 2.4 Dynamic Monod-Wyman-Changeux (MWC) model for chemotactic signalling

---

In our model for chemotactic signalling, which we call dynamic MWC model, we take into account the signalling of receptors in response to changes in concentration and receptor methylation level, the dynamics of adaptation, and the kinetics of concentration changes in the experiment. In this section, the components of the model are described in detail.

**Model for chemoreceptors.** Our starting point for modelling is the MWC model (denoted here by static MWC model), which has been successful in describing the chemotactic signalling response of non-adapting cells (Sourjik and Berg, 2004; Mello and Tu, 2005; Keymer et al., 2006; Endres and Wingreen, 2006; Endres et al., 2008). In the static MWC model, we consider mixed receptor complexes composed of the two main receptor types Tar (aspartate receptor) and Tsr (serine receptor, which also binds aspartate with lower affinity) in their *in vivo* ratio. The activity of a two-state receptor complex is given by its probability to be *on*, which depends on the free-energy difference  $F = F_{\text{on}} - F_{\text{off}}$  between its *on* and *off* state (cf. Eq. 1.14; Keymer et al., 2006; Endres et al., 2008),

$$A(c, m) = \frac{1}{1 + e^{F(c, m)}}. \quad (2.2)$$

Note that we drop the  $\Delta$  in the notation for energy differences compared to the *Introduction* for simplicity. The free-energy difference  $F(m, c)$  for a mixed receptor complex of Tar and Tsr is given by

$$F(c, m) = N \left[ \epsilon(m) + \nu_a \ln \left( \frac{1 + c/K_a^{\text{off}}}{1 + c/K_a^{\text{on}}} \right) + \nu_s \ln \left( \frac{1 + c/K_s^{\text{off}}}{1 + c/K_s^{\text{on}}} \right) \right]. \quad (2.3)$$

The free-energy difference is determined by two contributions, one from methylation (in terms of receptor methylation level  $m$ ) favouring the *on* state, and one from attractant binding at MeAsp concentration  $c$  favouring the *off* state. Similar free-energy based two-state models were recently used to describe clustering of ion channels (Ursell et al., 2007) and small GTPases in eukaryotic cells (Gurry et al., 2009). The parameters of this equation are explained in the following in detail:

The parameter  $N$  is the number of receptor dimers per complex. It was determined as follows: First, the receptor complex size was obtained for each ambient concentration

using a least-squares fit to addition dose-response curves (cf. Fig. 2.2 A). Consistent with previous modelling results, we find that the receptor complex size increases with increasing ambient concentration (Mello and Tu, 2007; Endres et al., 2008). As the simplest assumption, we used a linear relationship between receptor complex size and ambient concentration (Fig. 2.2 A). This linear fit is given by  $N(c_0) = a_0 + a_1 c_0$  with  $a_0 = 17.5$  and  $a_1 = 3.35 \text{ mM}^{-1}$ . Note that the complex size for removal may be different for each data point as cells are adapted to the increased concentration after each step change. Using the linear relationship allows us to interpolate the receptor complex size for removal dose-response curves.

The free-energy contribution  $\epsilon(m)$  is attributed to methylation, and was recently extracted from dose-response curves for mutants resembling fixed methylation states (Fig. 2.2 B; Endres et al., 2008). We used the interpolating function

$$\epsilon(m) = 1 - 0.5 m. \quad (2.4)$$

The indexes  $a$  and  $s$  denote Tar and Tsr receptor, respectively. We assumed fractions of Tar and Tsr in a complex according to their wild-type ratio,  $\nu_a : \nu_s = 1 : 1.4$ . The ligand dissociation constants for MeAsp are  $K_a^{\text{on}} = 0.5 \text{ mM}$ ,  $K_a^{\text{off}} = 0.02 \text{ mM}$ ,  $K_s^{\text{on}} = 10^6 \text{ mM}$ , and  $K_s^{\text{off}} = 100 \text{ mM}$  (Keymer et al., 2006). All energies are measured in units of  $k_B T$  ( $k_B$  being the Boltzmann constant and  $T$  the absolute temperature).

Tar and Tsr receptor dimers have 8 major residues which can be reversibly methylated (except for minor modification sites on Tsr which are methylated less strongly; cf. *Introduction*). The adapted methylation level  $m^*$  at ambient concentration  $c_0$  according to the MWC model is given by

$$m^* = 2 - 2 \left[ \frac{F^*}{N(c_0)} - \nu_a \ln \left( \frac{1 + c_0/K_a^{\text{off}}}{1 + c_0/K_a^{\text{on}}} \right) - \nu_s \ln \left( \frac{1 + c_0/K_s^{\text{off}}}{1 + c_0/K_s^{\text{on}}} \right) \right], \quad (2.5)$$

where the  $F^*$  indicates the adapted free energy difference, which is given by the adapted receptor complex activity according to  $F^* = \ln(1/A^* - 1)$ . The adapted activity is  $A^* = 1/2.9$  for wild-type cells as assessed from the maximum and minimum values of the experimental dose-response data (described in the next section). The receptor complex size  $N(c_0)$  changes with ambient concentration as discussed above. The adapted receptor methylation level is shown in Fig. 2.3. As can be seen from the figure, the receptor methylation level lies in the physiological range at ambient concentrations used in FRET experiments.

## 2.4. DYNAMIC MONOD-WYMAN-CHANGEUX (MWC) MODEL FOR CHEMOTACTIC SIGNALLING

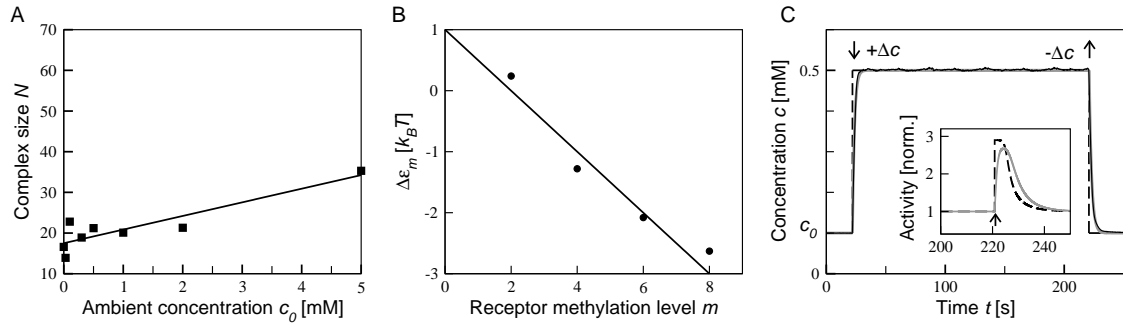


**Figure 2.2.:** Model ingredients. (A) Size of adapted receptor complex  $N$  (total number of Tar and Tsr receptors per complex) as function of ambient concentration  $c_0$  (corresponding to adapted methylation level  $m$ ). Individual complex sizes (symbols) were obtained by fitting the static MWC model to dose-response curves for addition of MeAsp. These values were fitted by a linear function (line). (B) Energy contribution to receptor complex free energy from methylation level  $m$  per receptor dimer. Shown are fitting parameters for Tar receptors from Endres et al. (2008) (symbols), as well as linear fit  $\epsilon(m)=1 - 0.5m$  (in units of  $k_B T$  with  $k_B$  the Boltzmann constant and  $T$  absolute temperature). (C) Profile of concentration step change as measured experimentally using fluorescent marker (solid black line; Sourjik and Berg, 2002b), exponential fit used in dynamic MWC model for WT1 MeAsp profile (grey line; rate constants  $\lambda_{\text{add}}=0.6/s$  and  $\lambda_{\text{rem}}=0.5/s$ ), and perfect step change (black dashed line). Addition and removal times are marked by arrows. (C *Inset*) Response of mixed receptor complex to MeAsp removal for perfect (black dashed line) and exponentially fitted step change (grey line). FRET and receptor complex activities were normalised by their adapted pre-stimulus values before addition of MeAsp.

**Dynamics of ligand concentration and down-stream signalling.** In experiments, changes in MeAsp concentration are established over several seconds, due to the finite flow speed and mixing effects in the flow chamber (Fig. 2.2 C). In our model, we assume exponentially rising and falling concentration changes upon addition and removal in line with previous measurements by Sourjik and Berg (2002b)<sup>2</sup>.

As shown in Appendix A, analysing the signalling pathway of *E. coli* we found that the phosphorylation reactions are sufficiently fast to assume that concentrations of phosphorylated (and unphosphorylated) proteins are in quasi-steady state during concentration step changes. Furthermore, the concentrations of activated proteins are approximately proportional to the receptor complex activity. Both these conditions allow us to use the receptor complex activity as a substitute for the down-stream activity measured by FRET, reducing greatly the number of model parameters for fitting to data. This approximation was also used in previous work, but was never explicitly tested (Endres and Wingreen,

<sup>2</sup>The time course of the ligand flow for an added and removed step follows respectively  $c_{\text{add}}(t) = c_0 + (1 - \exp(-\lambda_{\text{add}}t))\Delta c$  and  $c_{\text{rem}}(t) = c_0 + \exp(-\lambda_{\text{rem}}t)\Delta c$ . Exponential rate constants were obtained from fits to ligand flow profiles (cf. Fig. 2.2 C), with  $\lambda_{\text{add}}=0.6 \text{ s}^{-1}$  and  $\lambda_{\text{rem}}=0.5 \text{ s}^{-1}$  for flow speed  $1000 \mu\text{l}/\text{min}$ , and  $\lambda_{\text{add}}=0.27 \text{ s}^{-1}$  and  $\lambda_{\text{rem}}=0.28 \text{ s}^{-1}$  for flow speed  $500 \mu\text{l}/\text{min}$ .

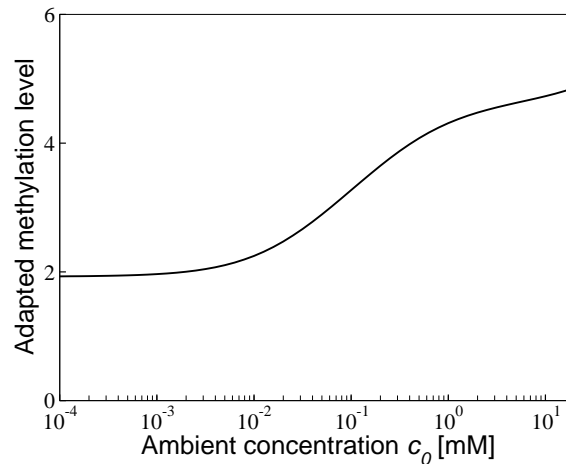


**Figure 2.3.:** Adapted receptor methylation level  $m^*$  as a function of ambient concentration  $c_0$  according to the static MWC model (cf. Eq. 2.5).

2006; Keymer et al., 2006; Endres et al., 2008).

In contrast, adaptation occurs on a similar time scale as the kinetics of the MeAsp concentration flow, and therefore needs to be modelled explicitly.

**Model for precise adaptation.** Adaptation is mediated by methylation and demethylation enzymes CheR and CheB, respectively. We describe the kinetics of the average receptor methylation level  $m$  in a receptor complex by

$$\frac{dm}{dt} = g_R(1 - A) - g_B A^3. \quad (2.6)$$

The first term describes the rate of methylation and the second term the rate of demethylation. The parameters  $g_R$  and  $g_B$  are the methylation and demethylation rate constants, which incorporate the total concentrations of CheR and CheB in a cell, respectively. The variable  $A$  is the receptor complex activity. Methylation and demethylation rates do not depend directly on the concentration of MeAsp or the methylation level, only on the receptor complex activity  $A$ . As discussed in the *Introduction* (Sec. 1.2.3), such dynamics leads to precise adaptation of the receptor complex activity to adapted level  $A^*$  for a constant MeAsp stimulus (Barkai and Leibler, 1997; Endres and Wingreen, 2006).

We determined the demethylation rate for WT1 to be  $g_B=0.11 \text{ s}^{-1}$  from a least-squares fit to addition and removal dose-response curves (WT1) using the receptor complex size  $N(c_0)$  from the static MWC model. The methylation rate  $g_R=0.0069 \text{ s}^{-1}$  is given by the condition that at steady state ( $dm/dt=0$ ) the activity equals  $A^*$  (Fig. 2.4-2.9). Alter-



## 2.4. DYNAMIC MONOD-WYMAN-CHANGEUX (MWC) MODEL FOR CHEMOTACTIC SIGNALLING

---

natively, least-square fitting the model to the data collapse (Fig. 2.11, 2.12) resulted in  $g_R=0.0019\text{ s}^{-1}$  (and  $g_B=0.030\text{ s}^{-1}$ ). For WT2 (Fig. 2.12 A), we used the same methylation rate constant as for WT1, but adjusted the demethylation rate constant to account for the increased adapted activity  $A^*$ .

We assumed an adapted receptor complex activity  $A^*=1/2.9\approx 0.34$  for WT1 as assessed from the maximum and minimum values of the experimental dose-response data in Fig. 2.4. Steady-state activities for WT2 and CheB mutant were estimated to be  $A^*\approx 1/2$ . For comparison of model and data, we normalised the receptor-complex activity for WT1, WT2 and CheB mutant by their respective activities when adapted to ambient concentration.

The adapted receptor-complex activity  $A^*$  is determined by the steady-state condition  $dm/dt = 0 = g_R(1 - A^*) - g_B A^{*3}$ . According to our model, receptors are methylated when the complex is inactive, and demethylated when it is active. Furthermore, we postulate a very strong sensitivity of the demethylation rate on activity due to the intrinsic receptor-activity dependence of the demethylation rate, as well as additional layers of feedback regulation for demethylation by CheB, including the activation of demethylation enzyme CheB by phosphorylation and potential cooperativity between phosphorylated CheB molecules (see below and Appendix A, Eq. A.7). This mechanism leads to a strong asymmetry, where adaptation of inactive receptors (methylation) is slow compared to the rapid adaptation of active receptors (demethylation). This corresponds to experimental time courses (cf. next section; Fig. 2.7). Note that the asymmetry between slow adaptation of inactive and active receptors, respectively, cannot simply be achieved by adjusting the rate constants of methylation and demethylation individually, since they are constrained by the adapted activity  $A^*$ .

Although our adaptation model is independent of biochemical details, our predicted fast demethylation at high activities may be due to cooperativity of two CheB-P molecules. According to *in vitro* experiments, CheB-P binding to the carboxyl-terminus of chemoreceptors induces an allosteric activation of the receptor, increasing the demethylation rate (Barnakov et al., 2002). However, in contrast to CheR, CheB-P binds only weakly to the tether (Barnakov et al., 2002). Reconciling these two observations, it is conceivable that two CheB-P molecules are necessary for efficient demethylation at high activities: one CheB-P molecule may bind to a tether to allosterically activate a group of receptors (assistance neighbourhood), while another CheB-P molecule demethylates the receptors in the neighbourhood. As two CheB-P molecules are not required to bind to the same recep-

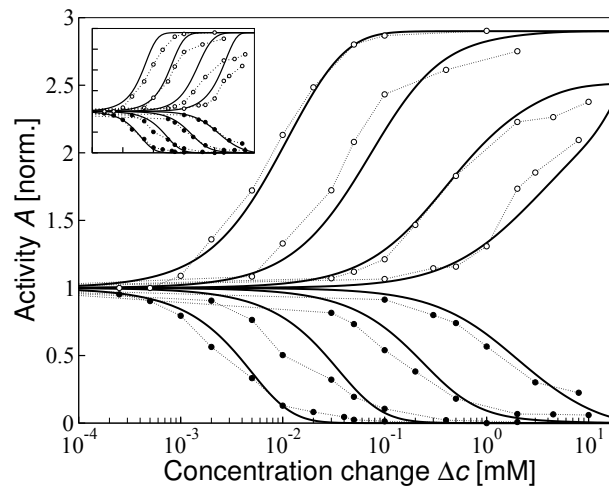


**Figure 2.4.:** Response of wild-type cells to step changes  $\Delta c$  of MeAsp concentration at different ambient concentrations. Dose-response curves: Symbols represent averaged response from FRET data (WT1) after adaptation to ambient concentrations 0, 0.1, 0.5 and 2 mM as measured by Sourjik and Berg (2002b) (filled and open circles correspond to response to addition and removal of attractant, respectively). Solid lines represent the dynamic MWC model of mixed Tar/Tsr-receptor complexes including ligand rise (addition) and fall (removal), as well as adaptation (receptor methylation) dynamics. (*Inset*) Dose-response curves for MWC model without adaptation dynamics (lines). FRET and receptor complex activities were normalised by adapted pre-stimulus values at each ambient concentration. Squared errors between model and experimental data for the four dose-response curves shown are 0.64 (dynamic MWC model) and 3.95 (static MWC model), respectively. For comparison, fitting to eight addition and removal dose-response curves using  $K_{a(s)}^{\text{on}}$ ,  $K_{a(s)}^{\text{off}}$ , as well as a linear function  $N(c_0)$  as fitting parameters, yields squared errors 0.83 (dynamic MWC model) and 2.09 (static MWC model).

tor, this mechanism is not contradicted by the small number of CheB molecules in a cell. An alternative, simpler mechanism for cooperativity is dimerisation of CheB-P molecules, which, however, has not been observed experimentally (Anand et al., 1998; Kentner and Sourjik, 2009).

## 2.5 Comparison of experiment and theory

**Dose-response curves.** The dynamic MWC model, which includes the effects of adaptation and MeAsp flow, quantitatively describes the experimental dose-response curves in Fig. 2.4 (additional, dose-response curves are provided in Appendix B). Specifically, adaptation leads to a non-saturated response for large MeAsp step changes  $\Delta c$  at high ambient concentrations, which is not seen in the static MWC model without adaptation dynamics (Fig. 2.4, *Inset*)<sup>3</sup>. This is due to adaptation reducing the initial response am-

<sup>3</sup>Note, however, that responses eventually do saturate according to the dynamic MWC model for even larger concentration step changes due to the presence of Tsr receptors (at 0.5 mM ambient for  $\Delta c > 40$  mM; not shown).

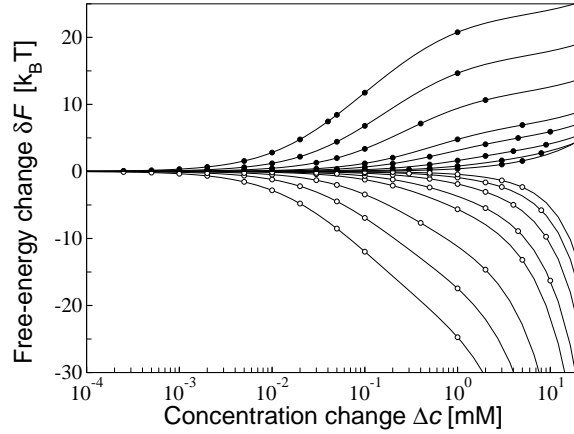


**Figure 2.5.:** Changes in the free-energy difference  $\delta F = F - F^*$  of a mixed-receptor complex upon concentration step changes  $\Delta c$  of MeAsp (lines), where  $F^*$  is the adapted free-energy difference. The curves correspond to ambient concentrations  $c_0=0, 0.03, 0.1, 0.3, 0.5, 1, 2$  and  $5$  mM with free-energy differences for experimental concentration step changes indicated by symbols (filled circles for addition, open circles for removal of MeAsp).

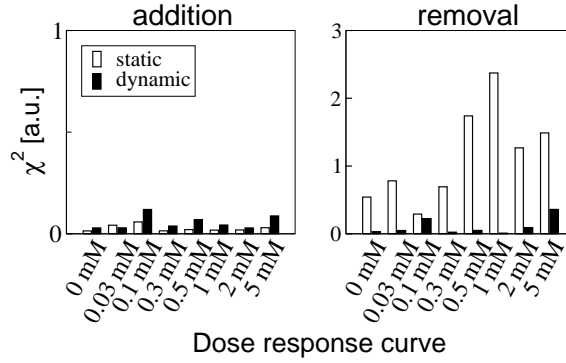


**Figure 2.6.:** Residual absolute squared errors per addition (left panel) and removal (right panel) dose-response curve for the static and dynamic MWC model as shown in Fig. 2.4 and B.1 A in Appendix B. Note the different axis scales for addition and removal plots.

plitude of receptor complexes during a concentration step change, which is particularly important for removal of concentration (cf. Fig. 2.2 C).

Figure 2.5 shows the free-energy change associated with each concentration step change. For increasing ambient concentrations, the free-energy changes generally decrease at a fixed concentration step change  $\Delta c$ . This is the reason for the reduced response amplitudes in the dynamic MWC model at large MeAsp step removals, because adaptation compensates for smaller free-energy changes at increasing ambient concentrations.

The dynamic MWC model describes the dose-response data significantly better than the static MWC model. Figure 2.6 quantifies the difference between measured dose-response curves and the static, as well as the dynamic MWC model, respectively. We plot squared errors for each addition and removal dose-response curve. While the error for the dy-

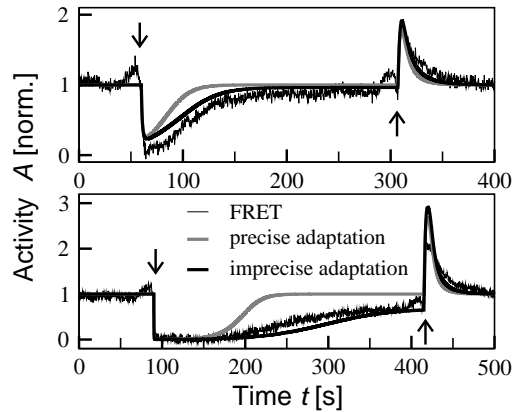


**Figure 2.7.:** Typical time courses of receptor complex activity in response to two different MeAsp concentration step changes,  $\Delta c=0.05$  mM (top) and  $\Delta c=0.4$  mM (bottom), at ambient concentration  $c_0=0.1$  mM. Experimental FRET measurement (thin black line), as well as dynamic MWC model for precise (grey lines) and imprecise adaptation (black lines;  $m_{max}=4.1$  and  $K=0.5$ ). FRET and receptor complex activities were normalised by adapted pre-stimulus values before addition of MeAsp.

dynamic MWC model is slightly larger for addition curves, its error for removal curves is much smaller than that for the static MWC model. Hence, the dynamic MWC model is suited better to describe the experimental data. Note also their overall squared errors are indicated in the caption of Fig. 2.4.

**Time courses.** Figure 2.7 shows example time courses for two different concentration steps (time points of addition and removal are indicated by arrows) from experiment and our precise adaptation model. Our model describes well the asymmetry of the adaptation dynamics for added and removed concentration step changes, the latter being much faster. However, there are discrepancies in the long-term behaviour of adaptation to added steps; namely, our model predicts precise adaptation and a faster dynamics than observed in experiment. Also plotted in Fig. 2.7 are time courses for a model of imprecise adaptation, which fits the experimental data better than the precise adaptation model. This model is discussed in detail in the next section, (cf. Eq. 2.9).

## 2.6 Model predictions, verification and adjustments

### 2.6.1. Data collapse of time courses for adaptation dynamics

The short-term behaviour in the time-course data in Fig. 2.7 is essential in deriving our adaptation model, used to quantitatively describe dose-response curves (Fig. 2.4). How well does our adaptation model describe the long-term behaviour in the time-course data,

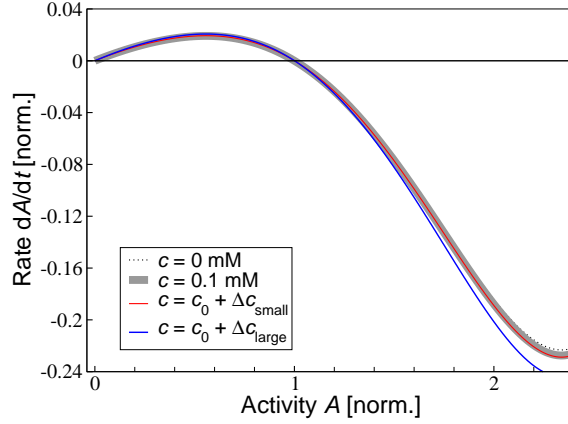


**Figure 2.8.:** Effect of ligand concentration-dependent receptor complex size  $N(c)$  on the predicted data collapse according to Eq. 2.7. Plotted are the predicted functions  $f(A)$  for  $N$  corresponding to ambient concentration  $c = 0.1$  mM (thick grey line), zero ambient (buffer; black dotted line), and concentration upon small ( $\Delta c = 0.03$  mM; red line) and large ( $\Delta c = 2$  mM; blue line) concentration changes.

and hence the complete adaptation dynamics? Our model for precise adaptation predicts that the observable rate of activity change is given by

$$\frac{dA}{dt} = \frac{\partial A}{\partial m} \frac{dm}{dt} + \frac{\partial A}{\partial c} \frac{dc}{dt}, \quad (2.7)$$

where the rate of change of the methylation level  $dm/dt$  is described by Eq. 2.6, and  $dc/dt$  is the rate of change of the MeAsp concentration. After a concentration step change, the MeAsp concentration is constant with  $dc/dt = 0$ , and the rate of activity change is given by

$$\frac{dA}{dt} = \frac{\partial A}{\partial m} \frac{dm}{dt} = A(1-A) \frac{N}{2} [g_R(1-A) - g_B A^3] \equiv f(A), \quad (2.8)$$

where we used  $\partial A / \partial m = (\partial A / \partial F)(\partial F / \partial m) = A(1-A)N/2$ . This expression depends on the receptor complex size  $N$ , which we found from fitting the MWC model to dose-response curves from FRET to increase with ambient concentration (Fig. 2.2 A).

**Dependence of the data collapse on receptor complex size.** As we do not have a model which describes how receptor complex size changes in time in response to concentration changes, we plot in Fig. 2.8 the data collapse for different  $N$  corresponding to the concentrations used in the experiments. This provides the envelope in which the data collapse is expected to change with  $N$ . We find that the data collapse does not change very much compared to the data collapse for ambient concentration  $c_0$ . Hence, we neglect this minor dependence on the receptor complex size on ligand concentration in the following, and

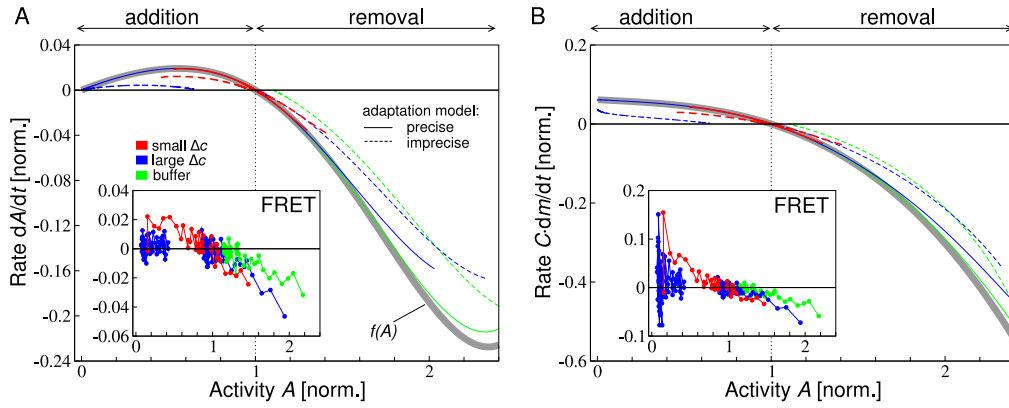


**Figure 2.9.:** Adaptation dynamics as function of receptor activity for WT1 at ambient concentration  $c_0 = 0.1$  mM for addition and subsequent removal of small (red lines and symbols) and large (blue lines and symbols) MeAsp concentration step changes, as well as removal of MeAsp back to zero ambient concentration (buffer; green lines and symbols). (A) Rate of change of receptor complex activity  $dA/dt$  as occurs during adaptation. Thick grey line is the analytical result from the dynamic MWC model, where activity change is purely from adaptation (methylation)  $dA/dt = (dA/dm)(dm/dt) = f(A)$ . coloured lines show results from simulated time series for small ( $\Delta c = 0.03$  mM) and large ( $\Delta c = 0.4$  mM) concentration step changes in MeAsp concentration, with activity dynamics recorded starting 10 s after the onset of concentration step change. Precise (solid lines), as well as imprecise adaptation (dashed lines;  $m_{max} = 4.1$  and  $K = 0.5$ ) are considered. (A *Inset*) Rate of FRET activity change from experimental time-course data. Small ( $\Delta c = 0.03$  mM) and large ( $\Delta c = 2$  mM) concentration step changes. (B) Rate of change of the methylation level  $dm/dt$  corresponding to panel A (normalised by adapted activity  $A^*$  and  $C = N/2$ , where  $N$  is the receptor complex size). Effective rate of change of methylation level for all time courses is obtained by  $(dA/dt)/[A(1 - A)]$ . (B *Inset*) Effective rate of change of methylation level from experimental time-course data. FRET and receptor complex activities, as well as activity rate changes were normalised by adapted pre-stimulus activities at ambient concentrations before addition of MeAsp.

the rate of activity change is a function  $f(A)$  of the activity only, independent of ligand concentration and receptor methylation level.

**Properties of predicted data collapse.** This predicts a data collapse of all adaptation time courses, independent of the duration, size and number of concentration step changes, onto a single curve  $dA/dt = f(A)$  (Fig. 2.9 A, thick grey line).

This non-monotonous function of the activity has three fixed points: the adapted activity  $A = A^*$ , where methylation and demethylation rates exactly balance each other, as well as  $A = 0$  and  $A = 1$ , where the receptor complex activity is saturated in the *off* and *on* state, respectively. Figure 2.9 A, *Inset* shows the experimental rate of activity change as extracted from our quantitative time-course data from FRET for different concentration step changes at an ambient concentration. We observe that, in contrast to the prediction of the model, the rate of activity change depends on the magnitude of the concentration step changes. For addition of large concentration step changes (blue symbols), the rate

---

## 2.6. MODEL PREDICTIONS, VERIFICATION AND ADJUSTMENTS

is reduced and the activity stays below the pre-stimulus value. Furthermore, for total removal of MeAsp concentration (replacement with buffer medium, green symbols), the magnitude of the rate is reduced and the activity remains above the pre-stimulus value.

**Ligand flow.** To explain the deviations from the predicted data collapse, we consider the effects of MeAsp flow and imprecise adaptation in our model. According to Eq. 2.7, each of the two effects contribute independently to the rate of activity change. First, we include the MeAsp flow for concentration step changes as described, and simulate time courses based on the precise adaptation model (Fig. 2.9 A, solid lines). We find that in the demethylation regime (negative rate of activity change), the kinetics of concentration step removal gives rise to minor deviations from the curve  $f(A)$  in qualitative agreement with experiment. However, in the methylation regime (positive rate of activity change), unlike the experimental data, all time courses lie accurately on the  $f(A)$  curve.

**Imprecise adaptation.** Next, we consider imprecise adaptation, i.e. the incomplete return of the activity to pre-stimulus level, which is apparent in the time courses (Fig. 2.7).

In our model for imprecise adaptation, the kinetics of the methylation level  $dm/dt$  depends explicitly on the receptor methylation level:

$$\frac{dm}{dt} = g_R \frac{m_{\max} - m}{m_{\max} - m + K} (1 - A) - g_B \frac{m}{m + K} A^3. \quad (2.9)$$

The parameter  $m_{\max}$  is the maximum number of methylation sites per receptor,  $K$  is the lower bound for the number of sites, which need to be available for efficient methylation or demethylation. We use  $m_{\max}=4.1$  to only allow Tar (not Tsr) receptors to become methylated (the total number of methylation sites of a receptor homodimer being 8). Further, we use  $K=0.5$  to implement reduced efficiency of methylation or demethylation at a low number of available sites. Note that time courses for this imprecise adaptation model are also shown in Fig. 2.7 ( $g_R$  and  $g_B$  are the same in both models). The imprecise adaptation model fits the time courses shown far better. However, there is a large variability of imprecision seen in different data sets and more experiments are needed to produce a general model of imprecise adaptation. This is quantified below in the next section.

Using the imprecise adaptation model leads to significant deviations from the data collapse (Fig. 2.9 A, dashed lines). Adaptation after addition of increasing concentration step changes results in a reduced adapted receptor complex activity (adapted activity

after removal is always the same as the concentration is the ambient concentration). Total removal of MeAsp concentration (buffer) results in an increased adapted activity. Our imprecise adaptation model is in line with the experimental data, showing that the data collapse is an effective way to compare experimental and theoretical time courses and to quantify the effects of ligand flow and imprecise adaptation.

**Kinetics of the receptor methylation level.** In addition to the adaptation dynamics, the data collapse allows us to determine the kinetics of the receptor methylation level, which is difficult to measure directly. Figure 2.9 B shows the rate of change of the methylation level as a function of the receptor complex activity for experimental data, as well as the dynamic MWC model. The data and curves were obtained by dividing the rate of activity change  $dA/dt$  following concentration step changes by  $A(1 - A)$ . If the activity change is caused only by the adaptation dynamics, this procedure yields a function proportional to the rate of change of the methylation level,  $dm/dt$ . According to our precise adaptation model Eq. 2.6, the rate of change of the methylation level is a monotonically decreasing function of activity with one steady state, marking the adapted receptor complex activity (Fig. 2.9 B, thick grey line). Corresponding to the rate of activity change in Fig. 2.9 A, the kinetics of ligand flow upon concentration step changes, as well as imprecise adaptation result in deviations from this curve. As before, we mainly find signatures of imprecise adaptation in the experimental data in Fig. 2.9 B, *Inset*.

### 2.6.2. Quantification of adaptation imprecision

In Fig. 2.10 we quantify the imprecision of adaptation. Cells were adapted to 100  $\mu\text{M}$  ambient concentration with adapted pre-stimulus activity  $A_{\text{pre}}^*$  measured by FRET. Concentration step changes of various sizes were added, and cells adapted to the new concentration with post-stimulus adapted activity  $A_{\text{post}}^*$ . We define a measure of imprecision as

$$\text{Imprecision} = \frac{A_{\text{post}}^* - A_{\text{pre}}^*}{A_{\text{pre}}^*}. \quad (2.10)$$

We find that adaptation is highly variable from experiment to experiment (high standard deviation). However, cells are found to consistently adapt imprecisely at high concentrations. In the following sections, we assume small concentrations and, therefore, that adaptation is precise.



## 2.6. MODEL PREDICTIONS, VERIFICATION AND ADJUSTMENTS

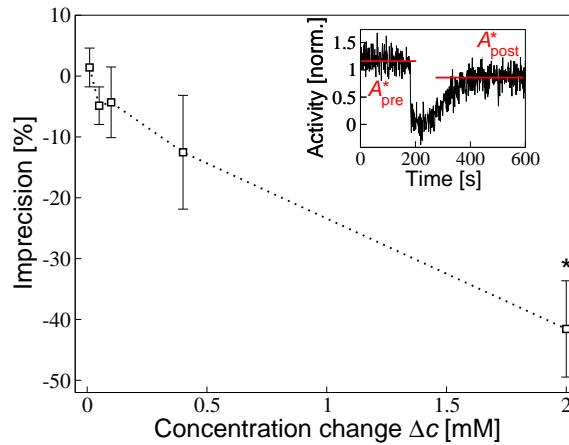


**Figure 2.10.:** Imprecision of adaptation. FRET time courses were measured for cells adapted to  $c_0 = 0.1$  mM ambient concentration, and subject to various concentration step changes  $\Delta c$ . Levels of adapted FRET activity were determined before and after each added concentration step change, and the imprecision was calculated as  $(A_{\text{post}}^* - A_{\text{pre}}^*)/A_{\text{pre}}^*$ . Symbols correspond to mean values of imprecision, and error bars indicate the standard mean error based on three replicates. The star indicates statistically significant difference from zero with Student's t-test p-value smaller than 0.05. (*Inset*) Example FRET time course for  $\Delta c = 2$  mM with adapted pre- and post-stimulus activity indicated.

### 2.6.3. Comparison of different adaptation models

The data collapse of experimental time courses enables the efficient evaluation of different adaptation models, including our model and other models from the literature (Fig. 2.11 A). In all models considered here the rates of methylation and demethylation only depend on the receptor complex activity. Hence, they show precise adaptation. The explicit activity dependencies given respectively by the first and second term in the legend of Fig. 2.11. For instance, the first model (solid red line) is given by Eq. 2.6. Two classes of models are analysed here. The first class of models, including our model, is based on a linear activity-dependence of the methylation and demethylation rates for binding of CheR and CheB to inactive and active receptor, respectively. Feedback from the activity-dependent phosphorylation of CheB is accounted for by additional factors of the receptor complex activity. Our model includes cooperative CheB feedback (solid red line), while linear CheB feedback (dashed red line) and no CheB feedback (dotted red line) are considered as well (Endres and Wingreen, 2006; Hansen et al., 2008; Vladimirov et al., 2008; Kalinin et al., 2009). Another class of models has been proposed, showing ultrasensitivity with respect to CheR and CheB protein levels. In these models, the activity-dependence of the methylation and demethylation rates for enzyme binding is described by Michaelis-Menten kinetics, and linear CheB feedback (solid blue line) and no CheB feedback (dashed blue

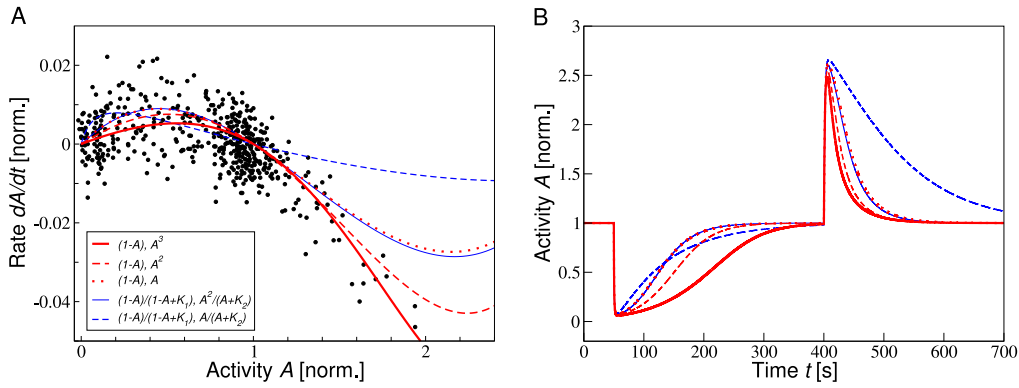


**Figure 2.11.:** Comparison of different adaptation models. (A) Rate of activity change during adaptation as a function of activity for FRET data (WT1; symbols) and different adaptation models (coloured lines). Experimental FRET activity change is measured at ambient concentration  $c_0=0.1$  mM for added and subsequently removed concentration step changes  $\Delta c=0.03, 0.05, 0.1, 0.4$  and  $2$  mM. For the five models, the dependencies of the methylation and demethylation rates on the receptor complex activity  $A$  are given in the legend and are explained in the text. Models were fitted to the experimental  $dA/dt$  data using a least-squares fit, where the methylation rate constant  $g_R$  was the only fitting parameter. The demethylation rate  $g_B$  was determined to produce the adapted activity  $A^*\approx 1/3$ . The parameters  $K_1$  and  $K_2$  were converted from Emonet and Cluzel (2008). (B) Representative time courses for the different models in panel A for a concentration step change  $\Delta c=0.1$  mM at ambient concentration  $c_0=0.1$  mM. FRET and receptor complex activities, as well as activity rate changes were normalised by adapted pre-stimulus activities at ambient concentrations before addition of MeAsp. Least-squares errors between experimental data and model in panel A are  $0.0021 [1 - A, A^3]$ ,  $0.0022 [1 - A, A^2]$ ,  $0.0025 [1 - A, A]$ ,  $0.0025 [(1 - A)/(1 - A + K_1), A^2/(A + K_2)]$ , and  $0.0036 [(1 - A)/(1 - A + K_1), A/(A + K_2)]$ .

line) is considered (Emonet and Cluzel, 2008). The last model has the property that the rate of change of methylation level becomes independent of activity around the steady-state, leading to extremely long adaptation times. Details of the alternative adaptation models and the fitting procedure are given in Appendix E. While several models are consistent with the experimental data, our model compares most favourably. The ultrasensitive Michaelis-Menten model without CheB feedback seems not to be consistent with the data. Comparing simulated time courses for the different adaptation models in Fig. 2.11 B, our model is best to capture the experimentally observed asymmetry between adaptation to addition and removal of concentration step changes. The quality of fit between the respective models and data is indicated by their least-squares errors in the caption of Fig. 2.11.

#### 2.6.4. Demethylation dynamics

To further validate our adaptation model, we experimentally tested two predictions about how changing the demethylation rate affects the adaptation dynamics. First, in our

## 2.6. MODEL PREDICTIONS, VERIFICATION AND ADJUSTMENTS

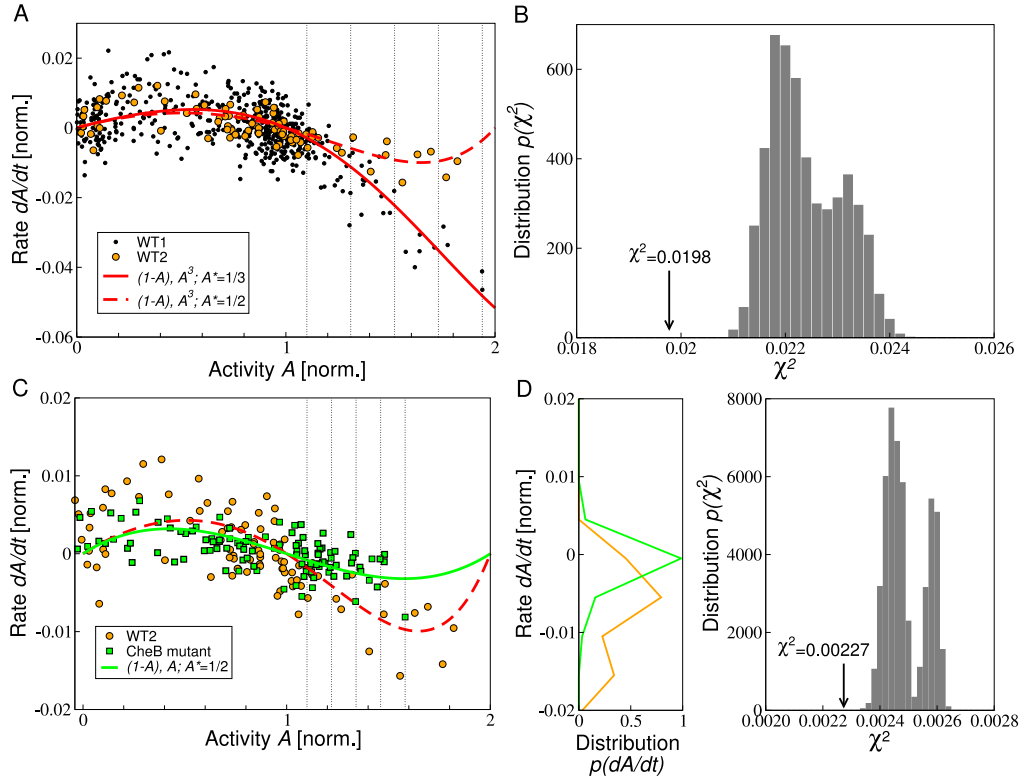


**Figure 2.12.:** Effects of (A) steady-state activity and (C) CheB regulation by phosphorylation. (A) Black and orange dots correspond to the rate of FRET activity change from experimental time-course data for WT1 (Fig. 2.11) and for WT2 (addition and subsequent removal of concentration step change  $\Delta c = 0.03$  mM at zero ambient concentration), respectively. Red lines correspond to the predicted rate of activity change  $dA/dt = f(A)$  purely from adaptation (solid and dashed lines correspond to steady-state activities  $A^* \approx 1/3$  and  $1/2$ , respectively). The methylation rate constant  $g_R = 0.0019$  s $^{-1}$  is the same in each case, whereas the demethylation rate constant  $g_B$  was adjusted to yield the adapted activity. Dotted lines indicate bins used to quantify the difference between data sets in panel B. (B) Distribution of squared errors ( $\chi^2$ ) between predicted rate of activity change and experimental data sets for WT1 and WT2, when randomly permuting  $10^4$  pairs of data points between the data sets, one pair chosen within each bin in panel A. The error is calculated as the sum of errors for each data set (including the permuted data points) against its respective model. The error of the unpermuted data sets is indicated by the arrow. (C) Green squares represent the rate of FRET activity change from experimental time-course data for CheB mutant (addition and subsequent removal of concentration step changes  $\Delta c = 0.03$  mM and  $0.1$  mM at zero ambient concentration). Orange dots and red dashed line are the same as in panel A. The green line represents the rate of change of receptor complex activity for CheB mutant purely from adaptation. The methylation rate  $g_R(1 - A)$  of the mutant is the same as for wild-type cells, whereas the demethylation rate is  $\tilde{g}_B A$ . The rate constant  $\tilde{g}_B$  was adjusted to yield the same adapted activity as in wild-type cells. Dotted lines indicate bins used to quantify the difference between data sets in panel D. (D, left) Distribution of data points of the rate of activity change for activities above  $A = 1.1$  WT2 and CheB mutant data in panel C. (D, right) Distribution of squared errors between predicted rate of activity change and experimental data sets for WT2 and CheB mutant, when randomly permuting  $10^4$  pairs of data points between the data sets, one pair chosen within each bin in panel C. The error is calculated as the sum of errors for each data set (including the permuted data points) against its respective model. The error of the unpermuted data sets is indicated by the arrow.

precise-adaptation model the data collapse depends strongly on the steady-state activity. For instance, increasing the steady-state activity from  $A^* \approx 1/3$  to  $1/2$  changes the data collapse from the solid to the dashed red line in Fig. 2.12 A. Such an increase in the steady-state activity can be achieved by decreasing CheB expression level, corresponding to a decreasing demethylation rate constant, at constant CheR expression level. To validate this prediction, a different wild-type strain (WT2) was created, in which CheB expression was induced from a plasmid, while all other chemotaxis proteins were expressed as before (WT1). The steady-state activity was estimated to be  $A^* \approx 1/2$  (compared to  $1/3$  in WT1). The data collapse (Fig. 2.12 A, orange circles) corresponds well to the predicted curve (dashed red line).

Second, considering adaptation without feedback through activity-dependent CheB phosphorylation, while keeping the steady-state activity constant (Fig. 2.12 C, green line), leads to the following dynamics:

$$\frac{dm}{dt} = g_R(1 - A) - \tilde{g}_B A, \quad (2.11)$$

where the activity-dependence of the demethylation rate is diminished. We assume that the methylation rate is the same as for wild-type cells. This prediction can be tested using a mutant strain, which contains non-regulatable CheB with about 10 percent of CheB-P activity. The CheB expression level was increased to produce the kinase activity of WT2 ( $A^* \approx 1/2$ ). All other chemotaxis proteins are expressed as in WT2 cells. In Eq. 2.11 these conditions translate into the demethylation rate constant being  $\tilde{g}_B = g_B A^{*2} = g_B/4$ , which incorporates the basal activity of non-phosphorylatable CheB, and the only dependence of the demethylation rate on receptor complex activity is due to binding of CheB to active receptors. We find that the experimental rate of FRET-activity change from time-course data (Fig. 2.12 C, green squares) is consistent with our prediction. Hence, for both predictions our model fits experimental data for the rate of activity change by adjusting only one parameter in the receptor demethylation dynamics.

The statistical significance for each of the two predictions (Fig. 2.12 A and C) was tested as follows: For each prediction, we randomly permuted a number of data points from the control experiment and the prediction-testing experiment. Then we calculated the distribution of squared errors between the rates of activity change from the model and FRET measurement for the permuted data sets (Fig. 2.12 B and D). For four permuted pairs of data points the error is always above the error for the unpermuted data sets (Fig. 2.12). For fewer permutations the error lies at the lower bound of the distribution (not shown).

This confirms that the control and prediction-testing data sets are significantly different and match our model.

## 2.7 Discussion

---

Sensing and adaptation are fundamental biological processes, enabling cells to respond and adjust to their external environment. Adaptation extends the range of stimuli a sensory pathway can respond to, while its dynamics determines how long a stimulus will affect the cell's behaviour. In this chapter, we developed a model to quantitatively describe experimental dose-response curves, as well as time courses of chemotaxis signalling in adapting wild-type cells. Our model includes (i) the signalling activity of two-state mixed chemoreceptor complexes in response to added or removed attractant concentration step changes based on the Monod-Wyman-Changeux model, (ii) the kinetics of the ligand concentration in the flow chamber, and (iii) a detailed mechanism for adaptation, including multiple layers of feedback regulation and imprecise adaptation. In particular, we find that the finite ligand flow speed and fast, activated demethylation explains for the first time the gradually reduced amplitudes in removal dose-response curves for increasing ambient concentrations (Fig. 2.4). Our adaptation model introduces a strong receptor-activity dependence of the demethylation rate, and hence is able to reproduce the observed asymmetry of slow adaptation to addition of attractant and fast adaptation to removal of attractant (Fig. 2.2 C). Such dynamics yields long runs up the gradient and short tumbles, sufficient for random reorientation of the cell and escape from potential toxins. Furthermore, this strong activity dependence has the additional benefit of reducing the fluctuations in receptor methylation level introduced by the adaptation mechanism itself. We found for the total variance of the receptor-complex methylation level  $\langle \delta M^2 \rangle = 0.87$  compared to 2 for a previous model for precise adaptation with weaker activity dependence (details of the calculation can be found in Appendix F). This is because a fluctuation in the receptor methylation level leads to an increased change in activity and hence increased rate to return to the adapted activity.

Our model for precise adaptation predicts the data collapse of adaptation time-courses, allowing the convenient study of the adaptation dynamics (Fig. 2.9 A). Specifically, the data collapse allows to evaluate the effects of ligand flow and adaptation dynamics, as well as imprecise adaptation. We found that adaptation to large concentration step changes is significantly imprecise (Fig. 2.10). We also extracted the kinetics of the receptor methyla-

tion level  $dm/dt$  from experimental time courses from the data collapse (Fig. 2.9 B), which is difficult to measure directly when relying on the quantification of the receptor methylation level using standard biochemical methods (Lai and Hazelbauer, 2005; Chalah and Weis, 2005). According to our model, the activity dependence of the receptor methylation level is a monotonously decreasing function of the receptor complex activity. Ultimately, this kinetics determines the compromise between long memory of previous concentrations and quick recovery for sensing new concentration changes (Clark and Grant, 2005). Furthermore, we experimentally tested two predictions to validate our adaptation model. We analysed the effect on the adaptation dynamics when changing the adapted receptor activity, as well as introducing a non-regulatable CheB mutant to remove the negative feedback from phosphorylation of CheB by the kinase CheA. In both cases, our model is consistent with experimental measurements (Fig. 2.12), supporting the finding of multiple layers of feedback regulation in adaptation.

While the MWC model is relatively well established (Sourjik and Berg, 2004; Mello and Tu, 2005; Keymer et al., 2006; Endres and Wingreen, 2006; Endres et al., 2008), we also considered alternative models for receptor signalling. These include a phase-separation model with mixed complexes separating into homogeneous complexes of Tar and Tsr at high ambient concentrations, as well as a lattice model with finite coupling between neighbouring receptors (Appendix C). Lattice models were previously suggested by Duke and Bray (1999) and Mello and Tu (2003b), including a lattice formed by coupled CheA molecules considered by Goldman et al. (2009), but were found to be inconsistent with FRET data by Skoge et al. (2006). We found that the dynamic MWC model describes dose-response curves far better than the alternative receptor signalling models investigated, particularly the reduced response amplitudes upon removal of attractant. Furthermore, the data collapse we introduced in this paper enabled us to compare different adaptation models proposed in the literature with FRET time-course data (Fig. 2.11). We found that while several models are consistent with the data, our model compared most favourably with the data.

We chose a simple model for adaptation with very few fitting parameters to explain the observed asymmetry in adaptation time-courses, i.e. slow adaptation to addition and fast adaptation to removal of attractant. Compared to the static MWC model, there are minor discrepancies between our model and experimental addition dose-response curves (Fig. 2.4). However, these can be rectified by refitting the dynamic MWC model

by adjusting adaptation rates and receptor complex size simultaneously (Appendix B), or by choosing an adaptation model with a more complex activity dependence. It should also be noted that adaptation rates needed to accurately describe dose-response curves are larger than those found when fitting the adaptation dynamics to the data collapse. This discrepancy may in part be due to using only a single set of experimental data for the data collapse, while dose-response curves were averaged over at least three sets. In addition, more complex processes not taken into account in our simple adaptation model, e.g. limited supply of substrate (methionine) for methylation, or the binding and unbinding kinetics of ligand, may be important for describing the dynamics.

Our adaptation model likely also applies to attractants other than MeAsp, since the dynamics of adaptation only depends on the activity of receptor complexes, independent of the details of external ligand concentration. According to the MWC model, different attractants (or their mixture) are integrated at the level of the free-energy of a receptor complex, which determines its activity. However, the imprecision of adaptation we found in FRET time courses at large MeAsp concentrations is in contrast to earlier experiments, which showed that the frequency of tumbling adapts precisely to aspartate, but not serine (Berg and Brown, 1972; Alon et al., 1999). The imprecision in adaptation to serine is readily explained if the number of Tsr receptors is larger than the number of Tar receptors per complex, since the available receptor methylation sites in a complex are more quickly used up in response to serine binding to Tsr receptors (Endres and Wingreen, 2006; Hansen et al., 2008). However, the ratio of Tar and Tsr per complex is strongly dependent on the growth conditions, making a definitive conclusion difficult (Kalinin et al., 2010). Future experiments may show if the imprecision observed in adaptation to MeAsp in FRET is reflected also in the tumbling frequency, or if imprecise adaptation is compensated for in order to yield perfect adaptation at the behavioural level.

## 3. Weber's law

### 3.1 Synopsis

---

Weber's law of sensation describes the relationship between the physical magnitude of a stimulus and its perceived intensity. This phenomenological law applies well to many sensory systems, including human vision and sound perception, suggesting a general design principle. However, how the law emerges from signalling pathways and molecular components is not understood. In this chapter, we consider the well-characterised sensory system of *Escherichia coli* chemotaxis to understand the molecular origin, limits, and biological significance of Weber's law in this system. We combine *in vivo* FRET data with our model for signalling and adaptation of cooperative two-state receptor complexes. We find an analytical expression for Weber's law in terms of physically intuitive parameters, such as the number of receptors per complex and ligand dissociation constants, and quantify the law's limits due to noise. Perception in chemotaxis is identified as the free-energy difference between the two signalling states of a receptor complex. Comparing perception of different concentration gradients suggests that Weber's law might be important for survival in dense competitive microbial communities.

### 3.2 Motivation & open questions

---

Sensory systems enable organisms to gain information about their environment by responding to external stimuli, such as mechanical, chemical, thermal or electromagnetic cues. However diverse these detected stimuli are, sensory systems share common design principles (Martin, 2000). An often cited example is Weber's law, which describes the relationship between the physical magnitude of a stimulus and its perceived intensity (Johnson et al., 2002). Specifically, the law states that the smallest noticeable difference  $\Delta S$  (threshold stimulus) between a stimulus and the background stimulus  $S_0$  increases directly pro-



portional to  $S_0$ ,

$$\Delta S = K \cdot S_0, \tag{3.1}$$

where  $K$  is the constant Weber fraction (Johnson et al., 2002). The ratio of threshold stimulus and background stimulus remains therefore constant,

$$\frac{\Delta S}{S_0} = \text{const.}, \tag{3.2}$$

representing coding of contrast, i.e. stimuli relative to the background. For instance, the human eye copes with 8 orders of magnitude of brightness from low light during a moonless night to bright daylight (Olshausen and Field, 2000; Dunn and Rieke, 2006). However, to distinguish objects from their background the visual system efficiently exploits the statistical similarity of light intensities in natural scenes, with the relative difference between light reflected from the object compared to the background being largely invariant under different illumination (Laughlin, 1987, 1989; Olshausen and Field, 2000). In its integrated form, Weber's law predicts an internal representation of the stimulus in the sensory system, the perception  $R$ . This scale of perceived stimulus magnitude is postulated to increase logarithmically with the stimulus  $S$ ,

$$R \sim \ln S. \tag{3.3}$$

This relationship, known as the Weber-Fechner law (Johnson et al., 2002), results in a logarithmic stimulus compression and hence a large dynamic range, found, e.g., in the visual and auditory system (Dunn and Rieke, 2006) and in the neural representation of numbers (Dehaene, 2003).

While Weber's law applies to many sensory systems, an explanation at the molecular level is difficult due to the complexity of the underlying molecular and neural processes. In higher organisms, Weber's law is best documented in the insect and vertebrate visual system, where multiple sensory adaptation mechanisms adjust the receptor sensitivity to ambient light levels. In the insect compound eye, receptor cells remain sensitive to light over a wide range of intensities due to adaptation, as voltage-dependent potassium channels repolarise the cell and restrict the response amplitude at higher light intensities for stimulus compression (Laughlin, 1989). In addition, further optical, cellular and neural adaptation mechanisms have been described, among them pigment migration, reduction of

response latency in the transduction process, and transient activation of synaptic transmitter. Phototransduction in the vertebrate eye involves even up to nine different mechanisms for adaptation (Pugh Jr et al., 1999). Activation of the photopigment following photon absorption leads to a drop in the concentration of second messenger cGMP and closure of cGMP-gated ion channels, hyperpolarising the cell. The decline in the intracellular calcium concentration associated with closed ion channels activates the production of cGMP and increases the binding affinity of cGMP to channels. This shifts the maximal sensitivity of the response to higher light levels and leads to adaptation. The compression of response amplitudes with increasing brightness is believed to be due to the calcium-dependent shortening of the lifetime of activated photopigment or cGMP, and the bleaching of photopigment. Several models have been developed to describe the complicated biochemical processes, but mostly speculate about the emergence of Weber's law (Dawis, 1991; Tamura et al., 1991; van Hateren and Snippe, 2007).

Compared to the complexity of the visual system, the chemotaxis system in *Escherichia coli* is relatively simple and well-characterised. Weber's law in this system was first studied using micropipette assays by Mesibov et al. (1973). In their work, bacteria accumulation was monitored in capillaries filled with an attractant (or repellent) of concentration different from the surrounding solution, which is a measure of the response to concentration gradients. It was found that bacteria show a response of similar magnitude for similar fractional concentration differences. Furthermore, there is a threshold of concentration below which bacteria do not accumulate significantly. This threshold is different for different receptors. The authors speculate that Weber's law may be observed for some attractants. Quantitative measurements and mathematical modelling were done recently by Kalinin et al. (2009), where swimming bacteria were tracked in linear concentration gradients. The authors found that bacteria drift velocity depends on the gradient of the logarithm of the concentration, termed logarithmic tracking. Recently, the topic has also attracted renewed theoretical interest. Tu et al. (2008) developed a model for chemotaxis signalling based on data from Block et al. (1983), who studied single-cell responses to time-dependent concentration signals at the level of the rotary motor. In particular, Tu et al. (2008) discuss logarithmic tracking by bacteria, i.e. that bacteria respond to the temporal gradient of the logarithm of the concentration rather than the gradient of the concentration itself. Logarithmic tracking in turn results in Weber's law, as a change in response is proportional to the fractional change in concentration. They discuss how

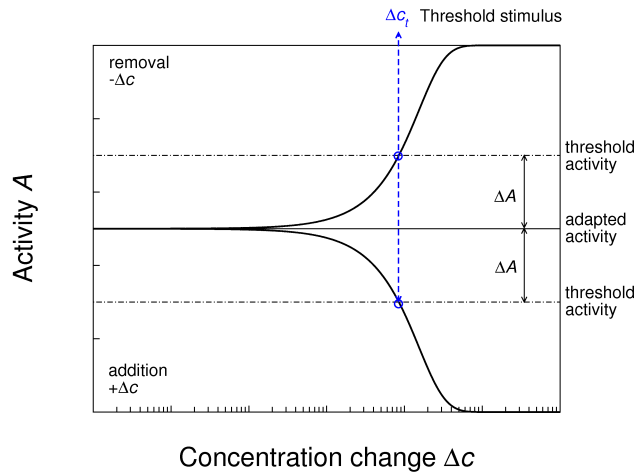


**Figure 3.1.:** Illustration of the method to determine the threshold stimulus  $\Delta c_t$ . A dose-response curve is shown (thick solid black line), as well as the adapted activity  $A^*$  and the threshold activities  $A^* \pm \Delta A$  for removal (upper curve) and addition (lower curve) of concentration step changes. The threshold stimulus  $\Delta c_t$  corresponds to the concentration change  $\Delta c$  where the activity reaches the threshold activity (intersection of dose-response curves with activity thresholds). We use a linear interpolation between closest data points above and below the threshold activities to calculate  $\Delta c_t$ .

Weber's law emerges due to precise adaptation and receptors responding to the logarithm of the concentration. Furthermore, they state another condition necessary for logarithmic tracking, namely the logarithmic mapping between the concentration and the methylation level of adapted receptors.

While the molecular origin of Weber's law has been discussed by Tu et al. (2008), its limits due to noise in the signalling pathway are unexplored. Furthermore, it is not known what constitutes the perception in chemotaxis. Finally, the physiological microenvironment in the mammalian intestines which *E. coli* encounters is not well characterised. In this chapter, we comprehensively investigate Weber's law using the FRET data and our detailed model for receptor signalling and adaptation from chapter 2. We use Weber's law to predict typical gradients the bacterium may have evolved to detect.

### 3.3 Weber's law in chemotactic signalling

Weber's law states that the threshold stimulus, i.e. the smallest noticeable difference in stimulus, grows linearly with background stimulus. We use the FRET dose-response curves and the dynamic MWC model with fitted parameters in Fig. 2.4 to extract the threshold stimulus for different background concentrations. The procedure is exemplified in Fig. 3.1: we devise the threshold stimulus  $\Delta c_t$  to be the concentration increment which produces the activity response  $\Delta A$  relative to the adapted level  $A^*$ . According to the

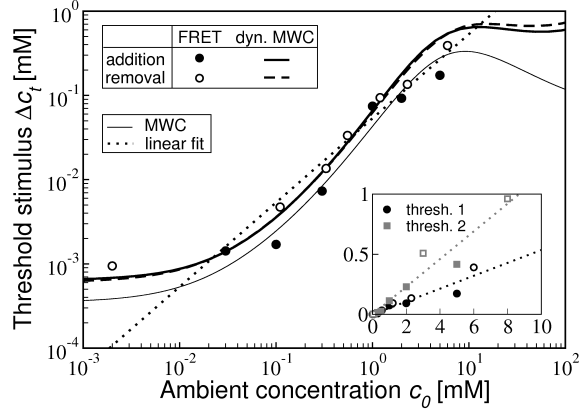


**Figure 3.2.:** Weber's law in the chemotaxis sensory system. (A) Threshold stimulus  $\Delta c_t$  of MeAsp to achieve a given response threshold  $\Delta A = 0.08 A^*$  (change in receptor complex activity), where  $A^*$  is the adapted activity, plotted as function of ambient concentration  $c_0$ . Experimental data points (symbols) were obtained from FRET dose-response curves by linear interpolation between measurement points close to threshold activity. Thick lines represent MWC model including ligand and adaptation dynamics. Solid and dashed lines are for addition or removal stimuli, respectively. Threshold stimulus  $\Delta c_t$  calculated from a linear expansion around the steady state receptor complex activity (static MWC model) and a linear fit of the experimental data points (dotted line) are shown as well. (A *Inset*) Experimental data points (symbols) and linear fits (dotted lines) are plotted on a linear scale for two different response thresholds. Threshold 1:  $\Delta A = 0.08 A^*$  (circles), threshold 2:  $\Delta A = 0.16 A^*$  (squares). Filled and open symbols represent addition and removal of MeAsp, respectively. Slopes of linear fits are 0.054 (threshold 1) and 0.115 (threshold 2).

MWC model, the signalling activity of cooperative receptor complexes of  $N$  receptors is given by Eq. 2.2,

$$A(c, m) = \frac{1}{1 + e^{F(c, m)}} \quad (3.4)$$

with the free-energy difference Eq. 2.3,

$$F(c, m) = N \left[ \epsilon(m) + \nu_a \ln \left( \frac{1 + c/K_a^{\text{off}}}{1 + c/K_a^{\text{on}}} \right) + \nu_s \ln \left( \frac{1 + c/K_s^{\text{off}}}{1 + c/K_s^{\text{on}}} \right) \right]. \quad (3.5)$$

We find from experimental dose-response curves, as well as our modelling that the chemotactic sensory system implements Weber's law in a range of concentrations (Fig. 3.2). Analysing the MWC model reveals that this range corresponds to the working range of the Tar receptor, i.e. between the ligand dissociation constants of the *off* and *on* states  $K_a^{\text{off}}$  and  $K_a^{\text{on}}$ . To obtain an analytical formula for the threshold stimulus, we expand the receptor complex activity up to linear order about the steady state activity  $A^*$  (Endres and Wingreen, 2006)

$$\Delta A = \left. \frac{\partial A}{\partial F} \right|_{F^*} \cdot \left. \frac{\partial F}{\partial \ln c} \right|_{c_0} \cdot \frac{\Delta c_t}{c_0} = \alpha \cdot k \cdot \frac{\Delta c_t}{c_0}, \quad (3.6)$$

where  $F^*$  is the free-energy difference corresponding to  $A^*$ ,  $\alpha = \partial A / \partial F|_{F^*} = A^*(A^* - 1)$  and  $k = \partial F / \partial \ln c|_{c_0} = \nu_a N [c_0 / (c_0 + K_a^{\text{off}}) - c_0 / (c_0 + K_a^{\text{on}})] \approx \nu_a N$  for  $K_a^{\text{off}} \ll c \ll K_a^{\text{on}}$ , neglecting MeAsp binding to Tsr for simplicity. This results in Weber's law (Tu et al., 2008)

$$\Delta c_t = K \cdot c_0 \quad (3.7)$$

where  $K = \Delta A / (\alpha k)$  is the constant Weber fraction in chemotaxis, which depends on the particular threshold activity  $\Delta A$ . For the thresholds  $\Delta A = 0.08 A^*$  and  $\Delta A = 0.16 A^*$  used in Fig. 3.2 the Weber fractions are 5.4 and 11.5 percent, respectively. We find, that for background concentrations below  $K_a^{\text{off}}$ , Weber's law breaks down and the threshold stimulus approaches a constant,

$$\Delta c_t = \Delta A \cdot K_a^{\text{off}} K_a^{\text{on}} / [\nu_a N A^* (1 - A^*) (K_a^{\text{off}} - K_a^{\text{on}})]. \quad (3.8)$$

At concentrations above  $K_a^{\text{on}}$ , Tar receptors become saturated. In this concentration range, Weber's law is maintained due to growing receptor complex size<sup>1</sup>. At high concentrations around 10 mM, Weber's law breaks down as MeAsp binding to Tsr becomes important. For the complete formula of the threshold stimulus including MeAsp binding to Tsr used in Fig. 3.2 A (thin solid line), see Appendix G.

### 3.4 Threshold stimulus

For convenience, we picked a value for the activity threshold  $\Delta A$  in the linear regime of the dose-response curves where we had experimental data points for the signalling response from FRET. In principle, the threshold  $\Delta A$  arises from the internal noise level of the signalling system. We estimated the noise in the activity from all chemoreceptors in a cell, considering fluctuations in ligand concentration and receptor methylation level. Details of the calculation are shown in Appendix H. Briefly, we calculate the fluctuations in activity of an individual complex  $\delta A$  according to

$$\delta A = \frac{\partial A}{\partial M} \delta M + \frac{\partial A}{\partial c} \delta c, \quad (3.9)$$

<sup>1</sup>Note that we found the receptor complex size to increase roughly linearly, cf. the discussion of Eq. 2.3 in chapter 2.

where  $M$  is the total methylation level of all receptors in a complex. We can calculate the fluctuations in methylation level assuming that  $N_R$  CheR and  $N_B$  CheB-P molecules modify receptors in the complex independently and with a constant average rate. Slow fluctuations in ligand concentration are translated into fluctuations in activity, and hence are compensated for by the negative feedback of adaptation. For the final result we neglect these (negative) correlations. The variance of fluctuations in ligand concentration  $\langle \delta c^2 \rangle$  has been calculated by numerous researchers (Berg and Purcell, 1977; Bialek and Setayeshgar, 2005, 2008; Endres and Wingreen, 2008). The total variance of the activity of all receptors results from the sum over all receptor complexes. We assume fluctuations at different complexes are uncorrelated. We obtain a response threshold  $\Delta A$  of about 2 percent of the adapted activity. This is a lower bound for the activity threshold as it was derived by only considering fluctuations from stochastic methylation and demethylation events, as well as ligand binding events. Other sources of noise, e.g. from stochastic phosphorylation and dephosphorylation events, are likely to further increase the threshold response. In Fig. 3.2 we used a response threshold of  $\Delta A = 0.08$  and  $0.16$ , respectively.

### 3.5 Perception

---

The Weber-Fechner law predicts the internal representation of the stimulus, the perception  $R$ , to obey  $R \sim \ln c$ . This results from the postulate that the threshold stimulus for a particular background stimulus corresponds to an increment  $\Delta R$  in the internal representation of the stimulus in the sensory system. This increment is a function of the fractional change in stimulus  $\Delta c/c$ . Hence, integrating  $\Delta R = \tilde{K} \Delta c/c$ , where  $\tilde{K}$  is a constant, yields  $R \sim \ln c$ .

Equation 3.6 cannot be integrated to obtain the perception with its logarithmic dependence, since  $\partial A/\partial F$  depends implicitly on the attractant concentration. Instead, integrating  $\delta F = k \cdot \delta c/c$  results in the perception given by the receptor complex free-energy difference

$$F \approx N \cdot \left[ \epsilon(m) + \nu_a \ln \left( \frac{c}{K_a^{\text{off}}} \right) \right], \quad (3.10)$$

valid for concentrations  $K_a^{\text{off}} \ll c \ll K_a^{\text{on}}$ . (The general, exact formula for the free-energy difference is given by Eq. 2.3.) As shown in Fig. 3.3 the perception  $R$  depends on the receptor methylation level  $m$ . At constant ambient concentration, adaptation leads to the perception  $R = F^*$ , corresponding to adapted activity  $A^*$  and a unique methylation

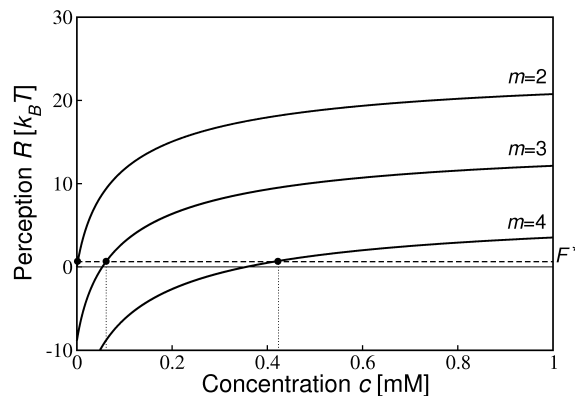


**Figure 3.3.:** Perception  $R$ , represented by receptor complex free-energy difference  $F$ , depends on ligand concentration  $c$  and methylation level  $m$ . Adapted perception is given by the steady-state free-energy difference  $F^*$  (dashed line). Three example curves corresponding to three different methylation levels are plotted. On each curve, the adapted perception  $R=F^*$  is indicated (solid circle) relating adapted methylation level to the respective ambient concentration (dotted lines).

level. Sudden concentration changes move the perception along the curve for a specific methylation level, whereas adaptation shifts the perception vertically.

### 3.6 Predicting typical gradients

To identify the typical gradients bacteria may experience in their environment, we compare how moving bacteria perceive different gradients. We predict that spatial gradients which can be perceived over a range of concentrations, i.e. in which the perception does not diminish due to adaptation, nor saturate, may be the typical gradients the sensory system has evolved to detect. We consider a number of spatial gradients which arise from diffusion processes. Free diffusion of a fixed number of ligand molecules deposited at a point produces a Gaussian gradient (Berg, 1993; Vladimirov et al., 2008). Diffusion from a point source expelling particles at a constant rate results in a hyperbolic gradient (Berg, 1993). Diffusion between points of constant-rate production and absorption produces a linear gradient (van Haastert and Postma, 2007; Vladimirov et al., 2008). Finally, diffusion from a constant source and homogeneous degradation in the medium results in an exponential gradient (Ibanes and Belmonte, 2008). Figure 3.4 shows these different spatial concentration gradients, where we have kept the value of the concentration the same at two points in space to make the gradients comparable.

We consider one-dimensional migration of bacteria with constant velocity  $v_s=20 \mu\text{m s}^{-1}$ . Therefore, we can translate the spatial gradient into a temporal gradient easily. We approximate the free-energy difference by its logarithmic form Eq. 3.10, which is valid for the

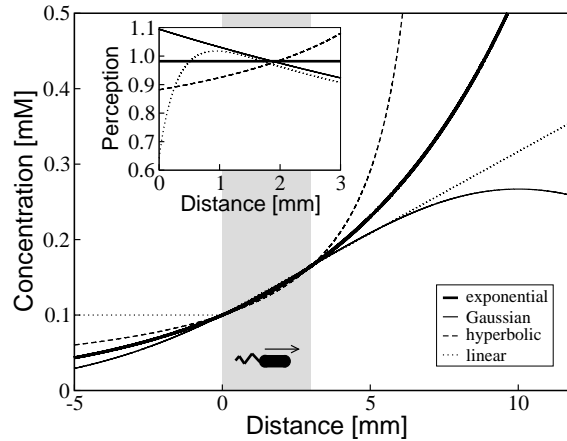


**Figure 3.4.:** Different spatial concentration profiles with equal concentrations at distances  $x=0$  and  $x=3$  mm. (*Inset*) Perception along a straight swimming path in the respective concentration profile for swimming velocity  $v_s=20 \mu\text{m s}^{-1}$  and free-energy difference  $F(m, c) = \epsilon(m) + \ln(c/K_a^{\text{off}})$  (in units of  $k_B T$ ).

range of concentrations where Weber's law applies, i.e.  $K_a^{\text{off}} \ll c \ll K_a^{\text{on}}$ . We find an exponential gradient is perceived as constant. In contrast, the perception in the other gradients either attenuates by sensory adaptation to the pre-stimulus steady-state value (Gaussian and linear gradients), or increases, eventually saturating the response (hyperbolic gradient) along the swimming path (Fig. 3.4, *Inset*). This indicates that exponential concentration gradients may commonly occur in the environments where bacteria are chemotactic, according to our hypothesis that the *E. coli* chemotaxis pathway has evolved to maintain perception over a range of concentrations of gradients, which are typically encountered.

### 3.7 Discussion

Sensory systems are optimised for the stimuli they typically encounter (Laughlin, 1987). Weber's law, which is found in many sensory systems, represents coding of contrast, i.e. sensing the relative change of stimulus rather than absolute magnitude. To investigate Weber's law in *E. coli*, in particular its molecular origin, limits, and biological significance, we use *in vivo* FRET data and our model of the chemotaxis sensory system, which includes the signalling activity of two-state mixed chemoreceptor complexes in response to added or removed attractant concentration step changes based on the Monod-Wyman-Changeux model, the ligand dynamics, and a detailed mechanism for adaptation, including multiple layers of feedback regulation (cf. chapter 2).

Phenomenological laws such as Weber's law are difficult to understand at a molecular level in complex sensory systems. We identified that the free-energy difference between



the *on* and *off* states of a receptor complex has the role of the perception in the Weber-Fechner law. The perception is a logarithmic function of the concentration in the validity range of Weber’s law, hence leading to a compressed internal representation of the physical stimulus magnitude. Weber’s law, contrast coding, and adaptation are related as follows: Adaptation to attractant by receptor methylation and demethylation adjusts the absolute sensitivity of the receptor complex activity by shifting the dose-response curve such that its slope is steepest at the new attractant concentration. The steepness of the dose-response curve, i.e. the relative sensitivity, is determined by Weber’s law, i.e. constant  $\Delta c/c_0$  (Eq. 3.7). This property in turn reflects coding of contrast. The resulting logarithmic dependence of the perception on attractant concentration is ultimately due to the competition between the gain of binding free-energy and loss of ligand volume entropy upon ligand-receptor binding (Keymer et al., 2006), and is in general a property of chemical and electro-chemical potentials (Nernst equation). For a detailed discussion in fly vision, see Laughlin (1989).

We find that Weber’s law applies in the range of concentrations where the designated receptor type Tar is sensitive to the attractant MeAsp and extends to higher concentrations (Fig. 3.2). Weber’s law breaks down at concentrations below the ligand dissociation constant of the receptor *off* state. In this regime, the threshold stimulus approaches a constant. The response threshold is determined by random fluctuations (noise) of the receptor complex activity. We estimated the activity noise from random receptor methylation and demethylation (Endres and Wingreen, 2006; Hansen et al., 2008), as well as ligand-receptor binding events (Berg and Purcell, 1977). As a result, the standard deviation of the activity is about 2 percent of the adapted activity in a cell. Other noise sources are likely to further increase the noise level. Any stimulus must therefore produce a response significantly above the level of noise in the sensory system for the cell to notice the difference with certainty (Gregory, 1998; Bialek, 1987). For convenience, we chose a response threshold  $\Delta A$  in the linear regime slightly above this estimate. At ambient concentrations above the ligand dissociation constant of the receptor *on* state, Tar receptors become saturated. However, Weber’s law remains valid for about an additional order of magnitude because the receptor complex size increases, amplifying the response. Weber’s law finally breaks down at even higher concentrations, but cells remain somewhat sensitive due to unspecific binding of MeAsp to Tsr receptors (Endres and Wingreen, 2006).

In the large intestine, hundreds of different bacterial species are present at high cell den-

sities (Poulsen et al., 1994), forming a dynamic microenvironment with complex spatio-temporal chemical gradients from partially digested food and host secretions (Mitchell and Kogure, 2006). Although the exact role of chemotaxis for non-pathogenic strains of *E. coli* in the intestines is unknown, it is conceivable that chemotaxis provides a selective advantage enabling cells to remain in their niche despite a highly dynamic turnover of mucosal surfaces and peristalsis in the gut, particularly in competition for nutrients (Kennedy, 1987; Hao and Lee, 2004; Rawls et al., 2007; Gauger et al., 2007). Alternatively, it might have advantages for the survival of bacteria when living outside the host. To identify the typical gradients predicted by Weber's law, we compare how moving bacteria perceive different gradients. In a concentration range where Weber's law is valid, we find an exponential gradient is perceived as constant (invariant). Such a gradient was previously also called constant-activity gradient (Vladimirov et al., 2008). In contrast, the perception in the other gradients either attenuates by adaptation to the pre-stimulus steady-state value (Gaussian and linear gradients), or increases, eventually saturating the response (hyperbolic gradient) along the swimming path (Fig. 3.4). This indicates that exponential concentration gradients may commonly occur in the intestines as food particles diffuse from localised areas of high concentration and are degraded by a consortium of competing microorganisms. Related gradients may originate from the mucus layer itself, which is secreted by epithelial cells, and which is constantly degraded by microorganisms. Chemotaxis is possibly optimised for moving in these gradients, as bacteria can follow them without "losing sight" or saturating the receptor response.

An alternative to the Weber-Fechner law is Stevens' law which proposes that the perception follows a power law of the stimulus magnitude (Johnson et al., 2002). In the bacterial chemotaxis sensory system, we explicitly found a logarithmic relationship for the perception in support of the Weber-Fechner law. As logarithmic response functions are implicated for ligand-receptor interactions, as well as simple membrane potentials, our findings may apply to a wide range of signal transduction processes in cells (Koshland Jr et al., 1982; Laughlin, 1989; Koester, 2000).

To establish a connection between Weber's law and the physiological role of *E. coli* chemotaxis in the intestines it will be necessary in the future to better characterise experimentally the microenvironments bacteria are exposed to, including chemical gradients and inter-species relations. These studies should be augmented by chemotaxis experiments in well-defined but complex gradients obtained from microfabricated devices (van Haastert

and Postma, 2007; Wolfaardt et al., 2008; Kang et al., 2008).

## 4. Signal transmission and noise filtering

### 4.1 Synopsis

---

Noise, i.e. random fluctuations in protein concentrations and signalling states, limits the external signals a cell can reliably sense. In this chapter, we comprehensively study the effects of sensing and signalling noise in the *E. coli* chemotaxis pathway. We develop a model which includes all signalling levels in the pathway, and discuss a simplified version of the model which captures the essential features of the full model. We consider fluctuations originating from ligand binding, receptor switching between their signalling states, adaptation, modification of proteins by phosphorylation and dephosphorylation, as well as the motor switching between its two rotational states. We study how cell-to-cell variation affects motor behaviour by varying a number of system parameters such as total protein concentrations. A similar analysis can readily be applied to other two-component signalling pathways.

### 4.2 Motivation & open questions

---

Biological systems respond to signals from their environment and pass them on to intracellular signalling pathways. Typically, signalling molecules are activated by modification, e.g. phosphorylation and methylation, and they interact in complicated biochemical reaction networks. Biochemical reactions rely on probabilistic collisions of a limited number of molecules. Hence, the number of signalling molecules fluctuates with time, i.e. the signal processing is noisy. The effects of noise has been recognised and studied extensively in gene expression (Elowitz et al., 2002; Pedraza and van Oudenaarden, 2005; Paulsson, 2005; Acar et al., 2010; Eldar and Elowitz, 2010). In contrast, noise in signal transduction is not well characterised, despite its importance for accurately measuring and adequately responding to signals. Examples of systems, where signalling noise has been considered include the ultrasensitive thresholding cascades (Thattai and van Oudenaarden, 2002),

cell-to-cell variation in yeast resulting from the pheromone response pathway (Colman-Lerner et al., 2005; Taylor et al., 2009), and feedback loops for noise suppression (Lestas et al., 2010).

An important class of signalling pathways in bacteria are two-component systems, including hundreds of pathways responsible for wide ranging functions such as sensing of and responding to nutrients, osmolarity, antibiotics, as well as quorum sensing (Laub and Goulian, 2007). Two-component systems consist of a kinase, which senses a particular environmental stimulus. Activation of the kinase results in its autophosphorylation, and subsequently, phosphorylation of its response regulator. Typically, response regulators are transcription factors, which bind to DNA and induce an appropriate transcriptional response. Using the *E. coli* chemotaxis pathway as a well-characterised example of a two-component pathway, we are interested in the behaviour of the rotary motor, i.e. the final cellular output, and how its rotation is affected by signalling and noise. We would like to address the following questions: Firstly, what types of signals are transmitted and what types are attenuated by the pathway? Early work showed that the system responds to the time-derivative of the input signal (Block et al., 1982). A number of research groups have measured the averaged response of cells to chemotactic stimuli (Block et al., 1982; Segall et al., 1986; Shimizu et al., 2010), and found that slowly, as well as rapidly changing input signals are not transmitted well by the pathway. The response to slowly changing signals is attenuated by adaptation, which reverses the activation by ligand binding (Block et al., 1983; Tu et al., 2008; Shimizu et al., 2010). Rapidly changing signals were conjectured to be attenuated by a third-order filter (Block et al., 1982; Segall et al., 1986). While the phosphorylation dynamics of CheY-P has been shown to contribute a first-order filter (Tu et al., 2008), the exact filtering dynamics of the full pathway has not been addressed.

Secondly, how is noise generated, amplified or filtered in the signalling pathway, and how do different sources of noise affect the motor behaviour? Time courses of motor rotation in CW and CCW direction have been measured. Specifically, the power spectrum, which captures the correlations fluctuations at different time points, was considered for wild-type cells and mutant cells lacking the chemotaxis signalling pathway (Korobkova et al., 2004). The spectrum was found higher at low frequencies in the wild-type cells, indicating that there is a dominant noise source in the signalling pathway with long correlations. Korobkova et al. (2004) showed, using simulations of the signalling network, that the adaptation dynamics plays an important role in generating long correlations. However,

they only analysed the signalling pathway up to CheY-P. The noisy biochemical reactions of the pathway have been simulated (Morton-Firth and Bray, 1998). Furthermore, a lot of research has focused on understanding the mechanism of motor rotation (Xing et al., 2006; Meacci and Tu, 2009; Mora et al., 2009a,b; van Albada et al., 2009), including thermodynamic modelling of the motor switching (Scharf et al., 1998; Turner et al., 1999; Tu and Grinstein, 2005). However, the noise generation, filtering and amplification has not been addressed systematically for the various levels of the signalling pathway from chemoreceptors to motors.

Finally, how are signals transmitted in the presence of noise? An important task for the cell is to generate an appropriate response to input signals in the presence of fluctuations in the input, as well as due to noise in the biochemical signalling network. Furthermore, cell-to-cell variation in protein expression influence signal transmission and noise filtering.

In this chapter, we present a mathematical model for the chemotaxis signalling pathway. Specifically, we use stochastic differential equations to describe the dynamics of each signalling protein. We assume throughout that concentration signals and fluctuations are small. We use a Langevin approach (van Kampen, 2007), which is based on the deterministic dynamics describing the mean concentration of a signalling molecule, and an additive noise term, which captures fluctuations around the mean value. Hence, our approach is intermediate between deterministic reaction-diffusion models (e.g. Mello and Tu, 2003a) and full stochastic simulations of the biochemical signalling network (e.g. Morton-Firth and Bray, 1998).

### 4.3 Simplified model for the pathway

---

Here, we discuss a simplified model for the chemotaxis pathway to illustrate the effects of signal and noise transmission, and a more detailed description is provided in Appendix J. The simplified model includes the dynamics of signalling by chemoreceptors, ligand concentration and receptor methylation, and the rotary motor. We consider  $N_C$  receptor complexes in a cell, each composed of  $N$  receptors, which signal independently. Each receptor signalling complex is described as a two-state system by the MWC model Eq. 2.2 in chapter 2. We explicitly take into account the magnitude of the signalling activity of receptor complexes, as opposed to the probability of a complex to be *on* in previous chapters.

### 4.3. SIMPLIFIED MODEL FOR THE PATHWAY

Hence, we define the activity as

$$A = \frac{N}{1 + e^{F(c,M)}}. \quad (4.1)$$

The free-energy difference  $F(c, M)$  between the active and inactive state is Eq. 2.3

$$F(c, M) = N - \frac{1}{2}M + N \left[ \nu_a \ln \left( \frac{1 + c/K_a^{\text{off}}}{1 + c/K_a^{\text{on}}} \right) + \nu_s \ln \left( \frac{1 + c/K_s^{\text{off}}}{1 + c/K_s^{\text{on}}} \right) \right]. \quad (4.2)$$

It is a function of the concentration  $c$  present at the receptor complex site and the total methylation level  $M$  of the receptor complex. Here, we consider two receptor types, Tar (indicated by index  $a$ ) constituting the fraction  $\nu_a$  of receptors in the complex, and Tsr (indicated by index  $s$ ) constituting the fraction  $\nu_s$  of receptors. Receptors are sensitive to attractant MeAsp with dissociation constants,  $K^{\text{off}}$  and  $K^{\text{on}}$  in the *off* and *on* state, respectively ( $K_a^{\text{off}} = 0.02$  mM,  $K_a^{\text{on}} = 0.5$  mM,  $K_s^{\text{off}} = 100$  mM,  $K_s^{\text{on}} = 10^6$  mM; Keymer et al., 2006).

The dynamics of the total activity  $A_c$  of all receptors in a cell is determined by the sum over all signalling complexes  $j$ ,

$$\frac{dA_c}{dt} = \sum_{j=1}^{N_c} \frac{\partial A}{\partial M} \frac{dM_j}{dt} + \frac{\partial A}{\partial c} \frac{dc_j}{dt} + \eta_{A_j}(t). \quad (4.3)$$

We assume that the dynamics of the complex activity is affected by changes in the receptor complex methylation level (first term), changes in ligand concentration (second term), as well as fluctuations due to the switching of the complex between its states (last term). We will discuss all noise terms  $\eta(t)$  introduced in this section in detail in Sec. 4.5.

Changes in the concentration originate from time-varying input signals  $\langle c(t) \rangle$ , as well as fluctuations due to ligand diffusion. The dynamics of the concentration at the  $j$ th receptor complex is given by

$$\frac{dc_j}{dt} = \frac{d\langle c(t) \rangle}{dt} + \eta_{c_j}(t), \quad (4.4)$$

where the first term captures average concentration changes (indicated by angular brackets  $\langle \dots \rangle$ ), affecting all receptors, and the second term describes concentration fluctuations at each receptor complex. Adaptation is provided by reversible receptor methylation and demethylation, whose dynamics is described by the following equation (cf. Eq. 2.6 in

chapter 2):

$$\frac{dM_j}{dt} = \gamma_R(N - A_j) - \gamma_B A_j^3 + \eta_{M_j}(t). \quad (4.5)$$

The total methylation level  $M_j$  of receptor complex  $j$  is changed by methylation of receptors in the inactive state (first term) and demethylation (second term). The latter rate is assumed to be strongly dependent on the receptor complex activity as only active receptors are demethylated by phosphorylated demethylation enzymes. The last term describes fluctuations due to the noisy processivity of the methylation and demethylation enzymes.

We model the motor as a two-state system with CW and CCW rotating states, corresponding to running and tumbling modes, respectively. The dynamics of the probability of tumbling mode (tumble bias)  $P_t$  is described by

$$\frac{dP_t}{dt} = k_+(A_c)(1 - P_t) - k_-(A_c)P_t + \eta_{P_t}(t), \quad (4.6)$$

where the first term represents the switching from CCW to CW with the transition rate  $k_+$ , the second term represents switching from CW to CCW with transition rate  $k_-$  and the third term describes temporal fluctuations in switching rates. The transition rates are modulated by the intracellular signalling activity. In the full pathway model, CheY-P represents the intracellular switching signal (see Appendix J). The transition rates have been derived in experiments using signalling mutants expressing varying amounts of constitutively active signalling molecule CheY (Turner et al., 1999). Figure 4.1 shows the switching rates we used, including a fit using the model for motor switching presented by Turner et al. (1999) (see Appendix J.2). In our simplified pathway model, the total receptor signalling activity  $A_c$  modulates the switching rates of the motor instead of CheY-P concentration. In the following, we discuss the average (deterministic) response of the signalling pathway to concentration signals in Sec. 4.4. We define the noise sources  $\eta_A$ ,  $\eta_c$ ,  $\eta_M$  and  $\eta_{P_t}$ , and analyse their effects on the dynamics of the signalling pathway in Sec. 4.5. Finally, we consider the effect of cell-to-cell variation on the noise power spectrum in Sec. 4.6, and the signal-to-noise ratio in Sec. 4.7.



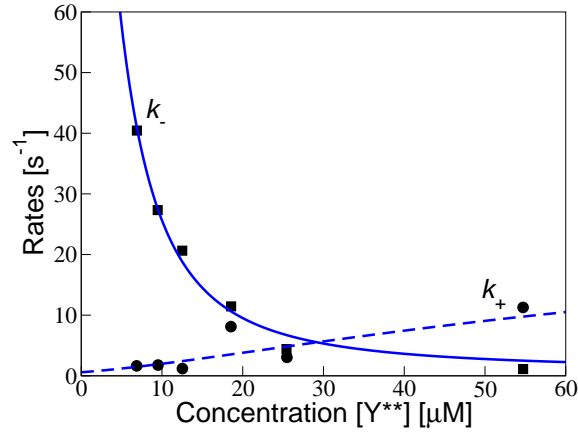


**Figure 4.1.:** Switching rates of the motor from CCW to CW rotation  $k_+$  (squares) and from CW to CCW rotation  $k_-$  (circles) as a function of the concentration of signalling-active mutant  $Y^{**}$ . A fit using the model of Turner et al. (1999) is shown as well (solid and dashed lines; cf. Appendix J.2).

## 4.4 Signal transmission

### 4.4.1. Definitions

We consider the response to concentration stimuli at various levels in the signalling pathway to study how signals are transmitted to the rotary motor. An input signal  $\Delta c(t)$  is a global concentration change from a constant background concentration  $c_0$ , which affects all receptors equally and represents a “meaningful” input to the chemotaxis signalling pathway, i.e. the concentration is

$$\langle c(t) \rangle = c_0 + \Delta c(t). \quad (4.7)$$

Cells are assumed to be adapted to the pre-stimulus concentration, with the various levels  $R$  of the signalling pathway assuming their adapted steady-state  $R^*$ . The time-dependent response  $\Delta R(t)$ , i.e. the deviation from the adapted state due to a small stimulus  $\Delta c(t)$ , is linear and determined by

$$\Delta R(t) = \int_{-\infty}^t \chi_R(t - \tau) \Delta c(\tau) d\tau, \quad (4.8)$$

where  $\chi_R(t)$  is the linear response function. The receptor activity is determined by the convolution of the linear response function and the stimulus. The linear response function describes the dynamics of the pathway, and the convolution with the stimulus represents the fact that the current state of the system is determined by the stimulus history (Kubo,

1957). The Fourier transform of this equation reads more simply

$$\Delta\hat{R}(\omega) = \hat{\chi}_R(\omega)\Delta\hat{c}(\omega), \quad (4.9)$$

where the notation  $\hat{x}(\omega)$  indicates the Fourier transform  $\hat{x}(\omega) = \int_{-\infty}^{\infty} x(t)e^{i\omega t} dt$ . For further analysis, we can write the Fourier transformed linear response function as

$$\hat{\chi}_R(\omega) = |\hat{\chi}_R(\omega)|e^{i\phi_R(\omega)}, \quad (4.10)$$

where  $|\hat{\chi}_R|$  is the modulus and  $\phi_R$  is the phase of the response function. The modulus characterises the amplitude of the response, indicating what frequency-components of input signals are transmitted well or attenuated. The phase of the Fourier transformed linear response function has an intuitive meaning for periodic stimuli. As responses are periodic with the stimulus frequency, the phase  $\phi_R(\omega)$  characterises the phase shift between stimulus and response. For general stimuli, the phase describes the phase shift of a particular frequency-component of the response. Knowing the response functions allows us to calculate the response to an arbitrary input signal. Furthermore, we can analyse the signal filtering at each level of the pathway.

To obtain a succinct measure for the signalling response due to an input concentration change  $\Delta c(t)$ , we define  $\Delta R^2$  the integral over the response over frequency

$$\Delta R^2 = \int_{-\infty}^{\infty} d\omega |\hat{\chi}_R(\omega)\Delta\hat{c}(\omega)|^2. \quad (4.11)$$

#### 4.4.2. Experimental determination of the response function

The response function has been measured in rotational assays of the motor (Block et al., 1982; Segall et al., 1986; cf. Sec. 1.1.2 in the *Introduction*) and at the level of CheY-P using fluorescence resonance energy transfer (FRET) (Shimizu et al., 2010; cf. Sec. 1.1.4), using short impulses of attractant concentration, as well as periodic stimuli. An impulse can be approximated by a Dirac-delta function,  $\Delta c(t) = A_0\delta(t)$ , and its Fourier transform is a constant,  $\Delta\hat{c}(\omega) = A_0$ . Therefore, the Fourier transformed measured response is equal to the Fourier transformed linear response function except for a constant factor.<sup>1</sup> A periodic

---

<sup>1</sup>Alternatively, any input signal shorter than any time scales in the dynamical system can be used. For instance, for the numerical simulation in Fig. 4.3, we applied a triangular pulse whose Fourier transform is

$$\Delta\hat{c}(\omega) = \frac{(c_{\max} - c_0)/T}{\omega^2} (2e^{i\omega T} - 1 - e^{2i\omega T}), \quad (4.12)$$

signal  $\Delta c(t) = A_0/(2\pi) \cos(\omega_0 t)$  has the Fourier transform  $\Delta \hat{c}(\omega) = A_0[\delta(\omega + \omega_0) + \delta(\omega - \omega_0)]$ . Hence, applying a periodic stimulus to a system yields the Fourier transformed linear response function at the stimulus frequency  $\omega_0$ . We use the response function to calibrate our model for the full pathway by adjusting the model parameters such that the model fits the experimental data shown in Fig. 4.2 well (see below).

#### 4.4.3. Analytical results for linear response function

We can analytically calculate the Fourier transformed linear response function from the dynamical equations Eq. 4.3-4.6 without noise. After linearising around the steady state and inserting the Fourier transforms we obtain

$$-i\omega \Delta \hat{A} = -i\omega \frac{\partial A}{\partial M} \Delta \hat{M} - i\omega \frac{\partial A}{\partial c} \Delta \hat{c} \quad (4.13)$$

$$-i\omega \Delta \hat{M} = -\omega_1 \Delta \hat{A} \quad (4.14)$$

$$-i\omega \Delta \hat{P}_t = \omega_2 \Delta \hat{A}_c - \omega_{P_t} \Delta \hat{P}_t. \quad (4.15)$$

We defined

$$\omega_1 = \gamma_R + 3\gamma_B A^{*2} = \gamma_R(3 - 2A_r^*)/A_r^*, \quad (4.16)$$

with  $A^* = N \cdot A_r^* = N/3$  being the adapted activity of a receptor complex,  $A_r^*$  denoting the adapted activity of individual receptors. In the second equality we have used that at the adapted state  $\gamma_R(N - A^*) = \gamma_B A^{*3}$ . The parameter  $\omega_2 = (1 - P_t^*) \frac{\partial k_+}{\partial A_c} - P_t^* \frac{\partial k_-}{\partial A_c}$  is the derivative of the motor switching rates with respect to activity, and  $\omega_{P_t} = k_+^* + k_-^*$  is a characteristic frequency due to motor switching at steady state.  $\Delta A$  is the response of every receptor signalling complex, and  $\Delta A_c = N_C \Delta A$  is the activity response of all receptor complexes in a cell. The Fourier transformed linear response function for the total activity of all receptors in a cell is

$$\hat{\chi}_{A_c}(\omega) = \frac{-i\omega N_C \frac{\partial A}{\partial c}}{\omega_M - i\omega}, \quad (4.17)$$

where  $\omega_M = \omega_1 \partial A / \partial M$  is a characteristic frequency due to adaptation. Similarly, the response of the motor is

$$\hat{\chi}_{P_t}(\omega) = \frac{\omega_2}{\omega_{P_t} - i\omega} \hat{\chi}_{A_c}(\omega). \quad (4.18)$$

---

with  $c_0$  the ambient concentration,  $c_{\max}$  the maximum concentration, and  $2T$  the duration of the pulse. In the range of relevant frequencies, the Fourier transform of the triangular pulse is a constant (cf. Fig. 4.3).

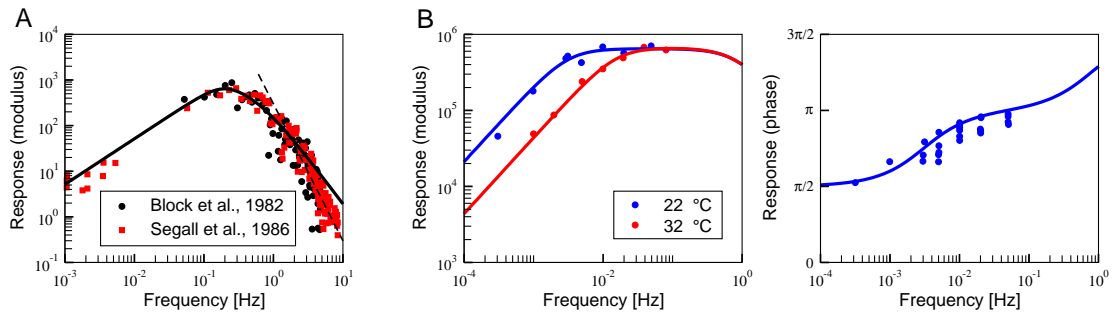


**Figure 4.2.:** Measured response function for the chemotaxis pathway. (A) Fourier transformed linear response function at the level of the rotary motor measured in rotational assays by Block et al. (1982; black circles) and Segall et al. (1986; red squares). A chemotactic impulse stimulus was applied, the motor response measured and subsequently Fourier transformed. The fit of our model is the black solid line. The black dashed line is a 3rd-order filter for comparison. (B) Response function at the level of the response regulator CheY measured in FRET experiments by Shimizu et al. (2010). A periodic chemotactic stimulus was applied and the (periodic) response measured. Modulus (*left*) and phase (*right*) are obtained from the amplitude and phase shift of the response with respect to the input signal, respectively. Our model was fitted to the modulus of the response. The blue (red) symbols and lines are measurement and fit for temperature 22 °C (32 °C), respectively.

The response functions of the full pathway including the phosphorylation reactions are shown in Appendix J.

#### 4.4.4. Model calibration

Figure 4.2 shows experimental data for the response function, as well as the fits of our full pathway model. For the fit of our model to the data by Shimizu et al. (2010), we adjusted only the adaptation rates, as measurements were restricted to low frequencies. The fit at 32 °C yields the same adaptation parameters as obtained from fitting dose-response curves of adapting cells (cf. chapter 2; Fig. 4.2, *Left*). The adaptation rates for room temperature are one order of magnitude smaller. Importantly, fitting to the modulus of the Fourier transformed response yields a good fit for the phase of the response as well (Fig. 4.2, *Right*). Data for the impulse response of the motor were obtained by Block et al. (1982) and Segall et al. (1986), to which we fit adaptation rates and motor switching rates. Compared to the data by Shimizu et al. (2010) at the same temperature, adaptation rates are one order of magnitude larger, i.e. adaptation is faster in these experiments. The parameter  $\omega_{P_t}$  of the motor switching is 2.1/s, consistent with switching rates of about 1 Hz (Block et al., 1983). It is not clear where the difference in adaptation rates between the two sets of experiments originates. Besides different experimental conditions, it may be due to Shimizu et al. (2010) using populations of cells, whereas measurements in Segall et al.

(1986) were done on single cells. Fitted parameters are given in Table J.4 in Appendix J.

#### 4.4.5. Model analysis

Figure 4.3 shows simulated time courses of the chemotactic response to an impulse stimulus and the corresponding Fourier transformed linear response functions. We observe how the input stimulus is transmitted through the pathway, with pulse durations becoming progressively longer along the pathway (Fig. 4.3, *Left*), including total receptor activity in a cell  $A_c$ , phosphorylated kinase CheA,  $A_p$ , phosphorylated response regulator CheY,  $Y_p$ , and finally the motor, characterised by its probability of tumbling,  $P_t$ .

In Fig. 4.3, *Right* we show the corresponding linear response functions. The receptor activity acts as a high-pass filter, i.e. it transmits high-frequency signals, but not low-frequency signals. As can be seen from our simple model (cf. Eq. 4.17), this property is due to adaptation which introduces the time-derivative of the signal  $\Delta c(t)$  up to the characteristic frequency  $\omega_M$ , eliminating the response to slowly changing attractant concentrations. The activity of chemoreceptors is the input to further levels in the pathway. The response of CheA-P is fast, and therefore shows no qualitative difference to the response of receptors in the frequency range shown. In contrast, due to the fast, but finite rates of phosphorylation and dephosphorylation, which prevents the CheY-P concentration from responding to rapidly changing input signals, the response at the level of CheY is reduced at high frequencies. Similarly, the motor introduces another high-frequency filter due to slow switching between its two states. This additional filter can be deduced from Eq. 4.18, where the motor response function takes the response of chemoreceptors as input, and additionally introduces a characteristic cut-off frequency  $\omega_{P_t}$  due to slow motor switching rates. Hence, the chemotaxis pathway acts as a band-pass filter (Block et al., 1982), which only transmits input signals within a selected frequency range, which is of the order of 1 to 10 s. This time scale corresponds to the average time between two tumbles, allowing the sensing of concentration changes during periods of running.

As shown in Fig. 4.3, *Right* the phase tends to  $\pi/2$ , i.e. a quarter period, at low frequencies. This has been analysed by Shimizu et al. (2010) only for the receptor complex activity. It is due to adaptation and represents the fact that the system takes the time derivative of the stimulus below the characteristic frequency  $\omega_M$  of adaptation. The phase shift of the receptor activity increases to  $\pi$  at high frequencies, indicating that the activity simply follows the output (a negative sign is due to the negative response of the activity

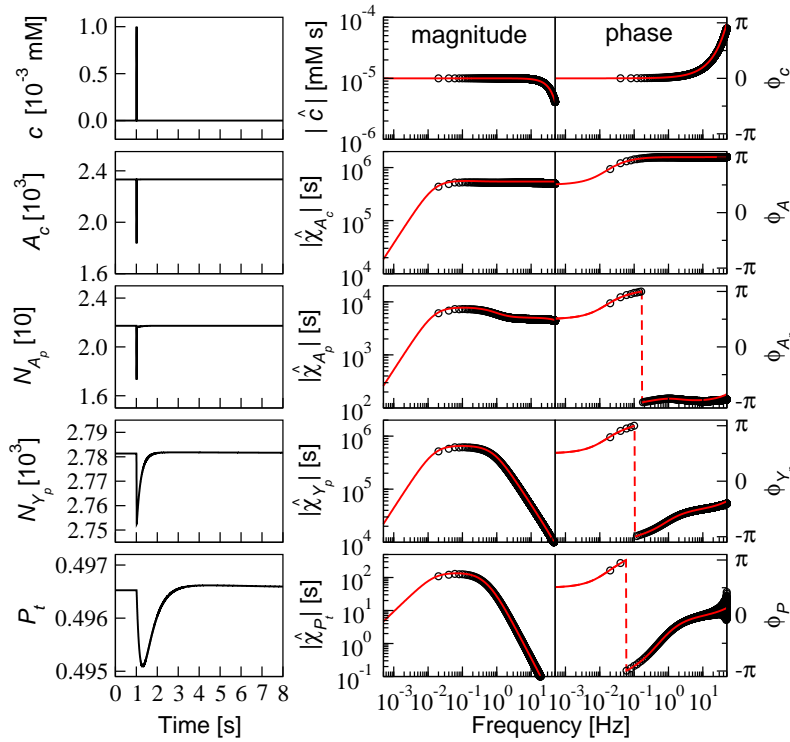


**Figure 4.3.:** Calculated chemotaxis pathway response upon impulse stimulation with attractant MeAsp. (*Left*) Time courses for MeAsp concentration  $c$ , total activity of receptors  $A_c$ , phosphorylated CheA and CheY, and tumble bias  $P_t$ . (*Right*) Fourier transform of the concentration, as well as response functions. Symbols correspond to numerical simulations and solid lines to analytically calculated response function.

to attractant concentration; Shimizu et al., 2010). The phase of the response of CheA-P follows the phase of the receptor activity at high frequencies, except for a small increase of the phase shift. In contrast, the phase of CheY-P and the motor response increase significantly beyond  $\pi$  indicating that slow rates of modification and motor switching introduce a lag of the response behind the stimulus.

## 4.5 Noise creation, amplification and filtering

To understand the noise characteristics of the motor, we consider the noise creation and transmission in the pathway. Each step in the signalling cascade is essentially probabilistic, hence, noisy: ligand diffusion and binding, receptor switching between its functional states *on* and *off*, as well as receptor methylation and demethylation, phosphorylation and dephosphorylation of signalling proteins CheA, CheY and CheB, and switching of the rotary motor between its two states, CW and CCW rotation.

### 4.5.1. Definitions

To characterise fluctuations  $\delta R(t)$  around the mean value  $\langle R(t) \rangle$ , we use the power spectrum  $S_R(\omega)$  and the variance  $\langle \delta R^2 \rangle = \langle R^2(t) \rangle - \langle R(t) \rangle^2$ . The power spectrum is the absolute square of the Fourier transform of time series  $\delta R(t) = R(t) - \langle R(t) \rangle$  measured

over a time interval  $T$ ,

$$S_R(\omega) = \lim_{T \rightarrow \infty} \frac{\langle \delta \hat{R}(\omega) \delta \hat{R}^*(\omega) \rangle}{T}, \quad (4.19)$$

where the Fourier transformation is defined on the finite measurement interval  $T$  and the average  $\langle \cdot \rangle$  is over multiple time series. For stochastic processes whose first and second moments do not vary with time, i.e. whose mean value  $\langle R(t) \rangle$  and variance  $\langle \delta R^2(t) \rangle$  are constant, the power spectrum is related to the autocorrelation function

$$K(\tau) = \langle \delta R(t) \delta R(t + \tau) \rangle. \quad (4.20)$$

The Wiener-Khinchin theorem states that the power spectrum is the Fourier transform of the autocorrelation function (Stratonovich, 1963),

$$S_R(\omega) = \int_{-\infty}^{\infty} K(t) e^{i\omega t} dt. \quad (4.21)$$

The variance of a stationary process can be calculated as the integral of the power spectrum over frequency,

$$\langle \delta R^2 \rangle = \frac{1}{2\pi} \int_{-\infty}^{\infty} d\omega S_R(\omega). \quad (4.22)$$

### 4.5.2. Intensities and spectra of noise sources

In the following, we characterise the noise terms in Eq. 4.3-4.6. Typically, we describe a biomolecular reaction or conformational change using a forward rate  $r_1$  and a backward rate  $r_2$ , as well as an additive noise term:

$$\frac{dx}{dt} = r_1 - r_2 + \eta(t). \quad (4.23)$$

The noise term  $\eta(t)$  is composed of two terms  $\eta_1(t)$  and  $\eta_2(t)$ , which are associated with the rates  $r_1$  and  $r_2$ , respectively, which in general depend on the variables of the signalling network. We assume  $\eta_1$  and  $\eta_2$  to be independent, i.e.  $\langle \eta_1(t) \eta_2(t) \rangle = 0$ . In general, this is justified as different reactions are catalysed by different proteins. Furthermore, we assume they are Gaussian white noise terms with zero mean and autocorrelation function  $\langle \eta_j(t) \eta_j(t') \rangle = Q_j \delta(t - t')$ , where  $Q_j$  is the noise intensity. The noise intensities can be calculated assuming Poisson processes with average rates  $r_1$  and  $r_2$  (Thattai and van Oudenaarden, 2002):  $Q_1 = r_1$  and  $Q_2 = r_2$ . As the two noises are independent, the noise

intensity of the total noise  $\eta(t)$  is  $Q = Q_1 + Q_2$ . As forward and backward rate are equal at steady state,  $Q$  is twice the reaction rate in one direction at steady state.

The power spectrum of the white noise  $\eta_j(t)$  is the Fourier transform of the autocorrelation function. Hence, the power spectrum  $S_{\eta_j}(\omega) = Q_j$  does not vary with frequency. Fluctuations in the protein concentrations are due to the rate fluctuations filtered by the dynamics of the biomolecular reactions and typically their power spectrum has a frequency dependence.

**Switching noise.** The switching noise  $\eta_A(t)$  in Eq. 4.3 is due to the microscopic switching of each receptor complex between *on* and *off* state. We assume the switching to be a fast process, which can be described by the following dynamics for the microscopic variable  $a$ :

$$\frac{da}{dt} = k_1(N - a) - k_2a + \eta_a(t). \quad (4.24)$$

The noise term  $\eta_a(t)$  is a Gaussian white noise with zero mean and noise intensity  $Q_a = 2k_2A^*$ , where we used that the receptor complex activity is equal to the (quasi) steady-state activity  $a$ ,  $A = \langle a \rangle$ , and  $A = A^*$  when adapted. The power spectrum of  $a$  is

$$S_a(\omega) = \frac{Q_a}{\omega^2 + (k_1 + k_2)^2}, \quad (4.25)$$

where  $k_1 + k_2$  is the characteristic frequency of switching noise. Hence, the high-frequency component of fluctuations  $\delta a(t)$  is reduced due to averaging by the finite rates of switching. The dynamics of the receptor complex activity  $A$  in Eq. 4.3 is determined by the rate of change of the microscopic variable, and hence the power spectrum of activity fluctuations  $\eta_A(t)$  is

$$S_{\eta_A}(\omega) = \omega^2 S_a(\omega). \quad (4.26)$$

**Ligand noise.** The number of ligand molecules in the vicinity of a receptor complex fluctuates due to binding/unbinding, and potential rebinding of previously bound ligand molecules at this complex, as well as diffusion (Bialek and Setayeshgar, 2005). Here, we use a simplified description of diffusion to calculate the spectrum of noise in the ligand dynamics  $\eta_c(t)$  in Eq. 4.4. Consider a volume whose dimensions are given by the diameter of a receptor complex  $s = \sqrt{N}s_R$ , where  $s_R = 1$  nm is the size of a receptor dimer (Hazelbauer, 1992). The change of ligand-molecule number  $L$  in this volume is determined by



---

#### 4.5. NOISE CREATION, AMPLIFICATION AND FILTERING

---

the exchange rate  $k_D = D/s^2$  due to diffusion:

$$\frac{dL}{dt} = k_D(c_0 s^3 - L) + \eta_L(t) \quad (4.27)$$

where  $k_D L$  is the rate of molecules moving out of the volume by diffusion, and  $k_D$  times the mean concentration  $c_0$  in solution serves as a proxy of the rate of ligand molecules moving into the volume. The noise term  $\eta_L(t)$  is assumed to be Gaussian and white, with zero mean and noise intensity  $Q_L = 2Dsc_0$ . The power spectra of the number  $L$  and concentration  $c$  of molecules at receptor complex  $j$  are

$$S_L(\omega) = \frac{2Dsc_0}{\omega^2 + k_D^2}; \quad S_c(\omega) = \frac{S_L(\omega)}{s^6}. \quad (4.28)$$

where  $s^6$  is the squared volume given by the dimension of the receptor complex. The zero-frequency limit of the power spectrum of the ligand concentration  $S_c(0) = 2c_0/(Ds)$ , which corresponds to calculations by Berg and Purcell (1977) and Bialek and Setayeshgar (2005) for the uncertainty in sensing ligand concentration. The noise  $\eta_c(t)$  in Eq. 4.4 is related to the rate of change of the ligand concentration, similar to the considerations of the switching noise above. Hence, the power spectrum of the ligand fluctuations  $\eta_c(t)$  is

$$S_{\eta_c}(\omega) = \omega^2 S_c(\omega). \quad (4.29)$$

**Methylation noise.** The size of fluctuations in the rate of methylation of a receptor complex  $j$  in Eq. 4.5 is estimated from the average rates of methylation and demethylation at the adapted state, respectively. The noise  $\eta_M(t)$  is assumed to be Gaussian and white, with zero mean, noise intensity  $Q_M = 2\gamma_R(N - A^*)$  and power spectrum

$$S_{\eta_M}(\omega) = Q_M. \quad (4.30)$$

**Motor switching noise.** The noise in motor switching rate in Eq. 4.6 is assumed to be a Gaussian white noise term, with zero mean, noise intensity  $Q_{P_t} = 2k_+(A_c^*)(1 - P_t^*)$  and power spectrum

$$S_{\eta_{P_t}}(\omega) = Q_{P_t}. \quad (4.31)$$

### 4.5.3. Analytical results for signalling noise spectra

Similar to the calculation of the response function in Sec. 4.4.3, we linearise the deterministic parts of Eq. 4.3-4.6 and formally Fourier transform the equations. We obtain

$$-i\omega\delta\hat{A}_c = -i\omega\frac{\partial A}{\partial M}\sum_j\delta\hat{M}_j + \frac{\partial A}{\partial c}\sum_j\hat{\eta}_{c_j} + \sum_j\hat{\eta}_{A_j} \quad (4.32)$$

$$-i\omega\delta\hat{M}_j = -\omega_1\delta\hat{A}_j + \hat{\eta}_{M_j} \quad (4.33)$$

$$-i\omega\delta\hat{P}_t = \omega_2\delta\hat{A}_c - \omega_{P_t}\delta\hat{P}_t + \hat{\eta}_{P_t}. \quad (4.34)$$

We solve for the Fourier transformed activity fluctuations  $\delta\hat{A}_c$  and obtain

$$\delta\hat{A}_c = \frac{\frac{\partial A}{\partial M}\sum_j\hat{\eta}_{M_j} + \frac{\partial A}{\partial c}\sum_j\eta_{c_j} + \sum_j\hat{\eta}_{A_j}}{\omega_M - i\omega}. \quad (4.35)$$

Hence, the power spectrum of activity fluctuations is

$$S_{A_c}(\omega) = N_C \frac{\omega^2 \left[ S_a(\omega) + \left(\frac{\partial A}{\partial c}\right)^2 S_c(\omega) \right] + \left(\frac{\partial A}{\partial M}\right)^2 Q_M}{\omega_M^2 + \omega^2}, \quad (4.36)$$

where we have assumed that fluctuations at different receptor complexes are independent. Therefore, we obtain the sum of  $N_C$  identical spectra for all complexes. The parameter  $\omega_M = \omega_1\partial A/\partial M$ , and we used Eq. 4.26 and 4.29. The power spectra of the noises  $S_a(\omega)$  and  $S_c(\omega)$  are given by Eq. 4.25 and 4.28, respectively, and  $Q_M$  is given by Eq. 4.30.

From Eq. 4.34 we obtain for the Fourier transformed fluctuations in the probability of tumbling mode  $\delta\hat{P}_t$

$$\delta\hat{P}_t = \frac{\omega_2\delta\hat{A}_c + \hat{\eta}_{P_t}}{\omega_{P_t} - i\omega}, \quad (4.37)$$

and their power spectrum is

$$S_{P_t}(\omega) = \frac{\omega_2^2 S_{A_c}(\omega) + Q_{P_t}}{\omega_{P_t}^2 + \omega^2}. \quad (4.38)$$

The noise spectra of the full pathway including the phosphorylation reactions are shown in Appendix J.

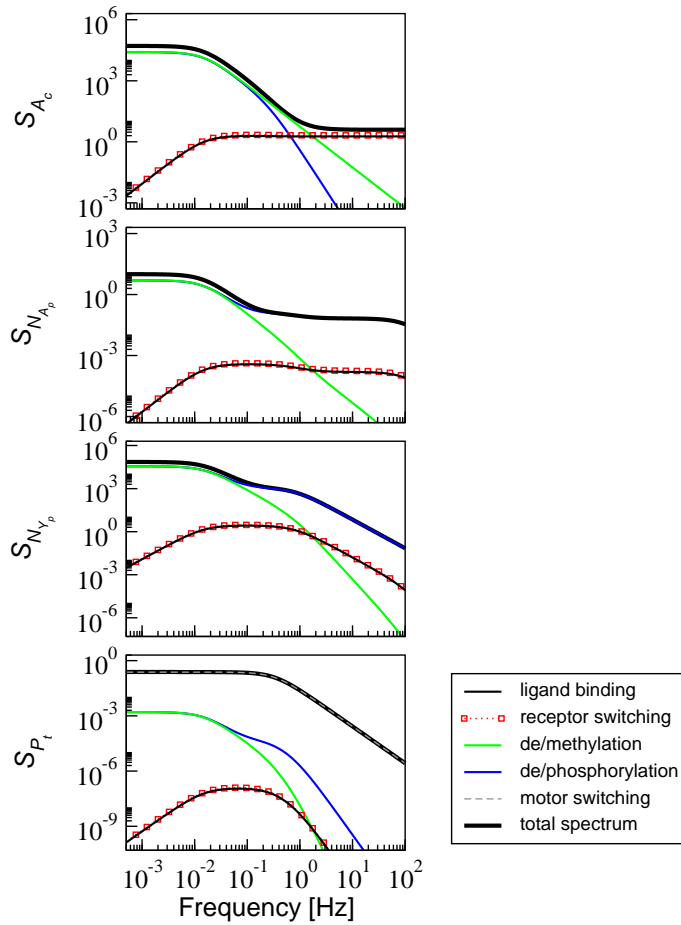


**Figure 4.4.:** Calculated noise spectra for the chemotaxis pathway (thick black lines) for the total activity of receptors  $A_c$ , phosphorylated CheA and CheY, and probability of tumbling mode  $P_t$ . Contributions to the spectrum from ligand binding (thin solid black lines), receptor switching (thin red lines and symbols), receptor methylation/demethylation (green lines), as well as phosphorylation/dephosphorylation of CheA, CheY and CheB (blue lines) and motor switching (dashed black lines) are also shown.

#### 4.5.4. Model analysis

In Fig. 4.4, we show the power spectrum of fluctuations at the various levels of the signalling pathway, i.e. total receptor activity, CheA-P, CheY-P and the motor. We also plot the individual contributions from processes generating noise, namely ligand diffusion, receptor switching, methylation and demethylation of receptors, and phosphorylation and dephosphorylation of proteins, as well as motor switching, to follow how noise is generated and transmitted at the various levels.

The noise spectrum of the receptor activity has its highest contribution at low frequencies, which mainly originate in the receptor methylation and phosphorylation dynamics. Most of the fluctuations from phosphorylation stem from CheB (the separate contributions to the phosphorylation noise are not shown in Fig. 4.4). At high frequencies, the activity noise spectrum is flat. This is due to ligand and receptor switching noise, which is removed at low frequencies by adaptation, but not at high frequencies. The general behaviour of the noise spectrum can be seen from Eq. 4.36: Intrinsic fluctuations from the

methylation dynamics (characterised by  $Q_M$ ) are filtered at frequencies higher than the characteristic frequency  $\omega_M$  of the adaptation dynamics. Ligand and receptor switching noise are filtered out by adaptation, which acts as a high-pass filter with characteristic frequency  $\omega_M$ .

The noise spectrum of CheA-P has generally the same shape as the activity spectrum with a high low-frequency component, mainly due to receptor methylation and CheB phosphorylation dynamics, and an almost flat high-frequency behaviour in the frequency range shown. Apart from ligand and receptor switching noise, the flat part of the spectrum is largely determined by fluctuations from CheA autophosphorylation, which has roughly the same shape as activity noise at high frequencies because autophosphorylation depends on the receptor activity.

The noise spectrum of CheY-P is also highest at low frequencies. However, at high frequencies the spectrum falls off as noise is filtered due to the finite rates of CheY phosphorylation and dephosphorylation.

The motor introduces another layer of filtering of transmitted noise with the characteristic motor switching frequency  $\omega_{P_t}$  (cf. Eq. 4.38). Hence, transmitted noise is filtered by two filters in the frequency range shown, namely due to the CheY-P and motor dynamics. However, the main contribution to the spectrum is due to the motor switching itself, which is filtered only by a first-order filter with characteristic frequency  $\omega_{P_t}$ .

### 4.6 Cell-to-cell variation of motor behaviour

---

How are the signal response, fluctuations and the signal-to-noise ratio (SNR) affected by changing system parameters such as protein concentrations, reaction rate constants, and the size of receptor complexes?

In this section, we discuss the effect of cell-to-cell variation on the power spectrum of the motor. In the following section, we discuss the SNR and its contributions, and how they depend on receptor complex size and adaptation rates. For simplicity, we only discuss the receptor activity in the text, while in the figures we show the contributions as transmitted to the motor.

According to our model parameters obtained from fitting the Fourier transformed linear response, the main contribution to the power spectrum comes from the steady-state switching of the motor between CCW and CW state. However, cell-to-cell variations in protein content, as well as motor switching rates, can lead to modifications of the largely

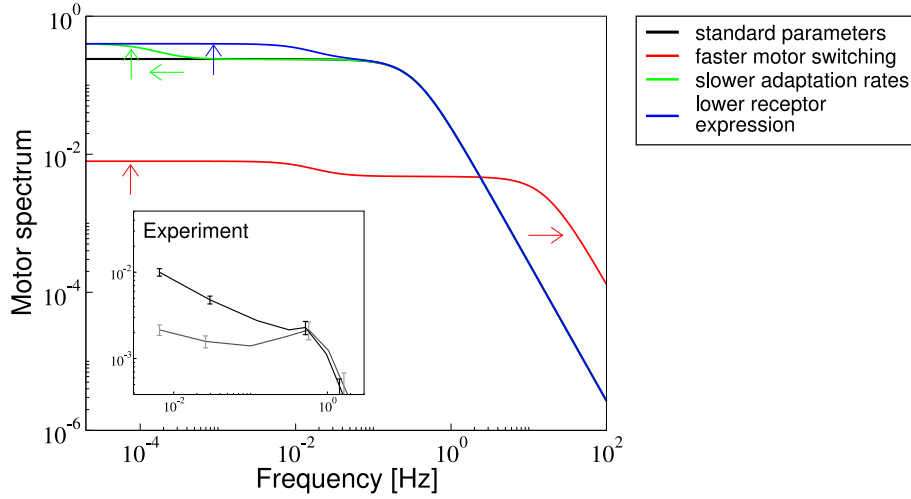


**Figure 4.5.:** Effect of cell-to-cell variation on power spectrum of the motor. The black line is the same as the total motor spectrum in Fig. 4.4. The motor spectra for the increased motor switching rates (red lines), as well as reduced receptor methylation and demethylation rates (green line) and the total number of receptors (blue line) are shown as well. Parameters are listed in Table J.5 in Appendix J. (*Inset*) Experimentally measured power spectra of wild-type cells (black line) and mutants lacking the signalling pathway (grey line). Error bars indicate the measurement uncertainty. Data was traced from Korobkova et al. (2004).

Lorentzian shape of the spectrum: As the transmitted noise from receptor methylation and phosphorylation dynamics (green and blue lines in Fig. 4.4) becomes more prominent, their high low-frequency contribution to the spectrum becomes apparent. Figure 4.5 shows the motor power spectrum for increased motor switching rates as well as reduced adaptation rates and number of chemoreceptors in a cell. In all cases the low-frequency component of the transmitted noise becomes more prominent. Hence, our model is able to reproduce spectra measured by Korobkova et al. (2004) (Fig. 4.5, *Inset*), who found a large low-frequency component in wild-type cells, but not in mutant cells lacking the chemotaxis signalling pathway.

## 4.7 Signal-to-noise ratio

### 4.7.1. Definition

To characterise how signals are transmitted in the presence of noise, we define the signal-to-noise ratio (SNR) at level  $R$  of the signalling pathway as

$$\text{SNR}_R = \frac{\Delta R^2}{\langle \delta R^2 \rangle} \quad (4.39)$$

with  $\Delta R^2$  and  $\langle \delta R^2 \rangle$  as previously defined in Eq. 4.11 and 4.22, respectively.

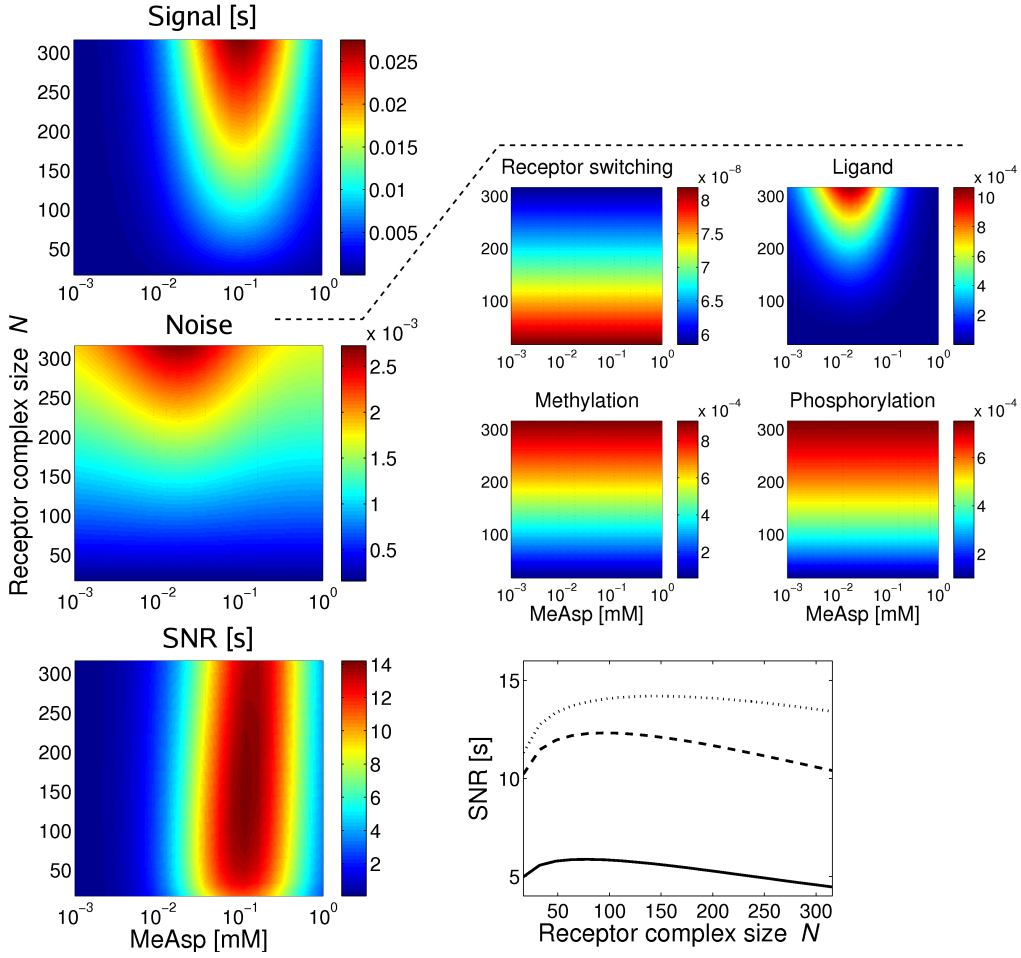


**Figure 4.6.:** Varying ambient concentration and receptor complex size. (*Top*) Integrated response of the motor bias  $\Delta P_t^2$  in response to a concentration step stimulus. The step size is 10 percent of the background concentration. (*Middle*) Variance of the motor bias  $\langle \delta P_t^2 \rangle$  including only from receptor switching, ligand diffusion, methylation and phosphorylation. The individual contributions are shown to the right of the main panel. (*Bottom left*) SNR based on the signal response and variance shown in the top and middle panel. (*Bottom right*) SNR as a function of receptor complex size at ambient concentration 0.02 (solid), 0.03 (dashed) and 0.05 mM (dotted line).

#### 4.7.2. Receptor complex size and ambient concentration

In Fig. 4.6, *Top* we show the integrated motor response  $\Delta P_t^2$  (cf. Eq. 4.11) to a concentration step stimulus for varying background concentration and receptor complex size. We assume that the step size is a constant fraction of the background concentration. The integrated response has a characteristic variation with background concentration, with the maximum in the sensitivity range of Tar receptors (indicated by their dissociation constants). Furthermore, the response increases with receptor complex size  $N$ . As calculated in Appendix K, the integrated signal response of the receptor activity scales as  $\Delta A_c \propto N$ , due to coherent addition of the signalling responses of different receptor com-

plexes, amplification of concentration changes by receptor complexes, as well as filtering by adaptation.

In the middle panel of Fig. 4.6, we show the variance  $\langle \delta P_t^2 \rangle$  (cf. Eq. 4.22) of the transmitted noise of the pathway at the level of the motor. Only the contribution to the variance from ligand diffusion depends on the background concentration. Compared to the signal response, the maximum of the variance is shifted to a slightly lower concentration. The contribution to the variance from switching of receptor complexes is relatively small compared to the other contributions and roughly constant with receptor complex size, whereas those from ligand diffusion, receptor methylation and phosphorylation dynamics increase with receptor complex size.

To see the qualitative behaviour, we consider the variance of the receptor activity. The details of the calculation are shown in Appendix K. The contribution to the variance of the receptor activity from receptor switching is indeed constant. The contribution from ligand diffusion scales as  $N^2$ , the difference between ligand noise and ligand signal amplification being due to (i) noise from different complexes being added up incoherently, and (ii) the main contribution to the variance coming from high-frequency noise, which is not filtered by adaptation. The contribution from receptor methylation grows approximately linearly with receptor complex size. The contribution to the variance from phosphorylation processes grows with receptor complex size similar to the contribution from the methylation dynamics. Overall, the total variance of transmitted noise at the level of the motor has a component from receptor switching, as well as the dynamics of receptor methylation and phosphorylation processes which is approximately constant or grows slower than the amplified signal response, whereas the component from ligand diffusion increases steeper than the signal response with growing receptor complex size.

The resulting SNR, i.e. the ratio of integrated signal response and variance of the noise, is shown in Fig. 4.6, *Bottom*. The SNR is best at background concentrations in the sensitivity range of Tar receptors. Furthermore, due to the different dependencies of the signal and the noise on the receptor complex size, the SNR has a maximum at a particular receptor complex size (Fig. 4.6, *Bottom right*). The SNR grows below that complex size due to signal amplification while the amplified ligand noise from ligand diffusion is still below the internal noise level from receptor switching, receptor methylation and phosphorylation processes. Above the optimal receptor complex size, the SNR decreases because the ligand noise is amplified more than the signal.

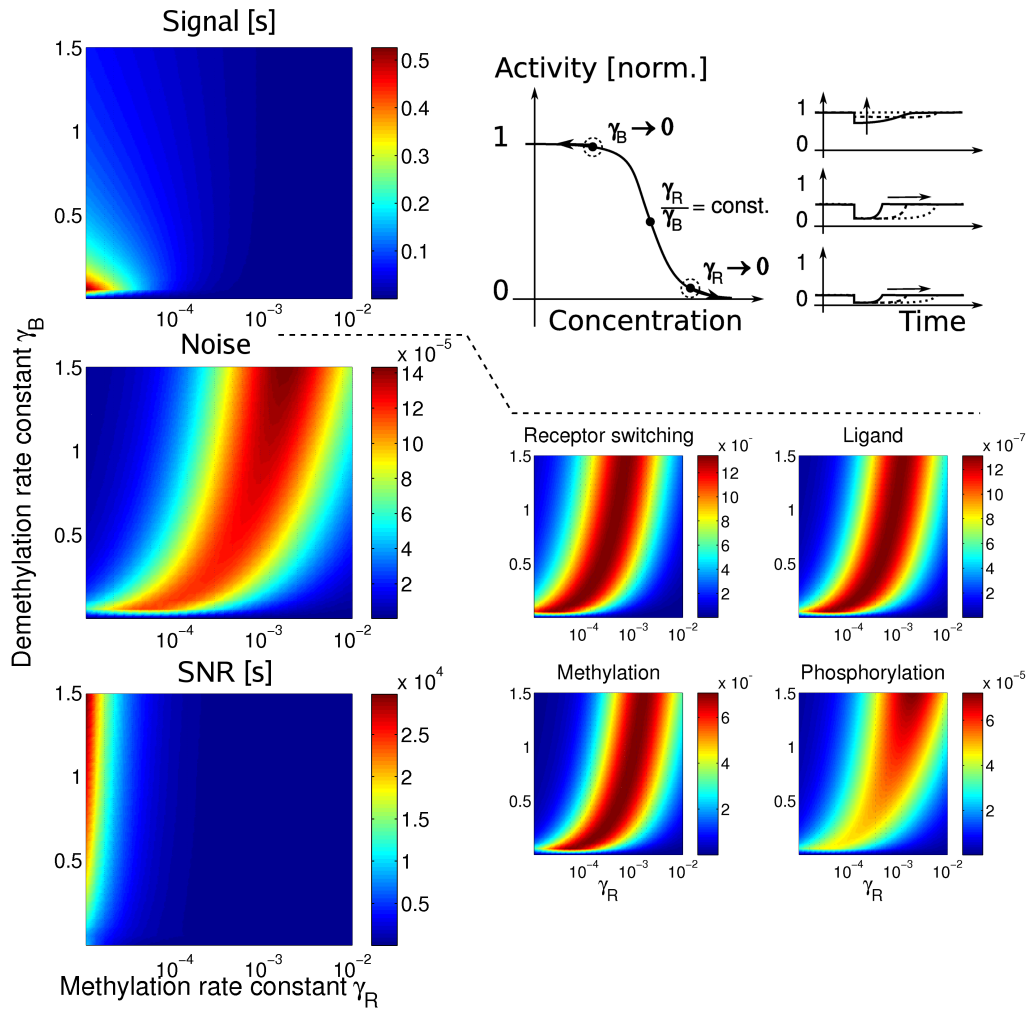


**Figure 4.7.:** Varying receptor methylation and demethylation rate constants  $\gamma_R$  and  $\gamma_B$ , respectively. (Top left) Integrated response of the motor bias  $\Delta P_t^2$  in response to a concentration step stimulus. The step size is 10 percent of the background concentration. (Top right) Illustration of the effects of vanishing  $\gamma_R$  and  $\gamma_B$  on adapted activity (indicated by dot and circle along dose-response curve; left), as well as on time courses (right) for 3 cases ( $\gamma_R \rightarrow 0$ ,  $\gamma_R/\gamma_B = \text{const.}$ ,  $\gamma_B \rightarrow 0$ ). Vanishing  $\gamma_R$  and  $\gamma_B$  result in an adapted activity in the saturated regime unless their ratio is kept constant. Rate constants are progressively smaller for solid, dashed and dotted lines, respectively. The initial response is quenched for progressively smaller  $\gamma_B$  due to saturation (indicated by the arrow). Keeping the ratio constant results in the same initial response, but progressively longer adaptation times. Reducing only  $\gamma_R$  results in progressively longer adaptation times with only a slight reduction in initial response due to saturation. (Middle) Variance of the motor bias  $\langle \delta P_t^2 \rangle$  including only from receptor switching, ligand diffusion, methylation and phosphorylation. The individual contributions are shown to the right of the main panel. (Bottom) SNR based on the signal response and variance shown in the top and middle panel.

### 4.7.3. Adaptation rate constants

Figure 4.7 shows the integrated signal response for varying rate constants of receptor methylation ( $\gamma_R$ ) and demethylation ( $\gamma_B$ ). Varying these parameters corresponds to changing the concentrations of receptor modification enzymes CheR and CheB. Interest-



ingly, varying the two parameters has different effects on the integrated signalling response: the signal increases for vanishing  $\gamma_R$ , whereas the signal decreases for vanishing  $\gamma_B$ . There are two effects to be considered in order to understand this behaviour: Firstly, if the concentration of one of the receptor modification enzymes is reduced, the receptors becomes modified by the other enzyme, hence driving receptors towards their saturated activities ( $A_r^* = 0$  or  $A_r^* = 1$ ). This effect would tend to quench the response by receptors. Secondly, as the concentration of modification enzymes is reduced, adaptation times increase. Hence, this effect increases the integrated signal as the time the receptor activity deviates from the adapted state increases. According to calculations shown in Appendix K for the integrated response of receptors, the first effect dominates in the case of reducing  $\gamma_B$ . Due to the strong activity dependence of the demethylation rate, reducing the demethylation rate constant affects the adapted activity of receptors more strongly than the methylation rate constant. Hence, receptors are quickly driven into saturation for vanishing  $\gamma_B$ . At large  $\gamma_B$ , the integrated response decreases again as expected, as adaptation times are reduced.

The variance of fluctuations is shown in the middle panel of Fig. 4.7. The individual contributions from transmitted noise at the level of the motor look qualitatively similar. All contributions decrease both for vanishing  $\gamma_R$  and  $\gamma_B$ , consistent with calculations for the variance of the receptor activity in Appendix K.

The SNR is shown in the bottom panel of Fig. 4.7. The SNR increases for vanishing  $\gamma_R$  and decreases for vanishing  $\gamma_B$ . According to Fig. 4.7 a good SNR is obtained for small  $\gamma_R$  and large  $\gamma_B$ , corresponding to the parameters of our model.

## 4.8 Discussion

---

Biological signalling pathways employ biochemical reaction networks and molecular state transitions to sense and process signals from the environment. Fluctuations inherent in these processes limit the signals which can be reliably transmitted. Here, we studied the signal and noise propagation in the *E. coli* chemotaxis signalling pathway, which controls the bacterial swimming behaviour in chemical gradients. Specifically, we considered the dynamics of ligand diffusion, receptor methylation and demethylation, receptor complex switching between *on* and *off* states, phosphorylation and dephosphorylation of the kinase CheA, and response regulators CheY and CheB, as well as from rotary motor switching between CW and CCW direction. We assume cooperative chemoreceptor signalling com-

plexes, whose activities depend on ligand concentration and receptor methylation level, described by the MWC model. We formulated a model which includes all processes in the signalling pathway (Appendix J). To make results intuitive we presented a simplified version of the model, which only includes the dynamics of the activity of chemoreceptors, ligand concentration and receptor methylation level, as well as the motor dynamics.

To calibrate the model, we first collected experimental data sets for the signalling pathway and rotary motor (Block et al., 1982; Segall et al., 1986; Shimizu et al., 2010), and the motor switching behaviour (Korobkova et al., 2004, 2006). Using the Fourier transformed linear response functions, we subsequently fitted our model parameters (Fig. 4.2). We found a range of parameters fitting different data sets, revealing a striking experimental variation, which may require further characterisation in the future.

The motor behaviour is the final cell output, which may contain characteristic noise signatures of all upstream signalling components, including the receptors (Fig. 4.4). We found that motor switching is the dominant contribution to the spectrum of the fluctuations in motor bias. However, there are also low-frequency contributions from the dynamics of receptor methylation and phosphorylation processes. Due to cell-to-cell variation of protein expression levels, this low-frequency component may be resolvable in rotational assays of the motor (Fig. 4.5). This analysis shows that our model can reproduce spectra similar to those measured by Korobkova et al. (2004).

Although chemotaxis is one of many capabilities a cell has, and may not be optimised in isolation without the rest of the cell, we speculate the cell aims to maximise the SNR for most efficient signalling and chemotaxis (Fig. 4.6 and Fig. 4.7). We found that the SNR is maximised at receptor complex sizes larger than found from FRET dose-response curves (Endres et al., 2008). However, the cell may be limited to form larger complexes than observed experimentally by the physical interactions necessary for receptor cooperativity. Furthermore, noise from ligand molecules rebinding to the same receptor complex (Bialek and Setayeshgar, 2005) has not been considered here, which may well increase the noise level from external noise and hence decrease the predicted “optimal” receptor complex size. We also analysed the effect of varying the methylation and demethylation rate constants. We found that a good SNR is obtained for small methylation and large demethylation rate constant, corresponding to our fitted model parameters from FRET dose-response curves (cf. chapter 2).

We predict that cell-to-cell variation leads to a high-frequency component in the noise

power spectrum. These predictions can be tested experimentally. For instance, adaptation rate constants can be varied using cells expressing different amounts of CheR and CheB from an inducible plasmid. Alternatively, the natural variability in protein expression between cells can be exploited. Numerous wild-type cells could be monitored, and by extracting the adaptation times for chemotactic stimuli, the adaptation rate constants for individual cells can be inferred. Subsequently, the same cells can be used to measure long time traces of motor switching and noise spectra can be calculated.

Using Langevin equations for the noisy dynamics of signalling proteins in our model assumes that their average follows a deterministic equation, and fluctuations around the average are small and well described by an additive noise term. While such an approach is expected to work for the phosphorylation and dephosphorylation of the abundant protein CheY, its applicability is less clear for receptor signalling due to both extrinsic ligand noise and intrinsic noise from receptor methylation. Furthermore, the switching of the binary motor constitutes large noise. Hence, the general Master equation, although difficult to solve, may be a more appropriate approach (Appendix L). However, for small noise both approaches yield the same results for receptor signalling (Aquino et al., 2011). In the case of the motor, we explicitly tested that the statistical properties of the time series obtained for two-state switching and Langevin equation respectively, are the same (Appendix M). Furthermore, to analytically calculate noise spectra we needed to linearise the dynamical equations for the signalling pathway. In Appendix N, we show that noise terms are indeed sufficiently small and linearisation is justified.

Fitting our model to the Fourier transformed linear response function of the motor yields a discrepancy at large frequencies. Block et al. (1982) and Segall et al. (1986) conjectured that the pathway is a third-order low-pass filter. In contrast, we find that the only relevant filters in the frequency range considered are due to CheY-P and motor dynamics, leading to only a second-order filter. One explanation for the missing filter is that experimental concentration pulses were not short enough, leaving a signature from the input signal at large frequencies. Alternatively, additional processes such as a slow release of CheY-P from the chemosensory complexes as discussed by Blat et al. (1998) could lead to an additional filter. However, CheY-P/CheZ complex formation and potential oligomerisation of CheY-P/CheZ complexes (Eisenbach, 2004; Blat and Eisenbach, 1996a,b) are not expected to contribute to high-frequency filtering (Appendix O).

The bacterial chemotaxis pathway is a member of the large class of two-component, con-

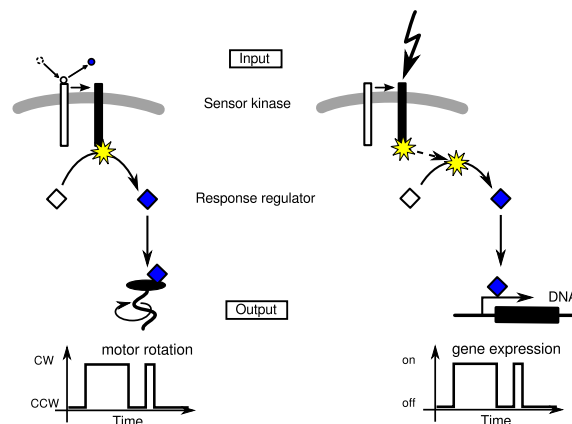


**Figure 4.8.:** Comparison of the chemotaxis pathway (*left*) and other two-component systems (*right*). The sensor kinase is activated by a signal, upon which it autophosphorylates and passes on a phosphoryl group to its response regulator, which typically induces a transcriptional response. Intermediate steps involving phosphotransfer to a phosphotransferase (indicated by dashed arrow) before phosphorylation of the response regulator are possible. The time course of the final output, i.e. gene expression, can be directly mapped onto the binary output of the chemotaxis pathway.

taining hundreds of closely related pathways (Laub and Goulian, 2007). In these pathways, activation of a sensor histidine kinase results in its autophosphorylation, and subsequently in the phosphorylation of a response regulator, which typically binds to DNA and regulates gene expression (Fig. 4.8). Particularly well-studied examples of two-component systems include the VanS (kinase)/VanR (response regulator) system conferring vancomycin resistance in Gram positive bacteria (Hutchings et al., 2006), quorum sensing in *Vibrio harveyi*, where the three kinases LuxN, LuxQ and CqsS respond to different autoinducers and first phosphorylate the phosphotransferase LuxO (which has no equivalent in the chemotaxis pathway), which then phosphorylates the response regulator LuxU (Henke and Bassler, 2004), as well as the system controlling sporulation in *Bacillus subtilis*, where there is a phosphorelay from at least four kinases KinA-KinB to the phosphotransferase Spo0F, which phosphorylates the response regulator Spo0A (Jiang et al., 2000). The final output, i.e. activation of gene expression, is again binary and hence similar to the bacterial chemotaxis pathway. As a result, the analysis presented here may also help elucidate the design of many other pathways and clarify the computational problems cells try to solve.

## 5. Information transmission

### 5.1 Synopsis

---

Sensory systems are expected to be optimised for the typical stimuli the organism encounters. In this chapter, we use dose-response curves for the *E. coli* chemotaxis pathway measured by FRET to predict typical distributions of concentrations as well as resulting signalling activities. We assume the chemotaxis sensory pathway maximises the information transmitted about the input stimulus. We discuss how the predicted distributions of concentrations may inform us of the gradients bacteria sense.

### 5.2 Motivation & open questions

---

*Escherichia coli* lives in a highly dynamic environment of nutrients and other microorganisms in the mammalian gut. Although of physiological importance, we do not have a good understanding of the typical chemical gradients microorganisms encounter. On the other hand, the chemotaxis sensory system, which enables cells to detect and navigate in their chemical environment, is experimentally well characterised. Thus, the response to specific input stimuli is known, e.g. from FRET dose-response measurements (cf. Sec. 1.1.4 in the *Introduction* and chapter 2). As sensory systems have evolved to detect specific stimuli, we may expect to find a matching between typical stimuli and the corresponding cellular responses. Specifically, taking into account natural limitations of cellular signal processing, such as noise and limited energy resources, the cell should translate an input into an output in such a way as to maximise the information transmission (Detwiler et al., 2000). An appropriate measure for the information contained in the output about the input stimulus is Shannon's mutual information (Detwiler et al., 2000; Ziv et al., 2007; Tkacik et al., 2008a,b; Tostevin and ten Wolde, 2009). For one input variable  $I$  and one

output variable  $O$  the mutual information is given by

$$\mathcal{I}[I; O] = \iint dI dO p(I, O) \log_2 \frac{p(I, O)}{p_I(I) p_O(O)} = \int dI p_I(I) \int dO p(O|I) \log_2 \frac{p(O|I)}{p_O(O)}. \quad (5.1)$$

Here,  $p_I(I)$  and  $p_O(O)$  are the probability distributions of the input and output, respectively,  $p(I, O)$  is the joint probability distribution, and  $p(O|I)$  the conditional probability distribution for the output value  $O$  given the input  $I$ . For the second definition we used the equality  $p(I, O) = p(O|I)p_I(I)$ . For simplicity, we use the same symbol  $p$  for the joint and conditional probability distributions, and distinguish them by their arguments.

Several examples have been found in biology where appropriate matching of distributions of relevant inputs, input/output relationships and distributions of outputs exists (Laughlin, 1981; Detwiler et al., 2000; Tkacik et al., 2008a,b; Mehta et al., 2009). Laughlin (1981) predicted the input/output relationship for a certain class of neurons in the fly compound eye based on the measured distribution of visual contrasts from natural scenes assuming maximum information transmission. He found a good agreement between the predicted curve and measured dose-response curve. Detwiler et al. (2000) considered enzymatic amplification. Specifically, they studied the example of phototransduction in vertebrate photoreceptors. Besides characterising engineering properties such as the gain, variance and response time of the signalling cascade, they also discussed the role of sensory adaptation as a slow mapping of the input/output relationship to the current statistics of input stimuli. For phototransduction, they showed that the dose-response curves, measured in cells which were adapted to different ambient light levels, correspond to input/output relationships predicted for typical distributions of light intensities, namely log-normal distributions. Information theory has been successfully applied in gene regulation (Tkacik et al., 2008a,b). Based on simultaneous measurement of Bicoid, transcription factor for hunchback, and hunchback during *Drosophila* embryonic development, Tkacik et al. (2008a) extracted the input/output relationship, and predicted the distribution of hunchback assuming maximum information transmission. The predicted distribution and experimentally measured distribution (Gregor et al., 2007) corresponded quantitatively. More theoretically, Tkacik et al. (2008b) studied a simple microscopic model for gene regulation. Assuming various gene-regulatory mechanisms, they investigated the amount of information that can be transmitted. A major finding is that regulatory elements generally are able to transmit more than one bit of information, i.e. they have more than two dis-

tinguishable states. Furthermore, Mehta et al. (2009) studied information transmission in quorum sensing in the bacterium *Vibrio harveyi* considering two independently transmitted inputs to a single output. They concluded that interference between the two pathways needs to be limited for the cell to be able to learn about each input, consistent with experiments (Long et al., 2009). Tostevin and ten Wolde (2009) state that information about stimuli is not only contained in instantaneous or steady-state values, but also in temporal correlations. Hence, they used the mutual information rate to calculate the information transmission for simple biochemical networks. They also studied a linear model for the *E. coli* chemotaxis pathway and predicted the power spectrum of input stimuli which is best transmitted by the pathway.

In this chapter, we aim to use the detailed information about the input/output relationships in *E. coli* chemotaxis from FRET dose-response measurements to predict the typical distributions of concentrations *E. coli* encounters. In the following, we first present some general results obtained for information transmission for Gaussian channels. We predict the optimal distributions of concentrations and corresponding signalling activities for the chemotaxis sensory system. We relate the input distributions to Weber's law in chapter 3, and finally discuss how distributions of concentrations may inform us about the typical gradients bacteria sense.

## 5.3 Results

### 5.3.1. Mutual information for a Gaussian channel with small noise

Generally, the mutual information can only be calculated analytically in special cases (Tkacik et al., 2008a). Here, we use the approximation of a so-called Gaussian channel. We assume that for a given input value  $I$  the output is distributed normally around a mean output value  $\bar{O}(I)$  with variance  $\sigma_O^2(I)$ . Hence, the input/output relationship is given by the conditional probability

$$p(O|I) = \frac{1}{\sqrt{2\pi\sigma_O^2(I)}} \exp\left\{-\frac{[O - \bar{O}(I)]^2}{2\sigma_O^2(I)}\right\}. \quad (5.2)$$

The mutual information can be calculated analytically if we assume that the distributions are tight, i.e. noise in the output is small, such that higher than linear orders in deviations of the output from the mean value  $\bar{O}$  are negligible. The mutual information for a Gaussian

channel with small output noise is (Tkacik et al., 2008b)

$$\mathcal{I}[I; O] = - \int d\bar{O} p_O(\bar{O}) \log_2 \left[ \sqrt{2\pi e \sigma_O^2} p_O(\bar{O}) \right], \quad (5.3)$$

i.e. the mutual information can be calculated knowing only the distribution of mean output values and the variance of the output. This result is derived in the following: We can rewrite Eq. 5.1 into

$$\mathcal{I}[I; O] = \int dI p_I(I) \int dO p(O|I) \log_2 p(O|I) - \int dI p_I(I) \int dO p(O|I) \log_2 p_O(O). \quad (5.4)$$

Substituting the Gaussian distribution for  $p(O|I)$ , the first term evaluates to  $\int dI p_I(I) \log_2 \left[ \sqrt{2\pi e \sigma_O(I)^2} \right]$ . Using that any function  $f(O)$  can be expanded around  $\bar{O}$  according to  $f(O) \approx f(\bar{O}) + f'(\bar{O})(O - \bar{O}) + 1/2 f''(\bar{O})(O - \bar{O})^2 + \dots$ , we obtain for the second term for small output noise

$$\begin{aligned} \int dO p(O|I) \log_2 p_O(O) &= \int dO p(O|I) \log_2 [p_O(\bar{O}) + p'_O(\bar{O})(O - \bar{O}) + \dots] \\ &\approx \log_2 p_O(\bar{O}), \end{aligned} \quad (5.5)$$

where we took  $f(O) = \log_2 p_O(O)$  and only considered terms up to linear order in  $(O - \bar{O})$ . The linear order term in the integral vanishes due to symmetry of the integrand. The mutual information is given by

$$\mathcal{I}[I; O] = \int dI p_I(I) \log_2 \left[ \sqrt{2\pi e \sigma_O^2(I)} p_O(\bar{O}(I)) \right]. \quad (5.6)$$

Due to the conservation of probability, it is  $dI p_I(I) = d\bar{O} p_{\bar{O}}(\bar{O})$ , where  $p_{\bar{O}}(\bar{O})$  is the distribution of *mean* outputs and we used the relationship  $\bar{O} = \bar{O}(I)$ . If we assume that the distribution of outputs at the mean output level  $\bar{O}$  is equal to the distribution of mean outputs, i.e.  $p_O(\bar{O}) = p_{\bar{O}}(\bar{O})$ , we finally obtain Eq. 5.3.

### 5.3.2. Optimal distributions of inputs and outputs

In order to calculate the distributions of inputs and outputs which yield maximum information transmission, given a specific mean input/output relationship and variance of the output, we need to maximise the mutual information. Formally, we form the Lagrangian  $\mathcal{L}[I; O] = \mathcal{I}[I; O] - \lambda \int d\bar{O} p_O(\bar{O})$ , where  $\lambda$  is a multiplier which implements the constraint



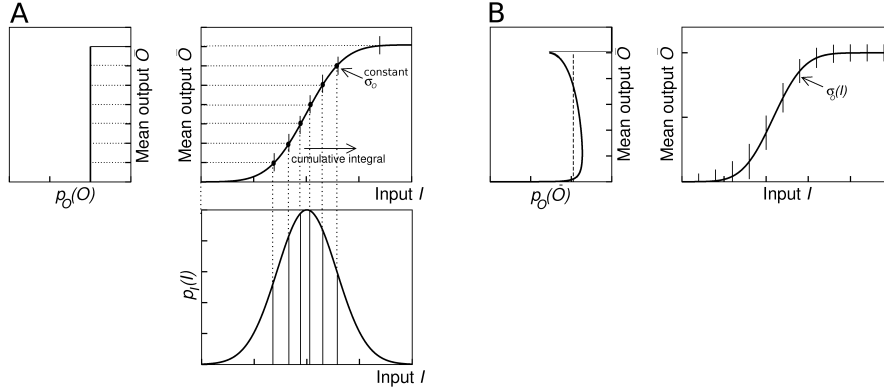


**Figure 5.1.:** Maximising the mutual information for small Gaussian output noise with uniform (A) and non-uniform variance (B). (A, *Top right*) Input/output relationship for the mean  $\bar{O}(I)$  (solid line) and constant standard deviation  $\sigma_O$  of the output states indicated by error bars. (A, *Top left*) Distribution of output levels  $O$ . (A, *Bottom right*) Distribution of input values  $I$ . For constant standard deviation, the input/output relationship for the mean  $\bar{O}(I)$  is given by the cumulative distribution of the input distribution. A sample of successive output states (dots) correspond to integration steps over the input distribution indicated by vertical lines. The distribution of output levels is uniform between minimum and maximum states. (B, *Right*) Input/output relationship for the mean  $\bar{O}(I)$  (solid line) and standard deviation  $\sigma_O(I)$  of the output states indicated by error bars. (B, *Left*) Optimal distribution of mean output levels  $\bar{O}$  (thick solid line). The case of uniform output variance (dashed line) is shown for comparison.

that  $p_O(\bar{O})$  must be normalised. Calculating the functional derivative  $\delta\mathcal{L}/\delta p_O(\bar{O})$  of the Lagrangian with respect to the output distribution and setting it to zero yields

$$0 = \frac{\delta\mathcal{L}[I; O]}{\delta p_O(\bar{O})} = \int d\bar{O} \log_2 \left[ \sqrt{2\pi e\sigma_O^2} p_O(\bar{O}) \right] - \int d\bar{O} p_O(\bar{O}) \frac{1}{p_O(\bar{O})} - \lambda \int d\bar{O}. \quad (5.7)$$

This equality is fulfilled if the integrand vanishes. Hence, the optimal distribution of outputs is

$$p_O^*(\bar{O}) = \frac{1}{Z} \frac{1}{\sigma_O(\bar{O})}, \quad (5.8)$$

where  $Z = \int 1/\sigma_O(\bar{O}) d\bar{O}$  is a normalisation constant. By conservation of probability  $dI p_I(I) = d\bar{O} p_O(\bar{O})$  the distribution of inputs, which optimises the mutual information given the input/output relationship, is

$$p_I^*(I) = p_O^*(\bar{O}) \frac{d\bar{O}}{dI}. \quad (5.9)$$

When all output states have the same variance, the optimal distribution of inputs is proportional to the slope of the mean input/output relationship,  $p_I^*(I) \propto d\bar{O}/dI$  (Laughlin, 1981). In other words, the optimal mean input/output relationship is given by the cumulative distribution of the input, i.e.  $\bar{O}(I) = \int^I dI' p_I(I')$  (Fig. 5.1 A).  $p_O(\bar{O})$  is uniform, i.e.

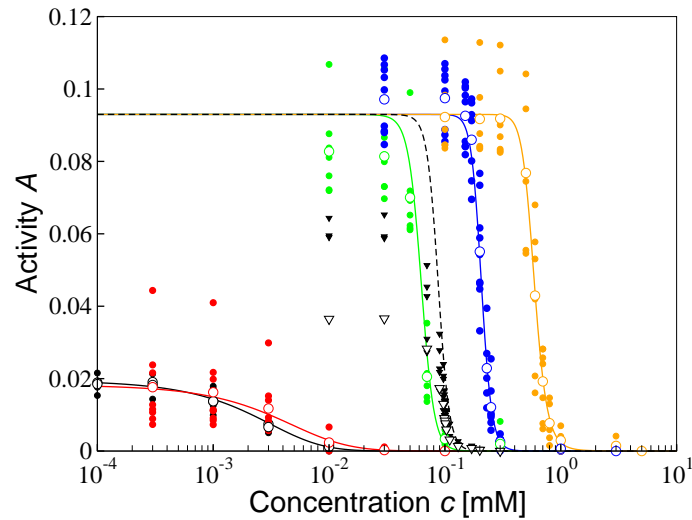


**Figure 5.2.:** FRET dose-response curves for adapting (WT) cells and non-adapting mutants in specific receptor methylation states. Cells express the Tar receptor only. Data points for various measurements of the FRET activity at different concentrations of MeAsp (filled symbols), as well as their mean values are shown (open symbols). Cells used were: WT adapted to zero (black circles) and  $100 \mu\text{M}$  (black triangles) ambient concentration, QEEE (red), QEQE (green), QEQQ (blue) and QQQQ (orange) mutant. Corresponding solid and dashed lines are the fits of the static MWC model.

all output states are used with equal probability. In general, the output states have a non-uniform variance, and the optimal distribution of mean output levels Eq. 5.8 is inversely proportional to the standard deviation of the output. This means that output states corresponding to input signals which can be measured reliably (with low variance in the output) should be used preferentially. With sigmoidal mean input/output relationships, this typically leads to bimodal distributions (Fig. 5.1 B).

### 5.3.3. FRET dose-response curves for Tar only cells

In the following, we apply the general findings presented in the previous subsections to the chemotaxis pathway. Figure 5.2 shows FRET dose-response measurements for populations of cells expressing only the Tar receptor (Endres et al., 2008). Adapting wild-type (WT) cells were used at two different ambient concentrations, as well as signalling mutants lacking the adaptation enzymes. In the mutants, Tar receptors were genetically engineered to have the amino acids glutamate (E) or glutamine (Q) at the four receptor modification sites for methylation and demethylation. E is an unmethylated modification site, while Q resembles a methylated modification site. The signalling activity was measured several times for step changes in MeAsp concentration. It is obvious that there is a large variation in signalling activity at each concentration. Endres et al. (2008) fitted the (static) MWC

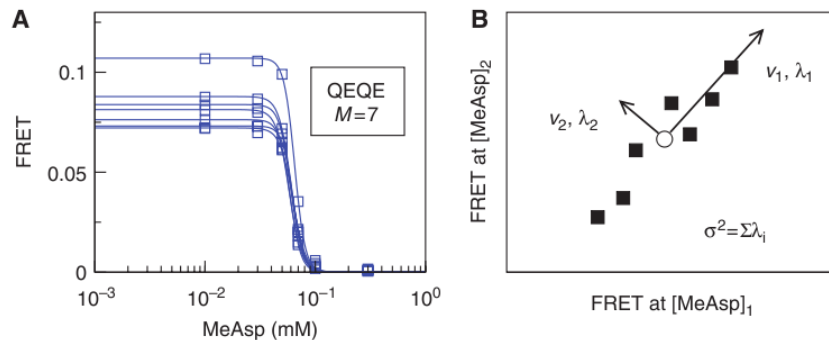


**Figure 5.3.:** Illustration of principle component analysis (PCA). (A) FRET dose-response curves. Shown are  $M$  curves measured at  $D$  concentrations for the QEQE mutant. (B) Representation of PCA in a scatter plot where each dot represents one dose-response curve. For simplicity, the projection of principle components onto two dimensions is shown. The eigenvectors of the two main principle components are indicated by arrows (the length of the vectors indicate the magnitude of the contribution to the variation by the corresponding principle component). The circle represents the mean value of the data. Figure taken from Endres et al. (2008).

model to dose-response curves using a principal component analysis. The parameters of the fit are shown in Appendix P.

#### 5.3.4. Principal component analysis (PCA)

Principal component analysis (PCA) is a method to represent noisy data along independent directions of variation. The method is illustrated in Fig 5.3:  $M$  dose-response curves are measured at  $D$  concentration (Fig 5.3 A). Hence, in a  $D$ -dimensional space with the coordinates corresponding to the FRET activity at a particular concentration  $c_i$  ( $i = 1, \dots, D$ ), each dose-response curve is represented by one data point. Plotting all dose-response curves results in a scatter plot (Fig. 5.3 B). PCA produces a new coordinate system centred around the mean value of the data, whose axes are orthogonal and a linear combination of the old axes. The coordinate axes are aligned along the directions of independent variation in the data (indicated by the arrows in Fig. 5.3 B). The coordinate transformation is obtained by diagonalising the covariance matrix

$$C_{ij} = \frac{1}{M} \sum_{l=1}^M [x_l(c_i) - \bar{x}(c_i)][x_l(c_j) - \bar{x}(c_j)], \quad (5.10)$$

where  $c_i$  are ligand concentrations,  $x_l$  are the measured FRET activities and  $\bar{x}(c_i)$  is the mean FRET activity measured at concentration  $c_i$ . The covariance matrix is diagonalised by  $V^{-1}CV = U$ , where  $V$  is the matrix containing the eigenvectors of  $C$  and  $U$  is a diagonal matrix of eigenvalues  $\lambda_i$  ( $i = 1, \dots, D$ ). The eigenvectors are the principle components of

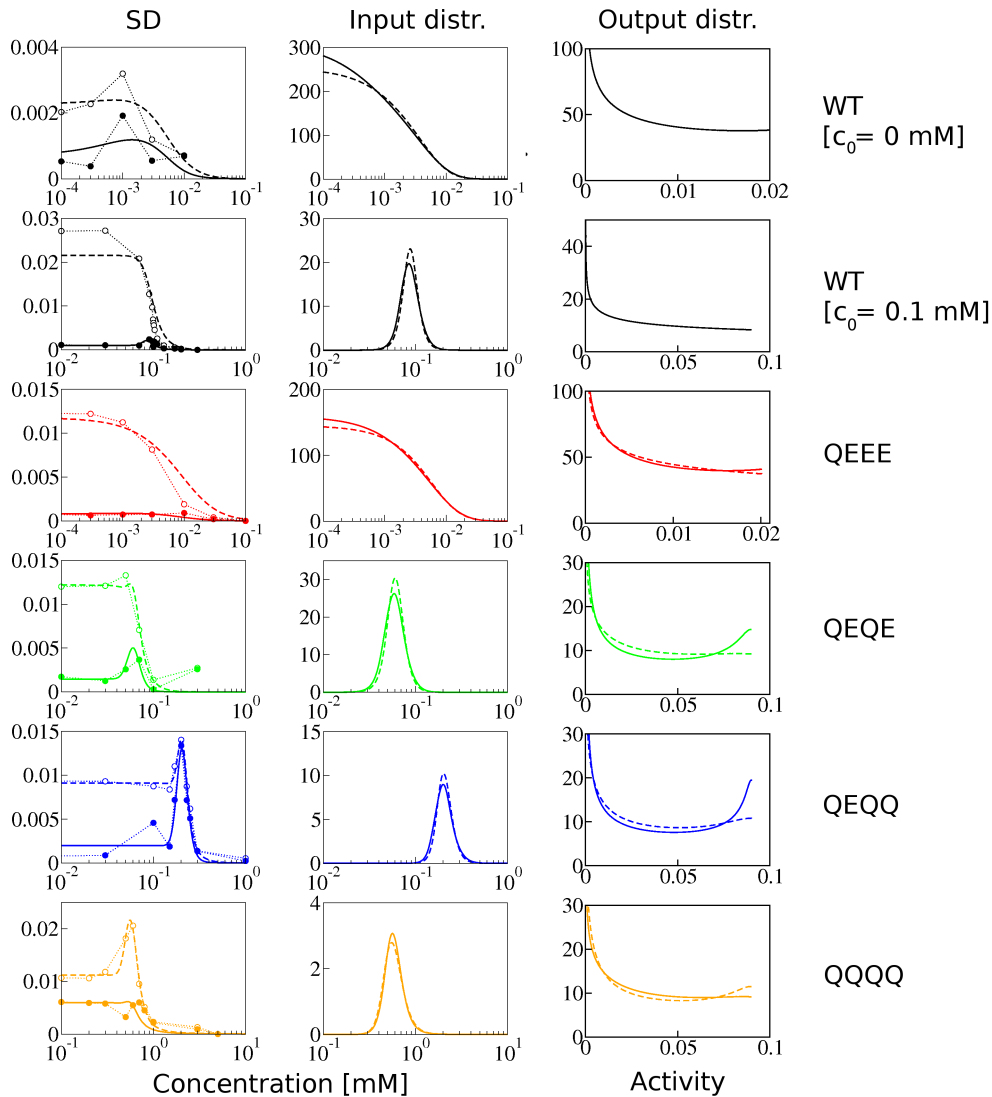


**Figure 5.4.:** Predicted optimal input and output distributions. (*Left*) Standard deviation of activity measured by FRET in Fig. 5.2 (open and filled symbols for including and excluding receptor expression noise, respectively). Fits to the standard deviations are shown as well (dashed and solid lines, respectively). (*Middle*) Predicted distributions of attractant concentrations (input). (*Right*) Predicted distributions of signalling activities (output).

the data. Typically, most of the variation in the data is described by a small number of principle components, such that PCA can be used for a dimensional reduction of the data.

### 5.3.5. Optimal input and output distributions for Tar only cells

We extracted the variance in the FRET activity in order to predict the input and output distributions for optimal information transmission. Using PCA enabled us to separate the largest component to the variation, which is due to an overall amplitude variation related to variable expression levels of receptors (Endres et al., 2008; supporting information).

In Fig. 5.4 (first column) we show the standard deviation (SD) for both, including as well as excluding that component from receptor expression noise (symbols). The two SD look qualitatively the same, although the SD excluding receptor expression noise is significantly smaller. The SD has a characteristic shape: WT adapted to zero ambient and QEEE mutant show a roughly monotonically decreasing SD with increasing MeAsp concentration as receptors become saturated by attractant. WT cells adapted to a higher ambient concentration, as well as mutants in higher receptor modification states, show a peak in the SD in the linear regime of the dose-response curve. In order to obtain smooth curves for the predicted optimal input and output distributions, we fitted the variance of the output according to the simple model for fluctuations in FRET activity

$$\sigma_A^2 = \left[ \alpha_1 \sqrt{c} \frac{dA}{dc} \right]^2 + \left[ \alpha_2 \sqrt{A} \right]^2, \quad (5.11)$$

where we assumed that transmitted input fluctuations (first term) and fluctuations from the intracellular pathway (second term) are independent. Therefore, we add their variances up. Input fluctuations have a concentration dependence as discussed in chapter 4 (Bialek and Setayeshgar, 2005), and are transmitted according to the mean input/output relationship given by the MWC model. Pathway fluctuations are assumed to be Poissonian, and the number of phosphorylated signalling proteins is assumed to be proportional to the signalling activity  $A$ . The parameters  $\alpha_1$  and  $\alpha_2$  are adjusted using a  $\chi^2$ -fit to the variance of the output (including as well as excluding the first principle component; see Appendix P). The predicted optimal input distributions calculated from the fitted SD (Fig. 5.4, second column) are monotonically falling for WT cells adapted to zero ambient concentration and for QEEE mutants, with a maximum at concentration zero. WT adapted to a higher ambient concentration, as well as mutants in higher receptor modification states display a peaked distribution with the maximum in the linear range of the dose-response curve around the ambient concentration corresponding to the receptor modification state. As the modification state increases, the peak shifts to higher concentrations. Simultaneously, the width of the distribution increases. There is no quantitative difference between the optimal input distributions calculated using SD including and excluding the component of the variance from receptor expression noise, respectively. The predicted optimal output distributions are shown in Fig. 5.4 (third column). Remarkably, in the output distributions, the effect of eliminating the receptor expression noise from the

variance is obvious. For the variance including receptor expression noise, the distributions for all cells are largely monotonically falling for increasing activity. Using the variance excluding the receptor expression noise, we obtain bimodal distributions for receptors in higher modification states. Note that we did not rescale FRET dose-response curves measured from populations of cells to account for single cells. Hence, activities and SD are for populations of cells. In principle, those can be rescaled if the number of cells is known. However, rescaling does not change the predicted input distributions, and only the range of output activities would be rescaled for predicted output distributions.

### 5.3.6. Scaling behaviour of predicted input distributions

The predicted optimal input distributions for high receptor modification states can be fit by log-normal distributions

$$p_{\ln}(x; \mu, \sigma^2) = \frac{1}{x\sqrt{2\pi\sigma^2}} \exp\left\{-\frac{[\ln(x) - \mu]^2}{2\sigma^2}\right\} \quad (5.12)$$

as shown in Fig. 5.5 (parameters of the fits are listed in Appendix P). The log-normal distribution is characterised by two parameters,  $\mu$  and  $\sigma^2$ . The mean of a log-normally distributed variable is  $\langle x \rangle = e^{\mu + \sigma^2/2}$  and its variance is  $\langle x^2 - \langle x \rangle^2 \rangle = (e^{\sigma^2} - 1)e^{2\mu + \sigma^2}$ . Hence, the ratio of variance and squared mean can be expressed only in terms of  $\sigma^2$ ,  $\langle x^2 - \langle x \rangle^2 \rangle / \langle x \rangle^2 = e^{\sigma^2} - 1$ . The inset in Fig. 5.5 shows that the distributions for different receptor modification states almost perfectly collapse onto one curve when scaling the distribution such that the peak positions coincide, indicating that the mean and width of the distribution indeed fulfil the scaling behaviour of log-normal distributions. The ratio of variance and squared mean for the distributions is about 0.05 ... 0.06.

## 5.4 Discussion

---

Sensory systems are expected to be optimised during the course of evolution to sense the stimuli which are typically encountered by the organism. Here, we assumed that the chemotaxis sensing process maximises the information transmitted about input stimuli to a cellular output. Based on this assumption, we used dose-response curves to predict typical distributions of concentrations sensed by cells in a specific receptor modification state and corresponding distributions of signalling activities (Fig. 5.2).

To characterise the microenvironment of *E. coli* we would need to know the spatial

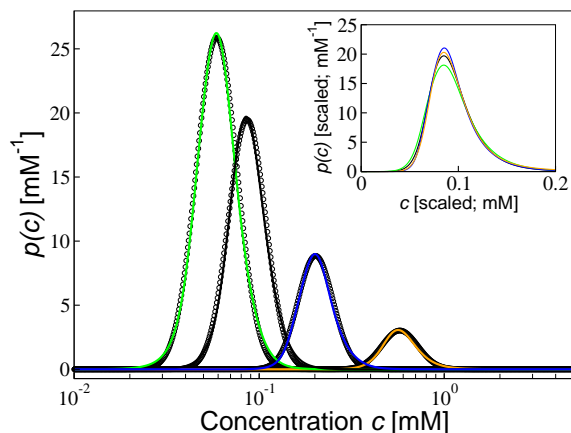


**Figure 5.5.:** Log-normal scaling of the optimal input concentrations. Coloured lines are the predicted input distributions from Fig. 5.4 (QEQE, green; WT 100  $\mu\text{M}$ , black; QEQQ, blue; QQQQ, orange) and symbols are log-normal fits to the distributions. (*Inset*) Input distributions from the main panel scaled to the peak position of the WT input distribution.

and temporal concentration profiles. An easier task is to track bacteria in well-defined chemical gradients, e.g. in microfabricated devices (van Haastert and Postma, 2007; Wolfaardt et al., 2008; Kang et al., 2008), and establish the distributions of concentrations they sample. As illustrated in Fig. 5.6, shallow gradients lead to a narrow distribution of concentrations sampled by bacteria in a particular receptor modification state. This is due to adaptation adjusting the receptor methylation level duly corresponding to the concentrations encountered. In contrast, steep gradients result in a wide distribution of concentrations as adaptation cannot keep up with concentration changes across the gradient. Distributions are typically skewed towards higher concentrations as bacteria tend to swim up the gradient. Hence, higher concentrations are sampled more frequently. Comparing the distributions of concentrations obtained from swimming bacteria in well-characterised gradients and those predicted from maximum information transmission suggests that *E. coli* typically encounters steep gradients, i.e. rapidly changing spatial or temporal gradients, as those lead to a wide spread of sampled concentrations. It is obvious from Fig. 5.6 that probably not one particular gradient generates the predicted optimal distributions of concentrations, but different gradients, weighted appropriately, give rise to the distribution. More work would be needed to analyse what types and distributions of gradients produce the predicted optimal distributions of concentrations.

Celani and Vergassola (2010) argue in a similar fashion that bacteria are optimised to sense complex and highly variable concentration profiles. They show that optimisation of the minimum uptake of nutrients in any concentration profile, i.e. without knowledge of

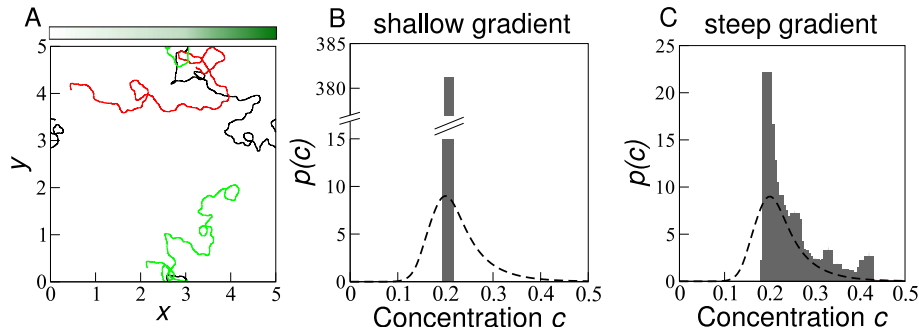


**Figure 5.6.:** Input distributions of simulated swimming bacteria using *RapidCell* (Vladimirov et al., 2008). (A) Three example traces of bacteria swimming in an exponential gradient in  $x$ -direction (indicated by the graded bar). (B and C) Distribution of sampled input concentrations in cells with receptor methylation level  $m=6$ . 5000 trajectories were simulated with time step 0.001 s. The gradients were  $c(x) = c^* \exp[\gamma/c^*(x - L_x/2)]$ , where  $L_x=5$  mm is the dimension in  $x$  and  $y$ , and  $c^*=0.2$  mM. The histograms are the distributions sampled by the bacteria in a shallow (B,  $\gamma=0.001$  mM/mm) and steep (C,  $\gamma=0.2$  mM/mm) gradient. The dashed line is the predicted distribution based on dose-response curves (cf. Fig. 5.4).

the exact statistics of environmental fluctuations, reproduces the experimentally measured linear response function (cf. chapter 4).

The predicted distributions of input concentrations are roughly log-normal distributions. Distributions for different receptor modification states coincide when scaled to the same concentration of the peak of the distribution. This constancy of fractional changes of concentration stimuli relative to the ambient concentration is reminiscent of Weber’s law in chapter 3. We showed that the smallest noticeable stimulus the chemotaxis sensory system responds to grows linearly with the background stimulus. If the predicted distributions of inputs are indeed encountered by *E. coli*, Weber’s law represents an adaptation of the sensory system to its environment; as the width of concentration distributions scales with ambient concentration, the range of inputs increases. Responding to the fractional change of stimuli makes sense in order to cover the limited range of outputs, i.e. number of signalling molecules.

Here, we considered an intermediate, intracellular output of the chemotaxis pathway, CheY-P/CheZ pairs, which can be measured by FRET. The final cellular output is the modulation of the swimming behaviour, i.e. running or tumbling. While the activation of CheY-P is fast (in the order of tenths of seconds), the motor reacts much slower on the timescale of seconds (cf. chapter 4). Hence, when treating the information transmission to the motor, temporal correlations between input and output should be taken into account (Tostevin and ten Wolde, 2009). However, we expect that if information transmission is to be optimised by the whole chemotaxis pathway, this should also be true for



every intermediate stage, as information can only be lost, not gained.

## 6. Conclusions

Chemotaxis in the bacterium *Escherichia coli* has become a paradigm for sensory and signalling pathways. Decades of research, including genetic, structural, microscopic, and biochemical studies have led to one of the most comprehensively understood biological systems. This makes it a testing field for quantitative modelling aimed at conceptualisation in biology. In this thesis, we studied sensory adaptation, signal and noise filtering, as well as information transmission in the *E. coli* chemotaxis pathway. In chapter 2, we used experimental FRET measurements to analyse the dynamics of sensory adaptation, i.e. the reversal of an initial signalling response by receptors after a concentration stimulus. We predict several layers of feedback regulation, which account for the different time scales found for adaptation to favourable and unfavourable stimuli. Although the molecular mechanism for the predicted feedback needs to be established in the future, our study exemplifies that mathematical modelling can reveal shortcomings in our current understanding. It also highlights that models in biology need to become more complex as increasingly quantitative experimental measurements are developed.

In chapter 3, we showed that the chemotaxis sensory pathway follows Weber's law, in common with many other sensory systems. Again based on experimental data, we extracted the smallest noticeable concentration stimulus, which is found to increase roughly linearly with the background stimulus. We explained Weber's law in chemotaxis as emerging from the binding properties of ligand molecules to chemoreceptors and sensory adaptation. We argue that Weber's law may be an evolutionary adaptation mechanism to sense the typical chemical gradients in the bacteria's environment. We predict typical gradients to be exponential as swimming in those gradients yields an invariant response, i.e. no attenuation by adaptation or saturation of the response along the gradient.

In chapter 4, we investigated the signal and noise filtering properties of the chemotaxis pathway. We used experimental data from the literature to calibrate our model. We found that all signalling processes may contribute to noise in the final cellular output of motor

---

rotation, hence making this more theoretical study accessible to experimental verification.

Finally, in chapter 5 we studied information transmission in the chemotaxis pathway in order to predict typical distributions of input concentrations. This study could help to characterise the chemical environment bacteria typically experience, and augments our discussion about Weber's law in chapter 3. We predict that concentrations sampled by swimming bacteria are roughly log-normally distributed and, furthermore, that steep gradients lead to the wide distributions of concentrations predicted.

In the future, it will be interesting to build on our understanding of the relatively simple *E. coli* chemotaxis pathway to study the dynamics of more complex signalling pathways. For instance, the photosynthetic bacterium *Rhodobacter sphaeroides* has several homologues of each of the chemotaxis proteins in *E. coli* (Porter et al., 2008). Interestingly, *Rhodobacter* has two chemotaxis receptor clusters, one polar cluster similar to *E. coli* and one cytoplasmic cluster, which is thought to sense the metabolic state of the cell. Both clusters need to be present for chemotaxis. The soil bacterium *Bacillus subtilis* has three adaptation systems (Glekas et al., 2010): one based on methylation and demethylation of receptors similar to *E. coli* and two independent of receptor methylation, the CheC/CheD system and the CheV system. Furthermore, in *B. subtilis*, sensory adaptation is not determined by the level of receptor methylation but the location of methylation at receptors. In eukaryotic cells, spatial dynamics play a major role in chemotaxis in addition to the temporal dynamics of signalling and adaptation. For instance, in the chemotactic organism *Dictyostelium*, the chemotaxis is determined by the polarisation of the cell, i.e. the activation and localisation of several molecules, including kinases and phosphatases of phospholipids and G-protein coupled receptors in the cell membrane to different sides of the cell (Funamoto et al., 2002). The dynamics of adaptation has been suggested to be essential in producing a gradient of signalling molecules across the cell during chemotaxis in gradients (Xiong et al., 2010).

Modelling *E. coli* chemotaxis exemplifies that the dynamics of cell signalling cannot always be described by a mass-action or Michaelis-Menten kinetics typically used for chemical reactions in diluted solutions and enzyme-catalysed reactions, respectively. As we have seen for the dynamics of the receptor methylation level, the rates of receptor modification depend on the activity state of receptors, even though according to a Michaelis-Menten dynamics, enzymes should be saturated and rates of modification constant, as the number of receptors exceed the number of modification enzymes by far. This is likely due to the

## CHAPTER 6. CONCLUSIONS

---

modification enzymes being tethered to receptors with slow exchange rates (Schulmeister et al., 2008).

Understanding chemotaxis in bacteria can be crucial as it is often needed for virulence of infections by pathological species (O'Toole et al., 1999; Pittman et al., 2001; Williams et al., 2007). Furthermore, bacteria secrete and sense small molecules of their own and other species called autoinducers, which trigger collective responses once a critical cell density is reached, a process called quorum sensing. Chemotaxis has been implicated in quorum sensing (Park et al., 2003). For instance, Tsr, one of the major chemotaxis receptors, is needed for quorum sensing of a specific autoinducer in *E. coli* (Hegde et al., 2010). This is interesting as quorum sensing has been shown to reduce virulence of pathogenic species in mixed populations of bacteria, suggesting a possibility of medical therapies (Ng and Bassler, 2009). Finally, bacteria are remarkable as they can utilise a number of substances for growth. It is interesting to think about using particular bacteria species, e.g. *Pseudomonas* (Liu and Parales, 2009), or reengineering chemotaxis pathways by synthetic biology approaches (Sinha et al., 2010) for bacteria to sense and transform environmental pollutants. These are exciting areas of potential medical and industrial applications of bacterial chemotaxis.

# Appendices

# A. Whole-pathway model for chemotactic signalling

We consider the following reactions (Fig. A.1): (1) auto-phosphorylation of CheA and formation of CheA-P (concentrations  $[A_p]$ ) when receptors are active, (2) phosphorylation of CheY and formation of CheY-P ( $[Y_p]$ ), (3) association of CheY-P and CheZ ( $[Y_pZ]$ ), leading to the dephosphorylation of CheY-P and dissociation into CheY and CheZ, and (4) phosphorylation of CheB and formation of CheB-P ( $[B_p]$ ).

Assuming the law of mass-action, our model comprises the following set of ordinary differential equations:

$$\frac{d[A_p]}{dt} = \underbrace{A \cdot k_A ([A]_{\text{tot}} - [A_p])}_{\text{CheA autophosphorylation}} - \underbrace{k_Y ([Y]_{\text{tot}} - [Y_p]) [A_p]}_{\text{CheY phosphorylation}} - \underbrace{k_B ([B]_{\text{tot}} - [B_p]) [A_p]}_{\text{CheB phosphorylation}} \quad (\text{A.1})$$

$$\frac{d[Y_p]}{dt} = \underbrace{k_Y ([Y]_{\text{tot}} - [Y_p]) [A_p]}_{\text{CheY phosphorylation}} - \underbrace{k_1 ([Z]_{\text{tot}} - [Y_pZ]) [Y_p]}_{\text{CheY-P/CheZ association}} + \underbrace{k_2 [Y_pZ]}_{\text{CheY-P/CheZ dissociation}} \quad (\text{A.2})$$

$$\frac{d[Y_pZ]}{dt} = \underbrace{k_1 ([Z]_{\text{tot}} - [Y_pZ]) [Y_p]}_{\text{CheY-P/CheZ association}} - \underbrace{(k_2 + k_3) [Y_pZ]}_{\text{CheY-P/CheZ dissociation and CheY-P dephosphorylation}} \quad (\text{A.3})$$

$$\frac{d[B_p]}{dt} = \underbrace{k_B ([B]_{\text{tot}} - [B_p]) [A_p]}_{\text{CheB phosphorylation}} - \underbrace{k_{-B} [B_p]}_{\text{spontaneous dephosphorylation of CheB-P}} \quad (\text{A.4})$$

where the  $k_i$  (with  $i = 1, 2, 3, A, B, -B$  and  $Y$ ) are kinetic rate constants for the individual reactions. Modelling the activity of chemoreceptors, we note that the dynamics of receptor switching between its *on* and *off* states, as well as ligand binding, are fast. Therefore, there is a time-scale separation between fast receptor activity dynamics and the slower phosphorylation and receptor methylation reactions. Hence, we can use the quasi-steady state activity  $A$  of a receptor complex as a function of ligand concentration and receptor

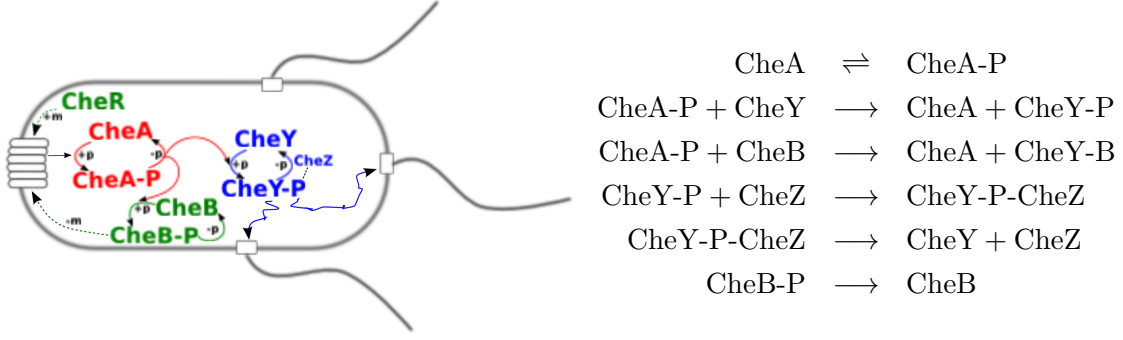


**Figure A.1.:** Schematics of the chemotaxis pathway (*left*) and biochemical reactions for phosphorylation and dephosphorylation in the pathway (*right*). When receptors activate the kinase CheA, it autophosphorylates. CheA-P can pass on a phosphoryl group to CheY and CheB, which subsequently become phosphorylated. CheY-P diffuses through the cell to rotary motors, and promotes tumbling. CheY-P can bind to its phosphatase CheZ (indicated by the dotted line in the pathway), and is subsequently dephosphorylated. CheB-P dephosphorylates spontaneously. Additionally, receptors can be modified by methylation and demethylation by enzymes CheR and CheB, respectively.

methylation level determined by the MWC model:

$$A = \frac{1}{1 + e^F}, \text{ with} \quad (\text{A.5})$$

$$F = N \left[ \epsilon(m) + \nu_a \ln \left( \frac{1 + c/K_a^{\text{off}}}{1 + c/K_a^{\text{on}}} \right) + \nu_s \ln \left( \frac{1 + c/K_s^{\text{off}}}{1 + c/K_s^{\text{on}}} \right) \right], \quad (\text{A.6})$$

as described in Eq. 2.2 and 2.3 in chapter 2. Furthermore, the adaptation dynamics by methylation and demethylation of receptors, catalysed by CheR and CheB-P, respectively, is given by (cf. Eq. 2.6 in chapter 2),

$$\frac{dm}{dt} = \underbrace{g_R(1 - A)}_{\text{methylation by CheR}} - \underbrace{\hat{g}_B[B_p]^2 A}_{\text{demethylation by CheB-P}}, \quad (\text{A.7})$$

$$= g_R(1 - A) - g_B A^3 \quad (\text{A.8})$$

where  $g_R$  and  $\hat{g}_B$  are effective rate constants, and  $\hat{g}_B[B_p]^2 \approx g_B A^2$  as  $[B_p]$  is approximately proportional to the receptor complex activity (Fig. A.2 D). The parameter values we used for the whole-pathway model are listed in Table A.1.

## A.1 Rescaling of parameters

In order to reduce the number of parameters, we normalise the protein concentrations by their respective total concentrations in the cell,  $[A_p] \rightarrow [a_p] = [A_p]/[A]_{\text{tot}}$ ,  $[Y_p] \rightarrow [y_p] = [Y_p]/[Y]_{\text{tot}}$ ,  $[Y_p Z] \rightarrow [y_p z] = [Y_p Z]/[Y]_{\text{tot}}$  and  $[B_p] \rightarrow [b_p] = [B_p]/[B]_{\text{tot}}$ . Furthermore, we

## APPENDIX A. WHOLE-PATHWAY MODEL FOR CHEMOTACTIC SIGNALLING

---

rescale the time by the autophosphorylation rate of CheA,  $k_A$ ,  $t \rightarrow \tau = k_A \cdot t$ , and introduce rescaled rate constants according to  $k_1 \rightarrow \kappa_1 = k_1[Y]_{\text{tot}}/k_A$ ,  $k_2 \rightarrow \kappa_2 = k_2/k_A$ ,  $k_3 \rightarrow \kappa_3 = k_3/k_A$ ,  $k_Y \rightarrow \kappa_Y = k_Y[A]_{\text{tot}}/k_A$ ,  $k_B \rightarrow \kappa_B = k_B[A]_{\text{tot}}/k_A$  and  $k_{-B} \rightarrow \kappa_{-B} = k_{-B}/k_A$ . Overall, this transformation yields dimensionless kinetic variables and parameters by measuring phosphorylated protein fractions in units of total protein concentrations and rate constants relative to the autophosphorylation rate constant of CheA. Using the ratios of total protein concentrations,  $\alpha_1 = [Y]_{\text{tot}}/[A]_{\text{tot}}$ ,  $\alpha_2 = [B]_{\text{tot}}/[A]_{\text{tot}}$ , and  $\alpha_3 = [Z]_{\text{tot}}/[Y]_{\text{tot}}$ , we obtain the transformed set of equations

$$\frac{d}{d\tau}[a_p] = A \cdot (1 - [a_p]) - \alpha_1 \kappa_Y (1 - [y_p]) [a_p] - \alpha_2 \kappa_B (1 - [b_p]) [a_p] \quad (\text{A.9})$$

$$\frac{d}{d\tau}[y_p] = \kappa_Y (1 - [y_p]) [a_p] - \kappa_1 (\alpha_3 - [y_p z]) [y_p] + \kappa_2 [y_p z] \quad (\text{A.10})$$

$$\frac{d}{d\tau}[y_p z] = \kappa_1 (\alpha_3 - [y_p z]) [y_p] - (\kappa_2 + \kappa_3) [y_p z] \quad (\text{A.11})$$

$$\frac{d}{d\tau}[b_p] = \kappa_B (1 - [b_p]) [a_p] - \kappa_{-B} [b_p]. \quad (\text{A.12})$$

The transformed equation for the methylation level of receptors is obtained by replacing time  $t \rightarrow \tau$ ,  $g_R \rightarrow \gamma_R = g_R/k_A$  and  $\hat{g}_B \rightarrow \gamma_B = \hat{g}_B B_{\text{tot}}^2/k_A$  in Eq. A.7, yielding

$$\frac{dm}{d\tau} = \gamma_R (1 - A) - \gamma_B [b_p]^2 A. \quad (\text{A.13})$$

The new parameter values of this transformed model are listed in Table A.1.

### A.2 Steady-state concentrations

---

We analysed the steady-state concentrations of phosphorylated proteins and CheY-P/CheZ pairs. Setting the time-derivatives of Eq. A.9-A.12 to zero, we solved for the steady-state concentrations of CheA-P, CheY-P and CheB-P, as well as the concentration of CheY-P/CheZ pairs as a function of the receptor complex activity  $A$ . The results are shown in Fig. A.2. CheA-P shows a strong non-linear dependence on the activity  $A$ , i.e., it is strongly activated at high receptor complex activity. It is also notable that only a small fraction of the CheA concentration is phosphorylated at maximal receptor activity  $A = 1$ , which nicely fits estimates from *in vitro* measurements (Wolanin et al., 2006). All other phosphorylated fractions of protein, as well as the concentration of CheY-P/CheZ pairs are approximately proportional to receptor complex activity  $A$ .



### A.3. TIME COURSES AND STEADY-STATE ASSUMPTION

**Table A.1.:** Parameters of the whole-pathway model for chemotaxis signalling for Eq. A.1-A.7, including references to literature values where possible, and rescaled parameters for Eq. A.9-A.13. The literature values are given in parentheses where different from our parameter values.  $k_1$  was determined by the condition that at steady-state with  $A^*=1/3$ , the concentration  $[Y_p]^* = [Y]_{\text{tot}}/3$  (Sourjik and Berg, 2002a).  $g_R$  was determined by the steady-state activity  $A^*$  and the value for  $\hat{g}_B$ .

Parameter	Value	Reference	Scaled parameter	Value
$[A]_{\text{tot}}$	5 $\mu\text{M}$	Sourjik and Berg (2002a)	$\alpha_1$	1.94
$[B]_{\text{tot}}$	0.28 $\mu\text{M}$	Li and Hazelbauer (2004)	$\alpha_2$	0.056
$[Y]_{\text{tot}}$	9.7 $\mu\text{M}$	Li and Hazelbauer (2004)	$\alpha_3$	0.113
$[Z]_{\text{tot}}$	1.1 $\mu\text{M}$	Sourjik and Berg (2002a)	$\kappa_Y$	50
$k_A$	10 $\text{s}^{-1}$	Wolanin et al. (2006)	$\kappa_B$	7.5
$k_Y$	100 $\mu\text{M}^{-1} \text{s}^{-1}$	Stewart et al. (2000)	$\kappa_1$	4.88
$k_B$	15 $\mu\text{M}^{-1} \text{s}^{-1}$	Stewart et al. (2000)	$\kappa_2$	0.05
$k_1$	5.0 $\mu\text{M}^{-1} \text{s}^{-1}$	Sourjik and Berg (2002a)	$\kappa_3$	20
$k_2$	0.5 $\text{s}^{-1}$	Sourjik and Berg (2002a)	$\kappa_{-B}$	0.135
$k_3$	200 $\text{s}^{-1}$	(30 $\text{s}^{-1}$ ) Sourjik and Berg (2002a)	$\gamma_R$	0.0006
$k_{-B}$	1.35 $\text{s}^{-1}$	(0.35 $\text{s}^{-1}$ ) Bray and Bourret (1995); Stewart (1993)	$\gamma_B$	0.0246
$g_R$	0.006 $\text{s}^{-1}$	—		
$\hat{g}_B$	3.14 $\mu\text{M}^{-2} \text{s}^{-1}$	—		

### A.3 Time courses and steady-state assumption

We tested if the phosphorylation and CheY-P/CheZ association reactions, Eq. A.9-A.12, are in quasi-steady state compared to the slower methylation and demethylation reactions of receptors, Eq. A.13. For this purpose, we increased all rate constants for phosphorylation, dephosphorylation, as well as CheY-P/CheZ association and dissociation by one order of magnitude, such that concentrations are forced to be in quasi steady-state at each time point. Comparing the results to the time courses with the original parameter values shown in Fig. A.3, we found only minor deviations (exemplified in insets). Therefore, the above mentioned reactions are indeed in quasi-steady state to a good approximation. This, together with the approximate linearity of the steady-state concentration of CheY-P/CheZ pairs as function of receptor complex activity  $A$ , permits us to replace the number of FRET (CheY-P/CheZ) pairs by the receptor complex activity (with appropriate proportionality factors) as assumed in chapter 2. Similarly, Eq. 2.6 in chapter 2 arises by replacing CheB-P concentration in the demethylation rate in Eq. A.13 by the receptor complex activity  $A$ , where the methylation and demethylation rate constants are

## APPENDIX A. WHOLE-PATHWAY MODEL FOR CHEMOTACTIC SIGNALLING

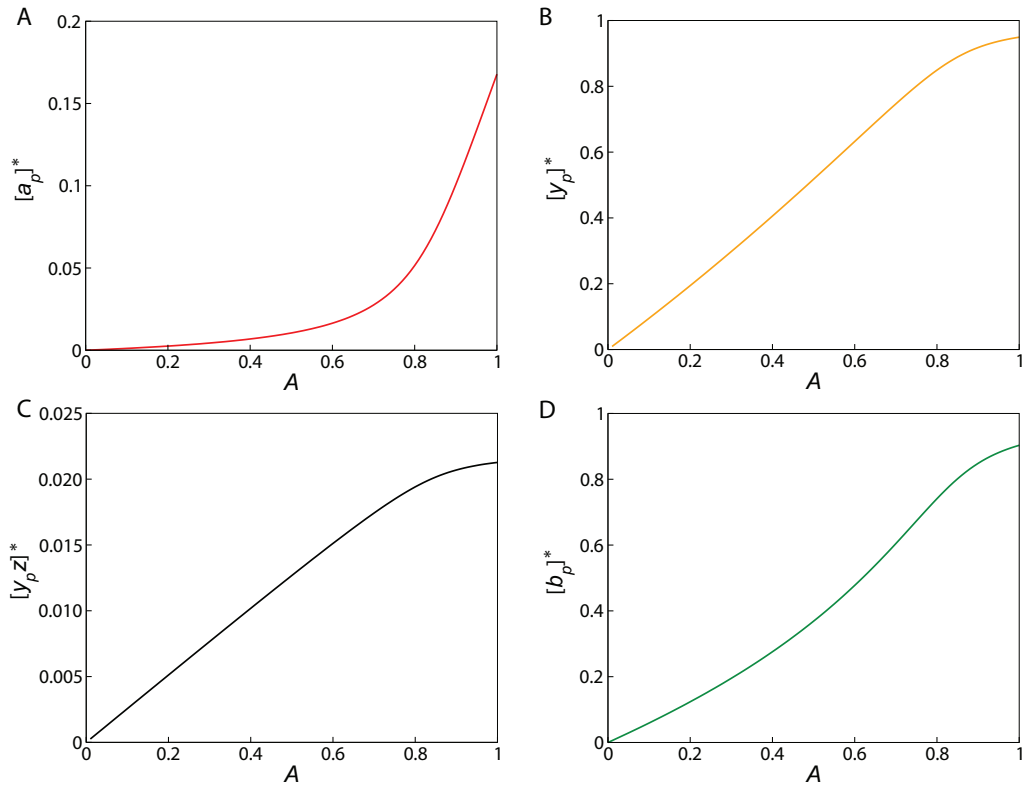


**Figure A.2.:** Steady-state concentrations of individual proteins and CheY-P/CheZ pairs for the whole-pathway model for Eq. A.9-A.12, as a function of the receptor complex activity  $A$ . Note the different scales of the vertical axes.

$g_R = \gamma_R k_A$  and  $g_B = \gamma_B k_A ([b_p]^*/A)^2 \approx \gamma_B k_A$ , respectively. The approximation holds true as the steady-state value of the rescaled variable  $[b_p]^*$  scales roughly linearly with  $A$  and almost all CheB is phosphorylated at  $A = 1$ .

### A.3. TIME COURSES AND STEADY-STATE ASSUMPTION

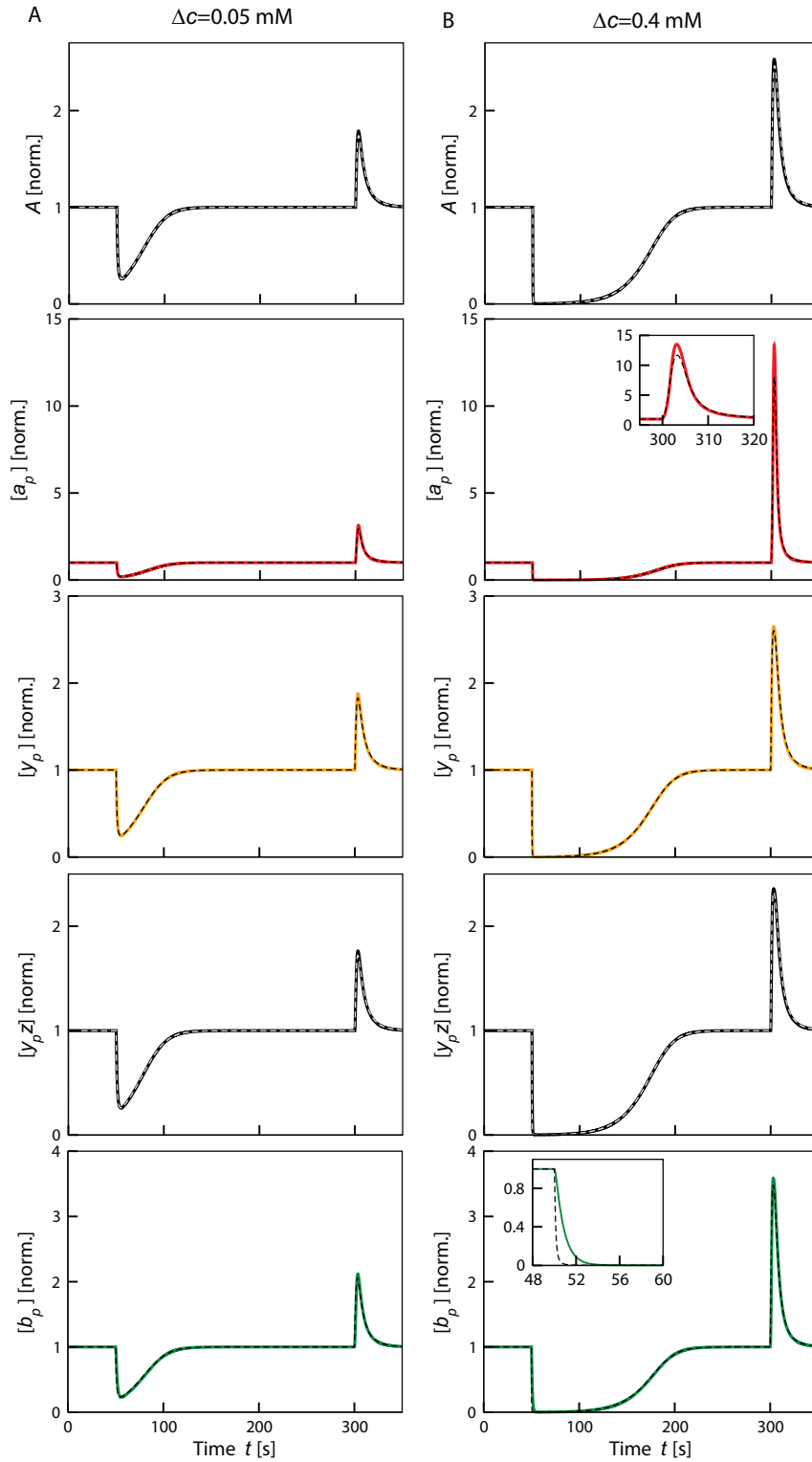


**Figure A.3.:** Time courses for the concentrations of phosphorylated proteins and CheY-P/CheZ pairs according to the whole-pathway model Eq. A.9-A.13, using ambient MeAsp concentration  $c_0 = 0.1$  mM and two different concentration step sizes,  $\Delta c = 0.05$  mM (column A) and  $\Delta c = 0.4$  mM (column B). Thick solid curves represent the model with parameter values as in table A.1, thin dashed lines assume the quasi steady-state for all phosphorylation reactions (phosphorylation and dephosphorylation kinetic constants in the model increased by a factor 20). Insets zoom into the dynamics around the addition or removal time, respectively. Concentrations were normalised to their respective adapted values.

## B. Additional data and best fit of dynamic MWC model

In Fig. B.1 we show additional dose-response data measured as described in chapter 2. The model in panel A is the dynamic MWC model from chapter 2. Panel B shows the best fit of the dynamic MWC model, where we used the demethylation rate constant  $g_B$ , the coefficients determining the receptor complex size as a linear function of ambient concentration, and the ligand dissociation constants of Tar and Tsr as fitting parameters. We found that parameters overall stay similar to the previously used parameters; in particular the ligand dissociation constants do not change significantly. The main difference is larger receptor complex sizes than determined by fitting the static MWC model to individual addition dose-response curves. To compensate for the larger complex sizes, the adaptation rates are also slightly increased, marking the trade-off between increased activity responses by larger complex sizes and reduced activity responses by faster adaptation (controlling for MeAsp concentration dynamics).

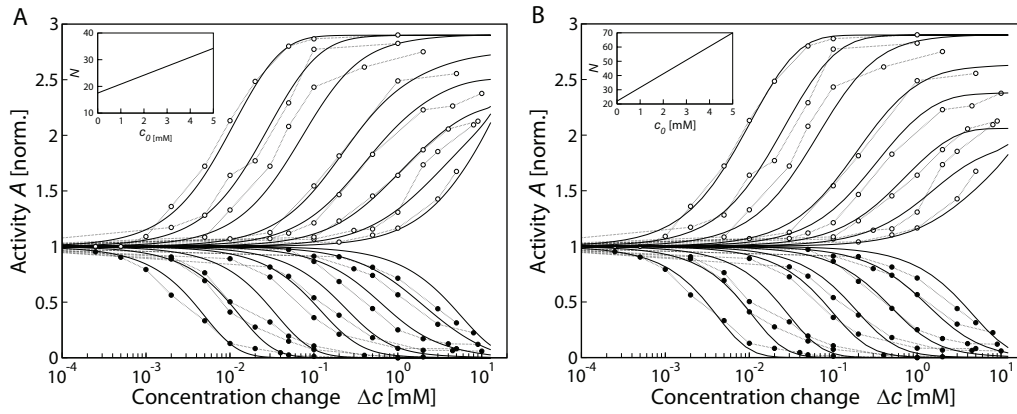


**Figure B.1.:** Dynamic MWC model. (A) Same as Fig. 2.4 in chapter 2 (main panel), however showing additional data. Shown are dose-response curves for wild-type cells to step changes of MeAsp concentration (after adaptation to ambient concentrations 0, 0.03, 0.1, 0.3, 0.5, 1, 2 and 5 mM). Symbols represent averaged response from FRET data as measured by Sourjik and Berg (2002b). Filled and open circles correspond to response to addition and removal of attractant, respectively. Solid lines represent the dynamic MWC model of mixed Tar/Tsr-receptor complexes, including ligand rise (addition) and fall (removal), as well as adaptation (receptor methylation) dynamics. (B) Best global fit of dynamic MWC model with fitting parameters  $g_B=0.127 \text{ s}^{-1}$ ,  $K_a^{\text{off}}=0.02 \text{ mM}$ ,  $K_a^{\text{on}}=0.50 \text{ mM}$ ,  $K_s^{\text{off}}=216 \text{ mM}$ ,  $K_s^{\text{on}}=10^6 \text{ mM}$ , as well as  $a_0 = 22$  and  $a_1=9.6 \text{ mM}^{-1}$  for the total receptor complex size  $N = a_0 + a_1 c_0$ .

## C. Unsuitable receptor signalling models

We tested four alternative models for receptor signalling in an attempt to find a model, which describes the gradually reduced response amplitudes upon MeAsp removals at increasing ambient concentrations (cf. Fig. 2.4 in chapter 2) without relying on adaptation and MeAsp dynamics. Dose-response curves for each model are shown in Fig. C.1. We found none of the models produced a satisfying fit to the experimental data.

### C.1 Saturation model

---

While ligand dissociation constants for the Tar receptor were previously determined from FRET data by Keymer et al. (2006), slightly different values may lead to saturation of Tar receptors at smaller concentrations of MeAsp and reduced response amplitudes. Figure C.1 A shows a fit of the static MWC model to addition as well as removal data. We fitted the parameters of the linear relationship between the receptor complex size and ambient concentration  $c_0$ , as well as the ligand dissociation constants for the Tar receptor,  $K_a^{\text{on}}$  and  $K_a^{\text{off}}$ . We find an unsatisfying fit, especially for the response to addition of MeAsp. Furthermore, the determined receptor complex size decreases with ambient concentration (see *Inset*). This contradicts experiments which indicate an increasing receptor complex size (Endres et al., 2008), as well as stabilisation of polar receptor clusters with increasing receptor methylation level (corresponding to increasing ambient concentration; Shiomi et al., 2005).

### C.2 Imprecise adaptation model

---

Figure C.1 B shows the effect of imprecise adaptation on the response amplitudes. For simplicity, we assume a linear decline of the adapted activity  $A^*(c_0)$  with increasing ambient concentration  $c_0$ , with  $A^*(0) = 1/3$  and a 20 percent imprecision at concentration 10 mM (see *Inset*). We observe that imprecise adaptation has only a small effect on the response

amplitudes. Furthermore, imprecise adaptation tends to increase response amplitudes at high ambient concentrations due to normalisation by a decreasing value of  $A^*(c_0)$ .

### C.3 Phase-separation model

---

In this model, a fraction  $w$  of mixed receptor complexes composed of Tar and Tsr receptors form homogeneous receptor complexes of only Tar and only Tsr receptors at high ambient concentrations. This separation reduces activity amplitudes at concentrations below the ligand dissociation constant  $K_s^{\text{off}}$  for Tsr, as complexes of Tsr do not contribute to the response. The total activity from mixed and homogeneous receptor complexes is

$$A = [1 - w(c_0)] A^{\text{mixed}} + w(c_0) (\nu_a A^{\text{Tar}} + \nu_s A^{\text{Tsr}}). \quad (\text{C.1})$$

The individual activities of mixed,  $A^{\text{mixed}}$ , and homogeneous receptor complexes of Tar,  $A^{\text{Tar}}$ , and Tsr,  $A^{\text{Tsr}}$ , were calculated according to the static MWC model. Mixed receptor complexes are composed of Tar and Tsr with ratio  $\nu_a : \nu_s = 1:1.4$ . Homogeneous receptor complexes of Tar and Tsr, respectively, have the same ratio. The resulting dose-response curves for this model are shown in Fig. C.1C, assuming the probability of separation  $w(c_0)$  from the *Inset*. As the ambient concentration does not correspond nicely to the data points with decreasing response, we did not find a well-fitting function  $w(c_0)$ . Furthermore, this model predicts a smaller response to MeAsp when cells are pre-adapted to a ligand for which Tsr, but not Tar is sensitive (e.g. Serine). This contradicts experiments, which show that cells remain sensitive (Sourjik and Berg (2004) and Victor Sourjik, manuscript in preparation).

### C.4 Receptor lattice model

---

In the static MWC model the absolute cooperativity of the receptors in a complex results in a saturating response upon removal of attractant (cf. *Inset* of Fig. 2.4 in chapter 2). Here, we consider an Ising lattice of  $N_T$  two-state receptor trimers, where each trimer is coupled to neighbouring trimers with finite interaction strength. We ask if a weaker coupling between receptors can describe the dose-response data, and in particular the reduced response amplitudes for removals.

Figure C.1D shows dose-response curves for different interaction strengths. We find, that in order to describe the addition data, a strong interaction between neighbouring

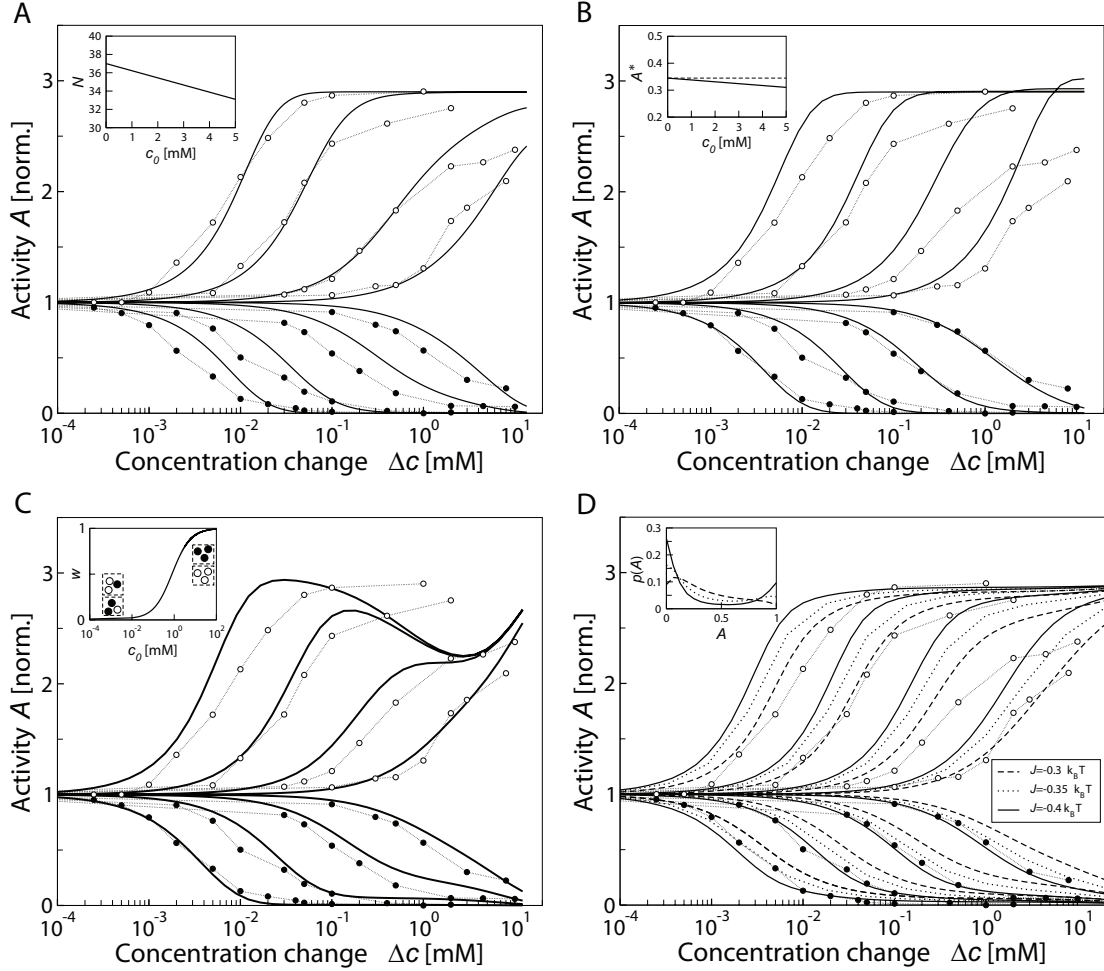


**Figure C.1.:** Alternative models for receptor signalling. (A) Saturation model. MWC model with optimised dissociation constants  $K_a^{\text{off}} = 0.056$  mM and  $K_a^{\text{on}} = 0.15$  mM. (A *Inset*) Total receptor complex size  $N = a_0 + a_1 c_0$  for fitted parameters  $a_0=37$  and  $a_1=-0.78$  mM $^{-1}$ . (B) Imprecise adaptation model. (B *Inset*) The steady-state activity decreases with ambient concentration,  $A^*(c_0)/A^*(0) = 1 - (0.2/10 \text{ mM})c_0$ , where 20% imprecision is reached at 10 mM. (C) Phase-separation model. Receptor complexes are found in separated complexes with probability  $w$  depending on the ambient concentration  $c_0$ . Receptor complex size is assumed constant,  $N = 18$ , for mixed and homogeneous receptor complexes. (C *Inset*) The probability  $w(c_0) = p_1 + p_2 \frac{c_0}{c_0 + p_3}$ , with  $p_1=0.01$ ,  $p_2=0.99$ ,  $p_3=0.8$  mM. (D) Receptor lattice model. Mixed trimers of Tar and Tsr dimers are arranged on a  $4 \times 4$  square lattice with periodic boundary conditions. The average activity of the lattice was calculated by exact enumeration. An attractive interaction between neighbouring trimers in the same state was assumed, with interaction energy  $J=-0.4 k_B T$  (solid line),  $J=-0.35 k_B T$  (dotted line), and  $J=-0.3 k_B T$  (dashed line). (D *Inset*) Corresponding distributions of activities from all states (lattice configurations) when adapted to zero ambient concentration.



trimers has to be assumed. In this limit, the lattice model resembles the MWC model where all lattice sites are infinitely strongly coupled with all other receptors. In the *Inset* of Fig. C.1D we show the activity distribution from all lattice states. As expected, the distribution becomes increasingly bimodal around the two states with *all receptors on* and *all receptors off*.

In the following we describe the details of the model and our simulations. We used a 4-by-4 square lattice of mixed receptor trimers with periodic boundary conditions. Each trimer consisted of Tar and Tsr receptors with probabilities  $\nu_a$  and  $\nu_s$ , respectively, where  $\nu_a:\nu_s=1:1.4$  is the *in vivo* ratio of Tar and Tsr in a cell. The distribution of Tar and Tsr in trimers on the lattice was the same in all simulations. Furthermore, each trimer has only two states, *on* and *off*. We numerate all possible states of the whole lattice (in total  $n = 2^{16}$  states for a 4-by-4 lattice, i.e.  $N_T=16$  receptor trimers). Assuming the lattice is in equilibrium, we can calculate the distribution of individual lattice states, and hence the average activity of the lattice. The probability of each lattice state depends on its energy, which has a contribution from the free-energy difference between the *on* and *off* states of each trimer and from the interaction between neighbouring trimers. The free-energy difference of trimer  $j$  is computed according to the MWC model

$$F^j = \epsilon(m^j) + \sum_{l=1}^3 \ln \left( \frac{1 + c/K_l^{\text{off}}}{1 + c/K_l^{\text{on}}} \right), \quad (\text{C.2})$$

where the index  $l = a, s$  describes the receptor type, Tar or Tsr, within a trimer. The average methylation level of receptors in a trimer  $j$  is denoted by  $m^j$ . The methylation energy is  $\epsilon(m^j) = 3 \cdot (1 - 0.5 m^j)$ .

The interaction energy between neighbouring trimers depends on their respective states. If they are in the same state (both *on* or both *off*), we assign the interaction energy  $J$ , if they are in different states, we assign the interaction energy  $-J$ . The total energy  $E_k$  of a lattice state  $k$  is determined by summing over all free-energy differences of individual trimers and interaction energies between neighbouring trimers.

The methylation level  $m^j$  of each trimer  $j$  cannot be calculated analytically due to the finite coupling strength between receptor trimers, and hence was determined numerically using our adaptation model

$$\frac{dm^j}{dt} = g_R(1 - A^j) - g_B(A^j)^3. \quad (\text{C.3})$$

## APPENDIX C. UNSUITABLE RECEPTOR SIGNALLING MODELS

---

According to this model, the methylation level  $m^j$  of the trimer  $j$  depends on its average activity

$$A^j = \frac{1}{Z} \sum_{k=1}^n s_k^j e^{-E_k}, \quad (\text{C.4})$$

where  $Z = \sum_k e^{-E_k}$  is the partition function, i.e. the sum over all lattice states and  $s_k^j$  is the state ( $1=on$ ,  $0=off$ ) of trimer  $j$  in lattice state  $k$ . The steady-state of Eq. C.3 determines the methylation level of each trimer, and therefore the adapted free-energy difference  $\epsilon(m^j)$  in Eq. C.2. The average activity of the whole lattice is determined by calculating the average trimer activity

$$A = \frac{1}{N_T} \sum_{j=1}^{N_T} A^j, \quad (\text{C.5})$$

where  $N_T$  is the number of trimers on the lattice.

## D. Parameters for static and dynamic MWC model

In Tab. D.1, we list all parameters of the static and dynamic MWC model used for Fig. 2.2-2.9 in chapter 2 and Fig. B.1 A, as well as Fig. B.1 B and C.1 A in Appendices B and C, respectively.

**Table D.1.:** Fitting parameters for the static and dynamic MWC model. Parameters include dissociation constants for Tar and Tsr receptors in the *on* and *off* states, respectively,  $K_a^{\text{off}}$ ,  $K_a^{\text{on}}$ ,  $K_s^{\text{off}}$ ,  $K_s^{\text{on}}$  (Keymer et al., 2006), the parameters of the linear approximation of the dependence of the receptor complex size on ambient concentration,  $N(c_0) = a_0 + a_1 c_0$ , as well as methylation and demethylation constants,  $g_R$  and  $g_B$  in Eq. 2.6 in chapter 2, respectively. Fitted parameters are indicated by crosses.

Parameter	Fig. 2.2-2.9, B.1 A		Fig. B.1 B		Fig. C.1 A			
	static	dynamic	dynamic (best fit)	static (best fit)	dynamic (best fit)	static (best fit)		
$K_a^{\text{off}}$ [mM]	0.02		0.02		0.02	x	0.056	x
$K_a^{\text{on}}$ [mM]	0.5		0.5		0.50	x	0.15	x
$K_s^{\text{off}}$ [mM]	100		100		216	x	100	
$K_s^{\text{on}}$ [mM]	$10^6$		$10^6$		$10^6$	x	$10^6$	
$a_0$	17.5	x	17.5		22	x	37	x
$a_1$ [mM <sup>-1</sup> ]	3.35	x	3.35		9.6	x	-0.78	x
$g_R$ [s <sup>-1</sup> ]	N/A		0.0069		0.0079		N/A	
$g_B$ [s <sup>-1</sup> ]	N/A		0.11	x	0.127	x	N/A	

## E. Comparison of different adaptation models

In Fig. 2.11 in chapter 2 we compare different adaptation models to FRET data by collapsing the time courses, plotting the rate of activity change  $dA/dt$  as a function of the activity  $A$ . Here, we describe in detail the different models analysed. In all of the models we assume precise adaptation, i.e. that methylation and demethylation rates only depend on the receptor complex activity. For each adaptation model, we use a least-squares fit to the FRET data to determine the methylation and demethylation rate constants, assuming an adapted activity  $A^*=1/3$  and receptor complex size  $N = 17.8$ . The parameters and quality of fit  $\chi^2$  for each of the models are listed in Table E.1.

Our model Eq. 2.6 in chapter 2

$$\frac{dm}{dt} = g_R(1 - A) - g_B A^3 \quad (\text{E.1})$$

is denoted by “ $(1 - A), A^3$ ”, referring to the activity dependence of the methylation and demethylation rates, respectively. The best fit to the rate of activity change from FRET (fitting parameter  $g_R=0.0019 \text{ s}^{-1}$ , resulting in  $g_B=0.030 \text{ s}^{-1}$  and quality of fit  $\chi^2=0.0021$ ), and a representative time course for this model are shown in Fig. 2.11 A and B in chapter 2, respectively (red solid lines). Note that this model describes the experimental data well, even at high activities. This model also shows a strong asymmetry in the time course with slow adaptation to addition and rapid adaptation to removal of MeAsp (cf. Fig. 2.7 in chapter 2).

We considered a variation of this model, denoted by “ $(1 - A), A^2$ ”, without cooperativity of CheB-P molecules,

$$\frac{dm}{dt} = g_R(1 - A) - g_B A^2, \quad (\text{E.2})$$

where only one CheB-P molecule is necessary for demethylation of a receptor. Together

**Table E.1.:** Parameters of the adaptation models when fitted to the rate of activity change from FRET shown in Fig. 2.11 A in chapter 2. The size of receptor complexes was assumed to be  $N = 17.8$  in all models. <sup>a</sup>  $K_1 = K_r/[T]$  and  $K_2 = K_b/[T]$ , where  $K_r=0.39 \mu\text{M}$  and  $K_b=0.54 \mu\text{M}$  are taken from Emonet and Cluzel (2008). <sup>b</sup>  $K_2 = K_b/[T]$  with  $K_b=1.25 \mu\text{M}$  (Barkai and Leibler, 1997). The concentration of receptors is  $[T]=17 \mu\text{M}$ .

Adaptation model	$g_R$ (fitted)	other parameters	$\chi^2$
“(1 - A), $A^3$ ”	0.0019 s <sup>-1</sup>	$g_B=0.030 \text{ s}^{-1}$	0.0021
“(1 - A), $A^2$ ”	0.0031 s <sup>-1</sup>	$g_B=0.017 \text{ s}^{-1}$	0.0022
“( $\frac{1-A}{1-A+K_1}$ , $\frac{A}{A+K_2}$ )”	0.0188 s <sup>-1</sup>	$g_B=0.020 \text{ s}^{-1}$ $K_1= 0.0229^a$ $K_2= 0.0318^a$	0.0036
“( $\frac{1-A}{1-A+K_1}$ , $\frac{A^2}{A+K_2}$ )”	0.0046 s <sup>-1</sup>	$g_B=0.014 \text{ s}^{-1}$ $K_1= 0.0229^a$ $K_2= 0.0318^a$	0.0025
“const, $\frac{A}{A+K_2}$ ”	0.00318 s <sup>-1</sup>	$g_B=0.014 \text{ s}^{-1}$ $K_2= 0.0735^b$	0.0032

with one factor  $A$  from the activity of receptors, this leads to a demethylation rate proportional to  $A^2$ . While this model is almost as well-suited to describe the rate of activity change from FRET as our main model (fitting parameter  $g_R=0.0031 \text{ s}^{-1}$ ;  $g_B=0.017 \text{ s}^{-1}$ ,  $\chi^2=0.0022$ ; see Fig. 2.11 A in chapter 2), the asymmetry of adaptation to addition and removal of MeAsp is less pronounced (Fig. 2.11 B in chapter 2). Fitting dose-response data using this adaptation model resulted in adaptation rates which were much higher than observed in FRET time courses.

Furthermore, the model denoted by “(1 - A),  $A$ ” without CheB-P feedback (Endres and Wingreen, 2006; Hansen et al., 2008; Vladimirov et al., 2008; Kalinin et al., 2009)

$$\frac{dm}{dt} = g_R(1 - A) - g_B A \quad (\text{E.3})$$

yields the fitting parameter  $g_R=0.0048 \text{ s}^{-1}$ , resulting in  $g_B=0.0091 \text{ s}^{-1}$  and quality of fit  $\chi^2=0.0025$ . Both, the fit of this model to the rate of activity change from FRET, and time courses, are described worse than with the other two models.

Another class of adaptation models was proposed by Emonet and Cluzel (2008), who introduced the idea of ultrasensitivity to the adaptation dynamics of CheR and CheB-P. We denote by “(1 - A)/(1 - A +  $K_1$ ),  $A/(A + K_2)$ ” the following model

$$\frac{dm}{dt} = g_R \frac{1 - A}{1 - A + K_1} - g_B \frac{A}{A + K_2}. \quad (\text{E.4})$$

## APPENDIX E. COMPARISON OF DIFFERENT ADAPTATION MODELS

---

In this model, CheR (CheB) methylates (demethylates) inactive (active) receptors with Michaelis-Menten-type kinetics with Michaelis-Menten constant  $K_1$  ( $K_2$ ). There is no CheB-P feedback on the demethylation rate. If  $K_1$  and  $K_2$  are small, the adaptation rate depends only weakly on the receptor activity. This results in long adaptation (relaxation) times, as well as strong sensitivity to protein fluctuations of either CheR or CheB through rates  $g_R$  and  $g_B$ . We used  $K_1 = K_r/[T] = 0.0229$  and  $K_2 = K_b/[T] = 0.0318$ , where we took  $K_r$  and  $K_b$  from Emonet and Cluzel (2008) and the concentration of receptors is  $[T]=17 \mu\text{M}$ . As shown in Fig. 2.11 A in chapter 2, the model without CheB-P feedback “ $(1-A)/(1-A+K_1), A/(A+K_2)$ ” does not describe the rate of activity change from FRET (fitting parameter  $g_R=0.0188 \text{ s}^{-1}$ ;  $g_B=0.020 \text{ s}^{-1}$ ,  $\chi^2=0.0036$ ). Furthermore, the time course shown in panel B looks qualitatively different from experimental time courses (cf. Fig. 2.7 in chapter 2).

Adding CheB-P feedback introduces another factor  $A$  in the demethylation rate. We denote this model by “ $(1-A)/(1-A+K_1), A^2/(A+K_2)$ ”, which corresponds to

$$\frac{dm}{dt} = g_R \frac{1-A}{1-A+K_1} - g_B \frac{A^2}{A+K_2}. \quad (\text{E.5})$$

This model fits the FRET activity change in Fig. 2.11 A in chapter 2 relatively well (fitting parameter  $g_R=0.0046 \text{ s}^{-1}$ ;  $g_B=0.014 \text{ s}^{-1}$ ,  $\chi^2=0.0025$ ). However, this model is not very different from the simpler model “ $(1-A), A^2$ ”, as the CheB-P feedback introduces a strong activity dependence.

In the model suggested by Barkai and Leibler (1997) CheR methylation does not depend on the activity state of receptors, and hence active, as well as inactive receptors get methylated. The kinetics of the methylation level is described by

$$\frac{dm}{dt} = g_R - g_B \frac{A}{A+K_2}, \quad (\text{E.6})$$

where the parameter value  $K_2 = K_b/[T]=0.074$  with  $K_b=1.25 \mu\text{M}$  (Barkai and Leibler, 1997), and  $[T]$  as above. Note that this model is a special case of above model “ $(1-A)/(1-A+K_1), A/(A+K_2)$ ” with  $K_1=0$ . Fitting to the FRET activity change yields  $g_R=0.00318 \text{ s}^{-1}$ , resulting in  $g_B=0.014 \text{ s}^{-1}$  and quality of fit  $\chi^2=0.0032$ . The predicted data collapse, as well as time courses are very similar to the model “ $(1-A)/(1-A+K_1), A/(A+K_2)$ ”, and is therefore not plotted in Fig. 2.11 in chapter 2.

## F. Analysis of adaptation noise

The receptor methylation level is subject to fluctuations due to the random nature of methylation and demethylation events. However, the adaptation dynamics also filters fluctuations in ligand concentration (translated into fluctuations of the receptor activity), averaging over and smoothing high-frequency noise by its slower dynamics. Here, we estimate the variance of the methylation level of a receptor complex due to these two noise sources. Equation 2.6 in chapter 2 describes the deterministic kinetics of the average methylation level of receptors in a mixed receptor complex,

$$\frac{dm}{dt} = g_R(1 - A) - g_B A^3. \quad (\text{F.1})$$

Now, we consider the kinetics of the total methylation level of a receptor complex. The total methylation level  $M$  is the sum of the individual methylation levels  $m_i$  of all receptors in a complex,  $M = \sum_{i=1}^N m_i$ , with  $N$  the number of receptors per complex. The rate of change of the total methylation level is

$$\frac{dM}{dt} = N_R k_R (1 - A) - N_B k_B A^3, \quad (\text{F.2})$$

where we explicitly indicated the number of the modifying CheR and CheB-P molecules,  $N_R$  and  $N_B$ , respectively. The modification rates for a single receptor are related to the rates for a receptor complex via  $g_R = N_R k_R / N$  and  $g_B = N_B k_B / N$ , respectively. To describe fluctuations about the mean total methylation level due to methylation and demethylation events, we introduce the noise  $\eta(t)$  and write

$$\frac{dM}{dt} = N_R k_R (1 - A) - N_B k_B A^3 + \eta(t). \quad (\text{F.3})$$

We assume  $\eta(t)$  is the sum of individual noise terms contributed from each modifying enzyme CheR and CheB-P acting on groups of receptors, so-called assistance neighbour-

## APPENDIX F. ANALYSIS OF ADAPTATION NOISE

---

hoods (Li and Hazelbauer, 2005; Endres and Wingreen, 2006; Hansen et al., 2008),

$$\eta(t) = \sum_{i=1}^{N_R} \eta_{R(i)}(t) + \sum_{i=1}^{N_B} \eta_{B(i)}(t), \quad (\text{F.4})$$

where  $\eta_{R(i)}$  and  $\eta_{B(i)}$  are independent Gaussian white noises with zero mean  $\langle \eta_{R(i)}(t) \rangle = \langle \eta_{B(i)}(t) \rangle = 0$ , autocorrelations  $\langle \eta_{R(i)}(t) \eta_{R(i)}(t') \rangle = q_R \cdot \delta(t - t')$  and  $\langle \eta_{B(i)}(t) \eta_{B(i)}(t') \rangle = q_B \cdot \delta(t - t')$ , and vanishing cross-correlations. To estimate the noise intensities  $q_R$  and  $q_B$ , we assume that the number of methyl groups, which are added (removed) by each enzyme molecule CheR (CheB-P) in a time interval, are Poisson distributed, i.e. their variance equals the mean number of added (removed) methyl groups. Therefore, the noise intensity  $q_R$  associated with each CheR molecule is determined by its mean rate of methylation,

$$q_R = k_R(1 - A^*). \quad (\text{F.5})$$

Similarly, the noise intensity  $q_B$  for demethylation is

$$q_B = k_B A^{*3}, \quad (\text{F.6})$$

where we only consider noise from one molecule of CheB-P. We are interested in the steady-state fluctuations of the total methylation level. Therefore, we linearise Eq. F.2 around the steady state to obtain the kinetics of the deviation  $\delta M$  from the mean methylation level

$$\frac{d(\delta M)}{dt} = - \left( N_R k_R + 3 N_B k_B A^{*2} \right) \delta A + \eta(t) \quad (\text{F.7})$$

$$= - \left( N_R k_R + 3 N_B k_B A^{*2} \right) \left( \frac{\partial A}{\partial F} \right) \left( \frac{\partial F}{\partial M} \cdot \delta M + \frac{\partial F}{\partial c} \cdot \delta c \right) + \eta(t). \quad (\text{F.8})$$

In the second step, we used that the receptor complex activity is subject to fluctuations from the methylation level, as well as the ligand concentration. The derivative of receptor complex activity with respect to the free-energy difference (at steady state) is given by

$$\frac{\partial A}{\partial F} = -A^*(1 - A^*). \quad (\text{F.9})$$



---

The total methylation level of a receptor complex enters the free-energy difference through

$$F = \underbrace{N - \frac{1}{2}M}_{=\sum_{i=1}^N (1 - \frac{1}{2}m_i)} + \nu_a N \ln \left( \frac{1 + c/K_a^{\text{off}}}{1 + c/K_a^{\text{on}}} \right) + \nu_s N \ln \left( \frac{1 + c/K_s^{\text{off}}}{1 + c/K_s^{\text{on}}} \right), \quad (\text{F.10})$$

where  $m_i$  are the methylation levels of receptors  $i$ . Therefore, the derivative of the free-energy difference  $F$  with respect to  $M$  is given by

$$\frac{\partial F}{\partial M} = -\frac{1}{2}. \quad (\text{F.11})$$

The derivative of the free-energy difference  $F$  with respect to  $c$  is given by

$$\frac{\partial F}{\partial c} = \nu_a N \left( \frac{1}{c + K_a^{\text{off}}} - \frac{1}{c + K_a^{\text{on}}} \right) + \nu_s N \left( \frac{1}{c + K_s^{\text{off}}} - \frac{1}{c + K_s^{\text{on}}} \right) \equiv \mu. \quad (\text{F.12})$$

In summary, the kinetics of  $\delta M$  is determined by

$$\frac{d(\delta M)}{dt} = - \underbrace{\left( N_R k_R + 3N_B k_B A^{*2} \right)}_{\equiv \lambda} A^* (1 - A^*) \cdot \left( \frac{1}{2} \delta M - \mu \delta c \right) + \eta(t). \quad (\text{F.13})$$

To calculate the variance of the methylation level, we Fourier transform Eq. F.13,

$$-i\omega \delta \hat{M} = -\lambda \left( \frac{1}{2} \delta \hat{M} - \mu \delta \hat{c} \right) + \hat{\eta}, \quad (\text{F.14})$$

where the hat symbol denotes the Fourier transform. Hence, the fluctuations in methylation level and in concentration are correlated, as part of the fluctuations in methylation level are due to fluctuations in the concentration. The Fourier transform of the (time-dependent) fluctuations in methylation level is

$$\delta \hat{M} = \frac{\hat{\eta} + \lambda \mu \delta \hat{c}}{-i\omega + \lambda/2}. \quad (\text{F.15})$$

The power spectrum  $S_M$  of fluctuations in  $M$  is defined as the Fourier transform of the autocorrelation function  $\langle \delta M(0) \delta M(t) \rangle$  and is given by

$$S_M(\omega) = \frac{Q_M + \lambda^2 \mu^2 \langle |\delta c|^2 \rangle}{\omega^2 + \lambda^2/4}. \quad (\text{F.16})$$

## APPENDIX F. ANALYSIS OF ADAPTATION NOISE

---

Here,  $Q_M$  denotes the noise intensity of methylation and demethylation, and  $\lambda^2 \mu^2 \langle |\delta c|^2 \rangle$  is due to the uncertainty from the ligand concentration<sup>1</sup>, where we assumed the two contributions are independent. In this formula, we see explicitly the noise filtering of fluctuations in ligand concentration by the kinetics of the methylation level, given by the frequency-dependent factor.

In the following, we calculate the variance of the methylation level of a receptor complex only due to methylation and demethylation events. The variance of the activity of receptor complexes due to methylation, as well as ligand noise, will be considered in Appendix H. As  $\eta(t)$  is composed of independent white noises, its total noise intensity  $Q_M$  is the sum of the individual noise intensities,

$$Q_M = N_{RqR} + N_{BqB} = 2N_{RqR} = 2N_R k_R (1 - A^*). \quad (\text{F.18})$$

The last equality uses the fact that at steady state methylation and demethylation rates balance each other in Eq. F.2. To calculate the variance of the methylation level we need to integrate the power spectrum over all frequencies  $\omega$ ,

$$\langle \delta M^2 \rangle = \int \frac{d\omega}{2\pi} \frac{Q_M}{\omega^2 + \lambda^2/4} = \frac{Q_M}{\lambda}, \quad (\text{F.19})$$

and obtain

$$\begin{aligned} \langle \delta M^2 \rangle &= \frac{2N_{RqR}}{(N_R k_R + 3N_B k_B A^{*2}) A^* (1 - A^*)} = \frac{2g_R}{(g_R + 3g_B A^{*2}) A^*} \\ &= \frac{2}{A^* + 3(1 - A^*)} = 0.87. \end{aligned} \quad (\text{F.20})$$

Here, we used that the adapted activity is  $A^* \approx 1/3$ , and that the relation between the methylation and demethylation rate constants  $g_R$  and  $g_B$  is given by the steady state of

---

<sup>1</sup>Fluctuations of the ligand concentration characterised by  $\langle \delta c^2 \rangle$  can be quantified as presented in Berg and Purcell (1977) and Bialek and Setayeshgar (2005) by

$$\langle \delta c^2 \rangle = \frac{\alpha}{\pi a D \tau} \cdot c, \quad (\text{F.17})$$

which corresponds to the time-averaged low-frequency limit of the noise power spectrum (Bialek and Setayeshgar, 2005, 2008). The parameter  $a$  is the size of the ligand binding site of a receptor,  $D$  is the ligand diffusion constant, and  $\tau$  is an averaging time due to slower downstream reactions. The parameter  $\alpha$  is of the order one and depends on further receptor details (Bialek and Setayeshgar, 2005, 2008). Using  $\alpha \approx 1$ ,  $a=1$  nm,  $D=100$   $\mu\text{m}^2/\text{s}$ , a typical ligand concentration  $c = \sqrt{K_a^{\text{off}} K_a^{\text{on}}} = 0.1$  mM (Vladimirov et al., 2008), and  $\tau = 1/k_A = 0.1$  s corresponding to slow autophosphorylation of CheA, we obtain  $\langle \delta c^2 \rangle = 5 \cdot 10^{-6}$   $\text{mM}^2$ .

---

the methylation kinetics Eq. F.1,

$$g_B = g_R \frac{1 - A^*}{A^{*3}}. \quad (\text{F.21})$$

This result can be compared to results for other adaptation models previously reported in the literature. Hansen et al. (2008) use a linear dependence of methylation and demethylation rates on the receptor activity, instead of the nonlinear dependence in Eq. F.1,

$$\frac{dm}{dt} = g_R(1 - A) - g_B A. \quad (\text{F.22})$$

In an equivalent approach using assistance neighbourhoods as described above, the authors calculate the variance of the total methylation level to be

$$\langle \delta M^2 \rangle = \frac{1}{|\partial F / \partial M|} = 2. \quad (\text{F.23})$$

Hence, the variance of the total methylation level of a receptor complex is reduced for adaptation kinetics with strong activity dependence of the demethylation rate (Eq. F.1), compared to the linear adaptation model (Eq. F.22). The reason for this is the stronger negative feedback, leading to the rapid attenuation of fluctuations in the receptor complex activity. Mathematically, the prefactor of the linearised demethylation rate in Eq. F.20 leads to the reduction of the variance of the methylation level of the receptor complex.

## G. Weber's law for Tar and Tsr receptors

For the ambient concentrations of MeAsp used in the FRET experiments, the activity response and hence the threshold stimulus  $\Delta c_t$  is mainly determined by Tar receptors as detailed in chapter 3 (Eq. 3.7 and Fig. 3.2). However, at higher ambient concentrations MeAsp binding to Tsr becomes important and the threshold stimulus is given by

$$\Delta c_t = \frac{\Delta A/[NA^*(1 - A^*)]}{\nu_a \left( \frac{c_0}{c_0 + K_a^{\text{on}}} - \frac{c_0}{c_0 + K_a^{\text{off}}} \right) + \nu_s \left( \frac{c_0}{c_0 + K_s^{\text{on}}} - \frac{c_0}{c_0 + K_s^{\text{off}}} \right)} \cdot c_0. \quad (\text{G.1})$$

Figure G.1 shows the threshold stimulus for mixed Tar/Tsr receptor complexes, as well as the threshold stimuli for homogeneous Tar and Tsr receptor complexes as a function of the ambient concentration. The sizes of homogeneous Tar and Tsr receptor complexes were set equal to their respective fractions in the mixed receptor complexes. It is apparent that Tar receptors are responsible for the threshold stimulus at ambient concentrations below one milli-molar, as their threshold stimulus corresponds to the threshold stimulus for mixed receptor complexes. In that range homogeneous Tsr complexes have a much higher and constant threshold stimulus, reflecting the low affinity for MeAsp binding. In contrast, at high ambient concentrations the threshold stimulus for homogeneous Tsr receptor complexes equals the threshold stimulus for mixed receptor complexes. This reflects that Tar receptors are saturated and Tsr receptors are able to bind MeAsp.

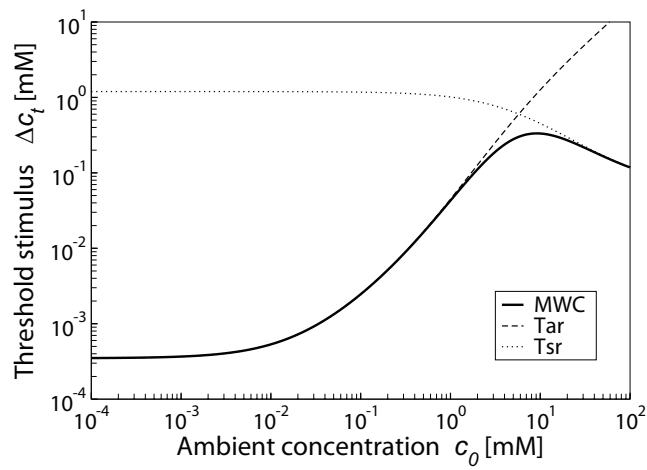


**Figure G.1.:** Threshold stimulus  $\Delta c_t$  as obtained by linear expansion of the receptor complex activity around the adapted activity  $A^*$  for threshold response  $\Delta A = 0.08 A^*$ . Shown are the threshold stimuli for mixed Tar/Tsr receptor complexes (MWC; thick solid line, cf. Fig. 3.2 in chapter 3), as well as those for homogeneous Tar and Tsr receptor complexes (dashed and dotted lines, respectively).

## H. Derivation of the threshold activity from signalling noise

The activity threshold  $\Delta A$  defined in Fig. 3.1 in chapter 3 defines the minimum activity response to a stimulus in order for the cell to distinguish the stimulus reliably from the background noise of the activity. Here, we estimate the magnitude of the threshold, assuming that the response  $\Delta A$  due to a stimulus needs to be above random fluctuations of the activity. We focus on noise from stochastic methylation and demethylation events by individual CheR and CheB-P molecules (Hansen et al., 2008), as well as ligand binding noise.

Fluctuations of the receptor methylation level, as well as ligand concentration, translate into fluctuations of the receptor activity. We first derive the variances of the methylation level and ligand concentration. Next, we calculate the variance of the activity of an individual receptor complex. Finally, we estimate the variance of the activity from all receptor complexes in a cell due to both sources of noise.

**Variance of methylation level.** As derived in Appendix F, Eq. F.1-F.15, the Fourier transform of fluctuations in the receptor complex methylation level  $\delta M$  are given by

$$\delta \hat{M} = \frac{\hat{\eta} + \lambda \mu \delta \hat{c}}{-i\omega + \lambda/2}, \quad (\text{H.1})$$

where  $\lambda = (N_R k_R + 3N_B k_B A^{*2}) A^*(1 - A^*)$  is the time scale of adaptation and  $\mu = \nu_a N \left( \frac{1}{c+K_a^{\text{off}}} - \frac{1}{c+K_a^{\text{on}}} \right) + \nu_s N \left( \frac{1}{c+K_s^{\text{off}}} - \frac{1}{c+K_s^{\text{on}}} \right)$  is the derivative of the receptor free-energy difference with respect to concentration.

**Time-averaged and total noise.** If for a moment we just consider fluctuations  $\eta(t)$  due to the methylation and demethylation enzymes, we can estimate the time scale of this noise by looking at time-averaged noise and total noise. The power spectrum  $S_M$  of fluctuations

---

in  $M$  only due to  $\eta(t)$ , which is defined as the Fourier transform of the autocorrelation function  $\langle \delta M(0) \delta M(t) \rangle$  is

$$S_M(\omega) = \frac{Q_M}{\omega^2 + \lambda^2/4}. \quad (\text{H.2})$$

The noise intensity  $Q_M$  of  $\eta(t)$  is Eq. F.18

$$Q_M = N_R q_R + N_B q_B = 2N_R q_R. \quad (\text{H.3})$$

If there is averaging of the noise by down-stream signalling over a typical duration time  $\tau$ , longer than the correlation time  $\tau_c = 2\lambda^{-1}$  of the noise, we can approximate the variance of the methylation level entering those reactions to lowest order by

$$\langle \delta M^2 \rangle \approx \frac{S_M(\omega \rightarrow 0)}{\tau} = \frac{8N_R q_R}{\lambda^2 \tau}, \quad (\text{H.4})$$

as only low frequencies of the methylation noise would contribute to the noise in the down-stream processes (e.g. activity from FRET). We calculated the correlation time for the methylation noise and obtain

$$\tau_c = \frac{2}{\lambda} = \frac{2}{(N_R k_R + 3N_B k_B A^{*2}) A^* (1 - A^*)} = \frac{2}{N (g_R + 3g_B A^{*2}) A^* (1 - A^*)} \approx 21 \text{ s}. \quad (\text{H.5})$$

This is much longer than the typical time-scales of down-stream reactions, and therefore we need to calculate the variance of methylation noise by integrating the power spectrum over all frequencies,

$$\langle \delta M^2 \rangle = \int \frac{d\omega}{2\pi} S_M(\omega) = \frac{Q_M}{\lambda}, \quad (\text{H.6})$$

and obtain for the variance of the total methylation level

$$\langle \delta M^2 \rangle = \frac{2N_R q_R}{(N_R k_R + 3N_B k_B A^{*2}) A^* (1 - A^*)} = \frac{2g_R}{(g_R + 3g_B A^{*2}) A^*}. \quad (\text{H.7})$$

For our parameters the variance of methylation level only due to the dynamics of the methylation and demethylation enzymes is  $\langle \delta M^2 \rangle \approx 0.87$ .

**Variance of ligand concentration.** The variance of the ligand concentration is given by (Berg and Purcell, 1977; Bialek and Setayeshgar, 2005)

$$\langle \delta c^2 \rangle = \frac{\alpha}{\pi a D \tau} \cdot c, \quad (\text{H.8})$$

## APPENDIX H. DERIVATION OF THE THRESHOLD ACTIVITY FROM SIGNALLING NOISE

---

where  $a$  is the size of the ligand binding site of a receptor,  $D$  is the ligand diffusion constant, and  $\tau$  is an averaging time due to slower downstream reactions. The parameter  $\alpha$  is of the order one and depends on further receptor details. It is reduced for cooperative ligand binding by receptors (Bialek and Setayeshgar, 2008) and is increased when ligand, once receptor-bound, is allowed to rebind to the same or a different receptor again (Bialek and Setayeshgar, 2005; Endres and Wingreen, 2008). The latter effect is enhanced by the close proximity of receptors in cell-polar clusters. Using  $\alpha \approx 1$ ,  $a=1$  nm,  $D=100$   $\mu\text{m}^2/\text{s}$ , a typical ligand concentration  $c = \sqrt{K_a^{\text{off}}K_a^{\text{on}}} = 0.1$  mM (Vladimirov et al., 2008), and  $\tau = 1/k_A = 0.1$  s corresponding to slow autophosphorylation of CheA, we obtain  $\langle \delta c^2 \rangle = 5 \cdot 10^{-6}$  mM<sup>2</sup>.

**Variance of the activity of one receptor complex.** The fluctuations of the activity  $\delta A$  of one receptor complex around its adapted state due to fluctuations of the methylation level and ligand binding are given by

$$\delta A = \frac{\partial A}{\partial M} \delta M + \frac{\partial A}{\partial c} \delta c. \quad (\text{H.9})$$

Fourier transforming this equation and using Eq. H.1, we find

$$\delta \hat{A} = -A^*(1 - A^*) \left( -\frac{1}{2} \frac{\hat{\eta} + \lambda \mu \delta \hat{c}}{-i\omega + \lambda/2} - \mu \delta \hat{c} \right) = A^*(1 - A^*) \frac{\hat{\eta}/2 + i\omega \mu \delta \hat{c}}{-i\omega + \lambda/2} \quad (\text{H.10})$$

The power spectrum of the activity is then

$$S_A(\omega) = (A^*(1 - A^*))^2 \frac{Q_M/4 + (\omega \mu)^2 S_c(\omega)}{\omega^2 + \lambda^2/4}, \quad (\text{H.11})$$

where we assumed that the fluctuations  $\eta(t)$  due to the action of methylation and demethylation enzymes and ligand binding  $\delta c(t)$  are uncorrelated. The variance of the activity of a receptor complex is the integral over the spectrum,

$$\langle \delta A^2 \rangle \approx (A^*(1 - A^*))^2 (Q_M/(4\lambda) + \mu^2 \langle \delta c^2 \rangle). \quad (\text{H.12})$$

For the integration of the second term we used that the ligand noise spectrum is mostly flat up to high frequencies, where it falls off, due to the fast binding dynamics. On the other hand, the  $\omega$ -dependent pre-factor varies only at low frequencies and is one at high frequencies. Hence, we make a small error by neglecting the small interval where the  $\omega$ -



---

dependent pre-factor varies in the integration, as most of the contribution to the activity noise comes from high frequencies. Integrating the spectrum of the ligand noise yields the variance  $\langle \delta c^2 \rangle$ . Effectively, this treatment neglects the reduction of ligand fluctuations by the adaptation dynamics at low frequencies. The activity noise from stochastic methylation and demethylation events is independent of the size of the receptor complex, since CheR and CheB-P molecules act on groups of receptors (assistance neighbourhoods; Hansen et al., 2008). The activity noise from ligand binding is about an order of magnitude smaller than the contribution from methylation. For our parameters the variance of the activity of a receptor complex due to methylation and ligand binding noise is

$$\langle \delta A^2 \rangle \approx 4/81 \cdot (0.189 + 0.015) = 0.01. \quad (\text{H.13})$$

**Variance of activity of all receptor complexes in a cell.** We assume that fluctuations from individual receptor complexes are independent. There are about 8,000 receptors (receptor dimers) per cell (Li and Hazelbauer, 2004). Assuming 20 receptors per receptor complex, there are approximately  $N_{\text{MWC}}=400$  receptor complexes. The normalised variance of the activity  $A_{\text{cell}}$  is then

$$\frac{\langle \delta A^2 \rangle_{\text{cell}}}{A_{\text{cell}}^2} = \frac{N_{\text{MWC}} \langle \delta A^2 \rangle}{(N_{\text{MWC}} A^*)^2} = \frac{\langle \delta A^2 \rangle}{N_{\text{MWC}} A^{*2}}. \quad (\text{H.14})$$

For our parameters this yields  $\langle \delta A^2 \rangle_{\text{cell}}/A_{\text{cell}}^2 \approx 0.0002$ , corresponding to a (normalised) standard deviation of  $\sqrt{\langle \delta A^2 \rangle_{\text{cell}}}/A_{\text{cell}} \approx 0.015$ , and an activity threshold

$$\Delta A/A^* = \sqrt{2 \langle \delta A^2 \rangle_{\text{cell}}}/A_{\text{cell}} \approx 0.021. \quad (\text{H.15})$$

This is a lower bound for the activity threshold as it was derived by only considering fluctuations from stochastic methylation and demethylation events, as well as ligand binding events. Other sources of noise, e.g. from stochastic phosphorylation and dephosphorylation events, are likely to further increase the threshold response. In chapter 2 we used  $\Delta A/A^*=0.08$ .

# I. Probing the adaptation dynamics using exponential ramps

Time-dependent concentrations can be used to probe the interplay of signalling and adaptation dynamics in the chemotaxis pathway. As shown by Block et al. (1983), exponential ramps, i.e. exponentially increasing or decreasing concentrations of attractant in time, lead to approximately constant (time-independent) rotational bias of the motor. Here, we consider exponential ramps  $c(t) = c_0 e^{\pm rt}$ , with the initial concentration  $c_0$  and rates  $+r$  and  $-r$  for up and down ramps, respectively. This time-dependent stimulus is the input to the dynamic MWC model with precise adaptation, whose receptor complex activity

$$A(m, c) = \frac{1}{1 + e^{F(m, c)}} \quad (\text{I.1})$$

is given in terms of the free-energy difference

$$F(m, c) = N \cdot \left[ 1 - 0.5m + \nu_a \ln \left( \frac{1 + c/K_a^{\text{off}}}{1 + c/K_a^{\text{on}}} \right) + \nu_s \ln \left( \frac{1 + c/K_s^{\text{off}}}{1 + c/K_s^{\text{on}}} \right) \right], \quad (\text{I.2})$$

depending on the time-dependent concentration  $c(t)$  and average receptor methylation level  $m(t)$  (cf. Eq. 3.5 in chapter 3).

Figure I.1 A shows simulated time courses. For slow ramp rates, the adaptation dynamics is able to catch up with the changing concentration, resulting in a new steady-state of the activity characterised by an approximately constant activity change. For high rates, the new steady-state is only valid for a short period of time. Specifically, for down ramps the activity subsequently goes back to the adapted pre-stimulus value, indicating that the free-energy change due to the adaptation dynamics becomes faster than the free-energy change due to concentration changes. This is expected as the concentration approaches zero, and the sensitivity of receptors to detect further concentration changes is impaired. For up ramps, after an initial drop the activity increases when the concentration increases

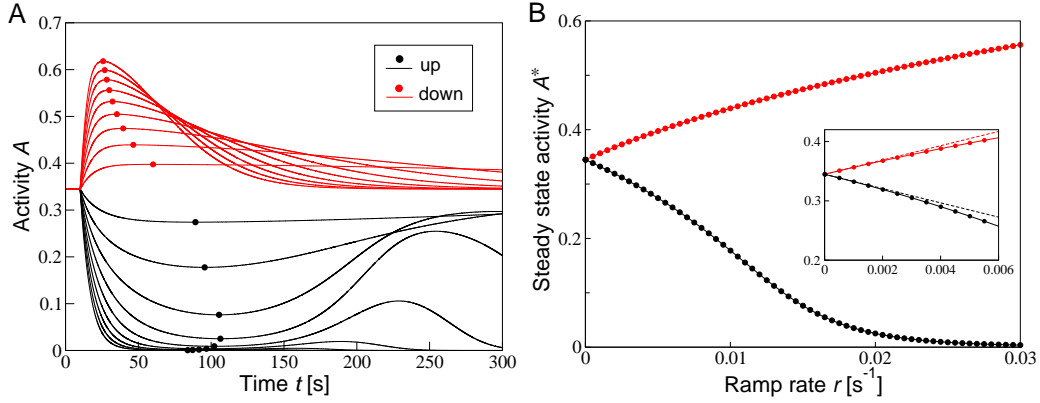


**Figure I.1.:** Receptor complex activity for exponential concentration ramps,  $c(t) = c_0 e^{\pm r t}$  with ramp rate  $\pm r$ . Shown are results for up ( $+r$ , black) and down ( $-r$ , red) ramps for initial concentration  $c_0=0.1$  mM. (A) Time courses of activity for ramps starting at  $t=10$  s with different rates  $r$ . Dots indicate the times when  $dA/dt = 0$  (steady-state) for the first time. (B) Steady-state activity as function of rate  $r$ . (B *Inset*) Same as B, only for small rates. The dashed lines represent the analytical result.

to values above the ligand dissociation constant of the *on* state of the Tar receptor,  $K_a^{\text{on}}$ , but below the ligand dissociation constant of the *off* state of the Tsr receptor,  $K_s^{\text{off}}$ . This is due to the low sensitivity of receptor complexes towards MeAsp at these concentrations. Ultimately, at very high MeAsp concentrations, Tsr starts to bind and the activity decreases again.

Figure I.1 B shows the steady-state activity, defined as the receptor complex activity when  $dA/dt=0$  is reached for the first time, as a function of the ramp rate. We do not find a threshold rate in the dynamic MWC model, below which the receptor complex activity remains at the pre-stimulus value as was indicated by early experiments (Block et al., 1983).

To obtain an additional insight, we analytically solve the dynamic MWC model for small deviations from the adapted activity  $A^*$ , e.g. valid for small ramp rates. For this calculation, we restrict the concentration to  $K_a^{\text{off}} \ll c \ll K_a^{\text{on}}$ . In this regime, the free-energy difference Eq. I.2 reduces to

$$F(m, c) = N \cdot \left[ 1 - 0.5m + \nu_a \ln \left( c / K_a^{\text{off}} \right) \right]. \quad (\text{I.3})$$

The rate of change of the free-energy difference is determined by the rates of change of the receptor methylation level  $m$  and the concentration  $c$ ,

$$\frac{dF}{dt} = \frac{\partial F}{\partial m} \frac{dm}{dt} + \frac{\partial F}{\partial \ln c} \frac{d \ln c}{dt} \quad (\text{I.4})$$

## APPENDIX I. PROBING THE ADAPTATION DYNAMICS USING EXPONENTIAL RAMPS

---

with the partial derivatives given by

$$\frac{\partial F}{\partial m} = -\frac{N}{2} \quad (\text{I.5})$$

$$\frac{\partial F}{\partial \ln c} = \frac{\nu_a N}{K_a^{\text{off}}}. \quad (\text{I.6})$$

We can approximate the deviation of the rate of change of the methylation level from zero (i.e., the steady-state) by linearisation

$$\frac{d(\delta m)}{dt} = (g_R + 3g_B A^{*2}) \delta A = (g_R + 3g_B A^{*2}) \frac{\partial A}{\partial F} F, \quad (\text{I.7})$$

where  $F = F - F^*$  is the deviation of the free-energy difference from its adapted value (corresponding to the adapted activity  $A^*$ ). Furthermore, the derivative of the exponential concentration  $c(t) = c_0 e^{\pm r t}$  is

$$\frac{d \ln c}{dt} = \pm r. \quad (\text{I.8})$$

Subsequently, we obtain the following dynamics for the deviation of the free-energy difference from steady-state

$$\frac{dF}{dt} = -\frac{F}{\tau} \pm br, \quad (\text{I.9})$$

where we introduced the abbreviations

$$\tau = \left[ \frac{N}{2} A^* (1 - A^*) (g_R + 3g_B A^{*2}) \right]^{-1} \quad (\text{I.10})$$

$$b = \frac{\nu_a N}{K_a^{\text{off}}} = \text{const.} \quad (\text{I.11})$$

Equation I.9 is solved by the function

$$F(t) = \pm \tau b r (1 - e^{\pm t/\tau}). \quad (\text{I.12})$$

For times  $t$  larger than the time scale  $\tau$ , i.e. after a transient period, this yields a time-independent change in the free-energy difference, which is proportional to the ramp rate

$$F(t) = \pm \tau b \cdot r \propto \pm r. \quad (\text{I.13})$$

This result indicates that in the limit of small deviations from steady-state, the activity assumes a new steady-state, shifted relative to its adapted pre-stimulus value when subject

---

to an exponential concentration ramp. Furthermore, the associated free-energy difference increases or decreases linearly with the rate  $r$  of the exponentially increasing or decreasing concentration, respectively. Consistent with our simulations, we do not obtain a threshold for the ramp rate, below which  $F \approx 0$  (cf. Fig. I.1 B, *Inset*).

# J. Response function and noise spectra for the full pathway model

## J.1 Stochastic differential equations

---

In chapter 4 we presented a simplified model of the chemotaxis pathway to illustrate signalling and noise transmission. Here, we discuss a model for the full signalling pathway and present the response functions and noise spectra. Equation 4.3 in chapter 4 describes the total signalling activity  $A_c$  of all receptor complexes in a cell in response to changes in the methylation level of the complexes and ligand concentration,

$$\frac{dA_c}{dt} = \sum_{i=1}^{N_c} \frac{\partial A}{\partial M} \frac{dM_j}{dt} + \frac{\partial A}{\partial c} \frac{dc_j}{dt} + \eta_{A_j}(t). \quad (\text{J.1})$$

The dynamics of the methylation level of a complex  $j$  is described by

$$\frac{dM_j}{dt} = \gamma_R(N - A_j) - \gamma_B A_j B_p^2 + \eta_{M_j}(t) = \gamma_R(N - A_j) - \frac{\gamma_B}{V_{\text{cell}}^2} A_j N_{B_p}^2 + \eta_{M_j}(t) \quad (\text{J.2})$$

Note that here we explicitly include the number of CheB-P molecules  $N_{B_p}$  in the demethylation term, with  $V_{\text{cell}}$  the cell volume (cf. Eq. 4.5 in chapter 4 and Eq. A.7 in Appendix A). We denote the activity of complex  $j$  by  $A_j$ . The dynamics of the concentration according to Eq. 4.4 in chapter 4 is

$$\frac{dc_j}{dt} = \frac{d\langle c \rangle}{dt} + \eta_{c_j}(t). \quad (\text{J.3})$$

In addition, we take into account phosphorylation and dephosphorylation of CheA, CheY and CheB, which are described by the following equations:

$$\begin{aligned} \frac{dN_{A_p}}{dt} = & A_c \left( \frac{k_A}{N_c N} \right) (N_{A,\text{tot}} - N_{A_p}) - \left( \frac{k_Y}{V_{\text{cell}}} \right) (N_{Y,\text{tot}} - N_{Y_p}) N_{A_p} + \\ & - \left( \frac{k_B}{V_{\text{cell}}} \right) (N_{B,\text{tot}} - N_{B_p}) N_{A_p} + \eta_{A,p}(t) + \eta_{A,Y_p}(t) + \eta_{A,B_p}(t) \end{aligned} \quad (\text{J.4})$$

$$\frac{dN_{Y_p}}{dt} = \left( \frac{k_Y}{V_{\text{cell}}} \right) (N_{Y,\text{tot}} - N_{Y_p}) N_{A_p} - k_{-Y} N_{Y_p} - \eta_{A,Y_p}(t) + \eta_{-Y_p}(t) \quad (\text{J.5})$$

$$\frac{dN_{B_p}}{dt} = \left( \frac{k_B}{V_{\text{cell}}} \right) (N_{B,\text{tot}} - N_{B_p}) N_{A_p} - k_{-B} N_{B_p} - \eta_{A,B_p}(t) + \eta_{-B_p}(t) \quad (\text{J.6})$$

with  $N_i$  the number of molecules of species  $i$  in a cell volume. These equations are similar to the model presented in Appendix A. Note, however, that we neglected the binding of CheY-P to its phosphatase CheZ (cf. Appendix A, Eq. A.3) for simplicity, and describe dephosphorylation of CheY-P by the effective dephosphorylation rate  $k_{-Y} N_{Y_p}$ . As shown in Appendix O, this simplification has no qualitative effect on the response function.  $\eta_{A,p}(t)$  describes the noise associated with CheA autophosphorylation,  $\eta_{A,B_p}(t)$  and  $\eta_{A,Y_p}(t)$  noise generated in phosphorylation of CheB and CheY by CheA, respectively, and  $\eta_{-B_p}(t)$  and  $\eta_{-Y_p}(t)$  the noise associated with dephosphorylation. Note that some noise terms appear in two equations. This is due to the fact that we assign noise terms to a specific process, e.g. phosphorylation of CheY by CheA. Hence, the corresponding noise term  $\eta_{A,Y_p}(t)$  appears in the dynamics of CheA-P and of CheY-P. As a positive fluctuation in the dynamics of CheA-P due to phosphorylation of CheY corresponds to a negative fluctuation in the dynamics of CheY-P, they appear with opposite signs. The noise intensities and parameter values of the model are summarised in Sec. J.6. Finally, the dynamics of the motor is described in terms of the probability of the tumbling mode  $P_t$

$$\frac{dP_t}{dt} = k_+(N_{Y_p})(1 - P_t) - k_-(N_{Y_p})P_t + \eta_{P_t}(t), \quad (\text{J.7})$$

where we use experimentally derived switching rates  $k_+$  and  $k_-$  as a function of CheY-P concentration (cf. next section and Fig. 4.1 in chapter 4).

---

## J.2 Model for motor switching

Turner et al. (1999) presented a model for motor switching to explain the observed motor switching rates. The model for motor switching is an MWC model, where 26 subunits

## APPENDIX J. RESPONSE FUNCTION AND NOISE SPECTRA FOR THE FULL PATHWAY MODEL

---

of the motor assume one of two states corresponding to CW and CCW rotation. While they bind the signalling molecule CheY-P independently of each other, the switch of states occurs cooperatively. The authors derive the overall rates of switching (averaging over all possible CheY-P occupancy states) as

$$k_+(Y_p) = k_+(0) \exp \left[ m_{\text{coop}} \ln \left( \frac{1 + \frac{\mu[Y_p]}{K_{\text{CCW}}}}{1 + \frac{Y_p}{K_{\text{CCW}}}} \right) \right] \quad (\text{J.8})$$

$$k_-(Y_p) = k_-(0) \exp \left[ m_{\text{coop}} \ln \left( \frac{1 + \frac{\mu[Y_p]}{K_{\text{CCW}}}}{1 + \frac{Y_p}{K_{\text{CW}}}} \right) \right], \quad (\text{J.9})$$

where  $m_{\text{coop}} = 26$  is the number of motor subunits,  $-k_B T \ln(\mu)$  is the free-energy difference of switching per molecule of CheY-P, and  $K_{\text{CCW}}$  and  $K_{\text{CW}}$  are the dissociation constants for binding CheY-P in the CCW and CW state, respectively.

Motor switching rates  $k_+$  and  $k_-$  have been derived experimentally as a function of the concentration of a signalling mutant CheY\*\*, which is constitutively active (Turner et al., 1999), as shown in Fig. 4.1 in chapter 4. To obtain the switching rates in terms of CheY-P, rather than signalling mutant CheY\*\*, we rescaled the dissociation constants of CheY binding to the motor such that the switching rates are equal, i.e. CW bias about 1/2, at CheY-P concentration  $3.2 \mu\text{M}$  (Cluzel et al., 2000). We fitted the above model to the experimental data in Fig. 4.1 and the CW bias at  $33^\circ\text{C}$  (Turner et al., 1999) and used the rates  $k_+$  and  $k_-$  in our full pathway model in Eq. J.7.

### J.3 Linearisation of the model

---

Similar to the presentation for the simplified model in chapter 4, we linearise Eq. J.1-J.7 and insert the Fourier transforms of the dynamical variables to obtain the Fourier transformed linear response functions  $\hat{\chi}_R(\omega)$  and noise spectra  $S_R(\omega)$  for the signalling



pathway. The linearised equations read

$$\frac{d}{dt}\delta A_c = -\sum_j \frac{\partial A}{\partial M} (\lambda_1 \delta A_j + \lambda_9 \delta N_{B_p}) + \frac{\partial A}{\partial c} \frac{d\delta c_j}{dt} + \frac{\partial A}{\partial M} \eta_{M_j}(t) + \eta_{A_j}(t) \quad (\text{J.10})$$

$$\frac{d}{dt}\delta N_{A_p} = \lambda_2 \delta A_c - \lambda_3 \delta N_{A_p} + \lambda_4 \delta N_{Y_p} + \lambda_{10} \delta N_{B_p} + \eta_{A_p}(t) + \eta_{A,Y_p}(t) + \eta_{A,B_p}(t) \quad (\text{J.11})$$

$$\frac{d}{dt}\delta N_{Y_p} = \lambda_5 \delta N_{A_p} - \lambda_6 \delta N_{Y_p} - \eta_{A,Y_p}(t) + \eta_{-Y_p}(t) \quad (\text{J.12})$$

$$\frac{d}{dt}\delta N_{B_p} = \lambda_{11} \delta N_{A_p} - \lambda_{12} \delta N_{B_p} - \eta_{A,B_p}(t) + \eta_{-B_p}(t) \quad (\text{J.13})$$

$$\frac{d}{dt}\delta P_t = \lambda_7 \delta N_{Y_p} - \lambda_8 \delta P_t + \eta_{P_t}(t) \quad (\text{J.14})$$

with linearised rate constants given in Table J.3.

## J.4 Response functions

The response functions can be calculated from the linearised equations J.10-J.14 without noise after inserting the Fourier transforms of the dynamical variables. The Fourier transformed response functions of CheA-P, CheY-P and the motor are

$$\hat{\chi}_{A_c}(\omega) = \frac{-i\omega N_c \frac{\partial A}{\partial c} - \lambda_9 N_c \frac{\partial A}{\partial M} \hat{\chi}_{N_{B_p}}(\omega)}{\lambda_1 \frac{\partial A}{\partial M} - i\omega} \quad (\text{J.15})$$

$$\begin{aligned} \hat{\chi}_{N_{A_p}}(\omega) = & \left( -i\omega \lambda_2 N_c \frac{\partial A}{\partial c} (\lambda_6 - i\omega) (\lambda_{12} - i\omega) \right) \cdot \\ & \left( \left( \lambda_1 \frac{\partial A}{\partial M} - i\omega \right) \cdot [(\lambda_3 - i\omega) (\lambda_6 - i\omega) (\lambda_{12} - i\omega) - \lambda_{10} \lambda_{11} (\lambda_6 - i\omega) + \right. \\ & \left. - \lambda_4 \lambda_5 (\lambda_{12} - i\omega)] + \lambda_2 \lambda_9 \lambda_{11} N_c \frac{\partial A}{\partial M} (\lambda_6 - i\omega) \right)^{-1} \end{aligned} \quad (\text{J.16})$$

$$\hat{\chi}_{N_{Y_p}}(\omega) = \frac{\lambda_5}{\lambda_6 - i\omega} \hat{\chi}_{N_a}(\omega) \quad (\text{J.17})$$

$$\hat{\chi}_{P_t}(\omega) = \frac{\lambda_7}{\lambda_8 - i\omega} \hat{\chi}_{N_y}(\omega) \quad (\text{J.18})$$

$$\hat{\chi}_{N_{B_p}}(\omega) = \frac{\lambda_{11}}{\lambda_{12} - i\omega} \hat{\chi}_{N_{A_p}} \quad (\text{J.19})$$

From these equations, we observe that CheA-P, CheY-P and the motor are in a cascade, as new filters proportional to  $(\lambda_i - i\omega)^{-1}$  are introduced which simply multiply the response function of the previous layer of the cascade. The characteristic frequencies  $\lambda_i$  contain the forward and backward rates of the relevant processes.

## J.5 Noise spectra

---

The noise spectra can be calculated from the linearised equations J.10-J.14. After inserting the Fourier transforms of the dynamical variables, calculating the absolute squared value and averaging, we obtain the noise spectra for CheA-P, CheY-P and the motor

$$\begin{aligned}
 S_{A_c}(\omega) = & \left( |(\lambda_3 - i\omega)(\lambda_6 - i\omega)(\lambda_{12} - i\omega) - \lambda_4\lambda_5(\lambda_{12} - i\omega) - \lambda_{10}\lambda_{11}(\lambda_6 - i\omega)|^2 \cdot \right. \\
 & N_c \left[ \omega^2 \left( \frac{\partial A}{\partial c} \right)^2 S_c(\omega) + \omega^2 (S_a(\omega) + Q_M) \right] + \\
 & + \left| -\lambda_9 N_c \frac{\partial A}{\partial M} [(\lambda_3 - i\omega)(\lambda_6 - i\omega) - \lambda_4\lambda_5] \right|^2 Q_{-B_p} + \\
 & + \left| \lambda_9 \lambda_{11} N_c \frac{\partial A}{\partial M} (\lambda_6 - i\omega) \right|^2 Q_{A_p} + \left| \lambda_4 \lambda_9 \lambda_{11} N_c \frac{\partial A}{\partial M} \right|^2 Q_{-Y_p} + \\
 & + \left| \lambda_9 N_c \frac{\partial A}{\partial M} [\lambda_4 \lambda_5 + \lambda_{11}(\lambda_6 - i\omega) - (\lambda_3 - i\omega)(\lambda_6 - i\omega)] \right|^2 Q_{A,B_p} + \\
 & + \left. \left| \lambda_9 \lambda_{11} N_c \frac{\partial A}{\partial M} [(\lambda_6 - i\omega) - \lambda_4] \right|^2 Q_{A,Y_p} \right) \\
 & \left| \left( \lambda_1 \frac{\partial A}{\partial M} - i\omega \right) [(\lambda_3 - i\omega)(\lambda_6 - i\omega)(\lambda_{12} - i\omega) - \lambda_{10}\lambda_{11}(\lambda_6 - i\omega) + \right. \right. \\
 & \quad \left. \left. - \lambda_4\lambda_5(\lambda_{12} - i\omega)] + \lambda_2 \lambda_9 \lambda_{11} N_c \frac{\partial A}{\partial M} (\lambda_6 - i\omega) \right|^{-2} \quad (J.20)
 \end{aligned}$$

$$\begin{aligned}
 S_{N_{A_p}}(\omega) = & \left( N_c \lambda_2^2 \omega^2 \left( \frac{\partial A}{\partial c} \right)^2 |(\lambda_6 - i\omega)(\lambda_{12} - i\omega)|^2 S_c(\omega) + \right. \\
 & + |\lambda_2(\lambda_6 - i\omega)(\lambda_{12} - i\omega)|^2 N_c (\omega^2 S_a(\omega) + Q_M) + \\
 & + \left| \left( \lambda_1 \frac{\partial A}{\partial M} - i\omega \right) (\lambda_6 - i\omega)(\lambda_{12} - i\omega) \right|^2 Q_{A_p} + \\
 & + \left| (\lambda_6 - i\omega) \left( -\lambda_2 \lambda_9 N_c \frac{\partial A}{\partial M} + \lambda_{10} \left( \lambda_1 \frac{\partial A}{\partial M} - i\omega \right) \right) \right|^2 Q_{-B_p} + \\
 & + \left| \lambda_4 \left( \lambda_1 \frac{\partial A}{\partial M} - i\omega \right) (\lambda_{12} - i\omega) \right|^2 Q_{-Y_p} + \\
 & + \left| (\lambda_6 - i\omega)(\lambda_{12} - i\omega) \left( \lambda_1 \frac{\partial A}{\partial M} - i\omega \right) + (\lambda_6 - i\omega) \left( \lambda_2 \lambda_9 N_c \frac{\partial A}{\partial M} + \right. \right. \\
 & \quad \left. \left. - \lambda_{10} \left( \lambda_1 \frac{\partial A}{\partial M} - i\omega \right) \right) \right|^2 Q_{A,B_p} + \\
 & + \left| \left( \lambda_1 \frac{\partial A}{\partial M} - i\omega \right) (\lambda_6 - i\omega)(\lambda_{12} - i\omega) - \lambda_4 \left( \lambda_1 \frac{\partial A}{\partial M} - i\omega \right) (\lambda_{12} - i\omega) \right|^2 Q_{A,Y_p} \right) \\
 & \left| \left( \lambda_1 \frac{\partial A}{\partial M} - i\omega \right) \cdot [(\lambda_3 - i\omega)(\lambda_6 - i\omega)(\lambda_{12} - i\omega) - \lambda_{10}\lambda_{11}(\lambda_6 - i\omega) + \right. \right. \\
 & \quad \left. \left. - \lambda_4\lambda_5(\lambda_{12} - i\omega)] + \lambda_2 \lambda_9 \lambda_{11} N_c \frac{\partial A}{\partial M} (\lambda_6 - i\omega) \right|^{-2} \quad (J.21)
 \end{aligned}$$

$$\begin{aligned}
S_{N_{Y_p}}(\omega) = & \frac{\lambda_5^2(\omega)}{|\lambda_6 - i\omega|^2} \cdot \left( N_c \lambda_2^2 \omega^2 \left( \frac{\partial A}{dc} \right)^2 |(\lambda_6 - i\omega)(\lambda_{12} - i\omega)|^2 S_c(\omega) + \right. \\
& + |\lambda_2(\lambda_6 - i\omega)(\lambda_{12} - i\omega)|^2 N_c (\omega^2 S_a(\omega) + Q_M) + \\
& + \left| \left( \lambda_1 \frac{\partial A}{\partial M} - i\omega \right) (\lambda_6 - i\omega)(\lambda_{12} - i\omega) \right|^2 Q_{A_p} + \\
& + \left| (\lambda_6 - i\omega) \left( -\lambda_2 \lambda_9 N_c \frac{\partial A}{\partial M} + \lambda_{10} \left( \lambda_1 \frac{\partial A}{\partial M} - i\omega \right) \right) \right|^2 Q_{-B_p} + \\
& + \left| \frac{\lambda_5}{\lambda_6 - i\omega} \left[ \lambda_4 \left( \lambda_1 \frac{\partial A}{\partial M} - i\omega \right) (\lambda_{12} - i\omega) \right] + 1 \right|^2 Q_{-Y_p} + \\
& + \left| (\lambda_6 - i\omega)(\lambda_{12} - i\omega) \left( \lambda_1 \frac{\partial A}{\partial M} - i\omega \right) + (\lambda_6 - i\omega) (\lambda_2 \lambda_9 N_c \frac{\partial A}{\partial M} + \right. \\
& \quad \left. - \lambda_{10} \left( \lambda_1 \frac{\partial A}{\partial M} - i\omega \right) \right|^2 Q_{A,B_p} + \\
& + \left| \frac{\lambda_5}{\lambda_6 - i\omega} \left[ \left( \lambda_1 \frac{\partial A}{\partial M} - i\omega \right) (\lambda_6 - i\omega)(\lambda_{12} - i\omega) + \right. \right. \\
& \quad \left. \left. - \lambda_4 \left( \lambda_1 \frac{\partial A}{\partial M} - i\omega \right) (\lambda_{12} - i\omega) \right] - 1 \right|^2 Q_{A,Y_p} \Big) \cdot \\
& \left| \left( \lambda_1 \frac{\partial A}{\partial M} - i\omega \right) \cdot [(\lambda_3 - i\omega)(\lambda_6 - i\omega)(\lambda_{12} - i\omega) - \lambda_{10} \lambda_{11}(\lambda_6 - i\omega) + \right. \\
& \quad \left. - \lambda_4 \lambda_5 (\lambda_{12} - i\omega)] + \lambda_2 \lambda_9 \lambda_{11} N_c \frac{\partial A}{\partial M} (\lambda_6 - i\omega) \right|^{-2} \tag{J.22}
\end{aligned}$$

$$S_{P_t}(\omega) = \frac{\lambda_7^2 S_{N_{Y_p}}(\omega) + Q_{P_t}}{|\lambda_8 - i\omega|^2} \tag{J.23}$$

## J.6 Parameters

Rate constants and total cell concentrations of proteins for the full pathway model are given in Table J.1. The noise terms  $\eta_{A_j}$ ,  $\eta_{c_j}$ ,  $\eta_{M_j}$  and  $\eta_{P_t}$  are the same as in Eq. 4.26 and 4.29-4.31 in chapter 4 and their power spectra are given there. The noise associated with phosphorylation and dephosphorylation  $\eta_{A_p}$ ,  $\eta_{A,B_p}$ ,  $\eta_{A,Y_p}$ ,  $\eta_{-B_p}$  and  $\eta_{-Y_p}$  are assumed to be Gaussian white noise terms with zero mean and autocorrelations  $\langle \eta_i(t) \eta_i(t') \rangle = Q_i \delta(t - t')$  with noise intensities  $Q_i$  given in Table J.2. The linearised rate constants for the full pathway model are given in Table J.3. Fitting parameters of the Fourier transformed linear response functions in Fig. 4.2 are listed in Table J.4. In Table J.5 we list parameters for Fig. 4.5 in chapter 4.

## APPENDIX J. RESPONSE FUNCTION AND NOISE SPECTRA FOR THE FULL PATHWAY MODEL

---

**Table J.1.:** Parameters of the full pathway model.

Parameter	Value
$[A]_{\text{tot}}$	$5 \mu\text{M}$
$[B]_{\text{tot}}$	$0.28 \mu\text{M}$
$[Y]_{\text{tot}}$	$9.7 \mu\text{M}$
$N_{A,\text{tot}}$	4215
$N_{B,\text{tot}}$	236
$N_{Y,\text{tot}}$	8177
$N_{\text{tot}} = NN_c$	7027
$V_{\text{cell}}$	1.4 fl
$k_2$	$10^3 \text{ s}^{-1}$
$k_A$	$10 \text{ s}^{-1}$
$k_Y$	$100 \mu\text{M}^{-1} \text{ s}^{-1}$
$k_B$	$15 \mu\text{M}^{-1} \text{ s}^{-1}$
$k_{-Y}$	$5 \text{ s}^{-1}$
$k_{-B}$	$1.35 \text{ s}^{-1}$
$\gamma_R$	$0.006 \text{ s}^{-1}$
$\gamma_B$	$3.14 \mu\text{M}^{-2} \text{ s}^{-1}$

**Table J.2.:** Intensities of Gaussian white noise terms in the full pathway model. Index “ $i$ ” represents the noise term  $\eta_i$ .

process	index $i$	noise intensity $Q_i$
receptor switching	$a$	$2k_2A^*$
ligand diffusion	$L$	$2Dsc_0$
receptor de/methylation	$M$	$2\gamma_R(N - A^*)$
CheA autophosphorylation	$A_p$	$A_c^* \left( \frac{k_A}{N_c N} \right) (N_{A,\text{tot}} - N_{A_p}^*)$
CheY phosphorylation	$A, Y_p$	$\left( \frac{k_Y}{V_{\text{cell}}} \right) (N_{Y,\text{tot}} - N_{Y_p}^*) N_{A_p}^*$
CheB phosphorylation	$A, B_p$	$\left( \frac{k_B}{V_{\text{cell}}} \right) (N_{B,\text{tot}} - N_{B_p}^*) N_{A_p}^*$
CheY dephosphorylation	$-Y_p$	$k_{-Y} N_{Y_p}^*$
CheB dephosphorylation	$-B_p$	$k_{-B} N_{B_p}^*$
motor switching	$P_t$	$\frac{2k_+^* k_-^*}{k_+^* + k_-^*}$

**Table J.3.:** Parameters of the linearised equations for the full pathway.

$\lambda_i$	expression
$\lambda_1$	$\gamma_R + \gamma_B B P^{*2}$
$\lambda_2$	$\left(\frac{k_A}{N_c N}\right) (N_{A,\text{tot}} - N_{A_p}^*)$
$\lambda_3$	$A_c^* \left(\frac{k_A}{N_c N}\right) + \left(\frac{k_Y}{V_{\text{cell}}}\right) (N_{Y,\text{tot}} - N_{Y_p}^*) + \left(\frac{k_B}{V_{\text{cell}}}\right) (N_{B,\text{tot}} - N_{B_p}^*)$
$\lambda_4$	$\left(\frac{k_Y}{V_{\text{cell}}}\right) N_{A_p}^*$
$\lambda_5$	$\left(\frac{k_Y}{V_{\text{cell}}}\right) (N_{Y,\text{tot}} - N_{Y_p}^*)$
$\lambda_6$	$\left(\frac{k_Y}{V_{\text{cell}}}\right) N_{A_p}^* + k_{-Y}$
$\lambda_7$	$\frac{1}{V_{\text{cell}}} \left( (1 - P^*) \frac{\partial k_+}{\partial Y_p} - P^* \frac{\partial k_-}{\partial Y_p} \right)$
$\lambda_8$	$k_+^* + k_-^*$
$\lambda_9$	$\frac{2\gamma_B A^* B_p^*}{V_{\text{cell}}}$
$\lambda_{10}$	$\left(\frac{k_B}{V_{\text{cell}}}\right) N_{A_p}^*$
$\lambda_{11}$	$\left(\frac{k_B}{V_{\text{cell}}}\right) (N_{B,\text{tot}} - N_{B_p}^*)$
$\lambda_{12}$	$\left(\frac{k_B}{V_{\text{cell}}}\right) N_{A_p}^* + k_{-B}$ .

**Table J.4.:** Fitting parameters for response function of the full pathway model for Fig. 4.2 in chapter 4.

Parameter	Block et al. (1982) and Segall et al. (1986) [s <sup>-1</sup> ]	Shimizu et al. (2010)	
		32 °C [s <sup>-1</sup> ]	22 °C [s <sup>-1</sup> ]
adaptation:			
$\lambda_1(\partial A/\partial M)$	0.178	0.018	0.0039
$\lambda_9$	0.0263	0.0027	$5.6 \cdot 10^{-4}$
motor switching:			
$\lambda_7$	$4.4 \cdot 10^{-4}$	–	–
$\lambda_8$	2.111	–	–

**Table J.5.:** Parameters for Fig. 4.5 in chapter 4. Parameters apart from those listed are as in Table J.1.

Parameter	standard parameters (black line)	red line	green line	blue line
$k_+^*$ [s <sup>-1</sup> ]	1.05	52.4	1.05	1.05
$k_-^*$ [s <sup>-1</sup> ]	1.06	53.0	1.06	1.06
$\gamma_R$ [s <sup>-1</sup> ]	0.0069	0.0069	$6.9 \cdot 10^{-5}$	0.0069
$\gamma_B$ [ $\mu\text{M}^{-2} \text{s}^{-1}$ ]	3.14	3.14	$3.14 \cdot 10^{-2}$	3.14
$N_{\text{tot}}$	7000	7000	7000	70

# K. Integrated signal response, variance and SNR of the total receptor activity

## K.1 Receptor complex size

---

The integrated response of the receptor activity to a step stimulus in chapter 4 is

$$\begin{aligned}\Delta A_c^2 &= \int_{-\infty}^{\infty} d\omega |\hat{\chi}_{A_c}(\omega) \Delta \hat{c}(\omega)|^2 \\ &= \frac{\pi N_C^2 \left(\frac{\partial A}{\partial c}\right)^2 (\alpha c)^2}{\omega_M},\end{aligned}\tag{K.1}$$

where we inserted Eq. 4.17. Hence, the activity response scales as

$$\Delta A_c^2 \propto (N_{\text{tot}}/N)^2 (N^2)^2 / N \propto N,\tag{K.2}$$

where we used that  $N_C = N_{\text{tot}}/N$  with  $N_{\text{tot}}$  the total number of receptors in a cell.

The variance of the receptor activity is given by the integral over the power spectrum of activity fluctuations Eq. 4.36

$$\begin{aligned}\langle \delta A_c^2 \rangle &= \frac{N_C}{2\pi} \int_{-\tau^{-1}}^{\tau^{-1}} d\omega \frac{\omega^2 \left[ S_a(\omega) + \left(\frac{\partial A}{\partial c}\right)^2 S_c(\omega) \right]}{\omega^2 + \omega_M^2} \\ &\quad + \frac{N_C}{2\pi} \int_{-\tau^{-1}}^{\tau^{-1}} d\omega \frac{\left(\frac{\partial A}{\partial M}\right)^2 Q_M}{\omega^2 + \omega_M^2},\end{aligned}\tag{K.3}$$

where we consider the frequency range relevant for motor switching indicated by  $\tau^{-1}$ .

The contribution from receptor switching is

$$\langle \delta A_c^2 \rangle_a = \frac{N_C}{2\pi} \int_{-\tau^{-1}}^{\tau^{-1}} d\omega \frac{\omega^2 S_a(\omega)}{\omega^2 + \omega_M^2} \approx \frac{2k_2 A_r^* N_{\text{tot}}}{\pi \tau (k_1 + k_2)^2}\tag{K.4}$$

where we used  $Q_a$ , inserted Eq. 4.25 for the power spectrum of receptor switching noise and used that it is almost constant and equal to its zero-frequency value over the integration

---

## K.2. METHYLATION AND DEMETHYLATION RATE CONSTANTS

---

range. Furthermore, the factor  $\omega^2/(\omega^2 + \omega_M^2) \approx 1$  and  $A_r^* = A^*/N$  is the adapted activity of an individual receptor. Hence, according to this simple calculation the contribution to the variance from receptor switching is roughly constant with receptor complex size.

The contribution from ligand diffusion is

$$\begin{aligned} \langle \delta A_c^2 \rangle_c &= \frac{N_C}{2\pi} \int_{-\tau^{-1}}^{\tau^{-1}} d\omega \frac{\omega^2 \left(\frac{\partial A}{\partial c}\right)^2 S_c(\omega)}{\omega^2 + \omega_M^2} \\ &\approx N_C \left(\frac{\partial A}{\partial c}\right)^2 \langle \delta c^2 \rangle, \end{aligned} \quad (\text{K.5})$$

where  $\langle \delta c^2 \rangle = 2c_0/(Ds\tau)$  is the variance of the ligand concentration measured during the time interval  $\tau$ . We used Eq. 4.28 and the same argument as for the switching noise to calculate the integral. Hence, the contribution to the variance from the ligand diffusion grows as  $\langle \delta A_c^2 \rangle_c \propto N^3$  as a result of incoherent addition of noise from different receptor complexes and the sensitivity  $\partial A/\partial c$  increasing as  $N^2$ .

The contribution to the variance from receptor methylation is

$$\begin{aligned} \langle \delta A_c^2 \rangle_M &= \frac{N_C}{2\pi} \left(\frac{\partial A}{\partial M}\right)^2 \int_{-\tau^{-1}}^{\tau^{-1}} d\omega \frac{Q_M}{\omega^2 + (\omega_1 \frac{\partial A}{\partial M})^2} \\ &\approx \frac{2N_{\text{tot}}\gamma_R(1 - A_r^*)A_r^*}{\omega_1} \frac{\partial A}{\partial M} \end{aligned} \quad (\text{K.6})$$

where we defined  $\omega_1 = \gamma_R + 3\gamma_B N^2 (A_r^*)^2$ , inserted  $Q_M = 2\gamma_R N(1 - A_r^*)$  and  $\omega_M = \omega_1 (\partial A/\partial M)$ . Hence,  $\langle \delta A_c^2 \rangle_M$  grows approximately linearly with receptor complex size. According to our simplified model, the SNR scales as  $\text{SNR} \propto N/(\text{const.} + N + N^3)$ , resulting in a non-monotonic behaviour.

## Methylation and demethylation rate constants

---

The integrated signal response of the receptor activity Eq. K.1

$$\Delta A_c^2 = \frac{\pi N_C^2 \left(\frac{\partial A}{\partial c}\right)^2 (\alpha c)^2}{\omega_1 \frac{\partial A}{\partial M}}, \quad (\text{K.7})$$

where the numerator expresses the initial response of receptors of concentration changes and the denominator the filtering by adaptation. The sensitivity  $\partial A/\partial c = NA_r^*(1 - A_r^*)h(c)$ , where  $h(c) = \partial F/\partial c$ ,  $\omega_1 = \gamma_R + 3\gamma_B N^2 (A_r^*)^2$ , and  $\partial A/\partial M = NA_r^*(1 - A_r^*)/2$ . The adapted activity can be obtained analytically for our simplified model from the steady

## APPENDIX K. INTEGRATED SIGNAL RESPONSE, VARIANCE AND SNR OF THE TOTAL RECEPTOR ACTIVITY

---

state of the methylation dynamics Eq. 4.5 in chapter 4,

$$A_r^* = \sqrt[3]{\frac{1}{2}\beta + \sqrt{\frac{\beta^2}{4} + \frac{\beta^3}{27}}} - \frac{\beta}{3\sqrt[3]{\frac{1}{2}\beta + \sqrt{\frac{\beta^2}{4} + \frac{\beta^3}{27}}}}, \quad (\text{K.8})$$

and is only a function of the ratio  $\beta = \gamma_R/\gamma_B$ . Expanding the adapted activity around  $A_r^* = 0$  (for  $\gamma_R \rightarrow 0$ ) yields  $A_r^* \propto \gamma_R^{1/3}$ , and around  $A_r^* = 1$  (for  $\gamma_B \rightarrow 0$ ) yields  $A_r^* \propto \gamma_B$ . Similarly,  $\omega_1 \propto \gamma_R^{2/3} (\text{const.} + \gamma_B^{4/3})$ . Hence,  $\partial A/\partial c \propto \gamma_R^{1/3} (\gamma_B)$  and  $\omega_1 \partial A/\partial M \propto \gamma_R^{4/3} (\gamma_B)$ . The initial response to concentration changes decreases slower than adaptation times, resulting in an increased signal response for vanishing  $\gamma_R$ . For vanishing  $\gamma_B$ , the initial response to concentration changes decreases faster than adaptation speed, hence yielding a vanishing signal response. The overall dependence of the integrated signal response is  $\Delta A_c^2 \propto \gamma_R^{-1/3} (\gamma_B)$ .

For the contributions to the variance of the receptor activity from receptor switching, ligand diffusion and receptor methylation dynamics we obtain  $\langle \delta A_c^2 \rangle_a \propto \gamma_R^{1/3} (\gamma_B)$ ,  $\langle \delta A_c^2 \rangle_c \propto \gamma_R^{2/3} (\gamma_B^2)$  and  $\langle \delta A_c^2 \rangle_M \propto \gamma_R (\gamma_B^{2/3})$ , respectively.

According to our simplified model the SNR of the receptor activity goes as  $\text{SNR} \propto \gamma_R^{-2/3} (\gamma_B^{4/3})$ .



## L. Master equation approach for receptor signalling

Alternative to the Langevin approach, which assumes small fluctuations, we can write down a Master equation for the pathway. Here, we focus on ligand and methylation dynamics at the receptor cluster. Each state of the pathway is described by the variables  $[L_j, M_j]$  at each of the receptor complexes, where  $L_j = c_j s^3$  is the number of molecules in a small volume at the receptor complex and  $M_j$  the total methylation level of the receptor complex. Assuming for simplicity only one receptor complex, the Master equation for the probability density  $p$  is

$$\begin{aligned}
\frac{\partial p(L, M, t)}{\partial t} = & k_D(s^3 c_0)p(L-1, M, t) \\
& + k_D(L+1)p(L+1, M, t) \\
& + \gamma_R[1 - A(L, M-1)]p(L, M-1, t) \\
& + \gamma_B[A(L, M+1)]^3 p(L, M+1, t) \\
& - \{k_D(s^3 c_0 + L) + k_D(s^3 c_0) + \gamma_R[1 - A(L, M)] \\
& + \gamma_B[A(L, M)]^3\} p(L, M, t)
\end{aligned} \tag{L.1}$$

For small noise, we obtain after expansion of the variables and using van Kampens  $\Omega$  expansion (van Kampen, 2007) for the variances of fluctuations in the number of ligand molecules and the methylation level at steady state (Aquino et al., 2011)

$$\langle \delta L^2 \rangle = c_0 s^3 \tag{L.2}$$

$$\langle \delta M^2 \rangle = \frac{1}{(3 - 2A^*)\beta} + \frac{\gamma_R(3 - 2A^*) \left(\frac{\partial A}{\partial c}\right)^2 c}{A^{*2}(1 - A^*)[k_D + \gamma_R(3 - 2A^*)(1 - A^*)\beta]\beta}, \tag{L.3}$$

with  $\beta = 1/2$  the free-energy difference due to adding one methyl group (in units of  $k_B T$ ). The first term is due to the processivity of modification enzymes and the second term is

## **APPENDIX L. MASTER EQUATION APPROACH FOR RECEPTOR SIGNALLING**

---

due to transmitted fluctuations in the activity from ligand noise. This corresponds to the results from the Langevin approach, i.e. for ligand fluctuation we obtain the same variance after integration of the power spectrum Eq. 4.28. For the receptor complex methylation level, the power spectrum is according to our approach from Appendix J

$$S_M(\omega) = \frac{Q_M + (\gamma_R + 3\gamma_B A^{*2})^2 \left(\frac{\partial A}{\partial c}\right)^2 S_c(\omega)}{\omega^2 + \omega_M^2}, \quad (\text{L.4})$$

and we obtain the same result for the variance of the methylation level after integration of the power spectrum.

## M. Langevin description for motor dynamics

We chose to describe the dynamics of the motor using the Langevin equation 4.6 in chapter 4

$$\frac{dP_t}{dt} = k_+(1 - P_t) - k_-P_t + \eta_{P_t}(t) \quad (\text{M.1})$$

with switching rates from CCW to CW (first term) and from CW to CCW (second term), as well as an additive Gaussian white noise term (last term) with zero mean and autocorrelation  $\langle \eta_{P_t}(t)\eta_{P_t}(t') \rangle = Q_{P_t}\delta(t - t')$  with  $Q_{P_t} = 2k_+(1 - P_t^*) = 2k_+k_-/(k_+ + k_-)$ . For constant switching rate constants  $k_+$  and  $k_-$ , the power spectrum  $P_t$  is (cf. Eq. 4.38 in chapter 4)

$$S_{P_t}(\omega) = \frac{Q_{P_t}}{\omega^2 + (k_+ + k_-)^2}. \quad (\text{M.2})$$

To see that this is a valid description of the binary motor switching process, we can calculate the spectrum precisely according to the derivation by Stratonovich (1963). For a stochastic two-state process, whose time interval lengths in each of the two states  $\tau_1$  and  $\tau_2$ , respectively, are independent and identically distributed random variables, the power spectrum is given in terms of the Fourier transforms of the waiting time distributions  $\Theta_1(\omega)$  and  $\Theta_2(\omega)$  for each of the states,

$$S(\omega) = \frac{2}{\omega^2(\langle\tau_1\rangle + \langle\tau_2\rangle)} \Re \frac{[1 - \Theta_1(\omega)][1 - \Theta_2(\omega)]}{1 - \Theta_1(\omega)\Theta_2(\omega)}. \quad (\text{M.3})$$

Assuming for the motor that switching between the states CW and CCW, respectively, follows exponential interval distributions determined by rates  $k_+$  and  $k_-$ , the Fourier transforms of the waiting time distributions are given by,

$$\Theta_{CW}(\omega) = \frac{k_+}{k_+ - i\omega}, \quad \Theta_{CCW}(\omega) = \frac{k_-}{k_- - i\omega}, \quad (\text{M.4})$$

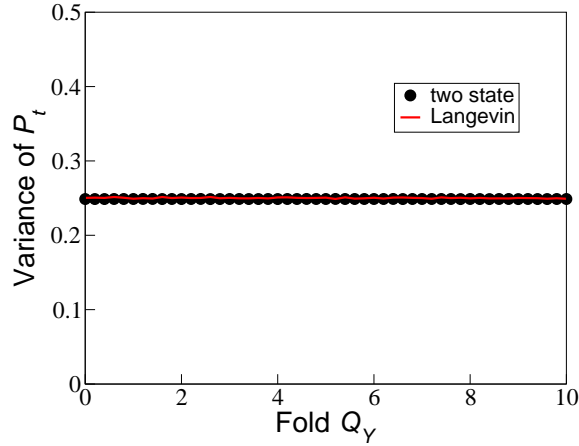


**Figure M.1.:** Variance of the motor bias as a function of CheY-P noise intensity for Langevin and two-state dynamics.

and the power spectrum is

$$S_2(\omega) = \frac{2k_+k_-}{(k_+ + k_-)} \frac{1}{\omega^2 + (k_+ + k_-)^2}. \quad (\text{M.5})$$

This result is equivalent to the spectrum obtained from the Langevin equation. Furthermore, we tested numerically that the statistics of the Langevin equation and binary process are equivalent for fluctuating rates  $k_+$  and  $k_-$  due to the CheY-P dynamics. We simulated time courses of CheY-P according to the simplified equation

$$\frac{dN_{Y_p}}{dt} = k_Y - k_{-Y}N_{Y_p} + \eta_{Y_p}(t) \quad (\text{M.6})$$

with rates  $k_Y = 5/s$  and  $k_Y$  such that  $\langle N_{Y_p} \rangle^*/V_{\text{cell}} = \langle [Y_p] \rangle^* = 3.2\mu M$ . The noise term  $\eta_{Y_p}(t)$  is Gaussian and white with zero mean and autocorrelation  $\langle \eta_{Y_p}(t)\eta_{Y_p}(t') \rangle = 2k_Y\alpha\delta(t-t') \equiv Q_Y\alpha\delta(t-t')$ , where we varied  $\alpha$ . Fluctuating CheY-P was translated into the rates  $k_+([Y_p])$  and  $k_-([Y_p])$  according to Fig. 4.1 in chapter 4. The Langevin equation was simulated using a Euler-Maruyama algorithm and the binary process using a Gillespie algorithm. Figure M.1 shows the variances of both processes as obtained from  $10^2$  runs for each value of  $\alpha$ . As can be seen from the figure, the Langevin equation reproduces the variance of the binary process of motor switching.

## N. Justification for linear noise approximation for intracellular signalling noise

To test whether the linearisation of Eq. J.11-J.13, which describe the phosphorylation and dephosphorylation dynamics of the intracellular signalling proteins in the full pathway model, is justified, i.e. fluctuations elicit a linear response, we simulated time courses using a Euler-Maruyama algorithm (Kloeden and Platen, 1992) and numerically calculated power spectra of CheY-P. We introduced the various noise sources,  $\eta_{A_p}$ ,  $\eta_{A,Y_p}$ ,  $\eta_{A,B_p}, \eta_{-B}, \eta_{-Y}$ , one by one and calculated spectra. Figure N.1 shows the analytically and numerically calculated spectra. We found a good correspondence. Hence, the linearisation of equations is justified.

**APPENDIX N. JUSTIFICATION FOR LINEAR NOISE APPROXIMATION FOR INTRACELLULAR SIGNALLING NOISE**

---

Contributions to  $Y_p$  power spectrum

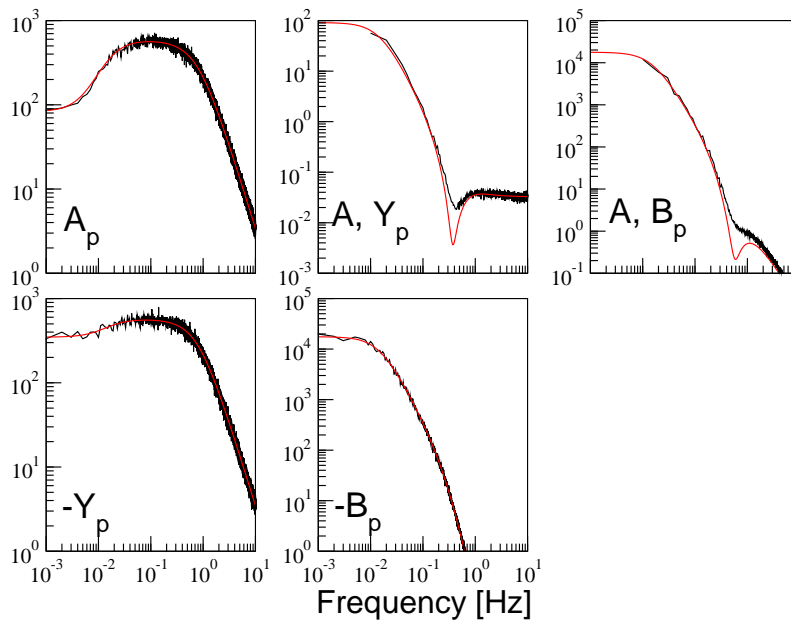


**Figure N.1.:** Contributions from CheA autophosphorylation, CheY and CheB phosphorylation and dephosphorylation to the power spectrum of CheY-P. Numerically calculated spectra from simulated time courses (black) and analytical spectra (red) are shown. Analytical results from Eq. J.22 in Appendix J and numerically calculated spectra from simulation and averaging of 100 time courses of duration 100 s (integration time step 0.001 s).

## O. High-frequency filters

In Fig. 4.2 A in chapter 4 it is apparent that our model does not fully reproduce the high-frequency response. The high-frequency response seems to be a third-order filter in the frequency range shown, while our model produces a second order filter due to the CheY-P and motor switching dynamics. Here, we discuss where an additional filter could originate.

We explicitly consider the CheY-P/CheZ binding step, and write down the equations for the dynamics of the concentration of CheY-P, denoted by  $[Y_p]$ , and of CheY-P/CheZ complex,  $[Y_pZ]$ ,

$$\frac{d[Y_p]}{dt} = k_Y ([Y]_{\text{tot}} - [Y_p]) [A_p] - k_1 ([Z]_{\text{tot}} - [Y_pZ]) [Y_p] + k_2 [Y_pZ] \quad (\text{O.1})$$

$$\frac{d[Y_pZ]}{dt} = k_1 ([Z]_{\text{tot}} - [Y_pZ]) [Y_p] - (k_2 + k_3) [Y_pZ], \quad (\text{O.2})$$

where  $[A_p]$  is the concentration of phosphorylated CheA and  $k_i$  are the rates of phosphorylation of CheY ( $k_Y$ ), CheY-P/CheZ complex formation ( $k_1$ ), dissociation of CheY-P/CheZ complexes ( $k_2$ ) and CheY-P dephosphorylation ( $k_3$ ). Linearising around the steady state ( $[A_p]^*$ ,  $[Y_p]^*$ ,  $[Y_pZ]^*$ ) yields

$$\begin{aligned} \frac{d\Delta[Y_p]}{dt} = & \underbrace{k_Y (Y_{\text{tot}} - [Y_p]^*)}_{\lambda_1} \Delta[A_p] - \underbrace{(k_Y [A_p]^* + k_1 (Z_{\text{tot}} - [Y_pZ]^*))}_{\lambda_2} \Delta[Y_p] \\ & + \underbrace{(k_1 [Y_p]^* + k_2)}_{\lambda_3} \Delta[Y_pZ] \end{aligned} \quad (\text{O.3})$$

$$\frac{d\Delta[Y_pZ]}{dt} = - \underbrace{(k_1 [Y_p]^* + k_2 + k_3)}_{\lambda_3 + k_3} \Delta[Y_pZ] + \underbrace{k_1 (Z_{\text{tot}} - [Y_pZ]^*)}_{\lambda_4} \Delta[Y_p]. \quad (\text{O.4})$$

Hence, we obtain for the Fourier transform of deviations in CheY-P concentration

$$\Delta[\hat{Y}_p] = \frac{\lambda_1(-i\omega + \lambda_3 + k_3)}{(-i\omega + \lambda_2)(-i\omega + \lambda_3 + k_3) - \lambda_3\lambda_4} \Delta[\hat{A}_p]. \quad (\text{O.5})$$

To make the analysis easier, we can factorise the polynomial in the denominator,

$$\Delta[\hat{Y}_p] = \frac{\lambda_1(-i\omega + \lambda_3 + k_3)}{(-i\omega + a_1)(-i\omega + a_2)} \Delta[\hat{A}_p], \quad (\text{O.6})$$

with  $a_{1,2} = (\lambda_3 + k_3 + \lambda_2)/2 \pm \sqrt{(\lambda_3 + k_3 + \lambda_2)^2/4 - \lambda_2(\lambda_3 + k_3) + \lambda_3\lambda_4}$ .

We are interested in the behaviour of the frequency-dependent prefactor. Specifically, we ask if by considering the CheY-P/CheZ complex formation we obtain an additional high-frequency filter compared to Eq. J.17. It is obvious from Eq. O.6 that under most parameter combinations we obtain  $1/\omega$  behaviour at high frequencies. Hence, no additional filter is introduced. A special case appears for  $\lambda_3 + k_3 \gg a_1, a_2$ . Then  $1/\omega^2$  behaviour is observed for medium frequencies  $\max(a_1, a_2) \gg \omega \gg \lambda_3 + k_3$ . Hence, an additional filter appears. At high frequencies  $\omega > \lambda_3 + k_3$ , the prefactor has  $1/\omega$  behaviour. However, analysing the expressions for  $a_1$  and  $a_2$  reveals that  $\max(a_1, a_2)$  is always greater or equal to  $(\lambda_3 + k_3 + \lambda_2)/2$ . Therefore, this case does not occur for our dynamics. In conclusion, the CheY-P/CheZ complex formation does not introduce an additional high-frequency filter.

Other processes in the signalling pathway neglected here are the potential oligomerisation of CheY-P/CheZ complexes (Eisenbach, 2004; Blat and Eisenbach, 1996a,b) and a potential slow release of CheY-P from the sensory complex as discussed by Blat et al. (1998). Oligomerisation of CheY-P/CheZ complexes for efficient dephosphorylation is similar to CheY-P/CheZ complex formation considered above, and by a similar discussion does not introduce an additional high-frequency filter. However, a delayed release of CheY-P represents effectively a step between CheY phosphorylation and motor switching in the signalling cascade, and hence could introduce a relevant filter if the process is sufficiently slow. Another possibility to explain the steep frequency-dependence of the response function is that the duration of experimental pulses was long enough to leave a signature in the impulse response.



## P. Parameters for predicted input and output distributions

**Table P.1.:** Parameters of the fit of the MWC model to the dose-response curves in Fig. 5.2 in chapter 5. Parameters adjusted were  $\Lambda$ ,  $N$  and  $\Delta\epsilon$  in the activity  $A = \Lambda/(1 + e^{\Delta F})$ , where  $\Delta F = N[\Delta\epsilon + \ln((1 + c/K_{\text{off}})/(1 + c/K_{\text{on}}))]$ ,  $K_{\text{off}} = 0.02$  mM and  $K_{\text{on}} = 0.5$  mM (Keymer et al., 2006). All energies are in units of  $k_B T$ .

Strain	$\Delta\epsilon$	$N$
WT 0 $\mu\text{M}$	0.14	8.34
WT 100 $\mu\text{M}$	-1.52	13.61
QEEE	0.24	5.2
QEQE	-1.28	13.56
QEQQ	-2.08	17.26
QQQQ	-2.63	19.48
	$\Lambda$	0.09

**Table P.2.:** Number of principle components used for fitting the MWC model to the dose-response curves in Fig. 5.2 in chapter 5.

Strain	#Principle components
WT 0 $\mu\text{M}$	3
WT 100 $\mu\text{M}$	4
QEEE	4
QEQE	3
QEQQ	4
QQQQ	3

## APPENDIX P. PARAMETERS FOR PREDICTED INPUT AND OUTPUT DISTRIBUTIONS

---

**Table P.3.:** Parameters for the fit of the variance in the FRET activity in Fig. 5.4 in chapter 5 to the formula  $\sigma_A^2 = [\alpha_1 \sqrt{c} \frac{dA}{dc}]^2 + [\alpha_2 \sqrt{A}]^2$ .

Strain	$\alpha_1$	$\alpha_2$
WT 0 $\mu\text{M}$	0.0063	0.0049
WT 100 $\mu\text{M}$	0.0030	0.0034
QEEE	0.0043	0.0057
QEQE	0.0061	0.0049
QEQQ	0.0243	0.0066
QQQQ	0.0158	0.0199

**Table P.4.:** Parameters of the fit of log-normal distributions to the predicted optimal input distributions in Fig. 5.4 in chapter 5.

Strain	$\mu$	$\sigma^2$	$\langle x \rangle$	$\langle x^2 - \langle x \rangle^2 \rangle$	$\langle x^2 - \langle x \rangle^2 \rangle / \langle x \rangle^2$
WT 100 $\mu\text{M}$	2.399	0.232	0.0932	$4.80 \cdot 10^{-4}$	0.0552
QEQE	2.767	0.253	0.0649	$2.79 \cdot 10^{-4}$	0.0663
QEQQ	1.554	0.218	0.2166	0.0023	0.0488
QQQQ	0.503	0.224	0.6199	0.0197	0.0513

## Bibliography

- M. Acar, B. F. Pando, F. H. Arnold, M. B. Elowitz, and A. van Oudenaarden. A General Mechanism for Network-Dosage Compensation in Gene Circuits. *Science*, 329:1656–1660, 2010.
- U. Alon, M. G. Surette, B. Barkai, and S. Leibler. Robustness in bacterial chemotaxis. *Nature*, 397:168–171, 1999.
- P. Ames, C. A. Studdert, R. H. Reiser, and J. S. Parkinson. Collaborative signaling by mixed chemoreceptor teams in *Escherichia coli*. *Proc Natl Acad Sci U S A*, 99:7060–7065, 2002.
- G. S. Anand, P. N. Goudreau, and A. M. Stock. Activation of methylesterase CheB: evidence of a dual role for the regulatory domain. *Biochemistry*, 37:14038–14047, 1998.
- B. W. Andrews, T. M. Yi, and P. A. Iglesias. Optimal noise filtering in the chemotactic response of *Escherichia coli*. *PLoS Comput Biol*, 2:e154, 2006.
- G. Aquino, D. Clausznitzer, S. Tollis, and R. G. Endres. Optimal receptor-cluster size determined by intrinsic and extrinsic noise. *Phys Rev E*, 83:021914, 2011.
- S. Asakura and H. Honda. Two-state model for bacterial chemoreceptor proteins: The role of multiple methylation. *J Mol Biol*, 176:349–367, 1984.
- F. Bai, R. W. Branch, D. V. Nicolau, T. Pilizota, B. C. Steel, P. K. Maini, and R. M. Berry. Conformational spread as a mechanism for cooperativity in the bacterial flagellar switch. *Science*, 327:685–689, 2010.
- M. D. Baker, P. M. Wolanin, and J. B. Stock. Systems biology of bacterial chemotaxis. *Curr Opin Microbiol*, 9:187–192, 2006.
- N. Barkai and S. Leibler. Robustness in simple biochemical networks. *Nature*, 387:913–917, 1997.

## Bibliography

---

- A. N. Barnakov, L. A. Barnakova, and G. L. Hazelbauer. Allosteric enhancement of adaptational demethylation by a carboxyl-terminal sequence on chemoreceptors. *J Biol Chem*, 277:42151–42156, 2002.
- H. C. Berg. *Random Walks in Biology*. Princeton University Press, Princeton, 1993.
- H. C. Berg. Motile behavior of bacteria. *Phys Today*, 53:24–29, 2000.
- H. C. Berg and D. A. Brown. Chemotaxis in *Escherichia coli* analysed by three-dimensional tracking. *Nature*, 239:500–504, 1972.
- H. C. Berg and E. M. Purcell. Physics of chemoreception. *Biophys J*, 20:193–219, 1977.
- W. Bialek. Physical limits to sensation and perception. *Ann Rev Biophys Chem*, 16:455–478, 1987.
- W. Bialek and S. Setayeshgar. Physical limits to biochemical signaling. *Proc Natl Acad Sci U S A*, 102:10040–10045, 2005.
- W. Bialek and S. Setayeshgar. Cooperativity, sensitivity, and noise in biochemical signaling. *Phys Rev Lett*, 100:258101, 2008.
- M. J. Blaser. Ecology of *Helicobacter pylori* in the human stomach. *J Clin Invest*, 100:759–762, 1997.
- Y. Blat and M. Eisenbach. Oligomerization of the phosphatase CheZ upon interaction with the phosphorylated form of CheY. *J Biol Chem*, 271:1226–1231, 1996a.
- Y. Blat and M. Eisenbach. Mutants with defective phosphatase activity show no phosphorylation-dependent oligomerization of CheZ. *J Biol Chem*, 271:1232–1236, 1996b.
- Y. Blat, B. Gillespie, A. Bren, F. W. Dahlquist, and M. Eisenbach. Regulation of phosphatase activity in bacterial chemotaxis. *J Mol Biol*, 284:1191–1199, 1998.
- S. M. Block, J. E. Segall, and H. C. Berg. Impulse responses in bacterial chemotaxis. *Cell*, 31:215–226, 1982.
- S. M. Block, J. E. Segall, and H. C. Berg. Adaptation kinetics in bacterial chemotaxis. *J Bacteriol*, 154:312–323, 1983.

- T. Boldog, S. Grimme, M. Li, S. G. Sligar, and G. L. Hazelbauer. Nanodiscs separate chemoreceptor oligomeric states and reveal their signaling properties. *Proc Natl Acad Sci U S A*, 103:11509–11514, 2006.
- D. Bray and R. B. Bourret. Computer analysis of the binding reactions leading to a transmembrane receptor-linked multiprotein complex involved in bacterial chemotaxis. *Mol Biol Cell*, 6:1367–1380, 1995.
- D. Bray, M. D. Levin, and C. J. Morton-Firth. Receptor clustering as a cellular mechanism to control sensitivity. *Nature*, 393:85–88, 1998.
- A. Briegel, H. J. Ding, Z. Li, J. Werner, Z. Gitai, D. P. Dias, R. B. Jensen, and G. J. Jensen. Location and architecture of the *Caulobacter crescentus* chemoreceptor array. *Mol Microbiol*, 69:30–41, 2008.
- S. M. Butler and A. Camilli. Going against the grain: chemotaxis and infection in *Vibrio cholerae*. *Nat Rev Micro*, 3:611–620, 2005.
- A. Celani and M. Vergassola. Bacterial strategies for chemotaxis response. *Proc Natl Acad Sci U S A*, 107:1391–1396, 2010.
- A. Chalah and R. M. Weis. Site-specific and synergistic stimulation of methylation on the bacterial chemotaxis receptor Tsr by serine and CheW. *BMC Microbiol*, 5:12, 2005.
- D. Chelsky, N. I. Gutterson, and D. E. Koshland. A diffusion assay for detection and quantitation of methyl-esterified proteins on polyacrylamide gels. *Anal Biochem*, 141:143–148, 1984.
- D. A. Clark and L. C. Grant. The bacterial chemotactic response reflects a compromise between transient and steady-state behavior. *Proc Natl Acad Sci U S A*, 102:9150–9155, 2005.
- D. Clausznitzer, O. Oleksiuk, L. Løvdok, V. Sourjik, and R. G. Endres. Chemotactic response and adaptation dynamics in *Escherichia coli*. *PLoS Comput Biol*, 6:e1000784, 2010.
- P. Cluzel, M. Surette, and S. Leibler. An ultrasensitive bacterial motor revealed by monitoring signaling proteins in single cells. *Science*, 287:1652–1655, 2000.

## Bibliography

---

- A. Colman-Lerner, A. Gordon, E. Serra, T. Chin, O. Resnekov, D. Endy, C. G. Pesce, and R. Brent. Regulated cell-to-cell variation in a cell-fate decision system. *Nature*, 437: 699–706, 2005.
- J. S. Condeelis, J. B. Wyckoff, M. Bailly, R. Pestell, D. Lawrence, J. Backer, and J. E. Segall. Lamellipodia in invasion. *Semin Cancer Biol*, 11:119 – 128, 2001.
- M. A. Croxen. Molecular mechanisms of *Escherichia coli* pathogenicity. *Nat Rev Micro*, 8:26–38, 2010.
- S. M. Dawis. A molecular basis for Weber’s law. *Vis Neurosci*, 7:285–320, 1991.
- S. Dehaene. The neural basis of the Weber-Fechner law: a logarithmic mental number line. *Trends Cogn Sci*, 7:145–147, 2003.
- P. B. Detwiler, S. Ramanathan, A. Sengupta, and B. I. Shraiman. Engineering aspects of enzymatic signal transduction: photoreceptors in the retina. *Biophys J*, 79:2801–2817, 2000.
- T. A. Duke, N. Le Novère, and D. Bray. Conformational spread in a ring of proteins: a stochastic approach to allostery. *J Mol Biol*, 308:541–553, 2001.
- T. A. J. Duke and D. Bray. Heightened sensitivity of a lattice of membrane receptors. *Proc Natl Acad Sci U S A*, 96:10104–10108, 1999.
- F. A. Dunn and F. Rieke. The impact of photoreceptor noise on retinal gain controls. *Curr Opin Neurobiol*, 16:363–370, 2006.
- M. Eisenbach. Bacterial chemotaxis. In M. Eisenbach, editor, *Chemotaxis*, pages 53–215. Imperial College Press, 2004.
- A. Eldar and M. B. Elowitz. Functional roles for noise in genetic circuits. *Nature*, 467: 167–173, 2010.
- M. B. Elowitz, A. J. Levine, E. D. Siggia, and P. S. Swain. Stochastic gene expression in a single cell. *Science*, 297:1183–1186, 2002.
- T. Emonet and P. Cluzel. Relationship between cellular response and behavioral variability in bacterial chemotaxis. *Proc Natl Acad Sci U S A*, 105:3304–3309, 2008.

- R. G. Endres and N. S. Wingreen. Precise adaptation in bacterial chemotaxis through “assistance neighborhoods”. *Proc Natl Acad Sci U S A*, 103:13040–13044, 2006.
- R. G. Endres and N. S. Wingreen. Accuracy of direct gradient sensing by single cells. *Proc Natl Acad Sci U S A*, 105:15749–15754, 2008.
- R. G. Endres, O. Oleksiuk, C. H. Hansen, Y. Meir, V. Sourjik, and N. S. Wingreen. Variable sizes of *Escherichia coli* chemoreceptor signaling teams. *Mol Syst Biol*, 4:211, 2008.
- J. J. Falke and G. L. Hazelbauer. Transmembrane signaling in bacterial chemoreceptors. *Trends Biochem Sci*, 26:257–265, 2001.
- S. Funamoto, R. Meili, S. Lee, L. Parry, and R. A. Firtel. Spatial and temporal regulation of 3-phosphoinositides by PI 3-kinase and PTEN mediates chemotaxis. *CELL*, 109:611–623, 2002.
- E. J. Gauger, M. P. Leatham, R. Mercado-Lubo, D. C. Laux, T. Conway, and P. S. Cohen. Role of motility and the *flhDC* operon in *Escherichia coli* MG1655 colonization of the mouse intestine. *Infect Immun*, 75:3315–3324, 2007.
- G. Gerisch. Chemotaxis in *Dictyostelium*. *Ann Rev Physiol*, 44:535–552, 1982.
- J. E. Gestwicki and L. L. Kiessling. Inter-receptor communication through arrays of bacterial chemoreceptors. *Nature*, 415:81–84, 2002.
- J. E. Gestwicki, A. C. Lamanna, R. M. Harshey, L. L. McCarter, L. L. Kiessling, and J. Adler. Evolutionary conservation of methyl-accepting chemotaxis protein location in bacteria and archaea. *J Bacteriol*, 182:6499–6502, 2000.
- J. A. Girón. *Colonization of mucosal surfaces*, chapter 16, pages 213–235. ASM Press, Washington, D.C., 2005.
- G. D. Glekas, J. R. Cates, T. M. Cohen, C. Rao, and G. W. Ordal. Site-specific methylation in *Bacillus subtilis* chemotaxis: The effect of covalent modifications to the chemotaxis receptor McpB. *Microbiology*, 2010.
- J. P. Goldman, M. D. Levin, and D. Bray. Signal amplification in a lattice of coupled protein kinases. *Mol BioSyst*, 5:1853–1859, 2009.

## Bibliography

---

- D. Greenfield, A. L. McEvoy, H. Shroff, G. E. Crooks, N. S. Wingreen, E. Betzig, and J. Liphardt. Self-organization of the *Escherichia coli* chemotaxis network imaged with super-resolution light microscopy. *PLoS Biol*, 7:e1000137, 2009.
- T. Gregor, D. W. Tank, P. F. Wieschaus, and W. Bialek. Probing the limits to positional information. *Cell*, 130:153–164, 2007.
- R. L. Gregory. *Eye and Brain: The Psychology of Seeing*. Oxford University Press, Oxford., 1998.
- T. Gurry, O. Kahramanođulları, and R. G. Endres. Biophysical mechanism for ras-nanocluster formation and signaling in plasma membrane. *PLoS ONE*, 4:e6148, 2009.
- C. H. Hansen, R. G. Endres, and N. S. Wingreen. Chemotaxis in *Escherichia coli*: a molecular model for robust precise adaptation. *PLoS Comput Biol*, 4:e1, 2008.
- W. L. Hao and Y. K. Lee. Microflora of the gastrointestinal tract: a review. *Methods Mol Biol*, 268:491–502, 2004.
- G. L. Hazelbauer. Bacterial chemoreceptors. *Curr Opin Struct Biol*, 2:505–510, 1992.
- G. L. Hazelbauer and W. C. Lai. Bacterial chemoreceptors: providing enhanced features to two-component signaling. *Curr Opin Microbiol*, 13:124–132, 2010.
- M. Hegde, D. L. Englert, S. S. W. B. and Cohn, C. Vogt, T. K. Wood, M. D. Manson, and A. Jayaraman. Chemotaxis to the quorum-sensing signal AI-2 requires the Tsr chemoreceptor and the periplasmic LsrB AI-2-binding protein. *J Bacteriol*, pages JB.01196–10, 2010.
- J. M. Henke and B. L. Bassler. Three parallel quorum-sensing systems regulate gene expression in *Vibrio harveyi*. *J Bacteriol*, 186:690214, 2004.
- M. A. Hilliard, A. J. Apicella, R. Kerr, H. Suzuki, P. Bazzicalupo, and W. R. Schafer. *In vivo* imaging of *C. elegans* ASH neurons: cellular response and adaptation to chemical repellents. *EMBO J*, 24:63–72, 2005.
- M. I. Hutchings, H. J. Hong, and M. J. Buttner. The vancomycin resistance VanRS two-component signal transduction system of *Streptomyces coelicolor*. *Mol Microbiol*, 59: 92335, 2006.



- M. Ibanes and J. C. I. Belmonte. Theoretical and experimental approaches to understand morphogen gradients. *Mol Syst Biol*, 4:176, 2008.
- M. J. Jaasma, W. M. Jackson, R. Y. Tang, and T. M. Keaveny. Adaptation of cellular mechanical behavior to mechanical loading for osteoblastic cells. *J Biomech*, 40:1938–1945, 2007.
- M. Jiang, W. Shao, M. Perego, and J. A. Hoch. Multiple histidine kinases regulate entry into stationary phase and sporulation in *Bacillus subtilis*. *Mol Microbiol*, 38:535–342, 2000.
- J. K. Johnson, S. S. Hsiao, and T. Yoshioka. Neural coding and the basic law of psychophysics. *Neuroscientist*, 8:111–121, 2002.
- Y. Kalinin, S. Neumann, V. Sourjik, and M. Wu. Responses of *Escherichia coli* bacteria to two opposing chemoattractant gradients depend on the chemoreceptor ratio. *J Bacteriol*, 192:1796–1800, 2010.
- Y. V. Kalinin, L. Jiang, Y. Tu, and M. Wu. Logarithmic sensing in *Escherichia coli* bacterial chemotaxis. *Biophys J*, 96:2439–2448, 2009.
- T. Kang, J. Han, and K. S. Lee. Concentration gradient generator using a convective-diffusive balance. *Lab Chip*, 8:1220–1222, 2008.
- M. J. Kennedy. Role of motility, chemotaxis, and adhesion in microbial ecology. *Ann NY Acad Sci*, 506:260–273, 1987.
- D. Kentner and V. Sourjik. Dynamic map of protein interactions in the *Escherichia coli* chemotaxis pathway. *Mol Syst Biol*, 5:238, 2009.
- J. E. Keymer, R. G. Endres, M. Skoge, Y. Meir, and N. S. Wingreen. Chemosensing in *Escherichia coli*: two regimes of two-state receptors. *Proc Natl Acad Sci U S A*, 103:1786–1791, 2006.
- C. M. Khursigara, X. Wu, and S. Subramaniam. Chemoreceptors in *Caulobacter crescentus*: Trimers of receptor dimers in a partially ordered hexagonally packed array. *J Bacteriol*, 190:6805–6810, 2008a.

## Bibliography

---

- C. M. Khursigara, X. Wu, P. Zhang, J. Lefman, and S. Subramaniam. Role of HAMP domains in chemotaxis signaling by bacterial chemoreceptors. *Proc Natl Acad Sci U S A*, 105:16555–16560, 2008b.
- H. Kim and S. K. Farrand. Opine catabolic loci from *Agrobacterium* plasmids confer chemotaxis to their cognate substrates. *Mol Plant Microbe Interact*, 11:131–143, 1998.
- P. Kim, E. Chung, H. Yamashita, K. E. Hung, A. Mizoguchi, R. Kucherlapati, D. Fukumura, R. K. Jain, and S. H. Yun. *In vivo* wide-area cellular imaging by side-view endomicroscopy. *Nat Methods*, 7:303–305, 2010.
- P. E. Kloeden and E. Platen. *Numerical solution of stochastic differential equations*. Springer-Verlag, Berlin, New York, 1992.
- J. Koester. pages 81–94. McGraw-Hill, New York, 2000.
- M. Kollmann, L. Løvdok, K. Bartholome, J. Timmer, and V. Sourjik. Design principles of a bacterial signalling network. *Nature*, 438:504–507, 2005.
- E. Korobkova, T. Emonet, J. Vilar, T. Shimizu, and P. Cluzel. From molecular noise to behavioral variability in a single bacterium. *Nature*, 428:574–578, 2004.
- E. Korobkova, T. Emonet, H. Park, and P. Cluzel. Hidden stochastic nature of a single bacterial motor. *Phys Rev Letters*, 96:58105, 2006.
- E. N. Kort, M. F. Goy, S. H. Larsen, and J. Adler. Methylation of a membrane protein involved in bacterial chemotaxis. *Proc Nat Acad Sci U S A*, 72:3939–3943, 1975.
- D. E. Koshland. Biochemistry of sensing and adaptation in a simple bacterial system. *Ann Rev Biochem*, 50:765–782, 1981.
- D. E. Koshland Jr, A. Goldbeter, and J. B. Stock. Amplification and adaptation in regulatory and sensory systems. *Science*, 217:220–225, 1982.
- R. Kubo. Statistical mechanical theory of irreversible processes i. *Journal of the Physical Society of Japan*, 12:570 – 586, 1957.
- W. C. Lai and G. L. Hazelbauer. Carboxyl-terminal extensions beyond the conserved pentapeptide reduce rates of chemoreceptor adaptational modification. *J Bacteriol*, 187:5115–5121, 2005.

- W. C. Lai, L. A. Barnakova, A. N. Barnakov, and G. L. Hazelbauer. Similarities and differences in interactions of the activity-enhancing chemoreceptor pentapeptide with the two enzymes of adaptational modification. *J Bacteriol*, 188:5646–5649, 2006a.
- W. C. Lai, B. D. Beel, and G. L. Hazelbauer. Adaptational modification and ligand occupancy have opposite effects on positioning of the transmembrane signalling helix of a chemoreceptor. *Mol Microbiol*, 61:1081–1090, 2006b.
- M. T. Laub and M. Goulian. Specificity in two-component signal transduction pathways. *Ann Rev Genet*, 41:121–145, 2007.
- S. Laughlin. A simple coding procedure enhances a neuron’s information capacity. *Z Naturforsch*, 36:910–912, 1981.
- S. B. Laughlin. Form and function in retinal processing. *Trends Neurosci*, 10:478–483, 1987.
- S. B. Laughlin. The role of sensory adaptation in the retina. *J Exp Biol*, 146:39–62, 1989.
- A. Lee, J. L. O’Rourke, P. J. Barrington, and T. J. Trust. Mucus colonization as a determinant of pathogenicity in intestinal infection by *Campylobacter jejuni*: a mouse cecal model. *Infect Immun*, 51:536–546, 1986.
- I. Lestas, G. Vinnicombe, and J. Paulsson. Fundamental limits on the suppression of molecular fluctuations. *Nature*, 467:174–178, 2010.
- G. Li and R. M. Weis. Covalent modification regulates ligand binding to receptor complexes in the chemosensory system of *Escherichia coli*. *Cell*, 100:357–365, 2000.
- J. Li, R. V. Swanson, M. I. Simon, and R. M. Weis. Response regulators CheB and CheY exhibit competitive binding to the kinase CheA. *Biochemistry*, 34:14626–14636, 1995.
- M. Li and G. L. Hazelbauer. Cellular stoichiometry of the components of the chemotaxis signaling complex. *J Bacteriol*, 186:3687–3694, 2004.
- M. Li and G. L. Hazelbauer. Adaptational assistance in clusters of bacterial chemoreceptors. *Mol Microbiol*, 56:1617–1626, 2005.
- M. Li and G. L. Hazelbauer. The carboxyl-terminal linker is important for chemoreceptor function. *Mol Microbiol*, 60:469–479, 2006.

## Bibliography

---

- Z. Li and J. B. Stock. Protein carboxyl methylation and the biochemistry of memory. *Biol Chem*, 390:1087–1096, 2009.
- X. Liu and R. E. Parales. Bacterial chemotaxis to atrazine and related s-triazines. *Appl Environ Microbiol*, 75:5481–5488, 2009.
- T. Long, K. C. Tu, Y. Wang, P. Mehta, N. P. Ong, B. L. Bassler, and N. S. Wingreen. Quantifying the integration of quorum-sensing signals with single-cell resolution. *PLoS Biol*, 78:e68, 2009.
- L. Løvdok, M. Kollmann, and V. Sourjik. Co-expression of signaling proteins improves robustness of the bacterial chemotaxis pathway. *J Biotechnol*, 129:173–180, 2007.
- R. Lux, A. Moter, and W. Shi. Chemotaxis in pathogenic spirochetes: directed movement toward targeting tissues? *J Mol Microbiol Biotechnol*, 2:355–364, 2000.
- R. M. Macnab. Flagella and motility. In F. Neidhardt, R. Curtiss, J. Ingraham, E. Lin, and K. Low et al., editors, *Escherichia coli and Salmonella: Cellular and Molecular Biology*, pages 123–145. ASM Press, Washington, D.C., 1996.
- J. H. Martin. *Flagella and motility*, chapter 13, pages 614–624. McGraw-Hill, New York, 2000.
- W. Marwan, S. I. Bibikov, M. Montrone, and D. Oesterhelt. Mechanism of photosensory adaptation in *Halobacterium salinarium*. *J Mol Biol*, 246:493–499, 1995.
- G. Meacci and Y. Tu. Dynamics of the bacterial flagellar motor with multiple stators. *Proc Natl Acad Sci U S A*, 106:3746–3751, 2009.
- P. Mehta, S. Goyal, T. Long, B. L. Bassler, and N. S. Wingreen. Information processing and signal integration in bacterial quorum sensing. *Mol Syst Biol*, 5:325, 2009.
- B. A. Mello and Y. Tu. Perfect and near-perfect adaptation in a model of bacterial chemotaxis. *Biophys J*, 84:2943–2956, 2003a.
- B. A. Mello and Y. Tu. Quantitative modeling of sensitivity in bacterial chemotaxis: The role of coupling among different chemoreceptor species. *Proc Natl Acad Sci U S A*, 100:8223–8228, 2003b.

- B. A. Mello and Y. Tu. An allosteric model for heterogeneous receptor complexes: understanding bacterial chemotaxis responses to multiple stimuli. *Proc Natl Acad Sci U S A*, 102:17354–17359, 2005.
- B. A. Mello and Y. Tu. Effects of adaptation in maintaining high sensitivity over a wide range of backgrounds for *Escherichia coli* chemotaxis. *Biophys J*, 92:2329–2337, 2007.
- R. Mesibov, G. W. Ordal, and J. Adler. The range of attractant concentrations for bacterial chemotaxis and the threshold and size of response over this range. Weber law and related phenomena. *J Gen Physiol*, 62:203–223, 1973.
- J. G. Mitchell and K. Kogure. Bacterial motility: links to the environment and a driving force for microbial physics. *FEMS Microbiol Ecol*, 55:3–16, 2006.
- J. Monod, J. Wyman, and J. P. Changeux. On the nature of allosteric transitions: A plausible model. *J Mol Biol*, 12:88–118, 1965.
- T. Mora, H. Yu, Y. Sowa, and N. S. Wingreen. Steps in the bacterial flagellar motor. *PLoS Comput Biol*, 5:e1000540, 2009a.
- T. Mora, H. Yu, and N. S. Wingreen. Modeling torque versus speed, shot noise, and rotational diffusion of the bacterial flagellar motor. *Phys Rev Lett*, 103:248102, 2009b.
- C. J. Morton-Firth and D. Bray. Predicting temporal fluctuations in an intracellular signalling pathway. *J Theor Biol*, 192:117–128, 1998.
- D. Muzzey, C. A. Gómez-Urbe, J. T. Mettetal, and A. van Oudenaarden. A systems-level analysis of perfect adaptation in yeast osmoregulation. *Cell*, 138:160–171, 2009.
- J. P. Nataro. *Colonization of mucosal surfaces*, chapter 13, pages 179–186. ASM Press, Washington, D.C., 2005.
- W.-L. Ng and B. L. Bassler. Bacterial quorum-sensing network architectures. *Annu Rev Genet*, 43:197–222, 2009.
- C. O’Connor and P. Matsumura. The accessibility of Cys-120 in CheAS is important for the binding of CheZ and enhancement of CheZ phosphatase activity. *Biochemistry*, 43: 6909–6916, 2004.
- B. A. Olshausen and D. J. Field. Vision and the coding of natural images. *Am Sci*, 88: 238–245, 2000.

## Bibliography

---

- R. O'Toole, S. Lundberg, S. Fredriksson, A. Jansson, B. Nilsson, and H. Wolf-Watz. The chemotactic response of *Vibrio anguillarum* to fish intestinal mucus is mediated by a combination of multiple mucus components. *J. Bacteriol.*, 181:4308–4317, 1999.
- S. Pandya, P. Iyer, V. Gaitonde, T. Parekh, and A. Desai. Chemotaxis of rhizobium SP.S2 towards *Cajanus cajan* root exudate and its major components. *Current Microbiology*, 38:205–209, 1999.
- S. Park, P. M. Wolanin, E. A. Yuzbashyan, P. Silberzan, J. B. Stock, and R. H. Austin. Motion to form a quorum. *Science*, 301:188, 2003.
- J. S. Parkinson. Signaling mechanisms of HAMP domains in chemoreceptors and sensor kinases. *Ann Rev Microbiol*, 64:101–122, 2010.
- J. Paulsson. Models of stochastic gene expression. *Phys Life Rev.*, 2:157–175, 2005.
- J. M. Pedraza and A. van Oudenaarden. Noise propagation in gene networks. *Science*, 307:1965–1969, 2005.
- R. Phillips, J. Kondev, and J. Theriot. *Physical Biology of the Cell*, chapter 6.4, pages 219ff, 248ff. Garland Science, Taylor and Francis Group, LLC, 2009.
- M. S. Pittman, M. Goodwin, and D. J. Kelly. Chemotaxis in the human gastric pathogen *Helicobacter pylori*: different roles for CheW and the three CheV paralogues, and evidence for CheV2 phosphorylation. *Microbiology*, 147:2493–2504, 2001.
- S. L. Porter, G. H. Wadhams, and J. P. Armitage. *Rhodobacter sphaeroides*: complexity in chemotactic signalling. *Trends in Microbiology*, 16:251 – 260, 2008.
- L. K. Poulsen, F. Lan, C. S. Kristensen, P. Hobolth, S. Molin, and K. A. Krogh. Spatial distribution of *Escherichia coli* in the mouse large intestine inferred from rRNA in situ hybridization. *Infect Immun*, 62:5191–5194, 1994.
- E. N. Pugh Jr, S. Nikonov, and T. D. Lamb. Molecular mechanisms of vertebrate photoreceptor light adaptation. *Curr Opin Neurobiol*, 9:410–418, 1999.
- J. F. Rawls, M. A. Mahowald, A. L. Goodman, C. M. Trent, and J. I. Gordon. *In vivo* imaging and genetic analysis link bacterial motility and symbiosis in the zebrafish gut. *Proc Natl Acad Sci U S A*, 104:7622–7627, 2007.

- B. E. Scharf, K. A. Fahrner, L. Turner, and H. C. Berg. Control of direction of flagellar rotation in bacterial chemotaxis. *Proc Natl Acad Sci U S A*, 95:201–206, 1998.
- S. Schulmeister, M. Rutterf, S. Thiem, D. Kentner, D. Lebedz, and V. Sourjik. Protein exchange dynamics at chemoreceptor clusters in *Escherichia coli*. *Proc Natl Acad Sci U S A*, 105:6403–6408, 2008.
- J. E. Segall, S. M. Block, and H. C. Berg. Temporal comparisons in bacterial chemotaxis. *Proc Natl Acad Sci U S A*, 83:8987–8991, 1986.
- W. Shi and D. R. Zusman. Sensory adaptation during negative chemotaxis in *Myxococcus xanthus*. *J Bacteriol*, 176:1517–1520, 1994.
- Y. Shi and T. Duke. Cooperative model of bacterial sensing. *Phys Rev E*, 58:6399–6406, 1998.
- T. S. Shimizu, Y. Tu, and H. C. Berg. A modular gradient-sensing network for chemotaxis in *Escherichia coli* revealed by responses to time-varying stimuli. *Mol Syst Biol*, 6:382, 2010.
- D. Shiomi, S. Banno, M. Homma, and I. Kawagishi. Stabilization of polar localization of a chemoreceptor via its covalent modifications and its communication with a different chemoreceptor. *J Bacteriol*, 187:7647–7654, 2005.
- J. Sinha, S. J. Reyes, and J. P. Gallivan. Reprogramming bacteria to seek and destroy an herbicide. *Nat Chem Biol*, 6:464–470, 2010.
- M. L. Skoge, R. G. Endres, and N. S. Wingreen. Receptor-receptor coupling in bacterial chemotaxis: Evidence for strongly coupled clusters. *Biophys J*, 90:4317–4326, 2006.
- V. Sourjik. Receptor clustering and signal processing in *E. coli* chemotaxis. *Trends Microbiol*, 12:569–576, 2004.
- V. Sourjik and H. C. Berg. Binding of the *Escherichia coli* response regulator CheY to its target measured in vivo by fluorescence resonance energy transfer. *Proc Natl Acad Sci U S A*, 99:12669–12674, 2002a.
- V. Sourjik and H. C. Berg. Receptor sensitivity in bacterial chemotaxis. *Proc Natl Acad Sci U S A*, 99:123–127, 2002b.

## Bibliography

---

- V. Sourjik and H. C. Berg. Functional interactions between receptors in bacterial chemotaxis. *Nature*, 428:437–441, 2004.
- V. Sourjik, A. Vaknin, T. S. Shimizu, and H. C. Berg. *In vivo* measurement by FRET of pathway activity in bacterial chemotaxis. *Methods Enzymol*, 423:363–391, 2007.
- Y. Sowa and R. M. Berry. Bacterial flagellar motor. *Q Rev Biophys*, 41:103–132, 2008.
- Y. Sowa, A. D. Rowe, M. C. Leake, T. Yakushi, M. H. A. Ishijima, and R. M. Berry. Direct observation of steps in rotation of the bacterial flagellar motor. *Nature*, 437:916–919, 2005.
- J. Spehr, S. Hagendorf, J. Weiss, M. Spehr, T. Leinders-Zufall, and F. Zufall.  $\text{Ca}^{2+}$ -calmodulin feedback mediates sensory adaptation and inhibits pheromone-sensitive ion channels in the vomeronasal organ. *J Neurosci*, 29:2125–2135, 2009.
- R. C. Stewart. Activating and inhibitory mutations in the regulatory domains of the methylesterase in bacterial chemotaxis. *J Biol Chem*, 268:1921–1930, 1993.
- R. C. Stewart, K. Jahreis, and J. S. Parkinson. Rapid phosphotransfer to CheY from a CheA protein lacking the CheY-binding domain. *Biochemistry*, 39:13157–13165, 2000.
- R. Stratonovich. *Topics in the Theory of Random Noise*, volume I. Gordon and Breach, New York, 1963.
- C. A. Studdert and J. S. Parkinson. Insights into the organization and dynamics of bacterial chemoreceptor clusters through *in vivo* crosslinking studies. *Proc Natl Acad Sci U S A*, 102:15623–15628, 2005.
- C. A. Studdert and J. S. Parkinson. *In vivo* crosslinking methods for analyzing the assembly and architecture of chemoreceptor arrays. *Methods Enzymol*, 423:414–431, 2007.
- T. Tamura, K. Nakatani, and K. W. Yau. Calcium feedback and sensitivity regulation in primate rods. *J Gen Physiol*, 98:95–113, 1991.
- R. J. Taylor, D. Falconnet, A. Niemistö, S. A. Ramsey, S. Prinz, I. Shmulevich, T. Galitski, and C. L. Hansen. Dynamic analysis of MAPK signaling using a high-throughput microfluidic single-cell imaging platform. *Proc Natl Acad Sci U S A*, 2009.
- M. Thattai and A. van Oudenaarden. Attenuation of noise in ultrasensitive signaling cascades. *Biophys J*, 82:2943–2950, 2002.



- 
- G. Tkacik, C. G. Callan Jr, and W. Bialek. Information flow and optimization in transcriptional regulation. *Proc Natl Acad Sci U S A*, 105:12265–12270, 2008a.
- G. Tkacik, C. G. Callan Jr, and W. Bialek. Information capacity of genetic regulatory elements. *Phys Rev E*, 78:011910, 2008b.
- M. Toews, M. Goy, M. Springer, and J. Adler. Attractants and repellents control demethylation of methylated chemotaxis proteins in *Escherichia coli*. *Proc Natl Acad Sci U S A*, 76:5544–5548, 1979.
- F. Tostevin and P. R. ten Wolde. Mutual information between input and output trajectories of biochemical networks. *Phys Rev Lett*, 102:218101, 2009.
- Y. Tu and G. Grinstein. How white noise generates power-law switching in bacterial flagellar motors. *Phys Rev Lett*, 94:208101, 2005.
- Y. Tu, T. S. Shimizu, and H. C. Berg. Modeling the chemotactic response of *Escherichia coli* to time-varying stimuli. *Proc Natl Acad Sci U S A*, 105:14855–14860, 2008.
- L. Turner, A. D. Samuel, A. S. Stern, and H. C. Berg. Temperature dependence of switching of the bacterial flagellar motor by the protein CheY(13DK106YW). *Biophys J*, 77:597–603, 1999.
- T. Ursell, K. C. Huang, E. Peterson, and R. Phillips. Cooperative gating and spatial organization of membrane proteins through elastic interactions. *PLoS Comput Biol*, 3:e81, 2007.
- S. B. van Albada, S. Tănase-Nicola, and P. R. ten Wolde. The switching dynamics of the bacterial flagellar motor. *Mol Syst Biol*, 5:316, 2009.
- P. J. M. van Haastert and M. Postma. Biased random walk by stochastic fluctuations of chemoattractant-receptor interactions at the lower limit of detection. *Biophys J*, 93:1787–1796, 2007.
- J. H. van Hateren and H. P. Snippe. Simulating human cones from mid-mesopic up to high-photopic luminances. *J Vis*, 7:1–11, 2007.
- N. G. van Kampen. *Stochastic processes in physics and chemistry*. North Holland, 2007.
- N. Vladimirov and V. Sourjik. Chemotaxis: how bacteria use memory. *Biol Chem*, 390:1097–1104, 2009.
-

## Bibliography

---

- N. Vladimirov, L. Løvdok, D. Lebiecz, and V. Sourjik. Dependence of bacterial chemotaxis on gradient shape and adaptation rate. *PLoS Comput Biol*, 4:e1000242, 2008.
- G. H. Wadhams and J. P. Armitage. Making sense of it all: bacterial chemotaxis. *Nat Rev Mol Cell Biol*, 5:1024–1037, 2004.
- S. M. Williams, Y. Chen, T. M. Andermann, J. E. Carter, D. J. McGee, and K. M. Ottemann. *Helicobacter pylori* chemotaxis modulates inflammation and bacterium-gastric epithelium interactions in infected mice. *Infect Immun*, 75:3747–3757, 2007.
- P. M. Wolanin, M. D. Baker, N. R. Francis, D. R. Thomas, D. J. DeRosier, and J. B. Stock. Self-assembly of receptor/signaling complexes in bacterial chemotaxis. *Proc Natl Acad Sci U S A*, 103:14313–14318, 2006.
- G. M. Wolfaardt, M. J. H. T. Birkham, A. Bressel, M. N. Gardner, A. J. Sousa, D. R. Korber, and M. Pilaski. Microbial response to environmental gradients in a ceramic-based diffusion system. *Biotechnol Bioeng*, 100:141–149, 2008.
- F. S. Wouters and P. I. Bastiaens. Imaging protein-protein interactions by fluorescence resonance energy transfer (FRET) microscopy. *Curr Protoc Cell Biol*, 17:17.1, 2001.
- J. Wu, J. Li, G. Li, D. G. Long, and R. M. Weis. The receptor binding site for the methyltransferase of bacterial chemotaxis is distinct from the sites of methylation. *Biochemistry*, 35:4984–4993, 1996.
- J. Xing, F. Bai, R. Berry, and G. Oster. Torque-speed relationship of the bacterial flagellar motor. *Proc Natl Acad Sci U S A*, 103:1260–1265, 2006.
- Y. Xiong, C. Huang, P. A. Iglesias, and P. N. Devreotes. Cells navigate with a local-excitation, global-inhibition-biased excitable network. *Proc Natl Acad Sci U S A*, 107:17079–17086, 2010.
- T. Yi, Y. Huang, M. I. Simon, and J. Doyle. Robust perfect adaptation in bacterial chemotaxis through integral feedback control. *Proc Natl Acad Sci U S A*, 97:4649–4653, 2000.
- J. Yuan and H. C. Berg. Resurrection of the flagellar rotary motor near zero load. *Proc Natl Acad Sci U S A*, 105:1182–1185, 2008.

- S. H. Zigmond and S. J. Sullivan. Sensory adaptation of leukocytes to chemotactic peptides. *J Cell Biol*, 82:517–527, 1979.
- E. Ziv, I. Nemenman, and C. H. Wiggins. Optimal signal processing in small stochastic biochemical networks. *PLoS ONE*, 2:e1077, 2007.
- L. Zonia and D. Bray. Swimming patterns and dynamics of simulated *Escherichia coli* bacteria. *J R Soc Interface*, 6:1035–1046, 2009.